

Study of Ecohydrological Responses to Global Warming and
Grazing Pressure Changes in Mongolian Semi-arid Region

June 2011

Ishgaldan BYAMBAKHUU

Study of Ecohydrological Responses to Global Warming and
Grazing Pressure Changes in Mongolian Semi-arid Region

A Dissertation Submitted to
the Graduate School of Life and Environmental Sciences,
the University of Tsukuba
in Partial Fulfillment of the Requirements
for the Degree of Doctor of Philosophy in Science
(Doctoral Program in Geoenvironmental Sciences)

Ishgaldan BYAMBAKHUU

Abstract

In this study we present a simple coupled modeling framework for studying ecohydrological processes by investigating them at two distinctive surface conditions (nongrazing and grazing, in which nongrazing condition was obtained by a fence enclosure experiment). The coupled model consists of the century ecosystem model (version 4) and the TOPLATS hydrological model. The two models were directly coupled through a one-way data transfer method, which was used to simulate the carbon cycle, hydrological cycle and energy fluxes between vegetation, soils, and the atmosphere. On one side of the interface, century ecosystem model simulated the monthly ecological components and evapotranspiration. On the other side, TOPLATS hydrological model estimated hourly hydrological components together with energy fluxes. As a validation of this modeling framework, we performed a 4-year simulation with each model at point scale using field measurement datasets of the study areas. The data in this study were obtained in Kherlen river basin (39400 km²) in Mongolian steppe region during RAISE (Rangeland Atmosphere-Hydrosphere-Biosphere Interaction Study Experiment in Northeastern Asia) project campaign between 2003 and 2006. Also we run the century ecosystem model and TOPLATS hydrological model at spatial scale within a Kherlen river watershed with 1 x 1 km resolution. Consequently, this coupled environmental modeling system produced estimates of ecohydrological components at point and spatial scale. For future simulation of ecohydrological components, we applied the downscaled future projection of A2 scenario of IPCC by the regional climate model (Terrestrial Environment Research Center - Regional Atmospheric Modeling System (TERC - RAMS)). The future projection of ecohydrological components and their processes in this study area were performed based on four grazing pressure change scenarios (GP1-GP4), one climate change scenario (GW) and four grazing + climate change scenarios (GWP1-GWP4). The application and validation of century ecosystem model and TOPLATS hydrological model showed that they were equally applicable for both surface conditions at point and spatial scale to simulate ecohydrological components and their processes in Mongolian semi-arid region. Our coupled modeling approach simulated energy and hydrological components well which can be used for future projection estimation in this region.

Annual mean of precipitation over Kherlen river watershed was decreased by 10% in projected A2 scenario. Air temperature was increased by about 5°C over Kherlen river basin. The comparison between projected results under GW, GP1, GP2, GP3, GWP1, GWP2, GWP3 and B scenarios are summarized as follow: From GW scenario, aboveground biomass, belowground biomass, evaporation, transpiration, soil moisture, infiltration and discharge were

decreased by 23.9, 10.3, 23.5, 1.6, 7.9, 0.9 and 20.2% as compared with those of the current condition (B scenario). From GP1 scenario, aboveground biomass, belowground biomass, evaporation, transpiration, soil moisture, infiltration and discharge were decreased by 17.7, 3.2, 21.3, 7.5, 34.2, 2.4 and 0.9% as compared with those of the B scenario. From GP2 scenario, aboveground biomass, belowground biomass, evaporation, transpiration, soil moisture, infiltration and discharge were decreased by 25.3, 2.4, 18.7, 9.3, 34.2, 1.7 and 0.4% compared with those of the B scenario. Under GP3 scenario, aboveground biomass, belowground biomass, evaporation, transpiration and soil moisture were increased by 17.8, 0.2, 8.7, 7.2 and 2.9%, whereas infiltration and discharge were decreased by 4.3 and 5.7% compared with those of the B scenario. In GP4 scenario, aboveground biomass, belowground biomass, evaporation, transpiration and soil moisture were increased by 18.1, 0.9, 9.1, 8.2 and 3.9%, whereas infiltration and discharge were decreased by 4.4 and 2.7% as compared with those of the B scenario. Under GWP1, aboveground biomass, belowground biomass, evaporation, transpiration, soil moisture, infiltration and discharge were decreased by 32.3, 14.1, 34.1, 4.9, 31.1, 2.9 and 20.1% as compared with those of the B scenario. From GWP2 scenario, aboveground biomass, belowground biomass, evaporation, transpiration, soil moisture, infiltration and discharge were decreased by 38.3, 14.4, 19.7, 7.9, 31.5, 2.3 and 15.4% as compared with those of the B scenario. From GWP3 scenario, aboveground biomass was increased by 1.96% from the B scenario, whereas belowground biomass, evaporation, transpiration, soil moisture, infiltration and discharge were decreased by 9.6, 15.3, 0.1, 18.2, 2.6 and 21.4 as compared with those of the B scenario. In GWP4 scenario, aboveground biomass was increased by 2.6% from the B scenario because of grazing pressure, whereas belowground biomass, evaporation, transpiration, soil moisture, infiltration and discharge were decreased by 5.6, 18.3, 0.5, 19.4, 3.6 and 22.4% as compared with those of the B scenario.

In summary, aboveground biomass under different scenarios, aboveground, belowground biomass, evapotranspiration and soil moisture were found to be most sensitive to change in the combination of precipitation and grazing pressure. The grazing pressure changes scenarios showed that the maximum sustainable grazing pressure was $0.8 \text{ SE}_u \text{ ha}^{-1}$ over the Kherlen river basin in present condition and $0.6 \text{ SE}_u \text{ ha}^{-1}$ for future condition. Lastly, global warming has larger effect than the grazing pressure changes on ecohydrological components in Mongolian semi-arid region.

Keywords; ecotone, semi-arid, ecohydrological components, century model, TOPLATS model, future projection

Table of contents

| | |
|---|-----|
| Abstract | i |
| Table of Contents | iii |
| List of Tables | v |
| List of Figures | vi |
| Introduction | 1 |
| 1.1 Review of ecohydrological concepts..... | 1 |
| 1.2 Review of previous studies on modeling application..... | 3 |
| 1.3 Review of environmental studies in Mongolia..... | 5 |
| 1.4 Objectives..... | 7 |
| 1.5 Outline of the study..... | 8 |
| 2. Methods | 11 |
| 2.1 Study area..... | 11 |
| 2.2 Data processing..... | 16 |
| 2.2.1 Plant physiological data..... | 16 |
| 2.2.2 Meteorological and hydrological data..... | 16 |
| 2.2.3 Regional climate model data..... | 17 |
| 2.2.3.1 Current climate condition..... | 18 |
| 2.2.3.2 Future climate condition..... | 19 |
| 2.2.4 Grazing pressure intensity..... | 19 |
| 2.3 Models..... | 27 |
| 2.3.1 Century ecosystem model..... | 27 |
| 2.3.2 TOPLATS hydrological model..... | 31 |
| 2.3.3 Coupling of century and TOPLATS models..... | 35 |
| 2.3.3.1 Variable selection..... | 35 |
| 2.3.3.2 Coupling methodology..... | 36 |
| 3. Results and Discussion | 37 |
| 3.1 Application and validation of century ecosystem model..... | 37 |
| 3.1.1 Model parameters..... | 37 |
| 3.1.2 Validation at point scale..... | 42 |
| 3.1.3 Model sensitivity response to climate inputs..... | 50 |
| 3.1.3.1 Precipitation..... | 50 |
| 3.1.3.2 Air temperature..... | 51 |
| 3.1.4 Validation at spatial scale..... | 55 |
| 3.1.4.1 Spatial forcing data and time constant maps..... | 55 |
| 3.2 Application and validation of TOPLATS hydrological model..... | 69 |
| 3.2.1 Model parameters..... | 69 |
| 3.2.1.1 Soil parameters..... | 69 |
| 3.2.1.2 Surface and plant parameters..... | 72 |
| 3.2.1.3 Vegetation root and soil layers..... | 72 |
| 3.2.2 Application at point scale..... | 75 |
| 3.2.2.1 Daily and seasonal patterns of energy partitions..... | 75 |
| 3.2.2.1 Validation of TOPLATS hydrological model (without coupling)..... | 79 |
| 3.3 Coupled modeling approach on ecohydrological processes..... | 89 |
| 3.3.1 Coupling methodology for environmental modeling system..... | 89 |
| 3.3.2 Parameter selection and sensitive analysis..... | 91 |
| 3.3.3 Validation of model and its coupling with century ecosystem model.. | 97 |
| 3.4 Spatial application of TOPLATS hydrological model..... | 104 |

| | |
|--|------------|
| 3.5 Future projection of ecohydrology under environmental changes..... | 114 |
| Conclusions..... | 203 |
| Acknowledgements..... | 206 |
| References..... | 208 |
| Appendixes..... | 217 |

List of Tables

| | |
|--|-----|
| Table 1 Number of hydroecological and ecohydrological articles (between 1991 and 2003) classified by dominant (a) approach & (b) scale of research (Hannah et al. (2004))..... | 2 |
| Table 2 List of site name and their station type with some related information (See also Figs. 3 and 4)..... | 12 |
| Table 3 List of IMH Metostation and Metopost with some related information (See also Fig. 7 for location)..... | 21 |
| Table 4 Instruments for the observation at grazing site surface condition in KBU site (after Kotani, 2006)..... | 22 |
| Table 5 Instruments for the observation at nongrazing site surface condition in KBU site (after Kato, 2007)..... | 23 |
| Table 6 Instruments for the observation at BGN, DH, JGN and UDH site..... | 24 |
| Table 7 Data used in century ecosystem model application..... | 29 |
| Table 8 Data used in TOPLATS hydrological model application..... | 33 |
| Table 9 Maximum air temperature from 1993 to 2007 at KBU site (Routine observation data by IMH Metostation)..... | 38 |
| Table 10 Minimum air temperature from 1993 to 2007 at KBU site (Routine observation data by IMH Metostation)..... | 39 |
| Table 11 Precipitation from 1993 to 2007 at KBU site (Routine observation data by IMH Metostation)..... | 40 |
| Table 12 Comparison between measured and simulated aboveground biomass (g C m^{-2}) in KBU site..... | 45 |
| Table 13 Comparison of statistics between simulated and measured aboveground biomass and evapotranspiration at grazing and nongrazing surface condition in KBU site..... | 45 |
| Table 14 Different air temperature scenarios..... | 52 |
| Table 15 Correlation analysis for aboveground biomass and precipitation..... | 66 |
| Table 16 Soil look-up table of FOR and KBU site..... | 70 |
| Table 17 LAI, roughness length and zero-plane displacement at two different surface conditions in KBU site..... | 73 |
| Table 18 Vegetation look-up table of FOR and KBU site..... | 74 |
| Table 19 Monthly mean of energy fluxes and derived ratios of H/R_n , LE/R_n , G/R_n , H/LE (i.e. Bowen ratio), PPT , ET and ratio of ET/PPT (grazing condition, 2003)..... | 76 |
| Table 20 Monthly mean of energy fluxes and derived ratios of H/R_n , LE/R_n , G/R_n , H/LE (i.e. Bowen ratio), PPT , ET and ratio of ET/PPT (grazing condition, 2003)..... | 76 |
| Table 21 Monthly mean wind speed at grazing and nongrazing condition, 2003..... | 76 |
| Table 22 Comparison of statistics between simulated and measured energy and hydrological fluxes at KBU and FOR site (from 2003/04 to 2003/12)..... | 82 |
| Table 23 Comparison of statistics between simulated and measured energy and hydrological fluxes at KBU based on coupled modeling approach (from 2004/01 to 2005/12)..... | 99 |
| Table 24 Future scenarios..... | 116 |
| Table 25 Percentage of ecohydrological components under different scenarios from B scenario..... | 175 |
| Table 26 Mean, standard deviation and coefficient of discharge different scenarios..... | 200 |

List of Figures

| | |
|--|----|
| Fig. 1 Mongolian natural grassland (west-north part of kherlenbayan-Ulaan site)..... | 9 |
| Fig. 2 A representative part of kherlen river between Baganuur and Kherlenbayan-Ulaan..... | 10 |
| Fig. 3 Vegetation map of Mongolia (Saandar and Sugita, 2004) with the main observation sites in semiarid region, major rivers and lakes. Open circles represents study sites within Kherlen river basin. The abbreviation of each site is shown in Table 2..... | 13 |
| Fig. 4 The topographic map of upper Kherlen river basin with main observation sites. The abbreviation of each site is shown in Table 2..... | 14 |
| Fig. 5 Topographic map with a Landsat ETM+ of the KBU site with location of the stations, fenced area, and a former agricultural field indicated. Details of the stations' setting are also shown as a separate map. (Sugita et al., 2007). (A1 station: grazing surface condition, A2 station: nongrazing surface condition)..... | 15 |
| Fig. 6 Changes in annual mean of grazing pressure intensity of observation sites in the Kherlen river basin. (See Fig. 4 for location)..... | 20 |
| Fig. 7 Topographic map with ASTER GDEM of northeastern part of Mongolia. List of IMH metostations (with circle) and metopost (with triangular) in Kherlen river (Refer Table 3 for abbreviation)..... | 25 |
| Fig. 8 Topographic map with a Landsat ETM+ true color image of the FOR site. Contour lines are shown at 30 m intervals, except for the upper side of the map as this is outside the ASTER image from which contour lines were created. The flux station is indicated by a circle. Also shown at the upright corner is aerial photograph of the site (Sugita et al., 2007)..... | 26 |
| Fig. 9 Century ecosystem model scheme..... | 30 |
| Fig. 10 TOPLATS hydrological model scheme (R_n is net radiation; H is sensible heat flux; LE is latent heat flux; G is ground heat flux)..... | 34 |
| Fig. 11 Annual mean precipitation, maximum and minimum air temperature at KBU site from 1993 to 2007..... | 41 |
| Fig. 12 Spun up for 60 years based on a ten years mean climatology (averaged over 1993-2002) in KBU site..... | 46 |
| Fig. 13 Comparison of simulated and measured aboveground biomass at grazing and in KBU site (2003- 2006)..... | 47 |
| Fig. 14 Same as Fig 13, but for nongrazing surface condition in KBU site (2003- 2006). 47 | 47 |
| Fig. 15 Comparison of simulated and measured evapotranspiration at grazing and in KBU site (2003- 2006)..... | 48 |
| Fig. 16 Same as Fig15, but for nongrazing surface condition in KBU site (2003- 2006).. 48 | 48 |
| Fig. 17 Comparison of simulated and measured evapotranspiration at FOR site (2003)... 49 | 49 |
| Fig. 18 Aboveground biomass and evapotranspiration are sensitive to precipitation. (T is air temperature; P is precipitation)..... | 53 |
| Fig. 19 Aboveground biomass and evapotranspiration are sensitive to air temperature. (T is air temperature; P is precipitation)..... | 54 |
| Fig. 20 Example data of spatial distribution of precipitation. Watershed boundary represented by red line.. | 57 |
| Fig. 21 Same as Fig. 17, but for temperature..... | 57 |
| Fig. 22 Comparison of grazing parameters of century ecosystem model (GI_M) and those obtained by Mongolian statistical office data (GI_S). (Note: circles with red color represents inside the study area; triangular with black color represent outside of study area)..... | 58 |
| Fig. 23 Spatial distribution of grazing pressure map of upper part of Kherlen river watershed. Contour line are indicates sum boundary and red circles are show | |

| | |
|--|----|
| study sites..... | 59 |
| Fig. 24 Same as Fig. 23, but for vegetation map | 59 |
| Fig. 25 Spatial distribution of simulated aboveground biomass (g C m^{-2}) at grazing surface condition in Upper Kherlen river watershed. (2003/07)..... | 61 |
| Fig. 26 Spatial distribution of simulated aboveground biomass (g C m^{-2}) at nongrazing surface condition in Upper Kherlen river watershed. (2003/07)..... | 61 |
| Fig. 27 Spatial distribution of simulated aboveground biomass (g C m^{-2}) at grazing surface condition in Upper Kherlen river watershed. (2003/08)..... | 62 |
| Fig. 28 Spatial distribution of simulated aboveground biomass (g C m^{-2}) at nongrazing surface condition in Upper Kherlen river watershed. (2003/08)..... | 62 |
| Fig. 29 Spatial distribution of simulated evapotranspiration (mm month^{-1}) at grazing surface condition in Upper Kherlen river watershed. (2003/07)..... | 63 |
| Fig. 30 Spatial distribution of simulated evapotranspiration (mm month^{-1}) at nongrazing surface condition in Upper Kherlen river watershed. (2003/07) | 63 |
| Fig. 31 Spatial distribution of simulated evapotranspiration (mm month^{-1}) at grazing surface condition in Upper Kherlen river watershed. (2003/08)..... | 64 |
| Fig. 32 Spatial distribution of simulated evapotranspiration (mm month^{-1}) at nongrazing surface condition in Upper Kherlen river watershed. (2003/08)..... | 64 |
| Fig. 33 Grazing pressure effect on simulated aboveground biomass..... | 65 |
| Fig. 34 Comparison of simulated and measured monthly aboveground biomass at grazing surface condition in spatial scale, 2003 | 67 |
| Fig. 35 Comparison of simulated and measured monthly aboveground biomass at nongrazing surface condition in spatial scale, 2003..... | 68 |
| Fig. 36 Changes of the RMSE (root mean square error) Unit is m s^{-1} | 71 |
| Fig. 37 Changes of the r (correlation coefficient). Unit is m s^{-1} | 71 |
| Fig. 38 Diurnal change of measured energy fluxes at grazing (panel a) and nongrazing (panel b) condition in KBU site from April to December of 2003..... | 77 |
| Fig. 39 Available energy ($Rn-G$) and LE for grazing and nongrazing condition in KBU site. (May to September, 2003)..... | 78 |
| Fig. 40 Comparison of simulated and measured energy fluxes at grazing condition in KBU site from April to December of 2003. | 83 |
| Fig. 41 Comparison of simulated and measured hydrological fluxes at grazing condition in KBU site from April to December of 2003. (Note: Top panel represents evapotranspiration, soil moisture content at 10 and 30 cm depth)..... | 84 |
| Fig. 42 Transpiration and evaporation at grazing condition in KBU site from April to December of 2003..... | 84 |
| Fig. 43 Comparison of simulated and measured energy fluxes at nongrazing condition in KBU site from April to December of 2003..... | 85 |
| Fig. 44 Comparison of simulated and measured hydrological fluxes at grazing condition in KBU site from April to December of 2003. (Note: Top panel represents evapotranspiration, middle for soil moisture content at 10 and bottom for 30 cm depth)..... | 86 |
| Fig. 45 Transpiration and evaporation at grazing condition in KBU site from April to December of 2003..... | 86 |
| Fig. 46 Comparison of daily simulated and measured energy fluxes at FOR site from April to December, 2003. | 87 |
| Fig. 44 Comparison of simulated and measured hydrological fluxes at nongrazing condition in KBU site from April to December of 2003. (Note: Top panel represents evapotranspiration, middle for soil moisture content at 10 and bottom for 30 cm depth)..... | 87 |
| Fig. 48 Comparison between measured LAI and those obtained from simulated | |

| | |
|--|-----|
| aboveground biomass by century ecosystem model. Left hand side panel represents the grazing condition and right hand side panel represents nongrazing condition (KBU site, 2003)..... | 90 |
| Fig. 49 Condition in two days. Left hand side represent the no rain day (2003/ 06/08) and right hand side represent rainy day (2003/ 06/26)..... | 93 |
| Fig. 50 Comparison of simulated soil moisture content at 10 cm depth. Left hand side panel represents the results showing no rain day and effect of adopting different LAI of 0.3, 0.6, and 0.9. Right hand side panel represents the results showing rainy day and effect of using different LAI of 0.3, 0.6, and 0.9..... | 93 |
| Fig. 51 Same as in Fig. 50, but for evapotranspiration..... | 93 |
| Fig. 52 Same as in Fig. 50, but for transpiration..... | 94 |
| Fig. 53 Same as in Fig. 50, but for evaporation..... | 94 |
| Fig. 54 Same as in Fig. 50, but for infiltration..... | 94 |
| Fig. 55 Same as in Fig. 50, but for net radiation..... | 95 |
| Fig. 56 Same as in Fig. 50, but for ground heat flux..... | 95 |
| Fig. 57 Same as in Fig. 50, but for sensible heat flux..... | 95 |
| Fig. 58 Same as in Fig. 50, but for latent heat flux..... | 96 |
| Fig. 59 Same as in Fig. 50, but for soil temperature..... | 96 |
| Fig. 60 Comparison of simulated and measured energy fluxes at grazing condition in KBU site from 2004 to 2005. | 100 |
| Fig. 61 Comparison of simulated and measured hydrological fluxes at grazing condition in KBU site from 2004 to 2005. (Note: Top panel represents evapotranspiration, middle for soil moisture content at 10 and bottom for 30 cm depth)..... | 101 |
| Fig. 62 Transpiration and evaporation at grazing condition in KBU site from 2004 to 2005..... | 101 |
| Fig. 63 Comparison of simulated and measured energy fluxes at nongrazing condition in KBU site from 2004 to 2005..... | 102 |
| Fig. 64 Comparison of simulated and measured hydrological fluxes at nongrazing condition in KBU site from 2004 to 2005. (Note: Top panel represents evapotranspiration, middle for soil moisture content at 10 and bottom for 30 cm depth)..... | 103 |
| Fig. 65 Transpiration and evaporation at grazing condition in KBU site from 2004 to 2005..... | 103 |
| Fig. 66 Upper Kherlen river basin map of topographic index calculated from (a) ASTER GDEM data..... | 107 |
| Fig. 67 Upper Kherlen river basin map of vegetation, derived from Mongolian digital atlas (Saandar and Sugita, 2004)..... | 108 |
| Fig. 68 Upper Kherlen river basin map of soil, derived from Mongolian digital atlas (Saandar and Sugita, 2004)..... | 108 |
| Fig. 69 Stream network of the upper part of Kherlen river basin which was determined based on IMH of river network data..... | 109 |
| Fig. 70 Water table of the upper part of Kherlen river basin based on groundwater (Red circles) measurements along the Kherlen river basin. (Unit is m) | 109 |
| Fig. 71 Data points dQ/dt plotted against Q observed during 1959-2005 of upper part of Kherlen river basin, with lower envelope lines with slopes 1 and 3, respectively.. | 110 |
| Fig. 72 Spatial distribution of model-simulated average daily average energy and hydrological fluxes. (2005/04/01 (Unit $W m^{-2}$ and $mm h^{-1}$)..... | 111 |
| Fig. 73 Comparison of modeled and measured discharge at UDN discharge station in upper part of Kherlen river watershed. The panel (a) shows comparison of discharge of 2004 (Precipitation: Thiessen method), panel (b) for 2004 (Precipitation: Spatial forcing) and panel (c) for 2005 (Precipitation: Spatial forcing)..... | 112 |

| | |
|---|-----|
| Fig. 74 Thiessen polygon determined for each rain gauge at observation sites..... | 113 |
| Fig. 75 Annual mean, standard deviation (SD) and coefficient of variation (CV) of precipitation in current and future condition. The panels a), b) and c) represent mean, SD and CV of precipitation in current condition. The panels d), e) and f) represent mean, SD and CV of precipitation in future condition. The panels g), e) and i) represent the difference mean, SD and CV of precipitation between future and current condition. | 120 |
| Fig. 76 Annual mean, standard deviation (SD) and coefficient of variation (CV) of air temperature in current and future condition. The panels a), b) and c) represent mean, SD and CV of air temperature in current condition. The panels d), e) and f) represent mean, SD and CV of air temperature in future condition. The panels g), h) and i) represent the difference mean, SD and CV of air temperature between future and current condition..... | 121 |
| Fig. 77 Annual mean, standard deviation (SD) and coefficient of variation (CV) of aboveground biomass (<i>AB</i>) under B and GW scenarios + CO ₂ . The panels a), b) and c) represent mean, SD and CV of <i>AB</i> in B scenario. The panels d), e) and f) represent mean, SD and CV of <i>AB</i> under GW+ CO ₂ scenario. The panels g), h) and i) represent the difference of mean, SD and CV of <i>AB</i> between GW+ CO ₂ and B scenarios. (Unit is g C m ⁻²) | 122 |
| Fig. 78 Annual mean, standard deviation (SD) and coefficient of variation (CV) of aboveground biomass (<i>AB</i>) under B and GW scenarios. The panels a), b) and c) represent mean, SD and CV of <i>AB</i> in B scenario. The panels d), e) and f) represent mean, SD and CV of <i>AB</i> under GW scenario. The panels g), h) and i) represent the difference of mean, SD and CV of <i>AB</i> between GW and B scenarios. (Unit is g C m ⁻²)..... | 123 |
| Fig. 79 Annual mean, standard deviation (SD) and coefficient of variation (CV) of aboveground biomass (<i>AB</i>) under B and GP1 scenarios. The panels a), b) and c) represent mean, SD and CV of <i>AB</i> in B scenario. The panels d), e) and f) represent mean, SD and CV of <i>AB</i> under GP1 scenario. The panels g), h) and i) represent the difference of mean, SD and CV of <i>AB</i> between GP1 and B scenarios. (Unit is g C m ⁻²) | 124 |
| Fig. 80 Annual mean, standard deviation (SD) and coefficient of variation (CV) of aboveground biomass (<i>AB</i>) under B and GP2 scenarios. The panels a), b) and c) represent mean, SD and CV of <i>AB</i> in B scenario. The panels d), e) and f) represent mean, SD and CV of <i>AB</i> under GP2 scenario. The panels g), h) and i) represent the difference of mean, SD and CV of <i>AB</i> between GP2 and B scenarios. (Unit is g C m ⁻²) | 125 |
| Fig. 81 Annual mean, standard deviation (SD) and coefficient of variation (CV) of aboveground biomass (<i>AB</i>) under B and GP3 scenarios. The panels a), b) and c) represent mean, SD and CV of <i>AB</i> in B scenario. The panels d), e) and f) represent mean, SD and CV of <i>AB</i> under GP3 scenario. The panels g), h) and i) represent the difference of mean, SD and CV of <i>AB</i> between GP3 and B scenarios. (Unit is g C m ⁻²)..... | 126 |
| Fig. 82 Annual mean, standard deviation (SD) and coefficient of variation (CV) of aboveground biomass (<i>AB</i>) under B and GP4 scenarios. The panels a), b) and c) represent mean, SD and CV of <i>AB</i> in B scenario. The panels d), e) and f) represent mean, SD and CV of <i>AB</i> under GP4 scenario. The panels g), h) and i) represent the difference of mean, SD and CV of <i>AB</i> between GP4 and B scenarios. (Unit is g C m ⁻²)..... | 127 |
| Fig. 83 Annual mean, standard deviation (SD) and coefficient of variation (CV) of aboveground biomass (<i>AB</i>) under B and GWP1 scenarios. The panels a), b) and c) represent mean, SD and CV of <i>AB</i> in B scenario. The panels d), e) and f) | |

| | | |
|---------|--|-----|
| | represent mean, SD and CV of <i>AB</i> under GWP1 scenario. The panels g), h) and i) represent the difference of mean, SD and CV of <i>AB</i> between GWP1 and B scenarios. (Unit is g C m^{-2}) | 128 |
| Fig. 84 | Annual mean, standard deviation (SD) and coefficient of variation (CV) of aboveground biomass (<i>AB</i>) under B and GWP2 scenarios. The panels a), b) and c) represent mean, SD and CV of <i>AB</i> in B scenario. The panels d), e) and f) represent mean, SD and CV of <i>AB</i> under GWP2 scenario. The panels g), h) and i) represent the difference of mean, SD and CV of <i>AB</i> between GWP2 and B scenarios. (Unit is g C m^{-2}) | 129 |
| Fig. 85 | Annual mean, standard deviation (SD) and coefficient of variation (CV) of aboveground biomass (<i>AB</i>) under B and GWP3 scenarios. The panels a), b) and c) represent mean, SD and CV of <i>AB</i> in B scenario. The panels d), e) and f) represent mean, SD and CV of <i>AB</i> under GWP3 scenario. The panels g), h) and i) represent the difference of mean, SD and CV of <i>AB</i> between GWP3 and B scenarios. (Unit is g C m^{-2}) | 130 |
| Fig. 86 | Annual mean, standard deviation (SD) and coefficient of variation (CV) of aboveground biomass (<i>AB</i>) under B and GWP4 scenarios. The panels a), b) and c) represent mean, SD and CV of <i>AB</i> in B scenario. The panels d), e) and f) represent mean, SD and CV of <i>AB</i> under GWP4 scenario. The panels g), h) and i) represent the difference of mean, SD and CV of <i>AB</i> between GWP4 and B scenarios. (Unit is g C m^{-2}) | 131 |
| Fig. 87 | Annual mean, standard deviation (SD) and coefficient of variation (CV) of belowground biomass (<i>BB</i>) under B and GW scenarios. The panels a), b) and c) represent mean, SD and CV of <i>BB</i> in B scenario. The panels d), e) and f) represent mean, SD and CV of <i>BB</i> under GW scenario. The panels g), h) and i) represent the difference of mean, SD and CV of <i>BB</i> between GW and B scenarios. (Unit is g C m^{-2}) | 132 |
| Fig. 88 | Annual mean, standard deviation (SD) and coefficient of variation (CV) of belowground biomass (<i>BB</i>) under B and GP1 scenarios. The panels a), b) and c) represent mean, SD and CV of <i>BB</i> in B scenario. The panels d), e) and f) represent mean, SD and CV of <i>BB</i> under GP1 scenario. The panels g), h) and i) represent the difference of mean, SD and CV of <i>BB</i> between GP1 and B scenarios. (Unit is g C m^{-2}) | 133 |
| Fig. 89 | Annual mean, standard deviation (SD) and coefficient of variation (CV) of belowground biomass (<i>BB</i>) under B and GP2 scenarios. The panels a), b) and c) represent mean, SD and CV of <i>BB</i> in B scenario. The panels d), e) and f) represent mean, SD and CV of <i>BB</i> under GP2 scenario. The panels g), h) and i) represent the difference of mean, SD and CV of <i>BB</i> between GP2 and B scenarios. (Unit is g C m^{-2}) | 134 |
| Fig. 90 | Annual mean, standard deviation (SD) and coefficient of variation (CV) of belowground biomass (<i>BB</i>) under B and GP3 scenarios. The panels a), b) and c) represent mean, SD and CV of <i>BB</i> in B scenario. The panels d), e) and f) represent mean, SD and CV of <i>BB</i> under GP3 scenario. The panels g), h) and i) represent the difference of mean, SD and CV of <i>BB</i> between GP3 and B scenarios. (Unit is g C m^{-2}) | 135 |
| Fig. 91 | Annual mean, standard deviation (SD) and coefficient of variation (CV) of belowground biomass (<i>BB</i>) under B and GP4 scenarios. The panels a), b) and c) represent mean, SD and CV of <i>BB</i> in B scenario. The panels d), e) and f) represent mean, SD and CV of <i>BB</i> under GP4 scenario. The panels g), h) and i) represent the difference of mean, SD and CV of <i>BB</i> between GP4 and B scenarios. (Unit is g C m^{-2}) | 136 |
| Fig. 92 | Annual mean, standard deviation (SD) and coefficient of variation (CV) of | |

| | |
|--|-----|
| belowground biomass (<i>BB</i>) under B and GWP1 scenarios. The panels a), b) and c) represent mean, SD and CV of <i>BB</i> in B scenario. The panels d), e) and f) represent mean, SD and CV of <i>BB</i> under GWP1 scenario. The panels g), h) and i) represent the difference of mean, SD and CV of <i>BB</i> between GWP1 and B scenarios. (Unit is g C m^{-2}) | 137 |
| Fig. 93 Annual mean, standard deviation (SD) and coefficient of variation (CV) of belowground biomass (<i>BB</i>) under B and GWP2 scenarios. The panels a), b) and c) represent mean, SD and CV of <i>BB</i> in B scenario. The panels d), e) and f) represent mean, SD and CV of <i>BB</i> under GWP2 scenario. The panels g), h) and i) represent the difference of mean, SD and CV of <i>BB</i> between GWP2 and B scenarios. (Unit is g C m^{-2}) | 138 |
| Fig. 94 Annual mean, standard deviation (SD) and coefficient of variation (CV) of belowground biomass (<i>BB</i>) under B and GWP3 scenarios. The panels a), b) and c) represent mean, SD and CV of <i>BB</i> in B scenario. The panels d), e) and f) represent mean, SD and CV of <i>BB</i> under GWP3 scenario. The panels g), h) and i) represent the difference of mean, SD and CV of <i>BB</i> between GWP3 and B scenarios. (Unit is g C m^{-2}) | 139 |
| Fig. 95 Annual mean, standard deviation (SD) and coefficient of variation (CV) of belowground biomass (<i>BB</i>) under B and GWP4 scenarios. The panels a), b) and c) represent mean, SD and CV of <i>BB</i> in B scenario. The panels d), e) and f) represent mean, SD and CV of <i>BB</i> under GWP4 scenario. The panels g), h) and i) represent the difference of mean, SD and CV of <i>BB</i> between GWP4 and B scenarios. (Unit is g C m^{-2}) | 140 |
| Fig. 96 Annual mean, standard deviation (SD) and coefficient of variation (CV) of evapotranspiration (<i>ET</i>) under B and GW scenarios. The panels a), b) and c) represent mean, SD and CV of <i>ET</i> in B scenario. The panels d), e) and f) represent mean, SD and CV of <i>ET</i> under GW scenario. The panels g), h) and i) represent the difference of mean, SD and CV of <i>ET</i> between GW and B scenarios. (Unit is mm y^{-1}) | 141 |
| Fig. 97 Annual mean, standard deviation (SD) and coefficient of variation (CV) of evapotranspiration (<i>ET</i>) under B and GP1 scenarios. The panels a), b) and c) represent mean, SD and CV of <i>ET</i> in B scenario. The panels d), e) and f) represent mean, SD and CV of <i>ET</i> under GP1 scenario. The panels g), h) and i) represent the difference of mean, SD and CV of <i>ET</i> between GP1 and B scenarios. (Unit is mm y^{-1}) | 142 |
| Fig. 98 Annual mean, standard deviation (SD) and coefficient of variation (CV) of evapotranspiration (<i>ET</i>) under B and GP2 scenarios. The panels a), b) and c) represent mean, SD and CV of <i>ET</i> in B scenario. The panels d), e) and f) represent mean, SD and CV of <i>ET</i> under GP2 scenario. The panels g), h) and i) represent the difference of mean, SD and CV of <i>ET</i> between GP2 and B scenarios. (Unit is mm y^{-1}) | 143 |
| Fig. 99 Annual mean, standard deviation (SD) and coefficient of variation (CV) of evapotranspiration (<i>ET</i>) under B and GP3 scenarios. The panels a), b) and c) represent mean, SD and CV of <i>ET</i> in B scenario. The panels d), e) and f) represent mean, SD and CV of <i>ET</i> under GP3 scenario. The panels g), h) and i) represent the difference of mean, SD and CV of <i>ET</i> between GP3 and B scenarios. (Unit is mm y^{-1}) | 144 |
| Fig. 100 Annual mean, standard deviation (SD) and coefficient of variation (CV) of evapotranspiration (<i>ET</i>) under B and GP4 scenarios. The panels a), b) and c) represent mean, SD and CV of <i>ET</i> in B scenario. The panels d), e) and f) represent mean, SD and CV of <i>ET</i> under GP4 scenario. The panels g), h) and i) represent the difference of mean, SD and CV of <i>ET</i> between GP4 and B | |

| | |
|---|-----|
| scenarios. (Unit is mm y^{-1}) | 145 |
| Fig. 101 Annual mean, standard deviation (SD) and coefficient of variation (CV) of evapotranspiration (<i>ET</i>) under B and GWP1 scenarios. The panels a), b) and c) represent mean, SD and CV of <i>ET</i> in B scenario. The panels d), e) and f) represent mean, SD and CV of <i>ET</i> under GWP1 scenario. The panels g), h) and i) represent the difference of mean, SD and CV of <i>ET</i> between GWP1 and B scenarios. (Unit is mm y^{-1}) | 146 |
| Fig. 102 Annual mean, standard deviation (SD) and coefficient of variation (CV) of evapotranspiration (<i>ET</i>) under B and GWP2 scenarios. The panels a), b) and c) represent mean, SD and CV of <i>ET</i> in B scenario. The panels d), e) and f) represent mean, SD and CV of <i>ET</i> under GWP2 scenario. The panels g), h) and i) represent the difference of mean, SD and CV of <i>ET</i> between GWP2 and B scenarios. (Unit is mm y^{-1}) | 147 |
| Fig. 103 Annual mean, standard deviation (SD) and coefficient of variation (CV) of evapotranspiration (<i>ET</i>) under B and GWP3 scenarios. The panels a), b) and c) represent mean, SD and CV of <i>ET</i> in B scenario. The panels d), e) and f) represent mean, SD and CV of <i>ET</i> under GWP3 scenario. The panels g), h) and i) represent the difference of mean, SD and CV of <i>ET</i> between GWP3 and B scenarios. (Unit is mm y^{-1}) | 148 |
| Fig. 104 Annual mean, standard deviation (SD) and coefficient of variation (CV) of evapotranspiration (<i>ET</i>) under B and GWP4 scenarios. The panels a), b) and c) represent mean, SD and CV of <i>ET</i> in B scenario. The panels d), e) and f) represent mean, SD and CV of <i>ET</i> under GWP4 scenario. The panels g), h) and i) represent the difference of mean, SD and CV of <i>ET</i> between GWP4 and B scenarios. (Unit is mm y^{-1}) | 149 |
| Fig. 105 Annual mean, standard deviation (SD) and coefficient of variation (CV) of soil moisture (<i>SM</i>) under B and GW scenarios. The panels a), b) and c) represent mean, SD and CV of <i>SM</i> in B scenario. The panels d), e) and f) represent mean, SD and CV of <i>SM</i> under GW scenario. The panels g), h) and i) represent the difference of mean, SD and CV of <i>SM</i> between GW and B scenarios. (Unit is %). | 150 |
| Fig. 106 Annual mean, standard deviation (SD) and coefficient of variation (CV) of soil moisture (<i>SM</i>) under B and GP1 scenarios. The panels a), b) and c) represent mean, SD and CV of <i>SM</i> in B scenario. The panels d), e) and f) represent mean, SD and CV of <i>SM</i> under GP1 scenario. The panels g), h) and i) represent the difference of mean, SD and CV of <i>SM</i> between GP1 and B scenarios. (Unit is %). | 150 |
| Fig. 107 Annual mean, standard deviation (SD) and coefficient of variation (CV) of soil moisture (<i>SM</i>) under B and GP2 scenarios. The panels a), b) and c) represent mean, SD and CV of <i>SM</i> in B scenario. The panels d), e) and f) represent mean, SD and CV of <i>SM</i> under GP2 scenario. The panels g), h) and i) represent the difference of mean, SD and CV of <i>SM</i> between GP2 and B scenarios. (Unit is %). | 152 |
| Fig. 108 Annual mean, standard deviation (SD) and coefficient of variation (CV) of soil moisture (<i>SM</i>) under B and GP3 scenarios. The panels a), b) and c) represent mean, SD and CV of <i>SM</i> in B scenario. The panels d), e) and f) represent mean, SD and CV of <i>SM</i> under GP3 scenario. The panels g), h) and i) represent the difference of mean, SD and CV of <i>SM</i> between GP3 and B scenarios. (Unit is %). | 153 |
| Fig. 109 Annual mean, standard deviation (SD) and coefficient of variation (CV) of soil moisture (<i>SM</i>) under B and GP4 scenarios. The panels a), b) and c) represent mean, SD and CV of <i>SM</i> in B scenario. The panels d), e) and f) represent mean, | |

| | |
|---|-----|
| SD and CV of <i>SM</i> under GP4 scenario. The panels g), h) and i) represent the difference of mean, SD and CV of <i>SM</i> between GP4 and B scenarios. (Unit is %). | 154 |
| Fig. 110 Annual mean, standard deviation (SD) and coefficient of variation (CV) of soil moisture (<i>SM</i>) under B and GWP1 scenarios. The panels a), b) and c) represent mean, SD and CV of <i>SM</i> in B scenario. The panels d), e) and f) represent mean, SD and CV of <i>SM</i> under GWP1 scenario. The panels g), h) and i) represent the difference of mean, SD and CV of <i>SM</i> between GWP1 and B scenarios. (Unit is %). | 155 |
| Fig. 111 Annual mean, standard deviation (SD) and coefficient of variation (CV) of soil moisture (<i>SM</i>) under B and GWP2 scenarios. The panels a), b) and c) represent mean, SD and CV of <i>SM</i> in B scenario. The panels d), e) and f) represent mean, SD and CV of <i>SM</i> under GWP2 scenario. The panels g), h) and i) represent the difference of mean, SD and CV of <i>SM</i> between GWP2 and B scenarios. (Unit is %). | 156 |
| Fig. 112 Annual mean, standard deviation (SD) and coefficient of variation (CV) of soil moisture (<i>SM</i>) under B and GWP3 scenarios. The panels a), b) and c) represent mean, SD and CV of <i>SM</i> in B scenario. The panels d), e) and f) represent mean, SD and CV of <i>SM</i> under GWP3 scenario. The panels g), h) and i) represent the difference of mean, SD and CV of <i>SM</i> between GWP3 and B scenarios. (Unit is %). | 157 |
| Fig. 113 Annual mean, standard deviation (SD) and coefficient of variation (CV) of soil moisture (<i>SM</i>) under B and GWP4 scenarios. The panels a), b) and c) represent mean, SD and CV of <i>SM</i> in B scenario. The panels d), e) and f) represent mean, SD and CV of <i>SM</i> under GWP4 scenario. The panels g), h) and i) represent the difference of mean, SD and CV of <i>SM</i> between GWP4 and B scenarios. (Unit is %). | 158 |
| Fig. 114 Difference of annual mean precipitation (<i>P</i>) and evapotranspiration (<i>ET</i>). Panel a) for B scenario, b) for GP1 scenario, c) for GP2 scenario, d) for GP3 scenario, e) for GP4 scenario, f) for GW scenario, g) for GWP1 scenario, h) for GWP2 scenario, k) for GWP3 scenario and l) for GWP4 scenario. (Unit is mm y ⁻¹) | 159 |
| Fig. 115 Relation between ecohydrological components under B scenario. | 164 |
| Fig. 116 Relation between ecohydrological components under GW scenario. | 165 |
| Fig. 117 Relation between ecohydrological components under GP1 scenario. | 166 |
| Fig. 118 Relation between ecohydrological components under GP2 scenario. | 167 |
| Fig. 119 Relation between ecohydrological components under GP3 scenario | 168 |
| Fig. 120 Relation between ecohydrological components under GP4 scenario | 169 |
| Fig. 121 Relation between ecohydrological components under GWP1 scenario. | 170 |
| Fig. 122 Relation between ecohydrological components under GWP2 scenario. | 171 |
| Fig. 123 Relation between ecohydrological components under GWP3 scenario | 172 |
| Fig. 124 Relation between ecohydrological components under GWP3 scenario | 173 |
| Fig. 125 Variation of aboveground biomass (g C m ⁻²) and belowground biomass (g C m ⁻²). | 174 |
| Fig. 126 Variation of evapotranspiration (<i>ET</i> : mm y ⁻¹), difference of precipitation (<i>P</i> : mm y ⁻¹) and <i>ET</i> (<i>P-ET</i> : mm y ⁻¹) and soil moisture (<i>SM</i> : %), discharge (<i>D</i> : m ³ s ⁻¹) ground water storage (<i>GWS</i> : m) and <i>P</i> under different scenarios. | 174 |
| Fig. 127 Annual mean, standard deviation (SD) and coefficient of variation (CV) of aboveground biomass (<i>AB</i>) under B and GW scenarios. The panels a), b) and c) represent mean, SD and CV of <i>AB</i> in B scenario. The panels d), e) and f) represent mean, SD and CV of <i>AB</i> under GW scenario. The panels g), h) and i) represent the difference of mean, SD and CV of <i>AB</i> between GW and B | |

| | |
|---|-----|
| scenarios. (Unit is g C m^{-2})..... | 177 |
| Fig. 128 Annual mean, standard deviation (SD) and coefficient of variation (CV) of aboveground biomass (<i>AB</i>) under GP1 and GWP1 scenarios. The panels a), b) and c) represent mean, SD and CV of <i>AB</i> in GP1 scenario. The panels d), e) and f) represent mean, SD and CV of <i>AB</i> under GWP1 scenario. The panels g), h) and i) represent the difference of mean, SD and CV of <i>AB</i> between GWP1 and GP1 scenarios. (Unit is g C m^{-2})..... | 178 |
| Fig. 129 Annual mean, standard deviation (SD) and coefficient of variation (CV) of aboveground biomass (<i>AB</i>) under GP2 and GWP2 scenarios. The panels a), b) and c) represent mean, SD and CV of <i>AB</i> in GP2 scenario. The panels d), e) and f) represent mean, SD and CV of <i>AB</i> under GWP2 scenario. The panels g), h) and i) represent the difference of mean, SD and CV of <i>AB</i> between GWP2 and GP2 scenarios. (Unit is g C m^{-2})..... | 179 |
| Fig. 130 Annual mean, standard deviation (SD) and coefficient of variation (CV) of aboveground biomass (<i>AB</i>) under GP3 and GWP3 scenarios. The panels a), b) and c) represent mean, SD and CV of <i>AB</i> in GP3 scenario. The panels d), e) and f) represent mean, SD and CV of <i>AB</i> under GWP3 scenario. The panels g), h) and i) represent the difference of mean, SD and CV of <i>AB</i> between GWP3 and GP3 scenarios. (Unit is g C m^{-2}) | 180 |
| Fig. 131 Annual mean, standard deviation (SD) and coefficient of variation (CV) of aboveground biomass (<i>AB</i>) under GP4 and GWP4 scenarios. The panels a), b) and c) represent mean, SD and CV of <i>AB</i> in GP4 scenario. The panels d), e) and f) represent mean, SD and CV of <i>AB</i> under GWP3 scenario. The panels g), h) and i) represent the difference of mean, SD and CV of <i>AB</i> between GWP4 and GP4 scenarios. (Unit is g C m^{-2}) | 181 |
| Fig. 132 Annual mean, standard deviation (SD) and coefficient of variation (CV) of belowground biomass (<i>BB</i>) under B and GW scenarios. The panels a), b) and c) represent mean, SD and CV of <i>BB</i> in B scenario. The panels d), e) and f) represent mean, SD and CV of <i>BB</i> under GW scenario. The panels g), h) and i) represent the difference of mean, SD and CV of <i>BB</i> between GW and B scenarios. (Unit is g C m^{-2}) | 182 |
| Fig. 133 Annual mean, standard deviation (SD) and coefficient of variation (CV) of belowground biomass (<i>BB</i>) under GP1 and GWP1 scenarios. The panels a), b) and c) represent mean, SD and CV of <i>BB</i> in GP1 scenario. The panels d), e) and f) represent mean, SD and CV of <i>BB</i> under GWP1 scenario. The panels g), h) and i) represent the difference of mean, SD and CV of <i>BB</i> between GWP1 and GP1 scenarios. (Unit is g C m^{-2}) | 183 |
| Fig. 134 Annual mean, standard deviation (SD) and coefficient of variation (CV) of belowground biomass (<i>BB</i>) under GP2 and GWP2 scenarios. The panels a), b) and c) represent mean, SD and CV of <i>BB</i> in GP2 scenario. The panels d), e) and f) represent mean, SD and CV of <i>BB</i> under GWP2 scenario. The panels g), h) and i) represent the difference of mean, SD and CV of <i>BB</i> between GWP2 and GP2 scenarios. (Unit is g C m^{-2}) | 184 |
| Fig. 135 Annual mean, standard deviation (SD) and coefficient of variation (CV) of belowground biomass (<i>BB</i>) under GP3 and GWP3 scenarios. The panels a), b) and c) represent mean, SD and CV of <i>BB</i> in GP3 scenario. The panels d), e) and f) represent mean, SD and CV of <i>BB</i> under GWP3 scenario. The panels g), h) and i) represent the difference of mean, SD and CV of <i>BB</i> between GWP3 and GP3 scenarios. (Unit is g C m^{-2}) | 185 |
| Fig. 136 Annual mean, standard deviation (SD) and coefficient of variation (CV) of belowground biomass (<i>BB</i>) under GP4 and GWP4 scenarios. The panels a), b) and c) represent mean, SD and CV of <i>BB</i> in GP4 scenario. The panels d), e) | |

| | |
|---|-----|
| and f) represent mean, SD and CV of <i>BB</i> under GWP3 scenario. The panels g), h) and i) represent the difference of mean, SD and CV of <i>BB</i> between GWP4 and GP4 scenarios. (Unit is $g\ C\ m^{-2}$) | 186 |
| Fig. 137 Annual mean, standard deviation (SD) and coefficient of variation (CV) of evapotranspiration (<i>ET</i>) under B and GW scenarios. The panels a), b) and c) represent mean, SD and CV of <i>ET</i> in B scenario. The panels d), e) and f) represent mean, SD and CV of <i>ET</i> under GW scenario. The panels g), h) and i) represent the difference of mean, SD and CV of <i>ET</i> between GW and B scenarios. (Unit is $mm\ y^{-1}$) | 187 |
| Fig. 138 Annual mean, standard deviation (SD) and coefficient of variation (CV) of evapotranspiration (<i>ET</i>) under GP1 and GWP1 scenarios. The panels a), b) and c) represent mean, SD and CV of <i>ET</i> in GP1 scenario. The panels d), e) and f) represent mean, SD and CV of <i>ET</i> under GWP1 scenario. The panels g), h) and i) represent the difference of mean, SD and CV of <i>ET</i> between GWP1 and GP1 scenarios. (Unit is $mm\ y^{-1}$) | 188 |
| Fig. 139 Annual mean, standard deviation (SD) and coefficient of variation (CV) of evapotranspiration (<i>ET</i>) under GP2 and GWP2 scenarios. The panels a), b) and c) represent mean, SD and CV of <i>ET</i> in GP2 scenario. The panels d), e) and f) represent mean, SD and CV of <i>ET</i> under GWP2 scenario. The panels g), h) and i) represent the difference of mean, SD and CV of <i>ET</i> between GWP2 and GP2 scenarios. (Unit is $mm\ y^{-1}$) | 189 |
| Fig. 140 Annual mean, standard deviation (SD) and coefficient of variation (CV) of evapotranspiration (<i>ET</i>) under GP3 and GWP3 scenarios. The panels a), b) and c) represent mean, SD and CV of <i>ET</i> in GP3 scenario. The panels d), e) and f) represent mean, SD and CV of <i>ET</i> under GWP3 scenario. The panels g), h) and i) represent the difference of mean, SD and CV of <i>ET</i> between GWP3 and GP3 scenarios. (Unit is $mm\ y^{-1}$) | 190 |
| Fig. 141 Annual mean, standard deviation (SD) and coefficient of variation (CV) of evapotranspiration (<i>ET</i>) under GP4 and GWP4 scenarios. The panels a), b) and c) represent mean, SD and CV of <i>ET</i> in GP4 scenario. The panels d), e) and f) represent mean, SD and CV of <i>ET</i> under GWP4 scenario. The panels g), h) and i) represent the difference of mean, SD and CV of <i>ET</i> between GWP4 and GP4 scenarios. (Unit is $mm\ y^{-1}$) | 191 |
| Fig. 142 Annual mean, standard deviation (SD) and coefficient of variation (CV) of soil moisture (<i>SM</i>) under B and GW scenarios. The panels a), b) and c) represent mean, SD and CV of <i>SM</i> in B scenario. The panels d), e) and f) represent mean, SD and CV of <i>SM</i> under GW scenario. The panels g), h) and i) represent the difference of mean, SD and CV of <i>SM</i> between GW and B scenarios. (Unit is %) | 192 |
| Fig. 143 Annual mean, standard deviation (SD) and coefficient of variation (CV) of soil moisture (<i>SM</i>) under GP1 and GWP1 scenarios. The panels a), b) and c) represent mean, SD and CV of <i>SM</i> in GP1 scenario. The panels d), e) and f) represent mean, SD and CV of <i>SM</i> under GWP1 scenario. The panels g), h) and i) represent the difference of mean, SD and CV of <i>SM</i> between GWP1 and GP1 scenarios. (Unit is %) | 193 |
| Fig. 144 Annual mean, standard deviation (SD) and coefficient of variation (CV) of soil moisture (<i>SM</i>) under GP2 and GWP2 scenarios. The panels a), b) and c) represent mean, SD and CV of <i>SM</i> in GP2 scenario. The panels d), e) and f) represent mean, SD and CV of <i>SM</i> under GWP2 scenario. The panels g), h) and i) represent the difference of mean, SD and CV of <i>SM</i> between GWP2 and GP2 scenarios. (Unit is %) | 194 |
| Fig. 145 Annual mean, standard deviation (SD) and coefficient of variation (CV) of soil | |

| | |
|--|-----|
| moisture (<i>SM</i>) under GP3 and GWP3 scenarios. The panels a), b) and c) represent mean, SD and CV of <i>SM</i> in GP3 scenario. The panels d), e) and f) represent mean, SD and CV of <i>SM</i> under GWP3 scenario. The panels g), h) and i) represent the difference of mean, SD and CV of <i>SM</i> between GWP3 and GP3 scenarios. (Unit is %) | 195 |
| Fig. 146 Annual mean, standard deviation (SD) and coefficient of variation (CV) of soil moisture (<i>SM</i>) under GP3 and GWP3 scenarios. The panels a), b) and c) represent mean, SD and CV of <i>SM</i> in GP3 scenario. The panels d), e) and f) represent mean, SD and CV of <i>SM</i> under GWP3 scenario. The panels g), h) and i) represent the difference of mean, SD and CV of <i>SM</i> between GWP3 and GP3 scenarios. (Unit is %) | 196 |
| Fig. 147 Mean flow duration curve of upper part of Kherlen river watershed (Current condition) | 198 |
| Fig. 148 Mean flow duration curve of upper part of Kherlen river watershed (Future condition) | 199 |
| Fig. 149 Mean discharge and CV of 95, 185, 275 and 355 day of a year. | 201 |
| Fig. 150 The influence of grazing pressure on mean aboveground biomass under present climate in Kherlen river basin..... | 202 |
| Fig. 151 The influence of grazing pressure on mean aboveground biomass under present climate in Kherlen river basin..... | 202 |

1 Introduction

1.1 Review of ecohydrological concepts

Recently, global changes and their impacts on natural environment have become more obvious in water resources, many natural disasters and so on. Thus it is necessary to solve these complex issues of environmental changes by means of integrated, interdisciplinary approaches and hypothesis testing through scientific logic in order to improve our fundamental understanding of the links between hydrological, biogeochemical, and ecological processes (Hansen, 1996).

The progress in ecology during recent years has created a background for integration of ecology and hydrology. Consequently, two branches of environmental science, namely ecology and hydrology could provide new insight into the interrelation between hydrosphere and biosphere components (Zalewski et al., 1997). Therefore, ecohydrology concept has been developed within the framework of the UNESCO, International Hydrological Programme (IHP-V) which created a new horizon to investigate into these complex environmental systems and help us to give improved forecasts of environmental changes (Zalewski et al., 1997). During past decades, ecohydrological concept has been revised or modified several times and, it is summarized now that ecohydrology can be defined as an integrative science focused on the effects of hydrological processes on biotic processes (Zalewski, 2002). It is quite interesting to see how the application of ecohydrological research or study has emerged as the main stream in environmental sciences (Table 1; Hannah et al., 2004).

Particularly ecohydrology in the "critical zone" such as the large heterogeneous area or ecotone received much attention, since they tend to be more susceptible to environmental changes has (Odorico and Porporato, 2006); Newman et al., 2006) and reliable forecasting of environmental changes based on broad range of integrated scientific information to understand environmental processes are required. Investigation of the various interactions between ecological and hydrologic properties in the terrestrial ecosystem by means of integrated environmental modeling approaches is central themes of ecohydrological research. Moreover, modeling framework based on interactive use of ecosystem and hydrological model is the first step towards the advances in ecohydrological research, because this approach could help to understand the fundamental application of ecosystem dynamics, their responses or impacts to different hydrological and climate systems on regional and global level, in particular in the arid and semi-arid ecosystem where interaction with hydrosphere is vital for biological survival.

Table 1 Number of hydroecological and ecohydrological articles (between 1991 and 2003) classified by dominant (a) approach & (b) scale of research (Hannah et al. (2004)).

| Categories | (a) Approach | | | | | (b) Scale | | |
|--------------|--------------|---------|-------|------------|------------|-----------|------|-------|
| | Pattern | Process | Model | Management | Discussion | Micro | Meso | Macro |
| Ecohydrology | 21 | 15 | 9 | 10 | 7 | 4 | 27 | 31 |
| Hydroecology | 5 | 3 | 6 | 10 | 1 | 1 | 15 | 9 |
| Total (N=87) | 26 | 18 | 15 | 20 | 8 | 5 | 42 | 40 |

(micro: particle-patch; meso: patch-reach; macro: reach-catchment)

1.2 Review of previous studies on modeling application

Arid ecosystems cover more than 25% of the Earth terrestrial surface (Matthews, 1983) and include shrub lands, arid grassland and dry savannas. Light, nutrients and water are fundamental resources for vegetation development but in arid and semiarid conditions, water is the major controlling factor (Rodriguez-Iturbe, 2000; Albertson and Kiely, 2001; Porporato et al., 2001). Therefore, hydrological balance is the primary factor for plant production and precipitation is the only source of water input while evapotranspiration represents the major path for water loss in arid and semi-arid regions (Li et al., 2007). Evapotranspiration is controlled by a number of environmental and biological factors and thus the understanding of the hydrological processes is complex yet critically important in these regions (Jarvis and McNaughton, 1986; Sugita et al., 2007; Liu et al., 2010).

Arid environments are highly sensitive to climate variability (e.g., Dirmeyer and Shukla, 1996; Myneni et al., 1996), and they are prone to disproportionately high land-use pressures in comparison to more mesic environments (Milchunas and Lauenroth, 1993). Although climate variability and land-use often lead to functional changes in arid ecosystems (e.g., Schlesinger et al., 1990; Scholes and Archer, 1997), the spatial extent and degree of vegetation changes resulting from these processes are not easily measured at large spatial scales. In fact, a number of recent studies have suggested that feedbacks from changing global vegetation patterns may have played an important role in the exchanges of carbon, water and energy fluxes at the land surface (e.g., Schimel et al., 2001; Hofmann and Jackson, 2000; Nemani et al., 1996), because of the vegetation controls or effects over ecohydrological components via its physiological properties such as leaf area index, stomatal resistance, rooting depth, albedo and surface roughness. The biophysical effects of vegetation on climate have been found in a number of studies which investigated the effects of deforestation (Lean and Rowntree, 1997; Xue, 1997), anthropogenic land cover change (Brovkin et al., 1997; Chase et al., 2000; Sitch et al., 2005; Chen et al., 2007) and changes in structural and physiological vegetation characteristics (Betts et al., 1997). At the global scale, vegetation also affects atmospheric processes through its effects on CO₂ exchange and the emission of other relatively active trace gases (Shaver et al., 1992). Changes in the structural and physiological properties of vegetation, in response to increases in atmospheric CO₂ concentration and climate warming are expected to have important effects on the overall sensitivity of the climate system.

Many complex environmental problems involve processes that occur both within and between atmosphere, biosphere and hydrosphere, thus these complex processes must be

investigated, understood and modeled (Brandmeyer and Karimi, 2000). When coupling existing models, identifying the components required to link them is central to the coupling design that could result in a systems integration problem (Abel et al., 1994). At the catchment or river basin scale the dynamic representation of vegetation in hydrological models offers a range of opportunities to understand and predict the behavior of ecosystems. The coupling of ecological models that explicitly model plant growth with physically based hydrological models and a soil-vegetation-atmosphere transfer schemes (SVAT schemes) offers a range of opportunities to explore the bidirectional interactions between vegetation and hydrology phenomena and also between vegetation and climate phenomena (Arora, 2002). This coupling also gives the ability to model carbon and nutrient fluxes together with water and energy fluxes, in a hydrological framework at the catchment and river basin scales (Aber, 1999).

Numerous studies have emphasized the importance of terrestrial ecosystems as an integral component of the Earth's climate system. This realization has already led to the efforts to link simple equilibrium vegetation models with Atmospheric GCMs (General Circulation Model) and hydrological models through iterative coupling procedures (e.g., Foley et al., 1998). An analysis of 17 years of moisture budget data from GCM, Arora and Boer (2002) showed that on a global average, vegetation processes more than 70% of the total precipitation, and the combined evaporation from canopy leaves and transpiration account for 72% of total evaporation from the land surface. This one example shows that how vegetation plays a significant role in influencing water and energy balance at the land surface via its effect on transpiration, interception and the evaporation of precipitation from the canopy leaves. Water-controlled ecosystems are complex. The soil and climate control the vegetation dynamic while the vegetation modulates the total water balance, being the main link between atmosphere and soil (Porporato and Rodriguez-Iturbe, 2002; Larcher, 2003). Moreover, soil moisture fluctuation is one of key variables in the soil-vegetation-atmosphere interaction (Rodriguez-Iturbe et al., 2001; Isham et al., 2005).

Seuffert et al. (2002) coupled TOPLATS (TOPMODEL - based Land surface - Atmosphere Transfer Scheme) hydrological model to an atmospheric model and applied the model to the regional scale at Sieg catchment (about 2000 km²) in Western Germany. Two case studies in their study show that how coupled modeling system can improve the outputs based on more accurate representation of vegetation, soil and hydrological processes. Lu et al. (2001) studied the interactions between the atmosphere and the biosphere by coupling the Regional Atmospheric Modeling System (RAMS) and the century ecosystem model. Shortly, century ecosystem model received meteorological data from RAMS. From century ecosystem model

produced aboveground biomass and then it converted to leaf area index (LAI) by simple algorithm. Calculated LAI returned to RAMS. In this way, they integrated RAMS and century ecosystem model and showed that how a dynamic vegetation component can modify particular climate regime.

1.3 Review of environmental studies in Mongolia

A climatic transition from humid region in the north to arid region in the south can be found in northeastern Asia around Mongolia, where a forest-grassland-desert ecotone is formed with a steep geographical change. This ecotone contains the largest grassland belt, covering 90% of the total land area of Mongolia, which corresponds to roughly 2.6% of the global grassland. In general, ecotone is sensitive to change of climate and vegetation cover.

Since late 19th century, mean annual global surface temperature has increased by about 0.3 - 0.6°C and it is projected to further increase by 1 - 3.5°C over the next 100 years (IPCC, 1995). This climate change appears and affects environments in the mid and high latitudes of the Northern Hemisphere, where temperatures have been obviously getting warmer since 1970s (IPCC, 2001). Some recent studies of RCM (Regional Climate Model) projection reported that the climate condition of northeastern Asia has been undergoing significant changes and that will dramatically increase in the future (Chase et al., 2000; McCarthy et al., 2001; Sato et al., 2007).

Another driving force of environmental changes results from human activities. In 1990s, Mongolian political system has changed from a centrally-planned economy into market oriented economy. As a result of privatization of livestock in 1990s, the number of livestock has increased drastically by about 50% in past two decades (Sugita et al., 2007). After privatization of livestock, overgrazing onto the grassland has been suspected, because about 90% of the total land area of Mongolia is represented by the grasslands and shrublands, which have been freely disturbed or grazed by livestock all year round (Fernandez-Grimenez and Allen-Diaz, 1999). On the other hand, this animal husbandry plays a key role in Mongolia's economy, producing 40% of the gross domestic product (GDP). Moreover, growth of livestock is highly dependent on the productivity of natural grassland and about half of population depends on livestock production for their livelihood.

There have been a few attempts to study grazing pressure influence on Mongolian grassland, but among them, Batjargal (1997) studied the relation between grazing and ecosystem, including soil erosion and vegetation amount and found that grazing pressure was one of the driving factors of plant production and soil erosion. Kojima (2004) described the relation

between grazing and vegetation amount based on a half-year field observation in Kherlen river basin and also suggested that grazing pressure was one of the controlling factors for vegetation growth. From the data analysis, carbon exchange and net primary production were found to be sensitive to precipitation, air temperature and again grazing pressure (Li et al., 2005). Also these results tend to indicate that the primary factors that determine steppe aboveground biomass are indeed the combination of precipitation and temperature in early growing season along with grazing pressure also additional factor. Urano (2005) suggested that the larger grazing intensity caused the steppe to be the source of carbon dioxide flux. From model and data analysis, the maximum sustainable grazing intensity was determined to be 0.7 sheep equivalent unit (SE_u) per ha⁻¹ in steppe site in northeastern Mongolia (Chen et al., 2006; Chen et al., 2007). If grazing intensity is greater than 0.7 SE_u h⁻¹, the aboveground biomass keeps decreasing. Kato (2007) has studied grazing pressure influence on water and energy balance in the same site and found that grazing pressure difference over three years did not cause in significant difference in water and energy balance. On the contrary, the previous studies have shown that grazing pressure reduced seasonal evapotranspiration by 6-8% in American grassland (Bremer et al., 2001; Frank, 2003). The overgrazing in the semi-arid region of Sonoran Desert in Mexico contributed large amount of latent heat flux and less amount of soil moisture available for vegetation growth (Bryant et al., 1990) and influence of overgrazing could accounts less than 1% of global warming (Nasrallaha and Balling Jr, 1994). Indeed, precipitation in any terrestrial ecosystem first intercepted by canopy, then infiltrated into soil, or produce surface runoff over the land surface. All of these processes depend on vegetation cover, soil characteristics and topography condition (Coronato and Bertiller, 1996). Therefore, removal of vegetation cover by grazing could also affect hydrological cycle and energy fluxes of Mongolian grassland. Since grassland are subjected to grazing pressure all year round in Mongolia, the influence of grazing pressure must be taken into account in order to improve comprehensive understanding of carbon cycle of Mongolian grassland ecosystem as well as hydrological cycle.

In case of Mongolia, analysis of meteorological records has shown that during last 60 years air temperature have increased significantly and precipitation tends to have decreased, particularly in spring period (Natsagdorj, 2000). Model projections suggest that global warming will result in increased temperature in and around Asia in the future, if the green house gases of atmospheric levels are to continue to increase and around Mongolia (McCarthy et al., 2001). The growing season precipitation, particularly in July will tends to be decreased due to global warming and droughts may occur more frequently (Sato et al., 2007) under the projection at A2 scenario. Note that, drought is one of the limiting factors for vegetation growth in arid and

semi-arid region (Seastedt et al., 1998). On the other side from the ecosystem modeling approach, it has been found that livestock carrying capacity of rangeland will decrease due to climate change and also net primary production will significantly decrease due to climate change and grazing pressure (Chen et al., 2006; Chen et al., 2007).

Although there have been some attempts to study grazing pressure and global warming influence on Mongolian grassland, studies are still needed to bridge the lacking information to get a concrete results of ecosystem functioning of Mongolian steppe and hydrological regime (Sugita et al., 2007). Furthermore, a sustainable use of natural resources in Mongolia requires a deeper understanding of how carbon, energy and water fluxes are coupled.

Therefore, we must recognize the need for integrated studies on ecohydrological processes based on model applications to simulate both current and future potential impacts on Mongolian ecosystem. That will allow developing better future scenarios with ecosystem sustainability considered. For this, an experimental projects and models must be designed to achieve a synthetic understanding of ecohydrological processes and their variation at the stand level. But validated simulation models must also provide information on how to maintain appropriate levels of production, suitable integrated function of ecosystems at regional scale.

1.4 Objectives

This study aims at understanding and clarifying the influence of global warming and grazing pressure changes to carbon, hydrology and energy fluxes in Mongolian semi-arid region with following specific objectives:

- To calibrate the parameters of ecological and hydrological models and validate them using measured data in the study area at point and a regional scale.
- To determine a variable, that can be used to link ecological and hydrological models and to evaluate effectiveness of interactive application of them.
- To simulate future ecohydrological components under the influence of global warming and grazing pressure changes.
- To clarify the effects of global warming and grazing pressure changes on ecohydrological components.

In order to achieve these purposes, the present study was carried out in one of the least studied regions of the world, i.e., Asian steppe region in Kherlen river basin (Figs. 1 and 2)

(Byambakhuu et al., 2010). The data acquisition of this exploratory research was obtained during the field campaigns of the Rangelands Atmosphere - Hydrosphere-Biosphere Interaction Study Experiment in Northeastern Asia (RAISE, Sugita et al., 2007).

1.5 Outline of the study

This thesis is organized as follows: **Chapter 1** clarifies the background information and objectives of the present study as mentioned above. **Chapter 2** describes study sites, related datasets and a comprehensive description of ecosystem model and hydrological model. **Chapter 3** gives the findings of this study with general discussion with respect to ecohydrological components, based on a series of simulation results and offers some suggestions.



Fig. 1 Mongolian natural grassland (west-north part of Kherlenbayan-Ulaan site, See Fig. 3 for location)



Fig. 2 A representative part of the Kherlen river between Baganuur and Kherlenbayan-Ulaan (See Fig. 3 for location)

2. Methods

2.1 Study area

The steppe region in Mongolia extends further towards central Asia and it constitutes the largest grasslands belt region on earth (Shiirevdamba, 1998). This largest biome (steppe) which covers 90% of the country (Fig. 3), also occupies about 2.6% of the global grassland vegetation (Shiirevdamba, 1998; World Recourse Institute, 2003). The study area for the present study located within and around the Kherlen river basin in northeastern semi-arid region of Mongolia. The study site names and their abbreviation are shown in Table 2. All study areas are located within part of larger ecotone, where clear distinctions of forest steppe and steppe region are observed. The elevation of study area ranges between 1040 and 1630 m (Fig. 4). The annual precipitation ranges from 150 mm to 300 mm (Sugita et al., 2007), and more than 70% of precipitation falls only during the summer period from June to August. The distribution of annual precipitation and the aridity index shows that whole area in Kherlen river basin lies in semiarid region and aridity index ranged from 0.32 to 0.42 (Sugita, 2003). Forest steppe is covered with mainly larch forest. In the grassland, it is covered by a typical short-grass steppe mostly dominates by the cool season C₃ species (mainly *Stipa krylovii*, *Carex duriuscula*, *Artemisia adamsii*, *Artemisia frigid*, *Leymus chinensis*, and *Caragana microphylla*), and some C₄ species (*Cheistogenes squarrosa*) (Li et al., 2005). The geological setting of the Kherlen river basin provided by Mineral Resources Authority of Mongolia (1999). Mesozoic and Paleozoic granites, and Carboniferous rocks can be seen from the mountainous upstream area to the area around the KBU. From KBU to UDH, the right bank of the Kherlen river mainly consists of Mesozoic rocks. Cenozoic deposits are distributed around the DH region and along the Kherlen river (Abe, 2004).

Land use change is one of the most conspicuous changes in cultural landscapes in many regions of the world. Main land-use in this study region is human activities as grazing pressure by nomadic livestock. Land-use change is expected to have a strong influence on surface hydrology, evaporation and soil moisture that produce significant difference in surface aridity (DeFries and Eshleman, 2004; Sugita et al., 2007) Therefore, ecohydrological processes were studied at two distinctive surface conditions i.e. grazing and nongrazing condition in our study. Here, nongrazing surface condition was obtained by a fence (200 m x 170 m) enclosure experiment in KBU site from August, 2002 and its detailed map is shown in Fig. 5. This allowed to study the possible grazing impact on ecohydrological processes (Li et al., 2005).

Table 2 List of site name and their station type with some related information (See also Figs. 3 and 4).

| Station type | Station site name | Abbreviations of site name | Vegetation cover | Location (degree) | | Altitude (m) |
|--|--------------------|-------------------------------|---------------------|-------------------|-----------|--------------|
| | | | | Latitude | Longitude | |
| Automatic weather station (AWS) | Baganuur | BGN | Grassland | 47.78 | 108.38 | 1360 |
| | Darkhan | DH | Grassland | 46.58 | 109.42 | 1270 |
| | Jargalkhaan | JGN | Grassland | 47.47 | 109.43 | 1360 |
| | Undurkhaan | UDH | Grassland | 47.32 | 110.67 | 1040 |
| Flux station | Kherlenbayan-Ulaan | KBU | Grassland | 47.28 | 108.87 | 1235 |
| | Mongonmorit | FOR | Forest | 48.44 | 108.65 | 1630 |

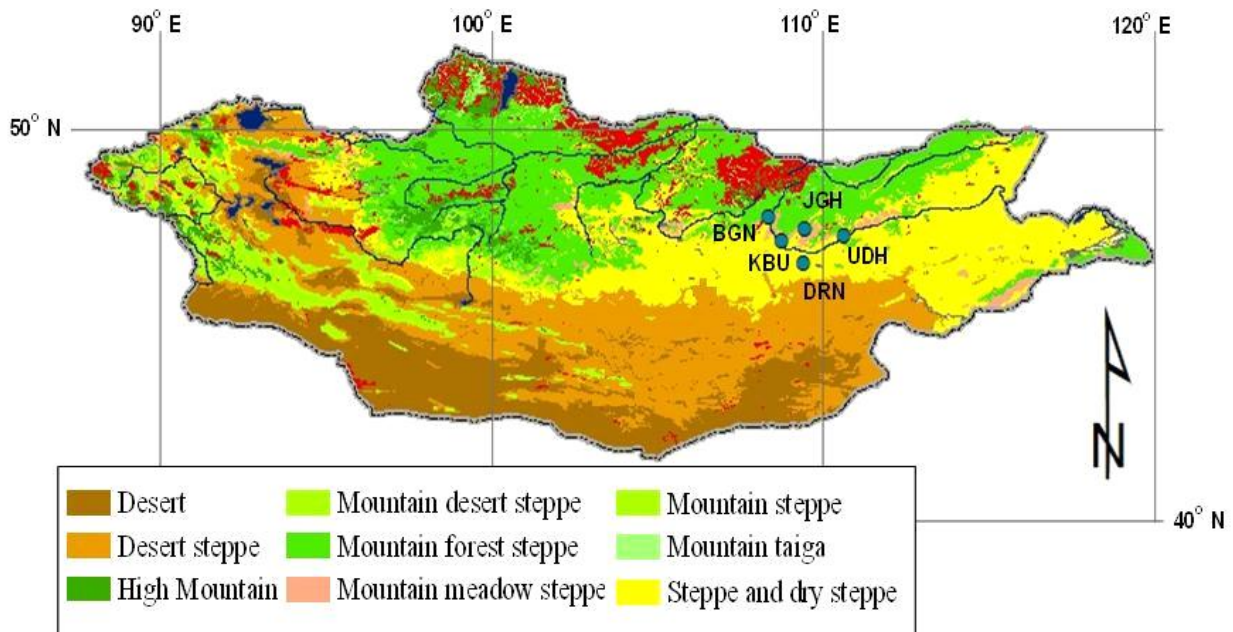


Fig. 3 Vegetation map of Mongolia (Saandar and Sugita, 2004) with the main observation sites in semiarid region, major rivers and lakes. Open circles represents study sites within Kherlen river basin. The abbreviation of each site is shown in Table 2.

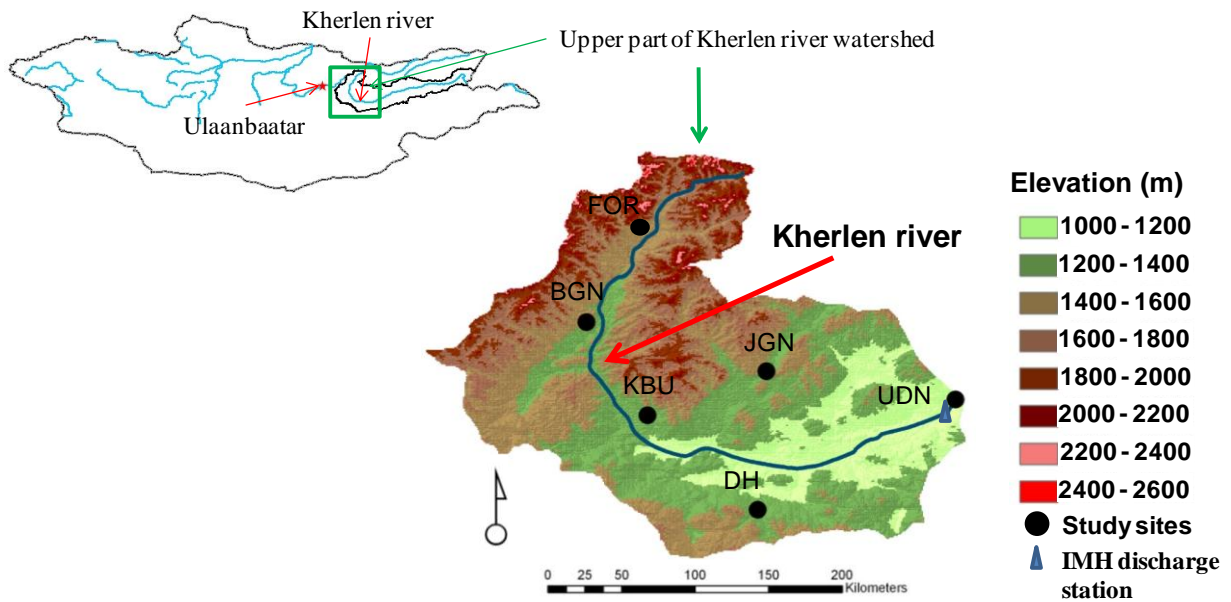


Fig. 4 The topographic map of upper Kherlen river basin with main observation sites. The abbreviation of each site is shown in Table 2. IMH represents Institute of Meteorology and Hydrology of Mongolia.

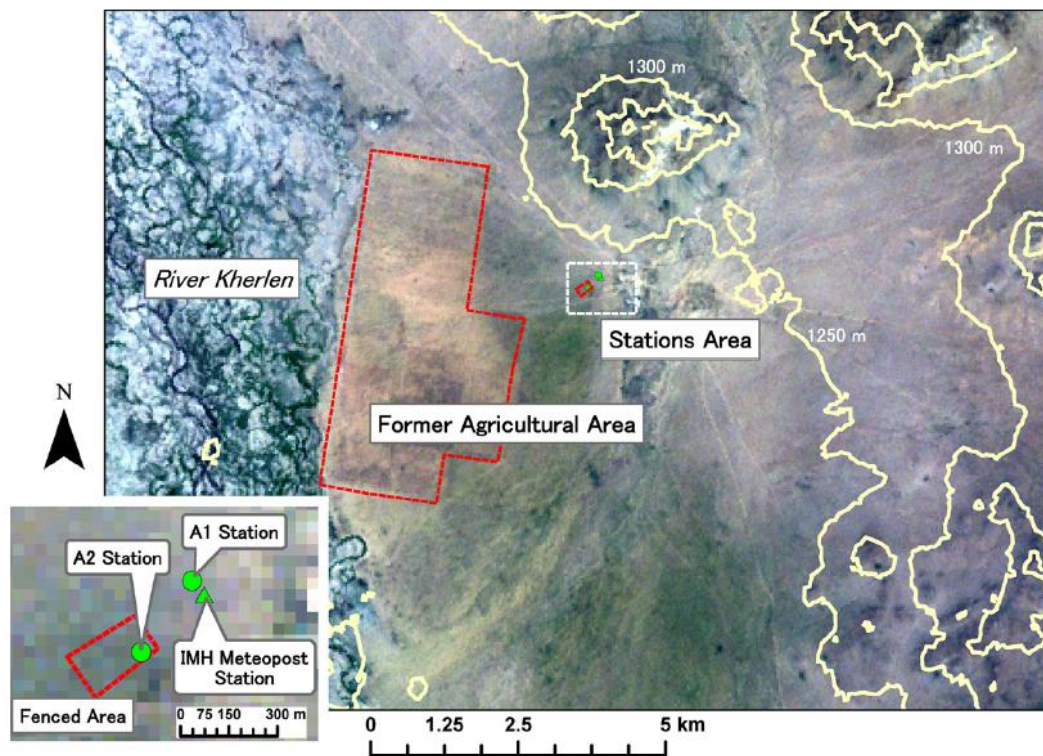


Fig. 5 Topographic map with a Landsat ETM+ of the KBU site with location of the stations, fenced area, and a former agricultural field indicated. Details of the stations' setting are also shown as a separate map. (Sugita et al., 2007). (A1 station: grazing surface condition, A2 station: nongrazing surface condition)

2.2 Data processing

From 2003 to 2007, upper Kherlen river watershed in semi-arid steppe region was the target of RAISE project (the Rangelands atmosphere-hydrosphere-biosphere Interaction Study Experiment in North-eastern Asia). This allowed the extensive data acquisition for this study in this watershed.

2.2.1 Plant physiological data

The plant physiological data were obtained from RAISE project data (Sugita et al., 2008) and IMH (Institute of Meteorology and Hydrology of Mongolia). During RAISE project campaigns, plant physiological data such as leaf area index (LAI), aboveground biomass and vegetation height were measured between June and September of 2003, July of 2004 and August of 2005. All these data were measured at grazing and nongrazing site at KBU site and those measured in June and July of 2003 at FOR site.

The quadrat size was 0.25m^2 with 12 replications at both locations. In short, live leaves were removed from the stems for determination of green LAI by a scanner and mean canopy heights and coverage were also measured. Detailed information of this procedure can be found in Li et al. (2005a). Five biological stations data of IMH (Fig. 7 and Table 3) also were used in this study.

2.2.2 Meteorological and hydrological data

The networks of meteorological, hydrological and biological stations have been in operation under Institute of Meteorology and Hydrology (IMH), Mongolia in the upper part of Kherlen river watershed. These stations consist of the Metostation, the Metopost station which measure the standard meteorological variables such as air temperature, air pressure, wind speed and precipitation (Sugita et al., 2007). The list of all IMH Metostations and Metoposts are shown in Fig. 7 and other related information of those stations is presented in Table 3. Moreover, the long term of discharge of Kherlen river has been measuring at UDH site.

In addition to the existing IMH stations, three flux stations and four automatic weather stations (AWS) (Table 2) were installed for the purpose of obtaining continuous measurements of meteorological and hydrological variables (Sugita et al., 2007). At KBU site, two flux

stations were installed at both of nongrazing and grazing surface condition and locations of these stations are shown in Fig. 5. The mean flux data at the interval of 30 minutes were obtained by the eddy covariance measurement system at the grazed steppe at KBU. The signal of wind speed and gas concentration was measured at 10 Hz, while radiation, temperature and humidity sensors were sampled at 0.2Hz. The details of those stations have been presented in previous studies (e.g., Li et al., 2005a; Kotani, 2006; Sugita et al., 2007); Kato, 2007). The other related information of those stations, including variables name, sensors and height and depth are given in Tables 4 and 5.

Another flux station was established in FOR site and location is shown in Fig. 8 (Sugita et al., 2007). In this site, flux station was installed at a height of 30 m above the ground surface and about 10 m above the average canopy height over the forest in late March of 2003. The outputs of wind speed, gas concentration, radiation, temperature and humidity sensors were sampled in the same manner as those measured at flux stations of KBU site. The details of this station have been presented in Li et al. (2005b).

The four AWSs were established in BGN, DH, JGN and UDH site. These AWSs provided a time series of temperature, humidity, radiation, precipitation and wind speed at each station. The related information of those stations, including height and depth of different variables and their sensors, are given in Table 6. The details of these stations also have been presented in Matsushima (2007).

2.2.3 Regional climate model data

Within modeling framework of RAISE project, regional atmospheric modeling system (RAMS) with downscaling technique has been developed at the Terrestrial Environment Research Center, University of Tsukuba, Japan (TERC-RAMS) by modifying the physical schemes in RAMS, which was originally developed at Colorado State University (Sato et al., 2007). Main purpose of this modification was to improve the predictability quality of regional climate simulation. The modification of precipitation calculation in TERC-RAMS includes Arakawa-Schubert type convective parameterization (Arakawa and Schubert, 1974) and microphysics parameterization (Walko et al., 1995). Also the formation of the sub-grid scale cumulus near the top of the convective boundary layer was parameterized by grid mean relative humidity. The concentration of carbon dioxide was assumed to be constant in all procedures by the TERC-RAMS experiments.

The grid system of TERC-RAMS covers the whole of Mongolia with a 30 km resolution. Each grid contains 30 vertical layers system. The thickness of the vertical layers varies from 110 m (at the lowest layer) to 800 m (in the uppermost layer). The top of the model atmosphere is 17,500 m. Surface initial conditions in the TERC-RAMS domains are given by a global land cover characterization dataset provided by the U. S. Geological Survey (Loveland et al., 2000), which is based on satellite observations by an Advanced Very High Resolution Radiometer (AVHRR). The TERC-RAMS also uses distributions of LAI, vegetation albedo, roughness height and other parameters of vegetation determined in the Biosphere-Atmosphere Transfer Scheme (BATS; Dickinson et al., 1986).

The uniform soil texture was assumed as sandy clay loam type with saturated volumetric soil water content of 0.42. The TERC- RAMS does not contain snow model. Initial soil moisture for numerical integration in grid systems was computed by one-month integration of TERC-RAMS starting from homogeneous soil moisture condition. Meteorological variables in the coarse grid system were nudged to the forcing dataset with the time coefficient of 10 minutes in six grids from the lateral boundaries. The inner part of the domain was also nudged very weakly with the coefficient of four days. For the ten-year calculations of both recent and future climate runs, time-slice experiment was performed in which each integration covers 35-day period initialized by the forcing dataset. The grid system in our study is represented by 1 x 1 km. Therefore, original forcing dataset of current and future climate condition produced by TERC-RAMS were interpolated by a geographic information system (ArcGIS 9.3) using Kriging interpolation method from 30 x 30 km into 1 x 1 km grid system. Each output of interpolation was stored in datasets of same grid size (1 km x 1 km) to provide basis for extracting a time series of variables for each grid. These adjusted outputs will be used in our study for a comprehensive comparison and assessment of the possible impact of current and future climate change on current and future regional carbon and water resources together with energy fluxes processes.

2.2.3.1 Current climate condition

The forcing meteorological variables, such as wind speed, temperature, humidity and geopotential height came from NCEP/NCAR reanalysis data set (Kalnay et al., 1996), which was produced by the models incorporating surface and upper air observations in the world. By use of the six-hourly reanalysis data, recent climate run prognoses meteorological variables from March of 1994 through February of 2004. Variables at each of 30 km resolution grids are archived with one-hour interval. The results from recent climate run were verified by comparing

them with three-hour-interval meteorological elements from 1993 through 2004 provided by IMH meteorological stations. Sensible and latent heat flux and four component radiation data at both of KBU site and FOR site were also used to validate the TERC-RAMS simulations.

2.2.3.2 Future climate condition

A forcing dataset for TERC-RAMS were made for the future climate condition by means of 6-hourly product of SRES-A2 (Nakicenovic and Swart, 2000) scenario run by MRICGCM2 (Yukimoto et al., 2001). The SRES-A2 is based on a scenario that carbon dioxide concentration increases up to 800 ppm in the late of 21st Century characterizing slow technical change and economical growth in the future. The meteorological variables in the future condition were computed using the atmospheric variables in NCEP/NCAR reanalysis data and sea surface temperature provided by Reynolds et al. (2002) from 1993 through 2004. More detail of configuration of TERC-RAMS for the RAISE project was described in Sato et al. (2007).

2.2.4 Grazing pressure intensity

The grazing pressure intensity was evaluated from the statistics showing the number of registered animal by the National Statistical Office of Mongolia (GI_s). In that data set, five different livestock number of every district (sum) was registered within upper Kherlen river watershed. Therefore, it was necessary to convert five different livestock value in every district into sheep equivalents unit (SE_u). According to USDA National Range and Pasture Handbook (1997), Kato (2007) suggested (1) to calculate SE_u from five different livestock number.

$$SE_u = 8.15 \times N_{Camel} + 6.25 \times N_{Horse} + 5 \times N_{Cow} + 0.75 \times N_{goat} + N_{sheep} \quad (1)$$

GI_s value of each district was calculated as follow:

$$GI_s = SE_u / A \quad (2)$$

where GI_s is statistical grazing pressure parameter ($SE_u \text{ ha}^{-1}$), SE_u is sheep equivalent unit and A (ha) is each district area within upper Kherlen river watershed obtained from Saander and Sugita, (2004). Fig. 6 shows changes of annual grazing pressure of each sum within the Kherlen river basin. After privatization of livestock in 1990, grazing pressure has increased at each site that may have resulted overgrazing onto the grassland. The mean grazing pressure of the Kherlen river basin was increased by 43.8% between 1984 and 2003.

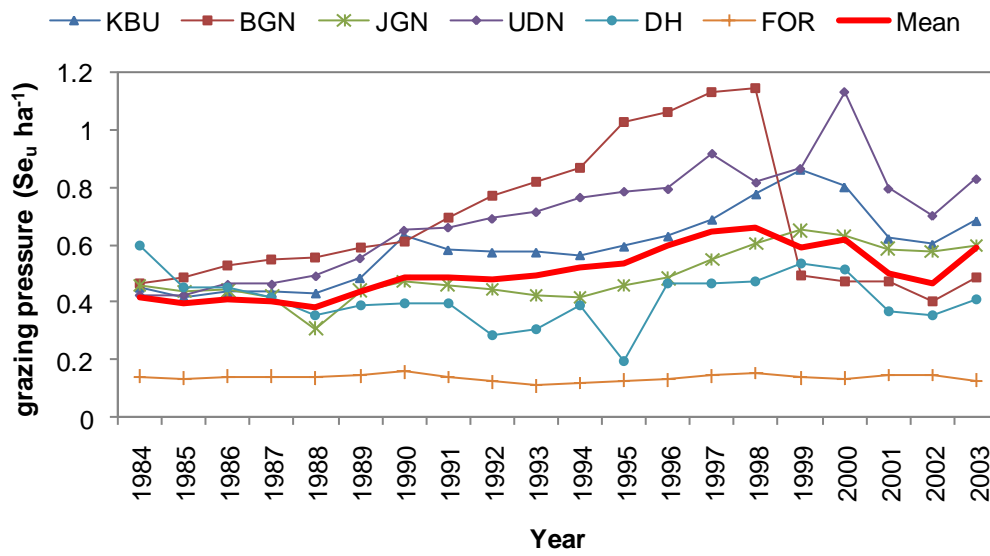


Fig. 6 Changes in annual mean of grazing pressure intensity of observation sites in the Kherlen river basin. (See Fig. 4 for location)

Table 3 List of IMH Metostation and Metopost with some related information (See also Fig. 7 for location)

| Station type | Station site name | Station abbreviation | Location | |
|--------------|--------------------|----------------------|----------|-----------|
| | | | Latitude | Longitude |
| Metostation | Baganuur | BN | 47.78 | 108.38 |
| | Galshar | GL | 46.45 | 110.91 |
| | Mongonmorit | MN | 48.44 | 108.65 |
| | Terelj | TR | 47.98 | 107.48 |
| | Undurkhaan* | UN | 47.32 | 110.67 |
| | Maanit* | MA | 47.34 | 107.48 |
| | Orgil* | OR | 46.58 | 109.42 |
| | Binder* | BI | 48.62 | 110.57 |
| | Dadal | DA | 49.03 | 111.62 |
| | Choir* | CH | 46.38 | 108.37 |
| Metopost | Batnovor | BA | 47.93 | 111.52 |
| | Bayanjargalan | BJN | 47.17 | 108.27 |
| | Bayanmunkh | BM | 46.87 | 109.75 |
| | Delgerkhaan | DN | 47.18 | 109.17 |
| | Erdene | ER | 47.68 | 107.97 |
| | Gurbanbayan | GB | 47.78 | 110.07 |
| | Ikhet | IK | 46.28 | 110.24 |
| | Jargalkhaan | JR | 47.47 | 109.43 |
| | Kherlenbayan-Ulaan | KBU | 47.28 | 108.87 |
| | Tsenkhermandal | TN | 47.87 | 109.08 |
| | Ulziit | UL | 47.53 | 110.25 |
| | Umnudelger | UM | 47.93 | 111.57 |

*: Biological station of IMH is also located here

Table 4 Instruments for the observation at grazing site surface condition in KBU site (after Kotani, 2006)

| Variable | Instrument | Model/Manufacturer (location) | Height and Depth | Sampling interval | Averaging time |
|------------------------------------|---|---|---|-------------------|----------------|
| Relative humidity | Capacitance hygrometer | HMP45A / Vaisala Oy.(Helsinki, Finland) | 2.5 m | 5 sec | 30 min |
| Air temperature | Platinum resistance thermometer in ventilation shelter | PVC-02-AC / Prede Co.Ltd. (Tokyo, Japan) | 2.5 m | 5 sec | 30 min |
| Surface temperature | Infrared thermometer | 303F / Konica Minolta Holdings, Inc. (Tokyo, Japan) | 2.5 m | 5 sec | 30 min |
| Sensible/ Latent heat flux | Sonic aemometerthermometer | SAT550/ Kaijo Sonic Co. (Tokyo, Japan) | 3.0 m | 10 Hz | 30 min |
| | CO ₂ /H ₂ O Infrared gas Analyser | Li7500 / Li-cor Inc. (Lincoln, U.S.) | | | |
| Up & downward short-wave radiation | Pyranometers ^{*1} | CM3 / Kipp and Zonen B.V. (Delft, Netherlands) | 2.5 m | 5 sec | 30 min |
| Up & downward long-wave radiation | Pygrometers ^{*1} | CG3 / Kipp and Zonen B.V. (Delft, Netherlands) | 2.5 m | 5 sec | 30 min |
| Air pressure | Barometer | PTB210 / Vaisala Oy. (Helsinki, Finland) | 1.3 m | 30 min | |
| Precipitation | Tipping bucket rain gauge | 52202 / R. M. Young Inc. (Traverse, U.S.) | | 30 min | 30 min |
| Soil heat flux | Heat flux plate | HFT1.1 / REBS ^{*2} Inc. (Seattle, U.S.) | -0.1; -0.3 m | 10 sec | 30 min |
| Soil temperature | Platinum resistance thermometer | C-PTG / Climatec Inc. (Tokyo, Japan) | -0.05; -0.1; -0.2; -0.3; -0.5; -0.7; -1.0; -1.5 m | 5 sec | 30 min |
| Volumetric water content | TDR sensor ^{*3} | CGP116 / Cambel Scientific Inc. (Logan, U.S.) | -0.1; -0.2; -0.3; -0.7; -1.0; -1.5 m | 10 sec | 30 min |

*1: Included in Net-radiometer (CNR1, Kipp and Zonen, B.V.); *2: Radiation and Energy Balance Systems; *3: Time Domain Reflectometry

Table 5 Instruments for the observation at nongrazing site surface condition in KBU site (after Kato, 2007)

| Variable | Instrument | Model/Manufacturer (location) | Height and Depth | Sampling interval | Averaging time |
|------------------------------------|--|---|---|-------------------|----------------|
| Relative humidity | Capacitance hygrometer | HMP45A / Vaisala Oy.(Helsinki, Finland) | 2.5 m | 5 sec | 30 min |
| Air temperature | Platinum resistance thermometer in ventilation shelter | PVC-02-AC / Prede Co.Ltd. (Tokyo, Japan) | 2.5 m | 5 sec | 30 min |
| Surface temperature | Infrared thermometer | 303F / Konica Minolta Holdings, Inc. (Tokyo, Japan) | 2.5 m | 5 sec | 30 min |
| Sensible/ Latent heat flux | Sonic aemometerthermometer | R3A/ Gill instruments Ltd. (Hampshire, U.K) | | 10 Hz | 30 min |
| | CO ₂ /H ₂ O Infrared gas analyser (until March 2004) | OP2 / ADC BioScientific Inc. (Hoddesdon, U.K.) | 3.0 m | | |
| | CO ₂ /H ₂ O Infrared gas analyser (since April 2004) | Li7500 / Li-cor Inc. (Lincoln, U.S.) | | | |
| Up & downward short-wave radiation | Pyranometers ^{*1} | CM3 / Kipp and Zonen B.V. (Delft, Netherlands) | 2.5 m | 5 sec | 30 min |
| Up & downward Long-wave radiation | Pygrometers ^{*1} | CG3 / Kipp and Zonen B.V. (Delft, Netherlands) | 2.5 m | 5 sec | 30 min |
| Air pressure | Barometer | PTB210 / Vaisala Oy. (Helsinki, Finland) | 1.3 m | 30 min | |
| Soil heat flux | Heat flux plate | HFT1.1 / REBS ^{*2} Inc. (Seattle, U.S.) | -0.1; -0.3 m | 30 min | 30 min |
| Soil temperature | Platinum resistance thermometer | C-PTG / Climatec Inc. (Tokyo, Japan) | -0.05; -0.1; -0.2; -0.3; -0.5; -0.7; -1.0; -1.5 m | 10 sec | 30 min |
| Volumetric water content | TDR sensor ^{*3} | CGP116 / Cambel Scientific Inc. (Logan, U.S.) | -0.1; -0.2; -0.3; -0.7; -1.0; -1.5 m | 5 sec | 30 min |

^{*1}: Included in Net-radiometer (CNR1, Kipp and Zonen, B.V.); ^{*2}: Radiation and Energy Balance Systems; ^{*3}: Time Domain Reflectometry

Table 6 Instruments for the observation at BGN, DH, JGN and UDH site.

| Variable | Instrument | Model/Manufacturer (location) | Sampling interval | Averaging time | Height and Depth | | | |
|------------------------------------|---|--|-------------------|----------------|------------------|---------|---------|---------|
| | | | | | BGN | DH | JGN | UDH |
| Relative humidity | Humidity probe ^{*1} | HMP45D, Vaisala Oyj. (Helsinki, Finland) | 10 sec | 10 min | 2.63m | 2.5m | 2.6m | 2.6m |
| Air temperature | Platinum resistance thermometer ^{*1} | MT-010, EKO Instruments. (Tokyo, Japan) | 10 sec | 10 min | 2.63m | 2.5m | 2.6m | 2.6m |
| Soil temperature | Platinum resistance thermometer | (MT-010S-4, EKO Instruments. (Tokyo, Japan) | 10 sec | 10 min | -0.03m | -0.03m | -0.03m | -0.03m |
| Up & downward short-wave radiation | Solar and infrared radiometer | (MR-40, EKO Instruments. (Tokyo, Japan) | 10 sec | 10 min | 2.98m | 2.9m | 3.0m | 3.1m |
| Up & Downward Long-wave radiation | Solar and infrared radiometer | (MR-40, EKO Instruments. (Tokyo, Japan) | 10 sec | 10 min | 2.98m | 2.9m | 3.0m | 3.1m |
| Air pressure | Barometer | PTB210, Vaisala Oyj. (Helsinki, Finland) | 10 sec | 10 min | | | | |
| Precipitation | Tipping bucket rain gauge | MW010, EKO Instruments, Japan) | 30 min | 10 min | | | | |
| Soil heat flux | Heat flux plate | MF-81, EKO Instruments, Japan) | 10 sec | 10 min | -0.05m | -0.05m | -0.05m | -0.05m |
| Volumetric water content | TDR sensor | Trime-IT, IMKO Micromodultechnik. (Germany) | 1 min | 10 min | -0.03 m | -0.03 m | -0.03 m | -0.03 m |
| Wind speed | 3-cup anemometer | Wind Sentry 03002, R. M. Young Company. (USA) | 10 sec | 10 min | 3.15m | 2.9m | 3.0m | 2.92m |
| Wind direction | Wind vane | Wind Sentry 03002, R. M. Young Company. (USA) | 10 sec | 10 min | 3.15m | 2.9m | 3.0m | 2.92m |

^{*1}within naturally ventilated radiation shield

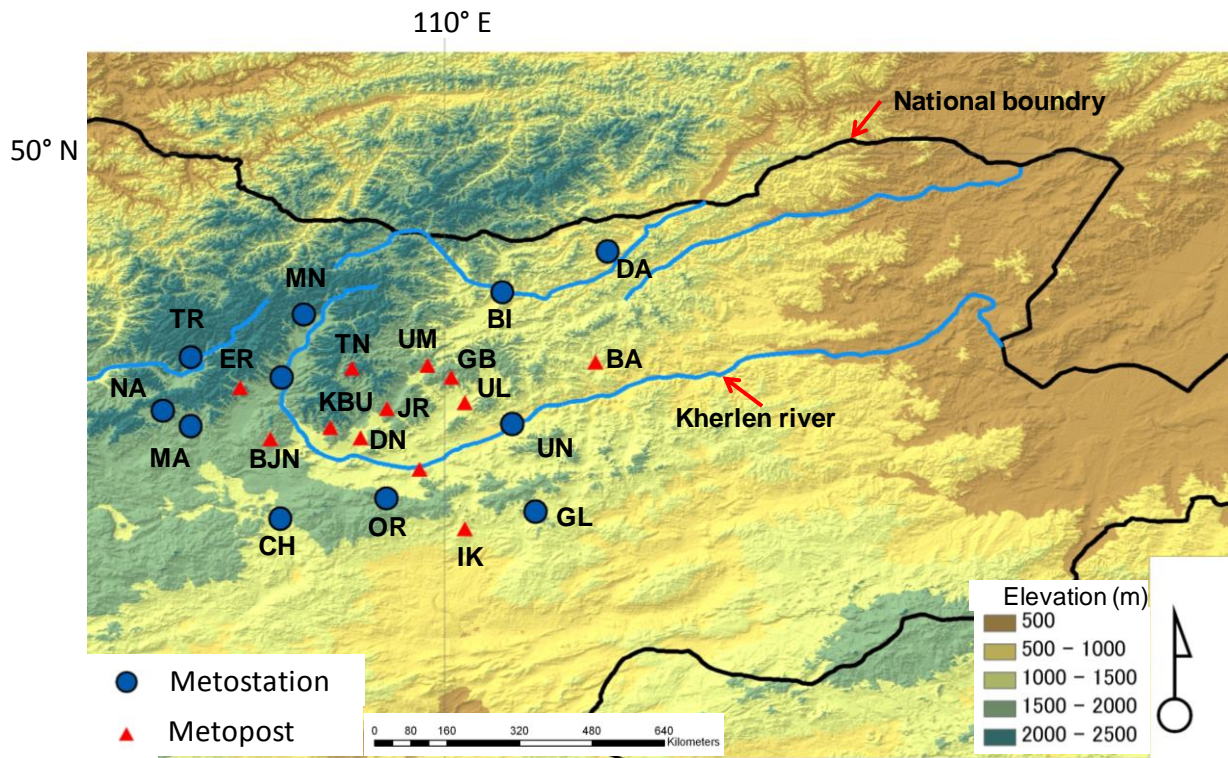


Fig. 7 Topographic map with ASTER GDEM of northeastern part of Mongolia. List of IMH metostations (with circle) and metopost (with triangular) in Kherlen river (Refer Table 3 for abbreviation)

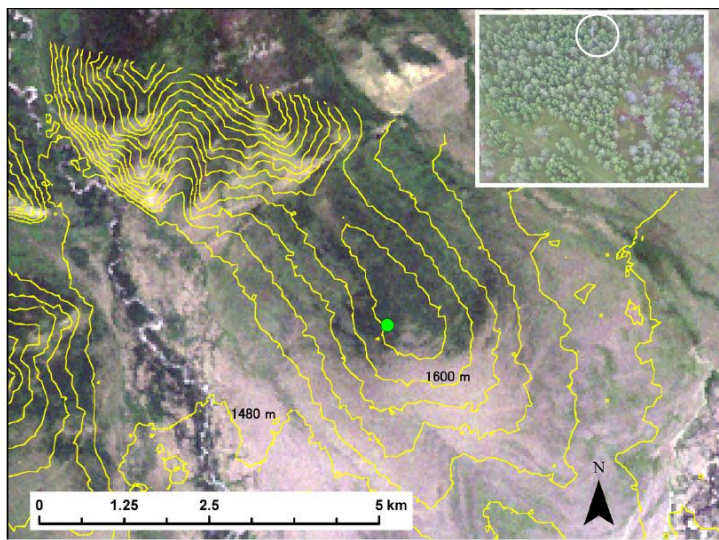


Fig. 8 Topographic map with a Landsat ETM+ true color image of the FOR site. Contour lines are shown at 30 m intervals, except for the upper side of the map as this is outside the ASTER image from which contour lines were created. The flux station is indicated by a circle. Also shown at the upright corner is aerial photograph of the site (Sugita et al., 2007).

2.3 Models

2.3.1 Century ecosystem model

The century ecosystem model has been designed and developed to require a minimum number of site-specific inputs for modeling of ecosystem processes using monthly time steps for long time periods, hence the name century. Originally, century ecosystem model was designed to simulate soil organic matter dynamics at monthly time step in the Great Plains Grasslands (Parton et al., 1987; 1988)). So far, it has been modified and expanded to simulate trace gases such as carbon (*C*), nitrogen (*N*), phosphorus (*P*) and sulfur (*S*) at grassland, forest, and savannah systems in the world (Parton et al., 1993). The primary purpose of century ecosystem model is to supply a tool for ecosystem analysis enabling the evaluation of changes in climate and the land use management of ecosystems (Ardo and Olsson, 2003). Generally, this model includes plant production, water cycle and soil organic matter and allows simulating carbon and hydrological cycles at the same time (Fig. 9). In our application, we used century ecosystem model (version 4; Parton et al., 1993) and mainly focused on *C* dynamics of aboveground biomass in order to study carbon processes in our study area.

The plant production models assume that the monthly maximum plant production is controlled by soil moisture and air temperature and that maximum plant production rates are decreased if there are insufficient nutrient supplies. The century ecosystem model includes a simplified water budget model which calculates monthly evaporation and transpiration water loss. Water loss occurs in century ecosystem model, first as interception and following by bare soil evaporation and transpiration. The potential evapotranspiration (*PET*) rate is calculated as a function of the average monthly, maximum and minimum air temperature using the equations developed by Linacre (1977). Bare soil water loss is a function of standing dead and litter biomass, rainfall and *PET*. Interception water loss is a function of aboveground biomass, rainfall and *PET*. Interception and bare soil water losses are calculated as fractions of the monthly precipitation and are subtracted from the total monthly precipitation, with the remainder of the water is added to the soil. Transpiration water loss occurs after the water was added to the soil. The maximum monthly evapotranspiration water loss rate is equal to potential evapotranspiration.

Average monthly soil temperature near the soil surface is calculated using equations developed by Parton (1984). These equations calculate maximum soil temperature as a function of the maximum air temperature and the canopy biomass while the minimum soil temperature is a function of the minimum air temperature and canopy biomass. The actual monthly soil

temperature used for decomposition and plant growth rate functions is the average of the monthly minimum and maximum as well as monthly soil temperatures. The soil organic matter submodel simulates the flow of *C*, *N*, *P* and *S* through plant litter and the different inorganic and organic pools in the soil. In the century model, the soil organic carbon is divided up into three major components which include active, slow and passive soil carbon. The effect of grazing pressure on plant production is represented in the model by employing Holland et al. (1992). All governing equations of century ecosystem model and parameters are shown in appendix A.

The site-specific input variables include monthly climate (minimum and maximum air temperature and mean precipitation), plant chemistry characteristics (lignin content, plant *N* content) and soil properties (soil texture, soil depth, soil *pH*, bulk density, *C* and *N* levels). Our work focused initially on the determination of parameter values that would generate quantitatively acceptable predictions of aboveground biomass and evapotranspiration. The details of datasets and parameters, used in century ecosystem model, are shown in Table 7.

Table 7 Data used in century ecosystem model application

| Data type | Data timeframe | Purposes | Reference and Investigator(s) name |
|-----------------------------------|------------------|--------------------------------|--|
| Plant physiological data | | | |
| Above & belowground biomass data | Monthly | Model calibration & validation | Sugita et al. (2008); Asano et al. |
| Root distribution | Fixed | Model input | |
| Soil properties data | | | |
| Soil texture and acidity | Fixed | Model input | Adyasuren et al. (2003) Asano et al. |
| Routine observation data | | | |
| Air temperature | Monthly | Model input | IMH datasets |
| Precipitation | Monthly | Model input | IMH datasets |
| Automatic weather station | | | |
| Evapotranspiration | Monthly | Model validation | Li et al. (2005) |
| ArcGIS data | | | |
| Soil map | Fixed | Model input | Saandar and Sugita (2004) |
| Land use map | Fixed | Model input | Saandar and Sugita (2004) |
| Mongolian statistical office data | | | |
| Animal number of each sum* | Changes annually | Model input | National Statistical Office of Mongolia (2003) |

*Sum is small hierarchier administrative unit in Mongolia

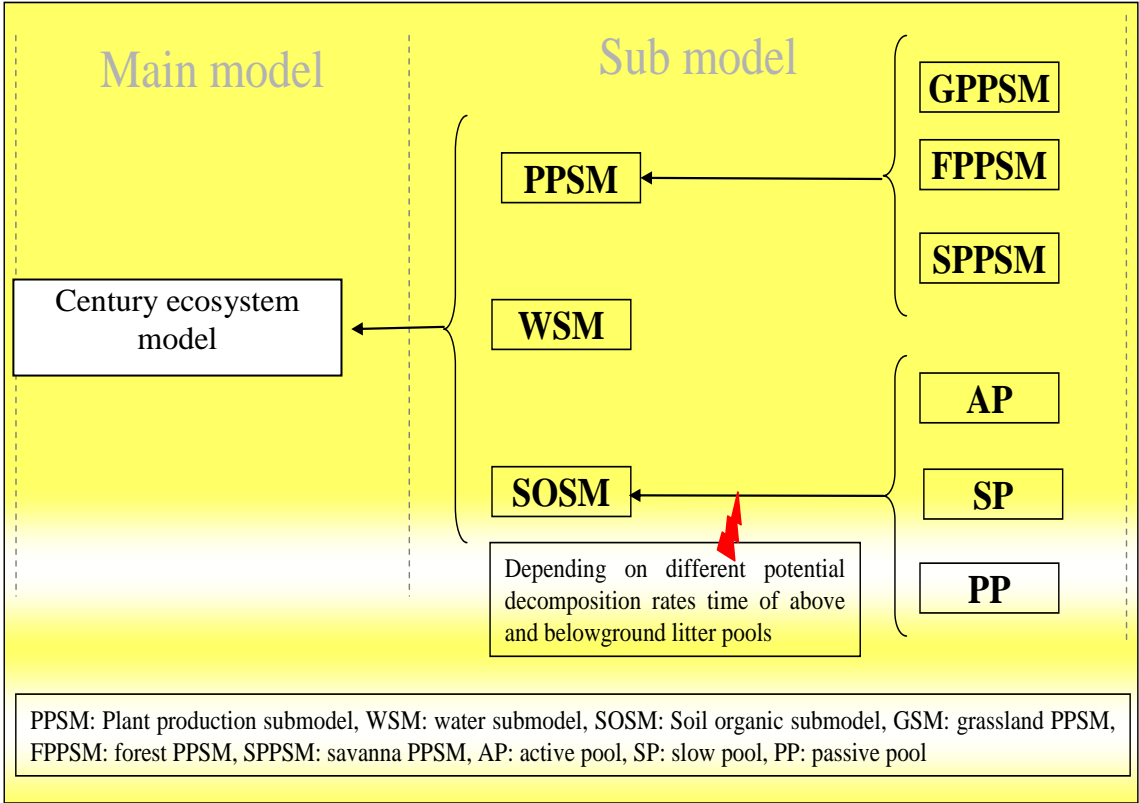


Fig. 9 Century ecosystem model scheme

2.3.2 TOPLATS land surface hydrological model

The TOPMODEL - Based Land Surface - Atmosphere Transfer Scheme (TOPLATS) used as a hydrological model was developed at Princeton University (Famiglietti et al., 1992). As suggested by the title, it is based on a TOPMODEL framework (Beven and Kirkby, 1979) and therefore, differs from other SVAT schemes by allowing topographic effects on water availability resulting from downslope flows. A detailed description of the original TOPLATS hydrological model is given by Famiglietti and Wood (1994a) and it has been applied to First International Satellite Land Surface Climatatology Project Field Experiment (FIFE) as described by Famiglietti and Wood (1994b).

Modifications of this original TOPLATS hydrological model are described by Peters-Lidard et al. (1997). The following modifications were done for energy and water balance part of the original model. For energy balance part, they (1) changed the ground heat flux estimation equation by adding heat storage, (2) included the calculation of the ground heat flux beneath the vegetation canopy and (3) added new formulation for soil thermal conductivity. For water balance part, they (1) changed the upper soil layer by adding thin soil layer for canopy root, (2) replaced the capillary fringe equation with a moisture diffusion formulation, (3) added calculation equation of bare soil evaporation rate, (4) included the effect of radiation and other environmental factors on stomatal resistance and (5) added atmospheric correction factor that separate roughness lengths for heat and momentum transfer. This modified version of TOPLATS hydrological model was used in this study.

There are two formulations of the model: one uses statistical distributions to describe spatial variability of topography and the other is fully spatially distributed. The following text will refer to both of the statistical and spatially distributed version. The scheme of TOPLATS hydrological model is shown in Fig. 10 and summary of the input datasets for TOPLATS hydrological model are given in Table 8.

The water balance was solved for a canopy (or bare soil) layer, a thin upper soil zone, a lower soil zone and the water table. The main assumptions of the TOPMODEL framework are that the saturated zone hydraulic gradient can be approximated by the local topographic index.

The topographic index was computed from DEM data by means of Eq. (3).

$$\lambda = \ln\left(\frac{a}{\tan B}\right) \quad (3)$$

where λ is topographic index, a is the upslope area of watershed and $\tan\beta$ is the grid slope angle acting on a grid. Higher topographic index values are associated with areas more likely to generate runoff.

Each pixel was assigned by a topographical index that represents the tendency for the point to be saturated and it was assumed that, every point in any part of the catchment with the same index value behaves in a similar hydrological way. The maximum canopy storage (or interception) capacity was calculated as a function of the leaf area index (Dickinson, 1984). Infiltration was calculated as a minimum of the net precipitation and soil infiltration capacity, after Milly (1986), and excess net precipitation was treated as surface runoff. Water exchange between the upper and lower zones is modeled by a diffusive flux (Peters-Lidard et al., 1997). Subsurface drainage and the local water table depth was based on the TOPMODEL principles assuming an exponential transmissivity profile as implemented by Sivapalan et al. (1987). Evaporation from bare soil was taken as minimum of actual evaporation from bare soil and potential evapotranspiration. For the soil-controlled rate, soil resistance was calculated assuming an exponential relationship between soil moisture and soil resistance (after Passerat de Silans, 1986, in Peters-Lidard et al., 1997). Transpiration from the dry canopy was taken as minimum of transpiration from bare soil and potential evapotranspiration. Canopy resistance was calculated using the method of Jacquemin and Noilhan (1990) based on the effects of solar radiation, the air humidity deficit, ambient temperature and water stress. Canopy resistance was described by Jacquemin and Noilhan (1990). All governing equations of TOPLATS hydrological model and parameters are shown in appendix B.

Table 8 Data used in TOPLATS hydrological model application

| Data type | Data timeframe | Purposes | Reference and Investigator(s) name |
|---|----------------|--------------------------|--|
| Plant physiological data | | | |
| Leaf area index | Monthly; fixed | Model input | Sugita et al. |
| Root distribution | Fixed | Model input | Asano et al. |
| Vegetation height | Monthly | Model input | Li et al, (2005) |
| Soil properties data | | | |
| Soil layer depth | Fixed | Model input | Asano et al. |
| Soil parameter (PF test) | Fixed | Model input | Tsujimura et al. |
| Automatic weather station and flux stations | | | |
| Air & soil temperature | Hourly | Model input & validation | Sugita et al. (2008) |
| Precipitation & soil moisture | Hourly | Model input & validation | Sugita et al. (2008) |
| Radiations | Hourly | Model input | Sugita et al. (2008) |
| Energy fluxes | Hourly | Model validation | Li et al.(2005) |
| Evapotranspiration | Hourly | Model validation | Li et al.(2005) |
| ArcGIS data | | | |
| Soil map | Fixed | Model input | Saandar and Sugita (2004) |
| Vegetation map | Fixed | Model input | Saandar and Sugita (2004) |
| DEM data | Fixed | Model input | Aster GDEM (Earth Remote Sensing Data Analysis Center, 2009) |

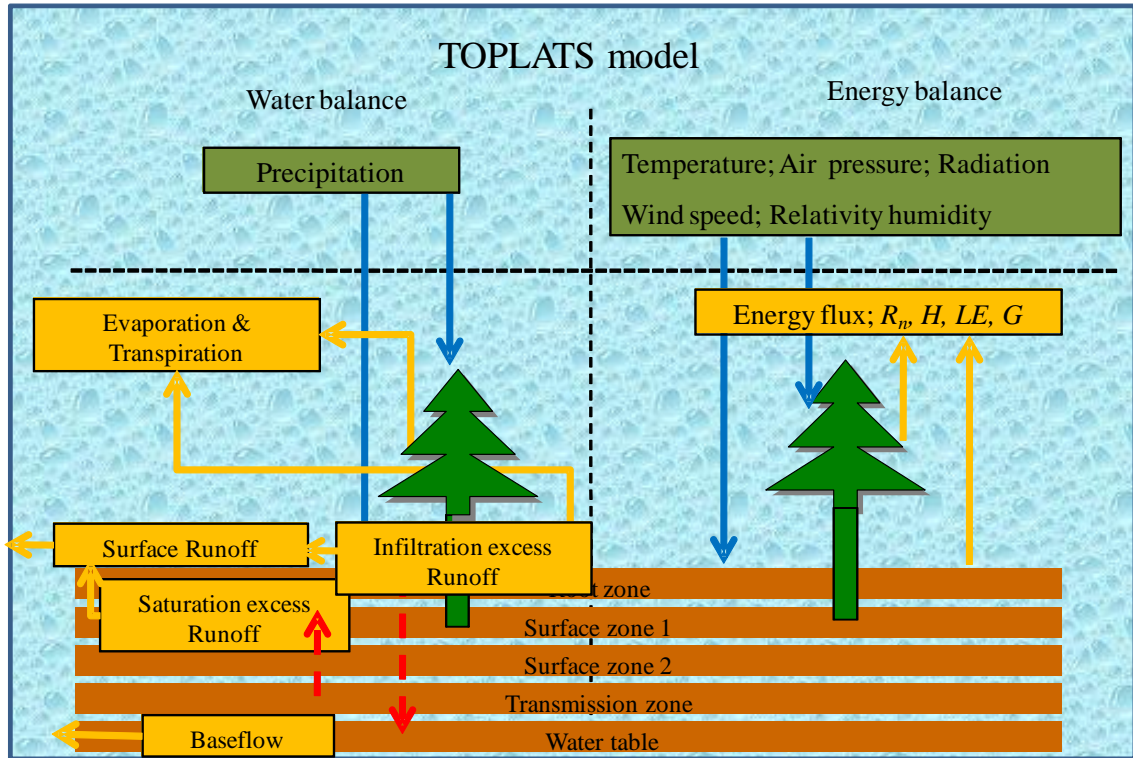


Fig. 10 TOPLATS hydrological model scheme (R_n is net radiation; H is sensible heat flux; LE is latent heat flux; G is ground heat flux)

2.3.3 Coupling of century and TOPLATS models

2.3.3.1 Variable selection

The coupling between the ecosystem and the hydrological model can be accomplished in different ways depending on (1) the processes that may be incorporated, (2) the time scales on which the ecosystem model is allowed to interact with the hydrological model and (3) the manner in which the modeling exercise may be set up, which itself depends on the purpose of the model (Arora, 2002). The coupling between an ecosystem model and a SVAT scheme is relatively complicated because SVAT schemes also explicitly simulate the energy balance and momentum fluxes that are required by the atmospheric models.

With regard to the energy balance, the LAI and the fact that whether leaves are present or not are used to estimate land-surface albedo and canopy resistance that in turn, affect the surface radiation balance and canopy energy balance. Evapotranspiration from the canopy also affects its energy balance and temperature. Both land-surface albedo and canopy resistance are functions of LAI. The energy and momentum fluxes from the canopy to the boundary layer in most SVAT schemes are modeled using the bulk aerodynamic approach. The aerodynamic resistance is a function of wind speed and surface drag coefficient which is a function of surface roughness length and stability. The surface roughness length in the most SVAT schemes is linearly related to the canopy height, which itself is a function of stem biomass.

With regard to the water balance, other than LAI and stomatal conductance, most SVAT schemes also require rooting depth (defined as the depth that includes 99% of the roots) and root distribution as vegetation-dependent input parameters. The soil column in SVAT schemes is divided into a number of layers usually varying between two and six. Rooting depth is used to estimate the soil water capacity available for transpiration and root distribution is used to estimate the fraction of roots in each soil layer. The interactions between the SVAT scheme and the vegetation model can occur with exchange of following variables viz. soil moisture, soil temperature, canopy temperature, LAI, roughness length, stomatal conductance, rooting depth and root distribution between these two models.

Among these variables, century ecosystem cannot produce canopy temperature, roughness length, stomatal conductance, rooting depth and root distribution whereas soil moisture and temperature can be produced only at monthly time step. However, soil moisture and temperature at monthly time step cannot be used for TOPLATS hydrological model because TOPLATS hydrological model works at different time step module as an input (i.e. TOPLATS hydrological model has hourly time step). The selection of exchangeable variables between

century ecosystem and TOPLATS hydrological model is depending mainly on dimension of their geometry structure and time step. Therefore, LAI was used to link our selected models and its sensitivity analysis will be discussed in the results section.

2.3.3.1 Coupling methodology

The primary purpose of coupling century ecosystem model with TOPLATS hydrologic model is to provide it with dynamic values of LAI. The LAI values in the century ecosystem model are estimated on the basis of the amount of carbon present in the leaf biomass. In general, as scientific understanding of modeling progresses, new models are developed and existing ones are updated. These challenges are addressed by many methodologies and found elsewhere (e.g., Karimi and Houston, 1996; Brandmeyer and Karimi, 2000), which some researchers have categorized. For example, Brandmeyer and Karimi (2000) present a synthesis of methodologies for coupling environmental models from the perspective of an environmental modeler.

Coupling methodologies were classified in their study as tool, joined, shared loose and one-way data transfer coupling methodology. As a reference, we mentioned one-way data transfer coupling methodology for our coupled modeling system, since only LAI can be selected as an exchange variable between century ecosystem model and TOPLATS hydrological model.

3. Results and Discussion

3.1 Application and validation of century ecosystem model

One of the main objectives of the present study is to understand the key processes leading land-use changes and their influence on carbon cycle in Mongolian semiarid region. Both of the field measurements and modeling efforts were used for this purpose. On the modeling front, the century ecosystem model (version 4) was used to describe the carbon dynamics at two different surface conditions of grazing and nongrazing conditions.

All modeling systems must be validated by examining the capability to capture the actual features of modeled variables, both in quantitative and qualitative manner. Two lines of simulation at point and spatial scales were employed to investigate into the validity of century ecosystem model, with respect to the capability to capture the actual biomass dynamics.

3.1.1 Model parameters

For the comparisons among different grassland sites worldwide, it was desirable for the majority of the model parameters to comprise a universal set, with relatively few numbers of site-specific parameters changing according to the different circumstances (Parton et al., 1993). Therefore, the most parameters used in century ecosystem model are indented to remain same in the majority of application and are referred to as fixed parameters.

As mentioned before, major site-specific input variables include monthly climate, parameters such as plant chemistry characteristics and soil properties. The site specific input variables of monthly climate datasets were prepared using ten years observation data from 1993 to 2002 obtained by the Metostation of IMH at KBU site. The trend of maximum and minimum air temperature shows slight increase during this period, whereas precipitation was slightly decreased (Tables 9 – 11 and Fig. 11).

Table 9 Maximum air temperature from 1993 to 2007 at KBU site (Routine observation data by IMH Metostation)

| Month | 1993 | 1994 | 1995 | 1996 | 1997 | 1998 | 1999 | 2000 | 2001 | 2002 | 2003 | 2004 | 2005 | 2006 | Mean |
|-------|-------|-------|-------|-------|-------|-------|-------|-------|-------|-------|-------|-------|-------|-------|--------------|
| Jan | -13.3 | -15.2 | -14.5 | -17.9 | -17.2 | -16.9 | -17.9 | -20.1 | -22.3 | -13.7 | -10.9 | -22.3 | -13.7 | -10.9 | -16.2 |
| Feb | -6.2 | -10.3 | -14.7 | -11.2 | -10.8 | -4.2 | -8.6 | -13.5 | -15.4 | -7.9 | -7.4 | -15.4 | -7.9 | -7.4 | -10.1 |
| Mar | -3.0 | 1.2 | -3.0 | -1.3 | -3.0 | 2.4 | -5.8 | 1.2 | -2.3 | -13.7 | -1.1 | -2.3 | -13.7 | -1.1 | -3.3 |
| Apr | 7.0 | 10.5 | 9.2 | 9.1 | 10.9 | 9.2 | 10.3 | 9.2 | 9.4 | 8.2 | 8.8 | 9.4 | 8.2 | 8.8 | 9.1 |
| May | 26.9 | 17.9 | 13.6 | 21.1 | 18.2 | 17.6 | 18.4 | 20.9 | 18.1 | 16.2 | 16.3 | 18.1 | 16.2 | 16.3 | 18.3 |
| Jun | 21.2 | 23.2 | 18.7 | 20.7 | 23.9 | 23.1 | 21.1 | 27.6 | 25.6 | 22.1 | 22.1 | 25.6 | 22.1 | 22.1 | 22.8 |
| Jul | 21.2 | 23.3 | 15.8 | 24.2 | 25.1 | 25.5 | 25.7 | 26.4 | 26.1 | 25.9 | 25.9 | 26.1 | 25.9 | 25.9 | 24.5 |
| Aug | 19.2 | 31.5 | 22.9 | 23.4 | 21.5 | 21.0 | 22.3 | 21.2 | 24.5 | 25.2 | 23.5 | 24.5 | 25.2 | 23.5 | 23.5 |
| Sep | 16.2 | 16.6 | 4.0 | 21.4 | 14.6 | 18.0 | 14.6 | 19.0 | 17.5 | 17.3 | 17.0 | 17.5 | 17.3 | 25.1 | 16.9 |
| Oct | 8.0 | 7.9 | 9.2 | 6.6 | 9.3 | 9.1 | 6.6 | 3.0 | 5.9 | 2.2 | 5.7 | 4.3 | 2.2 | 5.7 | 6.1 |
| Nov | -8.4 | 0.4 | 1.0 | -9.4 | -3.2 | -4.0 | -2.9 | -4.0 | -1.1 | -4.0 | -5.4 | -1.1 | -8.2 | -5.4 | -4.0 |
| Dec | -14.8 | -14.7 | -9.8 | -14.2 | -12.1 | -16.3 | -14.3 | -17.8 | -18.0 | -18.5 | -4.9 | -18.0 | -18.5 | -4.9 | -14.1 |

Unit: °C

Table 10 Minimum air temperature from 1993 to 2007 at KBU site (Routine observation data by IMH Metostation)

| Month | 1993 | 1994 | 1995 | 1996 | 1997 | 1998 | 1999 | 2000 | 2001 | 2002 | 2003 | 2004 | 2005 | 2006 | Mean |
|-------|-------|-------|-------|-------|-------|-------|-------|-------|-------|-------|-------|-------|-------|-------|--------------|
| Jan | -26.1 | -25.8 | -28.1 | -31.1 | -28.3 | -29.0 | -29.7 | -31.1 | -32.5 | -24.9 | -18.9 | -30.5 | -24.9 | -18.9 | -27.1 |
| Feb | -18.9 | -23.1 | -28.2 | -25.7 | -24.4 | -18.9 | -23.2 | -26.1 | -28.3 | -21.3 | -17.1 | -27.5 | -21.3 | -17.1 | -22.9 |
| Mar | -13.8 | -4.7 | -13.8 | -13.2 | -13.8 | -10.7 | -17.8 | -10.9 | -13.4 | -24.9 | -10.6 | -13.4 | -24.9 | -10.6 | -14.0 |
| Apr | 0.2 | 1.5 | -0.4 | -2.3 | -2.2 | -0.4 | -0.2 | -0.7 | -0.8 | -0.8 | 1.0 | -0.8 | -0.8 | 1.0 | -0.4 |
| May | 7.2 | 8.9 | 6.3 | 9.6 | 9.0 | 7.6 | 8.9 | 11.9 | 8.5 | 9.4 | 8.0 | 8.5 | 9.4 | 8.0 | 8.7 |
| Jun | 14.1 | 17.1 | 13.0 | 13.6 | 15.7 | 15.7 | 13.0 | 18.7 | 18.0 | 15.4 | 14.6 | 18.0 | 15.4 | 14.6 | 15.5 |
| Jul | 15.8 | 17.3 | 11.5 | 17.0 | 17.3 | 19.0 | 18.7 | 18.6 | 18.1 | 18.2 | 18.5 | 18.1 | 18.2 | 18.5 | 17.5 |
| Aug | 12.7 | 15.4 | 15.1 | 15.2 | 14.8 | 14.3 | 14.2 | 15.0 | 17.0 | 15.4 | 16.0 | 17.0 | 15.4 | 16.0 | 15.3 |
| Sep | 6.7 | 8.1 | 0.9 | 6.4 | 6.7 | 7.3 | 6.9 | 8.8 | 6.9 | 5.5 | 7.4 | 6.9 | 5.5 | 17.8 | 7.3 |
| Oct | -4.5 | -4.1 | -3.6 | -5.9 | -4.1 | -2.7 | -4.8 | -6.6 | -4.5 | -7.2 | -2.1 | -2.1 | -7.2 | -2.1 | -4.4 |
| Nov | -19.1 | -12.8 | -12.9 | -20.6 | -16.1 | -15.2 | -14.8 | -15.2 | -14.2 | -15.2 | -12.4 | -14.2 | -18.0 | -12.4 | -15.2 |
| Dec | -23.0 | -25.2 | -23.6 | -24.5 | -24.9 | -26.5 | -23.2 | -26.6 | -27.7 | -28.2 | -6.4 | -27.7 | -28.2 | -6.4 | -23.0 |

Unit: °C

Table 11 Precipitation from 1993 to 2007 at KBU site (Routine observation data by IMH Metostation)

| Month | 1993 | 1994 | 1995 | 1996 | 1997 | 1998 | 1999 | 2000 | 2001 | 2002 | 2003 | 2004 | 2005 | 2006 | Mean |
|-------|--------|--------|--------|--------|--------|--------|--------|--------|--------|--------|--------|--------|--------|--------|---------------|
| Jan | 0.06 | 0.29 | 0.00 | 0.33 | 0.00 | 0.28 | 0.00 | 0.19 | 0.59 | 0.32 | 0.02 | 0.07 | 0.52 | 0.13 | 0.20 |
| Feb | 0.17 | 0.41 | 0.00 | 0.00 | 0.45 | 0.02 | 0.00 | 0.11 | 0.09 | 0.19 | 0.32 | 0.09 | 1.37 | 1.24 | 0.32 |
| Mar | 0.31 | 0.00 | 0.31 | 0.21 | 0.31 | 0.01 | 0.13 | 0.12 | 0.16 | 0.31 | 0.13 | 0.15 | 0.00 | 1.90 | 0.29 |
| Apr | 0.61 | 0.14 | 0.34 | 0.04 | 0.04 | 0.34 | 0.08 | 0.20 | 0.26 | 0.39 | 0.10 | 1.36 | 0.10 | 0.08 | 0.29 |
| May | 0.42 | 0.69 | 0.12 | 0.36 | 0.17 | 0.24 | 0.81 | 0.00 | 0.40 | 3.13 | 2.56 | 1.12 | 0.00 | 1.45 | 0.82 |
| Jun | 2.54 | 1.80 | 2.18 | 1.77 | 2.06 | 3.41 | 6.23 | 0.84 | 3.93 | 7.56 | 4.15 | 5.26 | 3.69 | 1.48 | 3.35 |
| Jul | 8.99 | 6.04 | 1.85 | 8.14 | 7.48 | 4.13 | 3.89 | 6.66 | 3.30 | 4.11 | 5.11 | 6.43 | 5.10 | 7.79 | 5.64 |
| Aug | 15.22 | 6.79 | 5.96 | 5.55 | 5.03 | 10.72 | 1.41 | 7.67 | 2.76 | 2.74 | 6.05 | 2.04 | 4.50 | 1.13 | 5.54 |
| Sep | 1.68 | 2.02 | 0.74 | 0.45 | 1.55 | 2.20 | 2.89 | 0.86 | 3.12 | 0.13 | 3.73 | 1.80 | 3.40 | 2.48 | 1.93 |
| Oct | 0.98 | 0.13 | 0.19 | 0.67 | 0.00 | 1.16 | 0.00 | 1.18 | 1.36 | 0.62 | 0.00 | 1.36 | 0.00 | 0.43 | 0.58 |
| Nov | 0.63 | 0.03 | 0.00 | 0.64 | 0.25 | 0.43 | 2.45 | 0.43 | 0.22 | 0.29 | 0.06 | 0.00 | 0.00 | 0.90 | 0.45 |
| Dec | 0.54 | 0.86 | 0.23 | 0.13 | 0.18 | 0.00 | 0.32 | 0.12 | 0.48 | 0.14 | 0.09 | 0.32 | 0.70 | 0.32 | 0.32 |
| Total | 321.50 | 192.00 | 119.20 | 182.92 | 175.20 | 229.43 | 182.16 | 183.82 | 166.72 | 199.30 | 223.20 | 200.04 | 193.76 | 193.25 | 197.32 |

Unit: cm month⁻¹

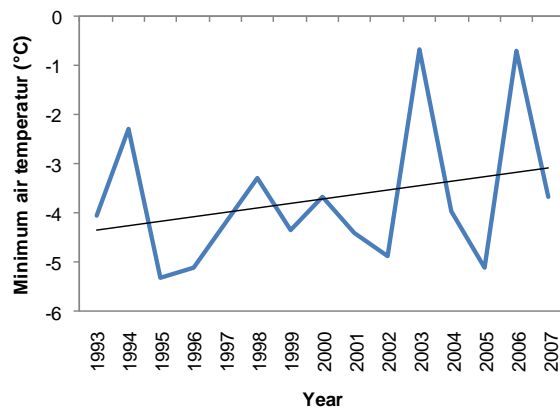
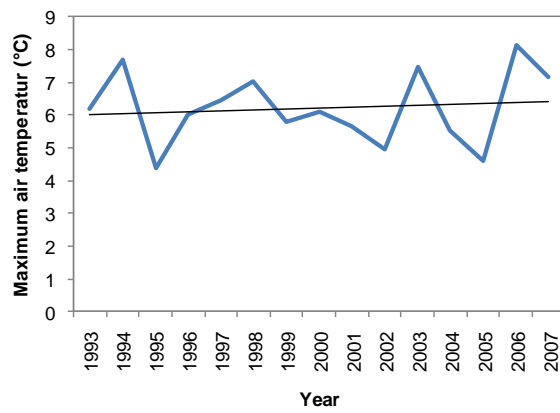
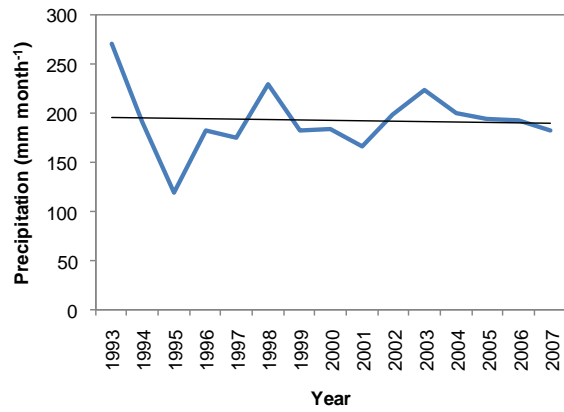


Fig. 11 Annual mean precipitation, maximum and minimum air temperature at KBU site from 1993 to 2007.

3.1.2 Validation at point scale

Century ecosystem model was first spun up for 60 years based on a ten years mean climatology (averaged over 1993-2002), which allows the state variables in the model to reach equilibrium as shown in Fig. 12. Second, actual climatology datasets from 2003 to 2006 were used to run century ecosystem model. The century ecosystem model was first applied and validated at KBU site and then at FOR site, where ecological and hydrological components were comprehensively measured from 2003 to 2006. The validation of century ecosystem model was carried out by comparing outputs with measured aboveground biomass and evapotranspiration. During simulation, for grazing surface condition, local grazing pressure intensity value of 0.45 was used, calculated based on Mongolian statistical office data of livestock number by Eq. (2).

The simulated results of aboveground biomass by means of century ecosystem model were compared with the measured aboveground biomass at grazing (Fig. 13) and nongrazing surface condition (Fig. 14) at KBU site. The simulation of aboveground biomass showed good agreement with the measurements with $r= 0.95$ and $RMSE = 5.77 \text{ g C m}^{-2}$ in both the magnitude and temporal patterns at grazing site in Fig. 13, whereas simulated aboveground biomass were compared with measurements with $r= 0.96$ and $RMSE = 8.15 \text{ g C m}^{-2}$ at nongrazing surface condition.

The century ecosystem model greatly simplified the real ecosystem. However, some differences can be observed between measured and simulated aboveground biomass. This can probably be explained by possible human error during the field measurement of aboveground biomass. For example, the sampling error can often be a problem in selecting quadrat. Despite these differences, the trends of magnitude and variation in simulated aboveground biomass agree with those of measured data. The sum of the peak aboveground biomass from 2003 to 2006 for grazing surface condition was equal to $117.77 \text{ g C m}^{-2}$ (measurement) and $110.75 \text{ g C m}^{-2}$ (simulation), and for nongrazing condition, they are $177.90 \text{ g C m}^{-2}$ (measurement) and $171.17 \text{ g C m}^{-2}$ (simulation) (Table. 12). These two sites yielded difference of 60.41 g C m^{-2} (measurement) and 60.43 g C m^{-2} (simulation) of aboveground biomass because of grazing pressure by livestock. We have also investigated the one year (2003) aboveground biomass reduction by the grazing pressure. The simulated annual aboveground biomass was $130.78 \text{ g C m}^{-2} \text{ y}^{-1}$ for nongrazing surface condition and $107.27 \text{ g C m}^{-2} \text{ y}^{-1}$ for grazing surface condition. This result gives aboveground biomass removal by grazing pressure was estimated as $23.5 \text{ g C m}^{-2} \text{ y}^{-1}$ which is close to value of $28.5 \text{ g C m}^{-2} \text{ y}^{-1}$ in Li et al. (2005) based on eddy correlation method.

Hydrological processes were studied by many using measurement of

hydro-meteorological variables and surface energy fluxes in Mongolian semi-arid steppe region (Zhang et al., 2005; Kato, 2007; Li et al., 2007; Lui et al., 2010). However, only a few studies were carried out to study the modeling responses on evapotranspiration in this region (e.g., Lee, 2006; Chen et al., 2007). Century ecosystem model simulates evapotranspiration by its simple water balance submodel. Figs. 15 and 16 show the comparison of measured and simulated evapotranspiration at grazing and nongrazing surface condition at KBU site from 2003 to 2006, which show similar patterns of evapotranspiration with $RMSE = 3.3 \text{ mm month}^{-1}$, $r = 0.84$ and regression coefficients of $\hat{y} = ax + b$ are $a=0.91$ and $b=1.81$ at grazing surface condition. Those obtained at nongrazing surface condition as $RMSE = 3.2 \text{ mm month}^{-1}$, $r = 0.85$ and regression coefficients of $\hat{y} = ax + b$ are $a=0.92$ and $b=1.23$ (Table 13). These statistical analyses indicate slight difference of evapotranspiration at grazing and nongrazing surface condition. However, some differences between measured and simulated evapotranspiration were observed and this can be explained mainly due to simple water balance of century ecosystem model. Total simulated evapotranspiration of 2003 was 221.47 mm y^{-1} at grazing and 221.64 mm y^{-1} at nongrazing surface condition. These values were very close to observed value of 241.0 mm y^{-1} reported in Li et al. (2007). In addition, simulated evapotranspiration gives very close value for both of grazing and nongrazing surface condition during our investigated period. Thus these results agree well with previous studies of Kato, (2007), who showed energy and hydrological balance in Mongolian steppe area.

The grazing pressure was found as a value of $0.13 \text{ SE}_u \text{ ha}^{-1}$ by means of Eq. (2) in FOR site and it was used to century ecosystem model to simulate aboveground biomass. Theoretically, coefficients of Eq. (2) should be different between forest and steppe. However, calculated grazing pressure value together with century ecosystem model in forest site gave good simulation. Fig. 17 shows comparison of measured and simulated aboveground biomass in FOR site and gives good agreement $RMSE = 6.32 \text{ g C m}^{-2}$. This result suggests that century ecosystem model also works satisfactory to reproduce aboveground biomass dynamics in forest area.

Several features can be noted from the century ecosystem model application at point scale. First, the difference in agreement between grazing and nongrazing surface condition seems small and thus, century ecosystem model can be judged equally applicable at both surface conditions in Mongolian semi-arid region and forest site as well. Second, century ecosystem model has very simple water budget submodel simulating evapotranspiration and it gives some difference of magnitude and variation. In general, any hydrological model requires hourly time series data to simulate water fluxes with good accuracy. Thus, it is necessary to employ high performance hydrological model in order to achieve good understanding about hydrological

processes in our study area. Third, the use of minimum input parameters together with century ecosystem to give quite good simulation of aboveground biomass and fair simulation of evapotranspiration, which means that century ecosystem model acts as a robust model for simulating aboveground biomass dynamics.

Table 12 Comparison between measured and simulated aboveground biomass (g C m^{-2}) in KBU site

| Time | | Grazing surface condition | | Nongrazing surface condition | |
|--------------|-------|---------------------------|---------------|------------------------------|---------------|
| Year | Month | Measurement | Simulation | Measurement | Simulation |
| 2003 | July | 33.21 | 27.70 | 49.00 | 43.89 |
| 2004 | July | 34.52 | 31.73 | 60.45 | 54.60 |
| 2005 | July | 22.51 | 23.72 | 33.45 | 34.01 |
| 2006 | July | 27.53 | 27.60 | 35.00 | 38.67 |
| Total | | 117.77 | 110.75 | 177.90 | 171.17 |

Table 13 Comparison of statistics between simulated and measured aboveground biomass and evapotranspiration at grazing and nongrazing surface condition in KBU site.

| Variables | Grazing | | | | Nongrazing | | | |
|---------------------|---------|----------|----------|----------|------------|----------|----------|----------|
| | RMSE | <i>a</i> | <i>b</i> | <i>r</i> | RMSE | <i>a</i> | <i>b</i> | <i>r</i> |
| Aboveground biomass | 5.77 | 0.78 | 4.86 | 0.95 | 8.15 | 0.79 | 8.52 | 0.96 |
| Evapotranspiration | 3.36 | 0.91 | 1.81 | 0.84 | 3.25 | 0.92 | 1.23 | 0.85 |

RMSE: root mean square error (g C m^{-2}), *a* and *b*: regression coefficients of linear equation of $\hat{y} = ax + b$.

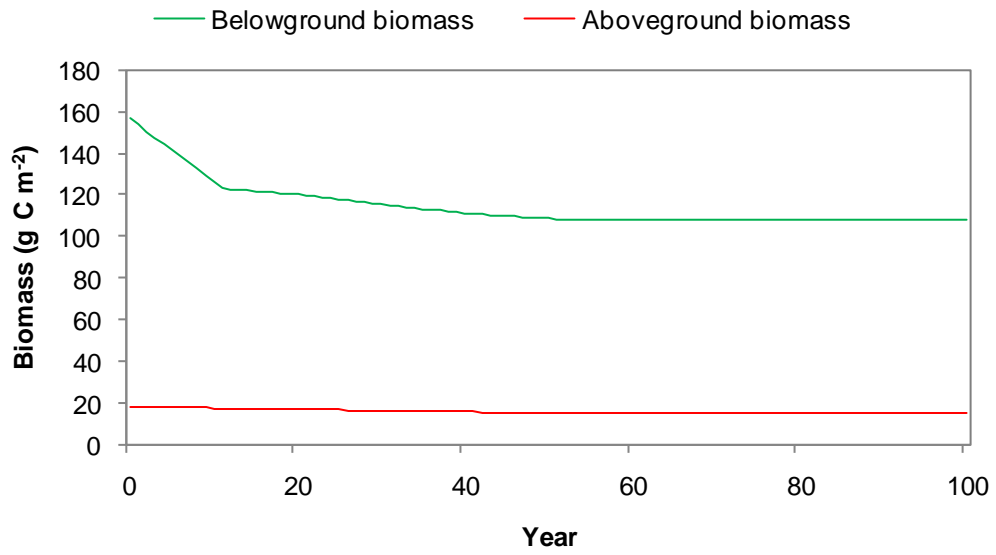


Fig. 12 Spun up for 60 years based on a ten years mean climatology (averaged over 1993-2002) in KBU site

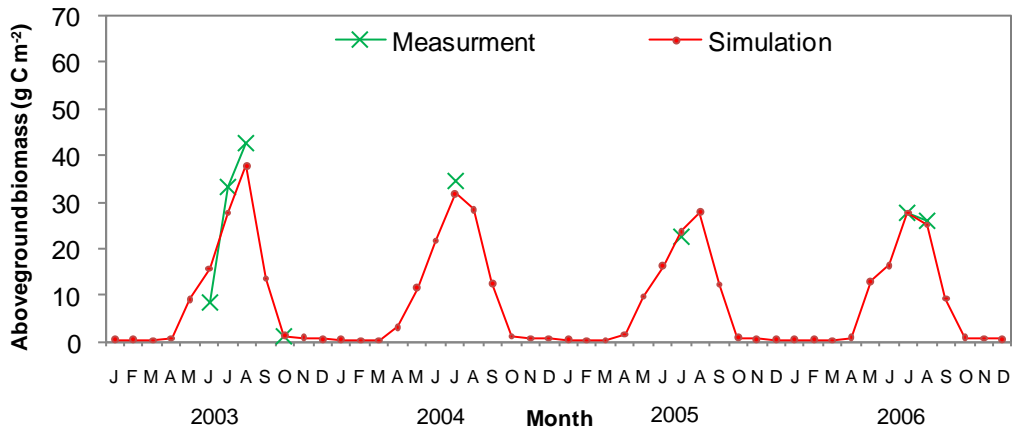


Fig. 13 Comparison of simulated and measured aboveground biomass at grazing and in KBU site (2003- 2006)

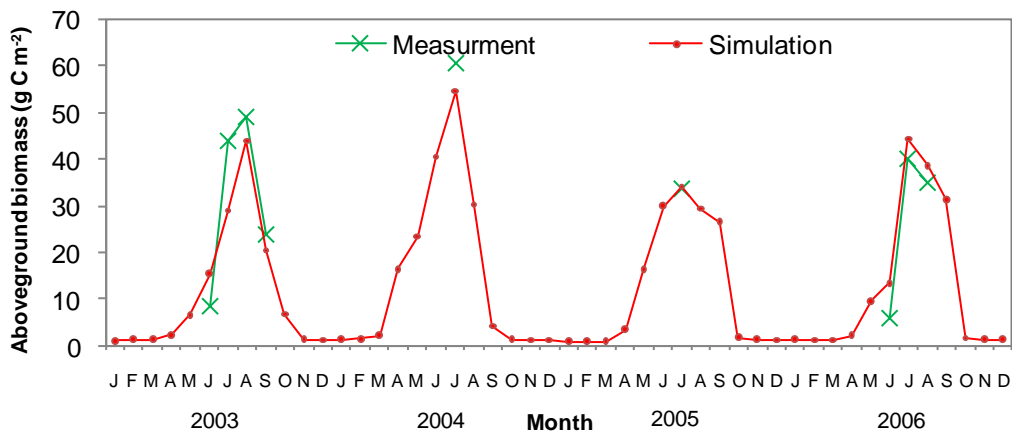


Fig. 14 Same as Fig. 13, but for nongrazing surface condition in KBU site (2003- 2006)

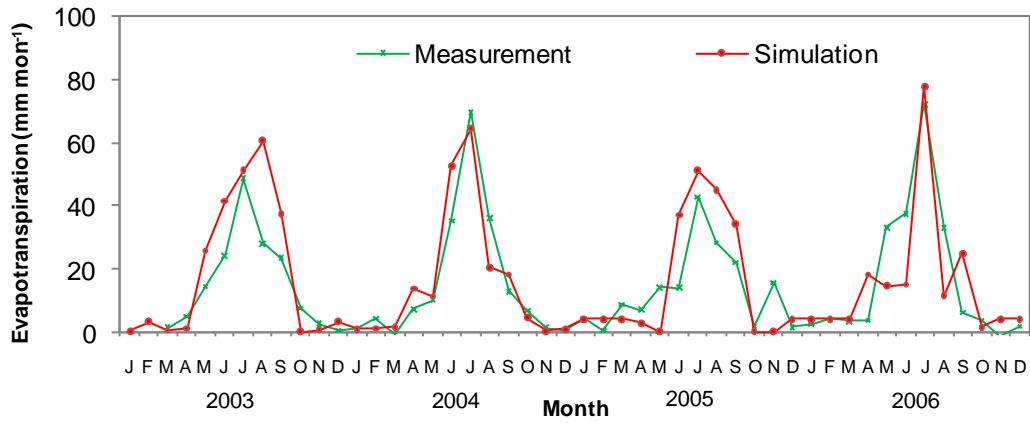


Fig. 15 Comparison of simulated and measured evapotranspiration at grazing and in KBU site (2003- 2006)

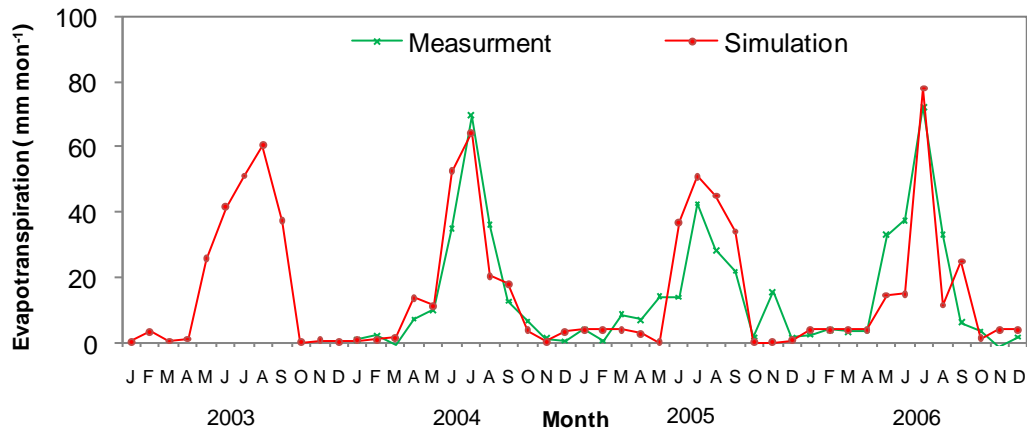


Fig. 16 Same as Fig. 15, but for nongrazing surface condition in KBU site (2003- 2006)

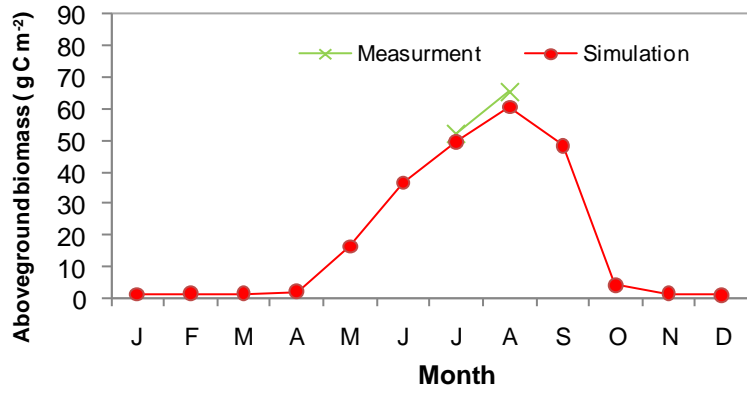


Fig. 17 Comparison of simulated and measured evapotranspiration at FOR site (2003)

3.1.3 Model sensitivity response to climate input

The purpose of a sensitivity analysis is to "challenge" the model by varying the parameters and variables (such as growth rates, increased or decreased initialization values) and observe the corresponding fluctuations and behavior. The sensitivity analysis may also identify variables that can be omitted or overlooked and which are missing (Silvert, 2001), or even interrelationships that are not described correctly in the model. If the model is large and complex it is probably not possible to perform sensitivity analysis on each parameter or state variable. Therefore a careful selection of the parameters with priorities is necessary. In this way the sensitivity analysis will help to expose the importance of each variable and parameter and thus identify towards which variables the model is "sensitive" to as well as how accurate data input should be to reach reasonable model output (Jorgensen and Bendoricchio, 2001). The parameters can be adjusted up and down which will influence the processes and thus the state of the system.

By holding the site specific parameters and grazing pressure parameter constant, century ecosystem model was ran using the different atmosphere forcing data to determine how century ecosystem model estimates ecohydrological components. The model was configured to run at KBU site driven by observed monthly mean, maximum and minimum air temperature and precipitation. Besides the control simulation, two sensitivities runs were conducted with precipitation and air temperature. Changes in precipitation were achieved by changing the input data to 50% and 100% more or 50% less than the actual precipitation data. For air temperature, we increased or decreased by 1σ and 0.5σ (i.e. standard deviation) from the actual air temperature data (See Table 14). All runs were compared to a control run with the unchanged actual data of precipitation and air temperature. Overall, we ran eight simulations, one control and three sensitivity runs for precipitation and four runs for air temperature. All sensitivity analysis were made between January and December of 2003 at KBU site.

3.1.3.1 Precipitation

To test sensitivity of precipitation, we increased the actual precipitation data by 50% and 100% and decreased it by 50%. This has major effects on both of aboveground biomass and evapotranspiration as shown in Fig. 18. The effect of changes in the precipitation is large if the precipitation was increased by 50% and 100%. The 100% change lead to an average of 38% increase of the peak aboveground biomass and an average of 27% increase of peak evapotranspiration. For the 50% decrease in the actual precipitation, the peak of aboveground

biomass was reduced by 55 %, whereas peak evapotranspiration was reduced by 65 %.

3.1.3.2 Air temperature

When we investigated the sensitivity of air temperature predictions, the actual air temperature was increased by factor of 1σ and 0.5σ and also decreased by 1σ and 0.5σ . From Fig. 19 we found that, if air temperature was 1σ or 0.5σ times higher or 1σ times lower than the actual air temperature, it results in the decrease in aboveground biomass. In contrast, if air temperature was decreased by 0.5σ , it leads to increase of aboveground biomass. In all cases of evapotranspiration similar patterns with control run was obtained but all air temperature treatments result reduced evapotranspiration, because of different influence of air temperature.

These results from sensitivity analysis by century ecosystem model suggest that Mongolian steppe biomass is more sensitive to precipitation than air temperature. These results agree with previous studies in semi-arid region that precipitation is the main controlling factor for plant growth than temperature. (e.g., Li et al., 2005; Natsagdorj, 2000; Seastedt et al., 1998; Wilhite, 1993).

Table 14 Different air temperature scenarios

| Month | T (°C) | $T-\sigma$ | $T+\sigma$ | $T-0.5\sigma$ | $T+0.5\sigma$ |
|-----------|----------|------------|------------|---------------|---------------|
| January | -22.8 | -45.6 | -11.7 | -37.1 | -20.2 |
| February | -17.0 | -40.8 | -6.9 | -32.4 | -15.4 |
| March | -8.2 | -30.7 | 3.2 | -22.2 | -5.3 |
| April | 4.4 | -17.6 | 16.3 | -9.1 | 7.8 |
| May | 13.9 | -8.3 | 25.6 | 0.2 | 17.2 |
| June | 19.1 | -1.5 | 32.4 | 6.9 | 23.9 |
| July | 20.5 | 0.2 | 34.1 | 8.7 | 25.6 |
| August | 19.1 | -2.1 | 31.8 | 6.4 | 23.4 |
| September | 11.2 | -10.5 | 23.4 | -2.1 | 14.9 |
| October | 1.0 | -21.8 | 12.1 | -13.3 | 3.7 |
| November | -9.8 | -32.8 | 1.1 | -24.4 | -7.4 |
| December | -20.1 | -42.4 | -8.5 | -33.9 | -16.9 |

T : air temperature, σ : the standard deviation

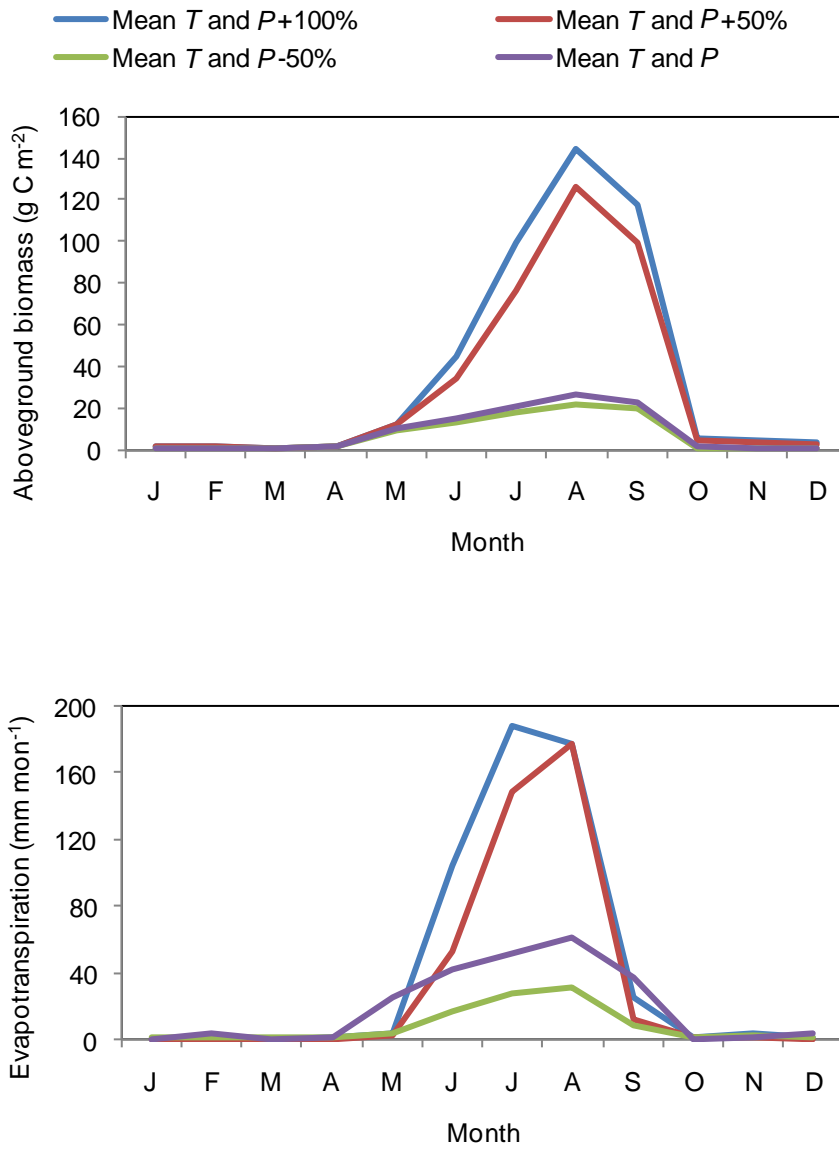


Fig. 18 Test results of precipitation changes on aboveground biomass and evapotranspiration (T is air temperature; P is precipitation; mean P and T are mean values of monthly actual measurement data of P and T)

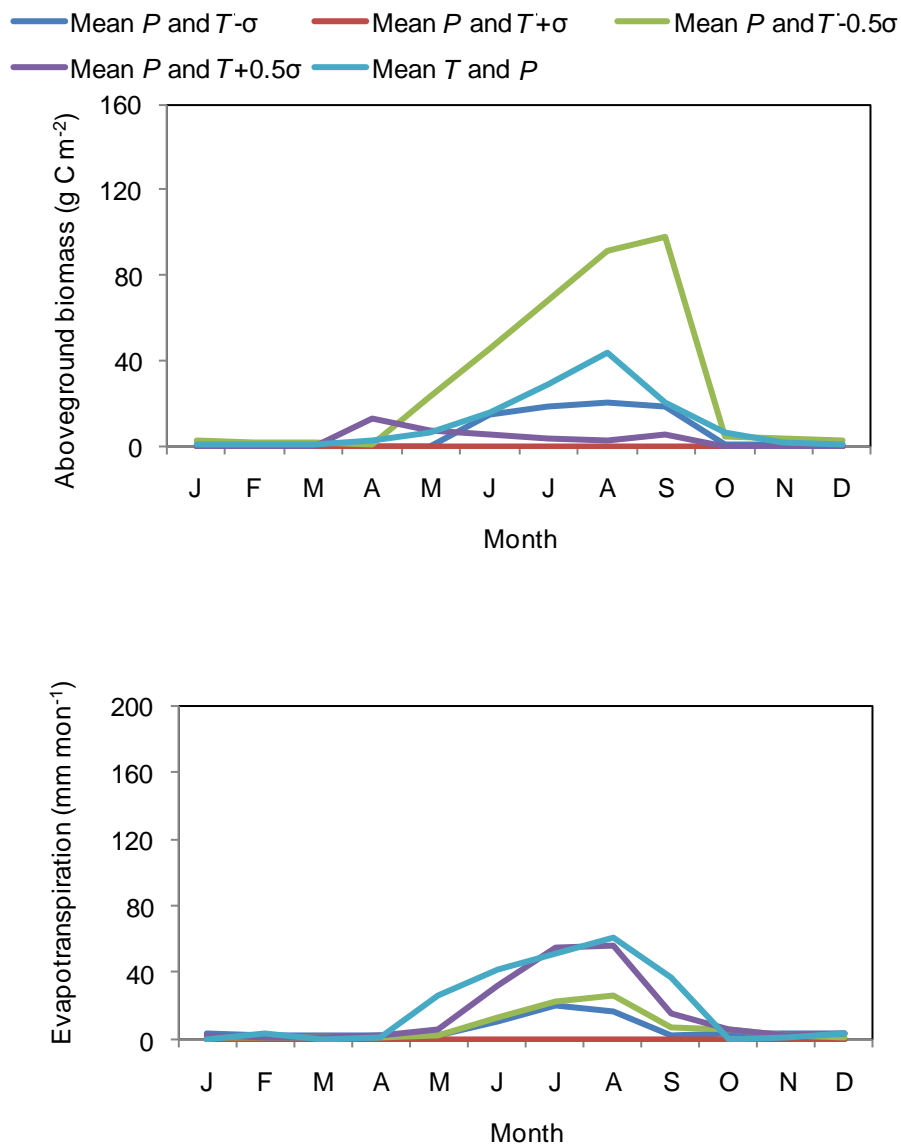


Fig. 19 Test results of air temperature changes on aboveground biomass and evapotranspiration. (T is air temperature; P is precipitation; mean P and T are mean values of monthly actual measurement data of P and T ; σ is the standard deviation)

3.1.4 Validation at spatial scale

3.1.4.1 Spatial forcing data and time constant maps

Across any region, interactions among driving variables are complex; simulation modeling is an important tool for analyzing such interactions. The linkage of ecosystem simulation models to geographic information systems (GIS) provides technological support for analyzing spatial variability in ecosystem properties and processes. Major controlling variables over river catchment processes have inherently different patterns and scales of variation. An ArcGIS is an appropriate tool to integrate databases as multiple layers of driving variables for modeling ecosystem processes. Therefore, we used the GIS for preparing all spatial forcing data over entire watershed area, which allowed running of century ecosystem model at basin scale to study ecohydrological components.

For century ecosystem model, a continuous monthly mean, minimal and maximal air temperature and monthly mean precipitation dataset were prepared from 1993 to 2006 based on daily observations of air temperature and precipitation, from six Metostations and seven Metoposts station of IMH located within or adjacent to our study area. Datasets from 2003 to 2006 were used for simulation of outputs of century ecosystem model. All the Metostations and Metoposts data were entered into ArcGIS 9.3 registered by latitude and longitude. Data for each station included 3 variables; monthly data for maximum and minimum temperature and precipitation and then we created three climate maps of mean precipitation and maximum and minimum air temperature using Kriging interpolation method. Each output of interpolation was stored in datasets of same grid size (1 km x 1 km) to provide basis for extracting a time series of mean precipitation and mean maximum and minimum air temperature for each grid (Figs. 20 and 21).

Before spatial application, century ecosystem model was applied to other four grassland and three forest sites to obtain grazing pressure parameters of each site. In fact, century ecosystem model has two kinds of grazing pressure model i.e., linear (light effect) and quadratic effect (heavy effect) that affects on outputs of model. These two different grazing pressure models were used during this calibration procedure, because the effect of human activities was different from site to site. Especially, urban area (i.e. BGN and UDN site) has much direct influence of human activities than other rural sites (JGN, KBU and DH). However, it was difficult to determine exact human direct effect on pastureland. Therefore, grazing pressure parameters of each sites were calculated based on calibration procedure. As we know, calibration

procedure searches for parameter values in order to match the model results with observations as good as possible.

After grazing pressure parameters at each site were calculated by means of Eq. (2), century ecosystem model was running until it produce good match between simulated and measured based on grazing pressure parameters from century ecosystem model. After we found suitable grazing pressure parameters from century ecosystem model were compared against calculated grazing pressure parameters by Eq. (2) as shown in Fig. 22. Measured aboveground biomass of July, 2003 was used for this calibration. Finally, following linear equation with $r = 0.85$ was obtained between grazing pressure parameters of the model and statistical data in our study area.

$$Y = 0.95X + 0.16 \quad (4)$$

where Y : grazing pressure parameters of century ecosystem model; X (Unit is $SE_u \text{ ha}^{-1}$) : those obtained by Mongolian Statistical Office data.

Eq. (4) allowed to create spatial distribution of grazing pressure map of 2003 from Mongolian Statistical Office data over the entire watershed area as shown in Fig. 23. This created grazing pressure distribution map (Fig. 23) and vegetation map (Saandar and Sugita, 2004, Fig. 24) was used for spatial application of century ecosystem model.

Figs. 25-32 show spatial distribution of simulated aboveground biomass and evapotranspiration in entire area of upper part of Kherlen river watershed. Figs. 25 and 26 show spatial distribution of simulated aboveground biomass at grazing and nongrazing surface condition of July, 2003 whereas Figs. 27 and 28 show those obtained from August, 2003. Comparison of these figures and also Fig. 33 show that aboveground biomass was reduced by grazing pressure. Spatial distribution of simulated aboveground biomass gives very similar pattern of spatial distribution of precipitation (Figs. 20, 26 and 28). Statistical investigation also clarified the relationship between aboveground biomass and precipitation. The aboveground biomass is usually reached to peak on July in Mongolia. Therefore, it is also necessary to clarify precipitation in which month is more important for plant growth in Mongolia. We selected simulated aboveground biomass of July and precipitation data from May, June and July as shown in Table 15. A simple correlation analysis was used. From this analysis, high correlation was found between aboveground biomass and June precipitation. However, a statistical test has shown that the differences of correlation between June and May, also between June and July are not significant at both 0.01 and 0.05 levels. Thus, growing season precipitation from May to July is important for plant growing in Mongolia.

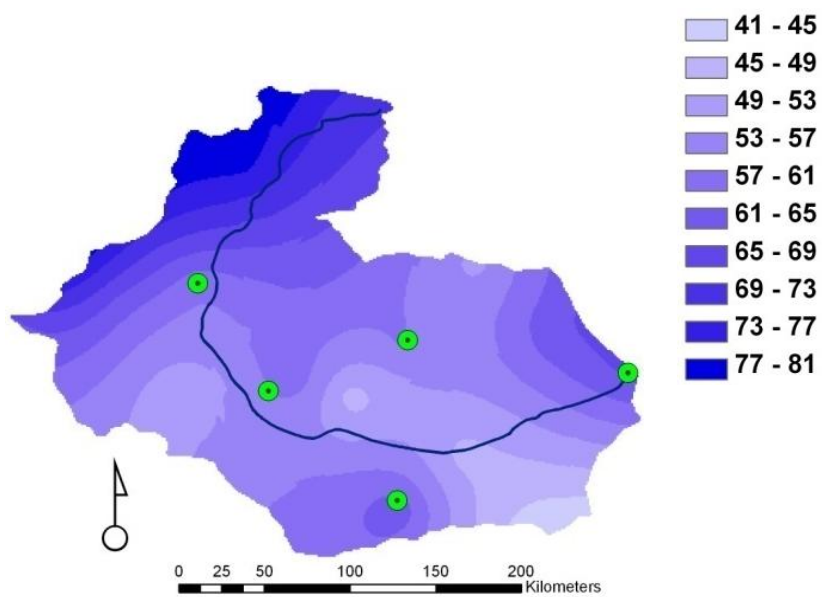


Fig. 20 Example data of spatial distribution of precipitation (mm month^{-1}) of July, 2003. Watershed boundary represented by red line.

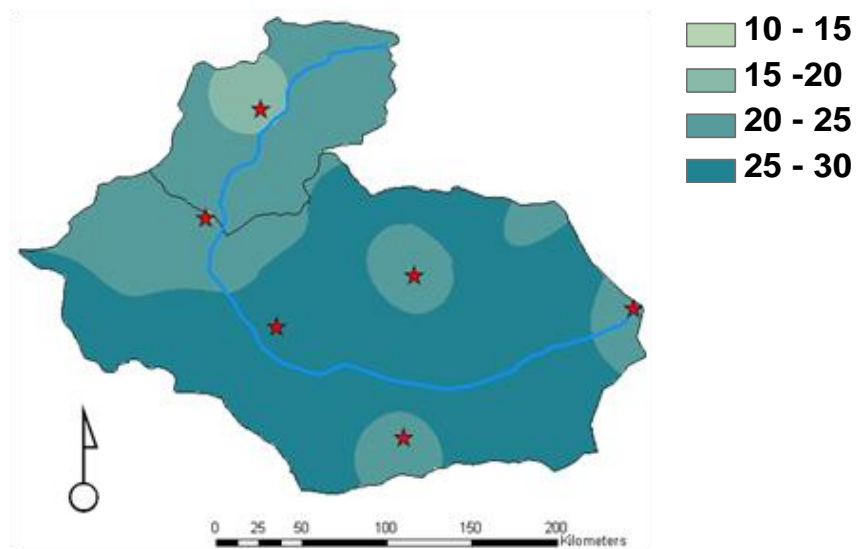


Fig. 21 Same as Fig. 20, but for air temperature ($^{\circ}\text{C}$)

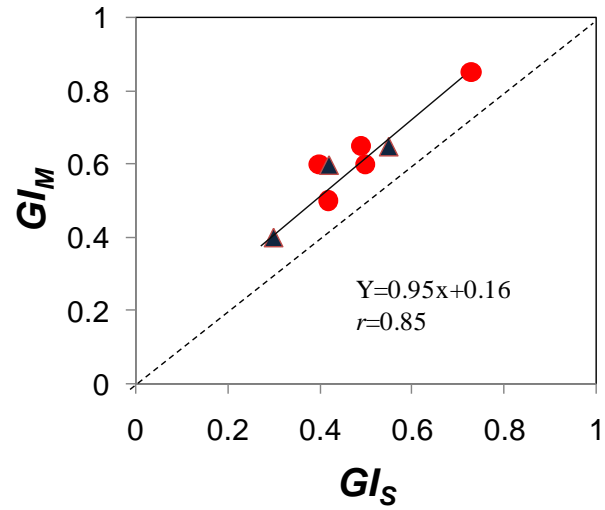


Fig. 22 Comparison of grazing parameters of century ecosystem model (GI_M) and those obtained by Mongolian statistical office data (GI_S). (Note: circles with red color represents inside the study area; triangular with black color represent outside of study area; Unit is sheep equivalent unit ha^{-1})

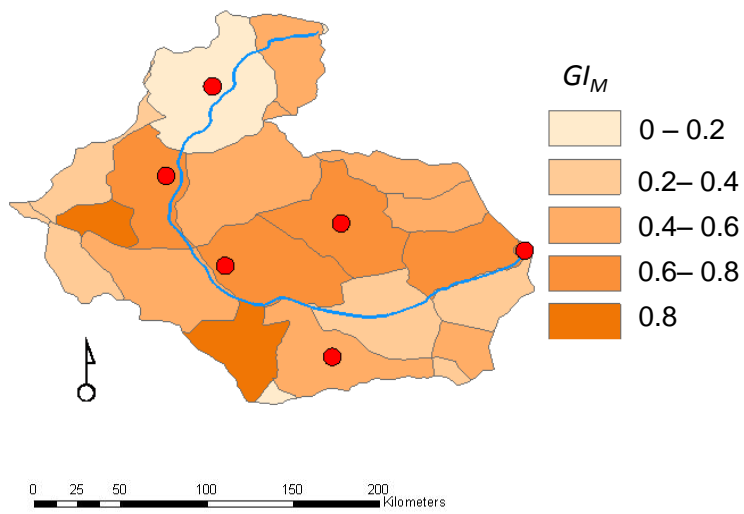


Fig. 23 Spatial distribution of grazing pressure map of 2003 in upper part of Kherlen river watershed. Contour line are indicates sum boundary and red circles are show study sites.

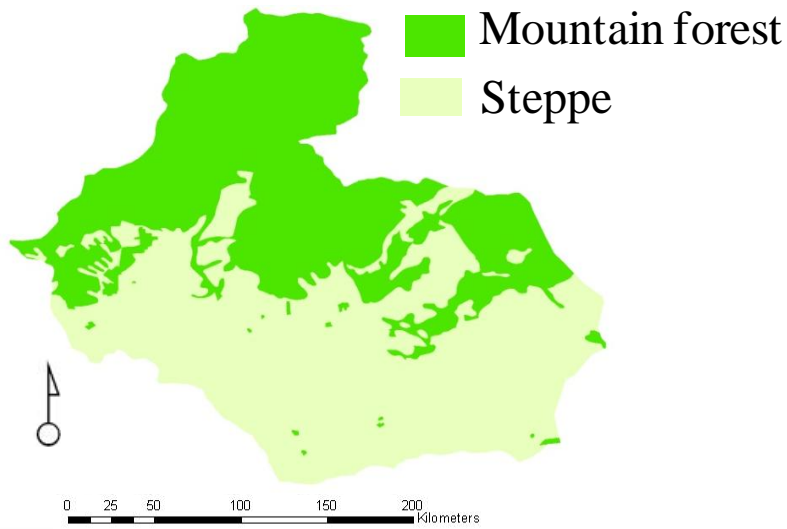


Fig. 24 Same as Fig. 23, but for vegetation map

In addition to this analysis, a multiple correlation analysis was also employed in order to determine which one among the precipitation and grazing pressure has more influence on plant growth in Mongolia.

The result indicates that there is an interrelationship between aboveground biomass, precipitation, and grazing pressure and multiple correlations coefficient was 0.65. However, aboveground biomass has positive and strong relationship with precipitation ($r = 0.68$) and indirect relationship with grazing pressure ($r = - 0.35$).

In case of spatially simulated evapotranspiration, both grazing (Figs. 29 and 31) and nongrazing (Figs. 30 and 32) sites give very close patterns. Same situation was also found in point application of century ecosystem model. This result also suggests that more realistic hydrological model needs to be applied at spatial scale in order to understand magnitude and variation pattern of changes in hydrological processes at spatial scale in our study area.

Validation of spatially explicit model outputs principally demands spatially explicit validation data. This however is practically impossible unless the simulated outputs by means of the model are extractable from continuous data set such as remote sensing data. Thus, although performing spatially explicit modeling, the model outputs still have to be validated with point values (Zhang et al., 2004). The only option for validating the spatially explicit application of the century ecosystem model in this study was by the use of the point measured data of aboveground biomass.

The spatial outputs of century ecosystem model were validated mainly by the measured aboveground biomass provided by IMH. Comparison of monthly simulated and measured aboveground biomass in Figs. 34 and 35 shows quite good performance of spatial application of century ecosystem model at both of grazing ($r= 0.82$ and $RMSE = 8.4 \text{ g C m}^{-2}$) and nongrazing surface condition ($r= 0.84$ and $RMSE = 8.1 \text{ g C m}^{-2}$).

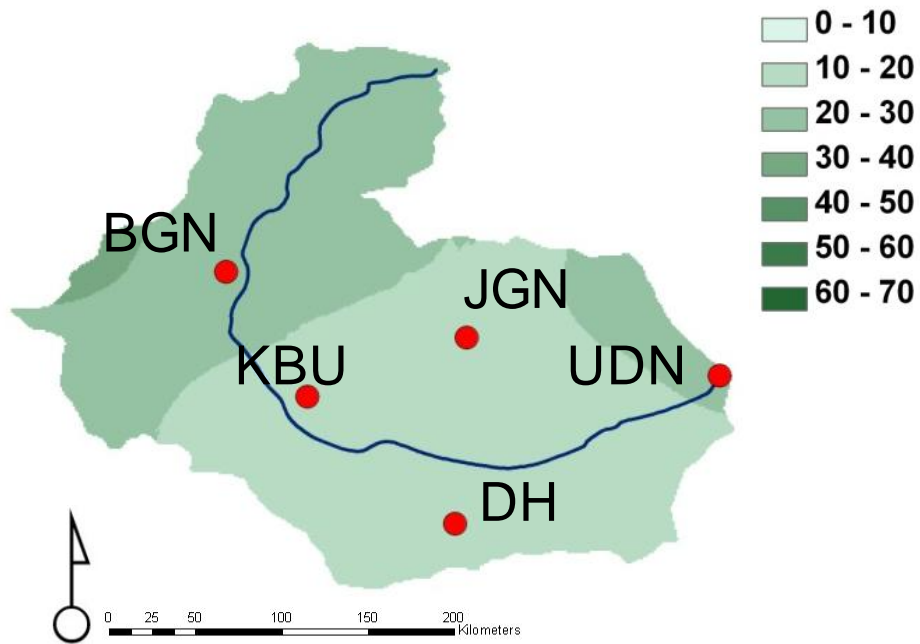


Fig. 25 Spatial distribution of simulated aboveground biomass (g C m⁻²) at grazing surface condition in Upper Kherlen river watershed. (2003/07)

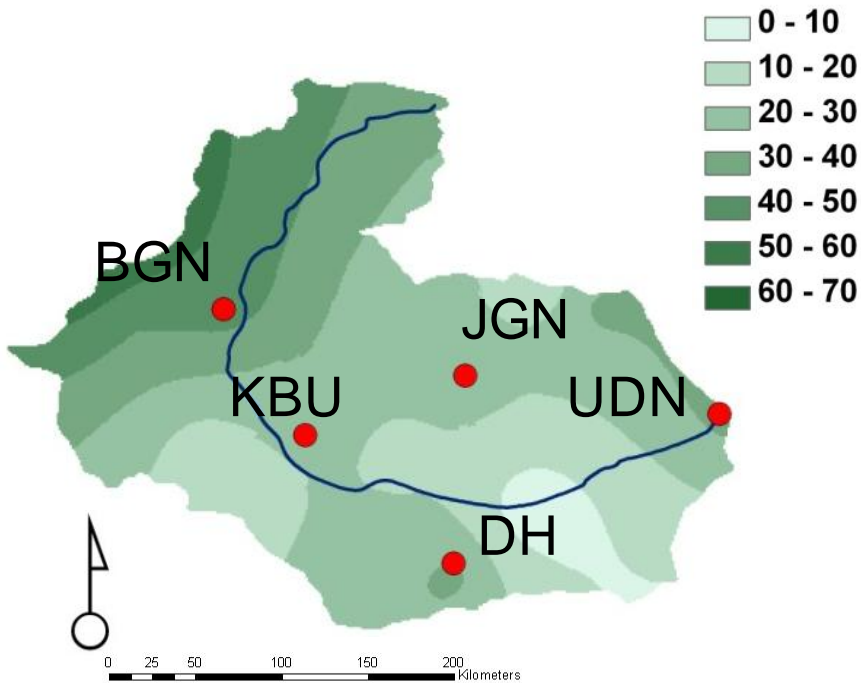


Fig. 26 Spatial distribution of simulated aboveground biomass (g C m⁻²) at nongrazing surface condition in Upper Kherlen river watershed. (2003/07)

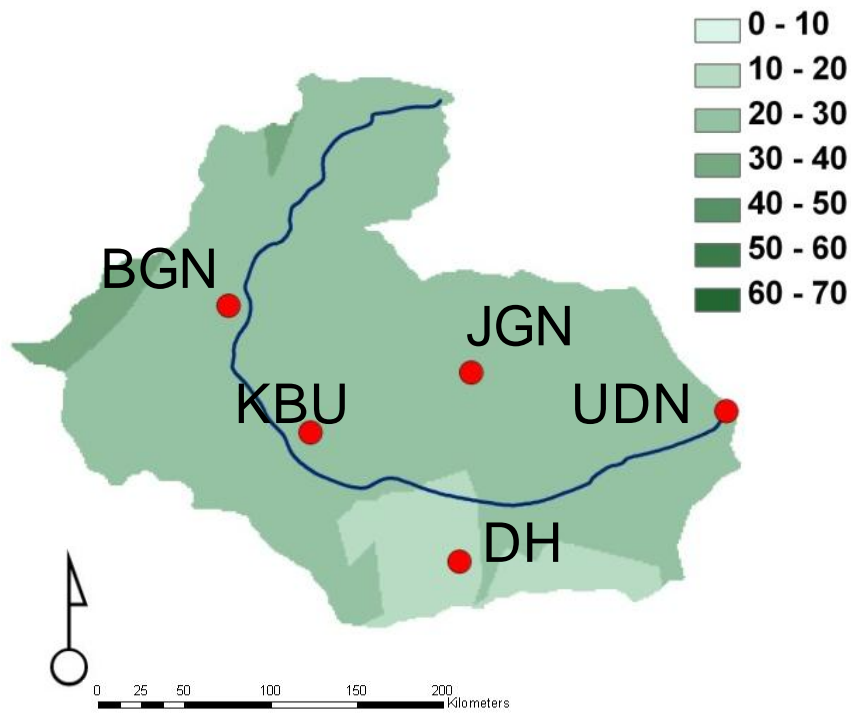


Fig. 27 Spatial distribution of simulated aboveground biomass (g C m^{-2}) at grazing surface condition in Upper Kherlen river watershed. (2003/08)

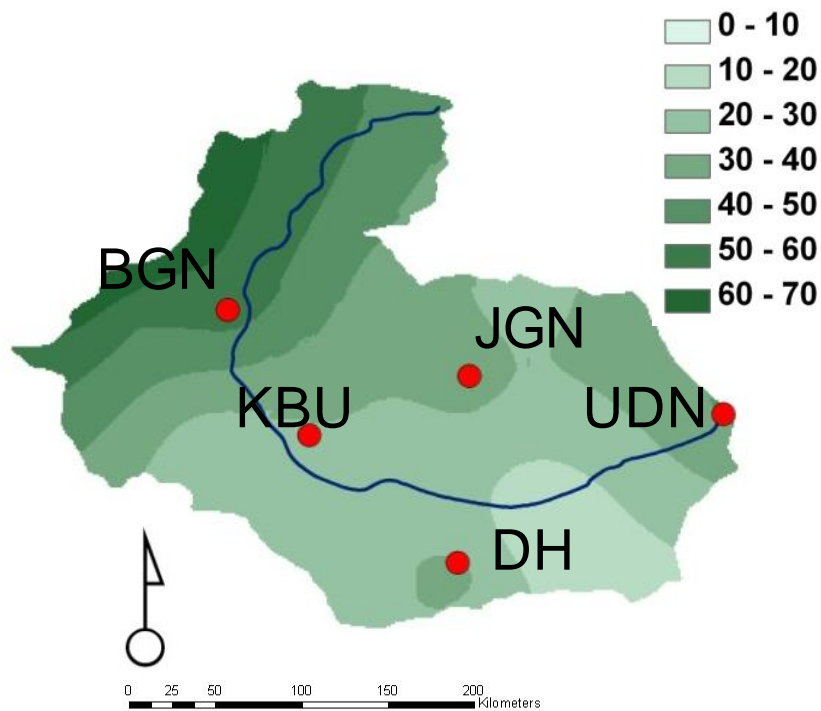


Fig. 28 Spatial distribution of simulated aboveground biomass (g C m^{-2}) at nongrazing surface condition in Upper Kherlen river watershed. (2003/08)

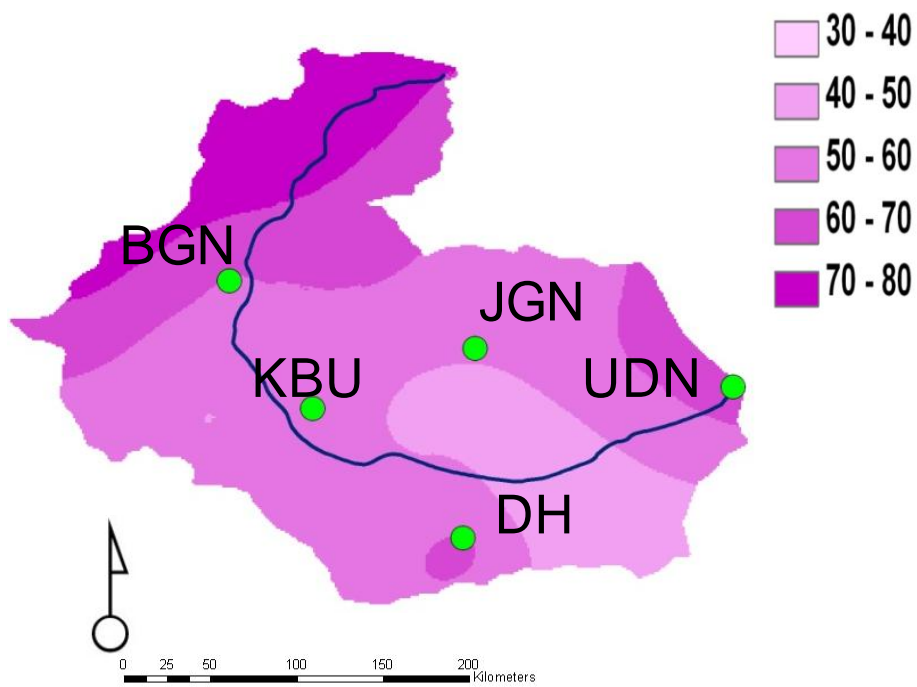


Fig. 29 Spatial distribution of simulated evapotranspiration (mm month^{-1}) at grazing surface condition in Upper Kherlen river watershed. (2003/07)

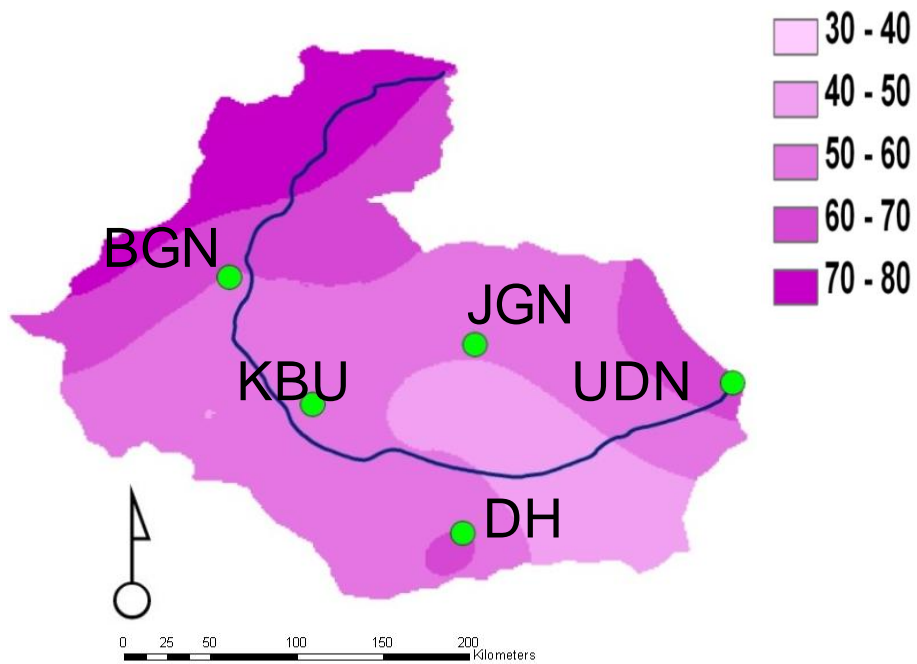


Fig. 30 Spatial distribution of simulated evapotranspiration (mm month^{-1}) at nongrazing surface condition in Upper Kherlen river watershed. (2003/07)

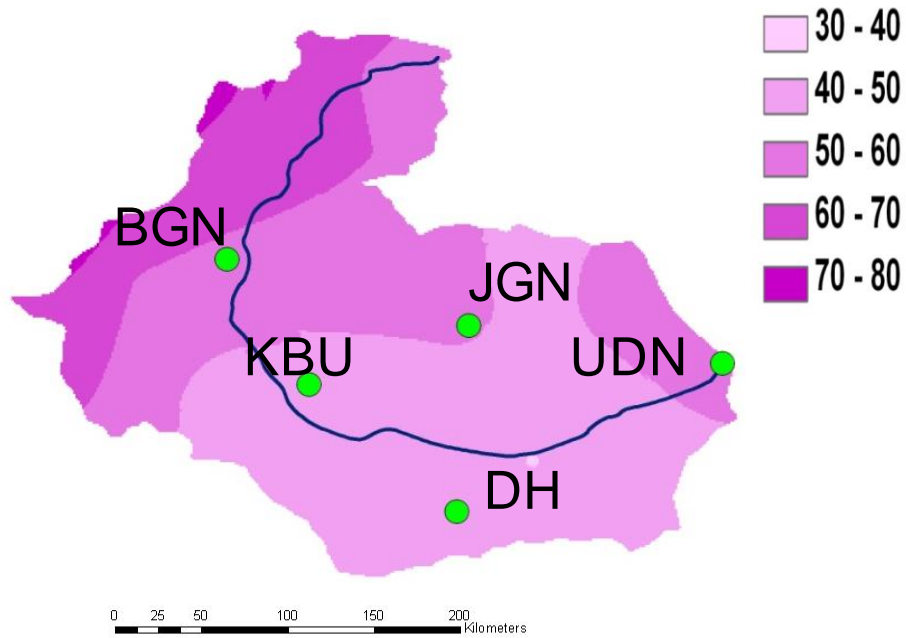


Fig. 31 Spatial distribution of simulated evapotranspiration (mm month^{-1}) at grazing surface condition in Upper Kherlen river watershed. (2003/08)

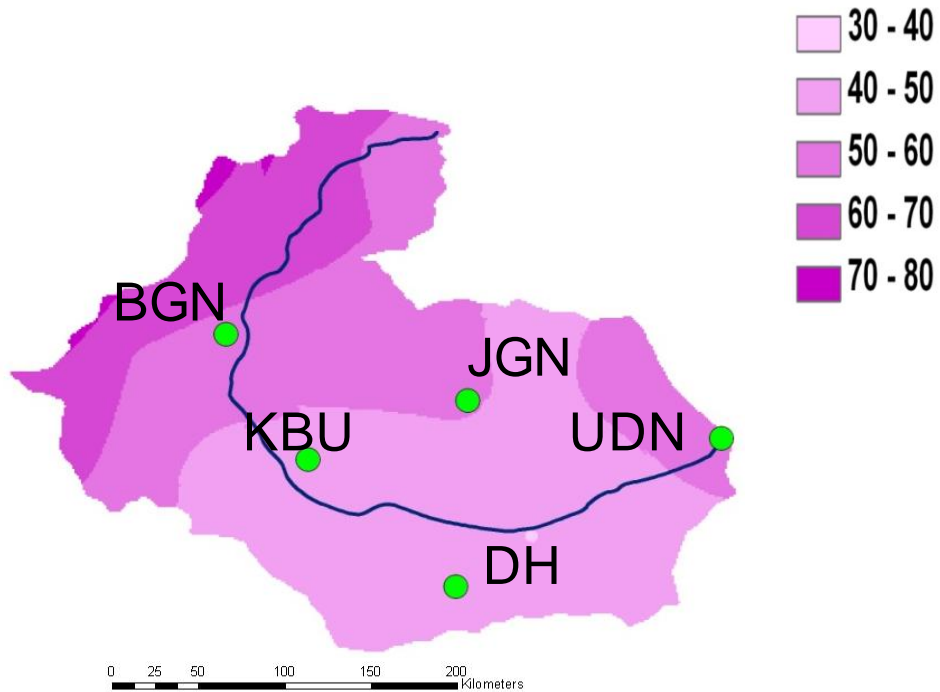


Fig. 32 Spatial distribution of simulated evapotranspiration (mm month^{-1}) at nongrazing surface condition in Upper Kherlen river watershed. (2003/08)

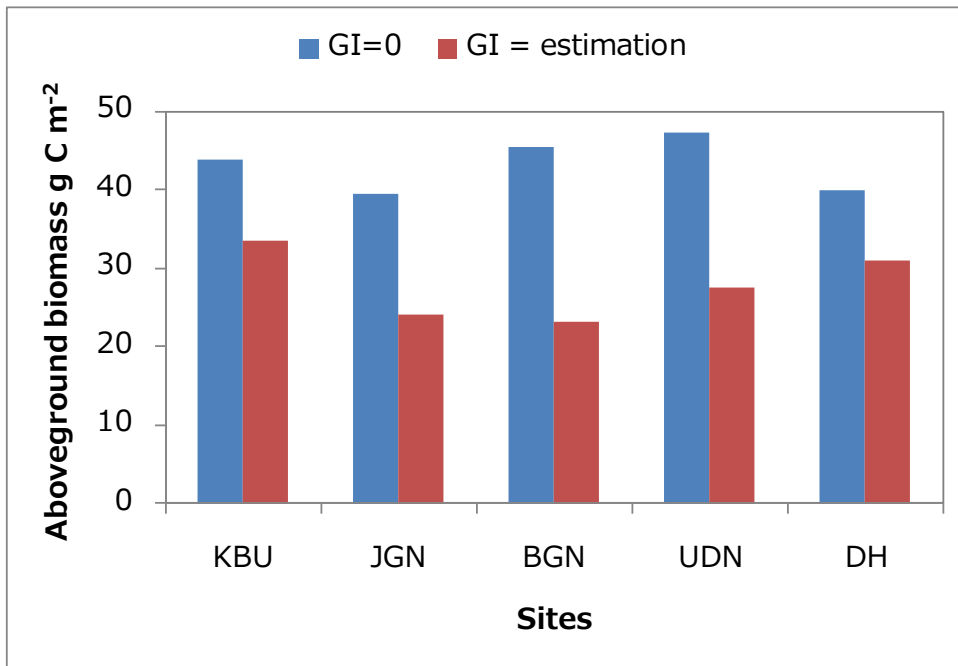


Fig. 33 Grazing pressure effect on simulated aboveground biomass

Table 15 Correlation analysis for aboveground biomass and precipitation

| Combination | Coefficients of regression equation ($y=ax+b$) | | Correlation coefficient (r) |
|--|--|------|---------------------------------|
| | a | b | |
| P_{May} and AB_{July} | 0.65 | 20.4 | 0.85 |
| P_{June} and AB_{July} | 0.51 | 7.4 | 0.87 |
| P_{July} and AB_{July} | 0.11 | 26.4 | 0.84 |
| $P_{\text{May}} + P_{\text{June}}$ and AB_{July} | 0.66 | 57.2 | 0.87 |
| $P_{\text{June}} + P_{\text{July}}$ and AB_{July} | 1.18 | 21.3 | 0.88 |

P is precipitation; AB is aboveground biomass

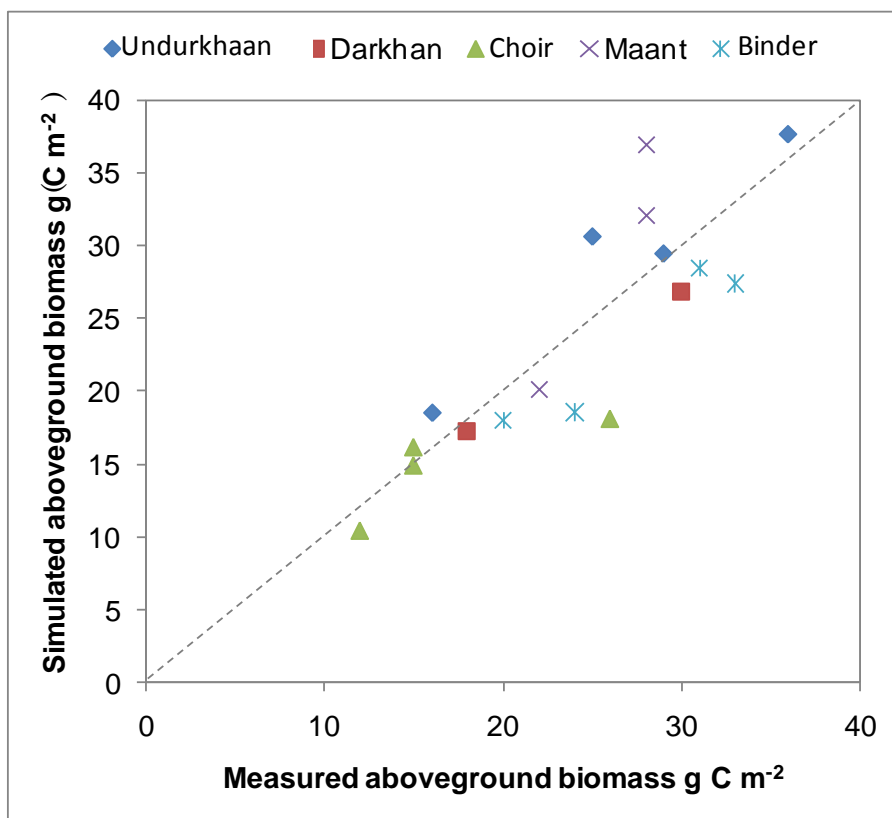


Fig. 34 Comparison of simulated and measured mean monthly aboveground biomass from June to August at grazing surface condition in spatial scale, 2003. (See Fig. 7 for location of sites and Table 3 for list of site name)

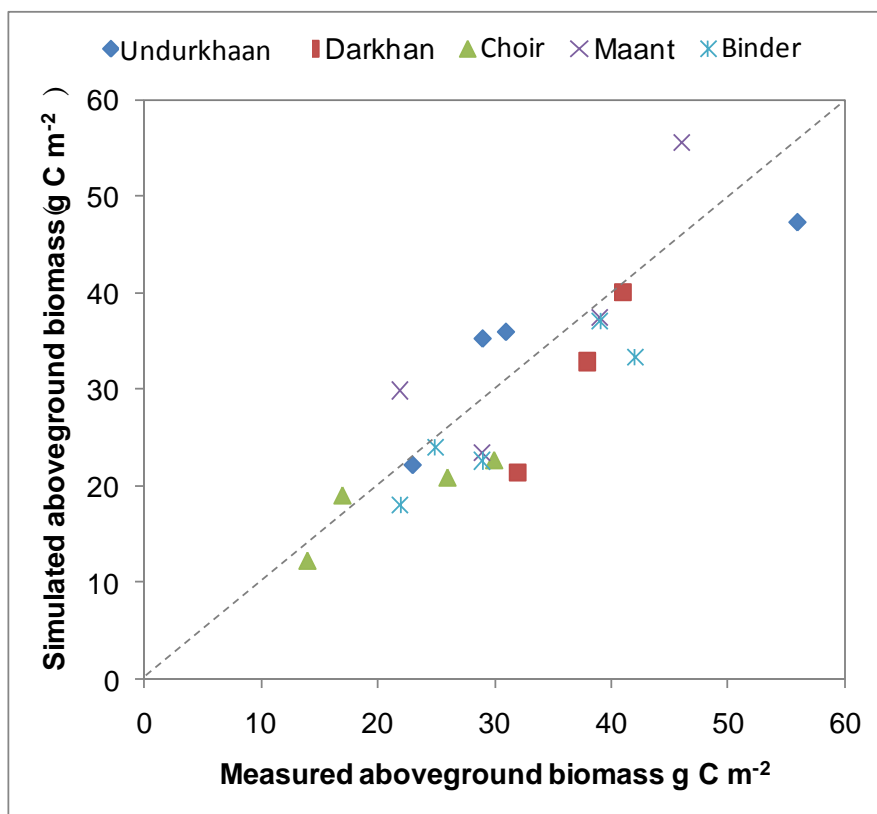


Fig. 35 Comparison of simulated and mean measured monthly aboveground biomass from June to August at nongrazing surface condition in spatial scale, 2003. (See Fig. 7 for location of sites and Table 3 for list of site name)

3.2 Application and validation of TOPLATS hydrological model

3.2.1 Model parameters

As stated in the introduction, one of our objectives in this study is to investigate the model calibration associated with the adaptation of a model developed and its validation to a new site.

3.2.1.1 Soil parameters

Several soil parameters are needed in order to specify soil hydrological and thermal properties required by TOPLATS-SVAT scheme. These parameters consist of the saturated soil moisture, residual soil moisture, pore size index and bubbling pressure. By employing the method of Brooks and Corey (1966), all of these parameters were determined from the soil-water retention curve, which was derived by using measured of volumetric water content at multiple pressure head conditions at 0-10 cm from the experimental site (Appendix C). From soil-water retention curve, the initial values of soil properties parameters were determined and used for model calibration for experimental sites (Table 8). Finally, the optimum values of soil hydrological parameters which produced smaller root mean square error (RMSE) and high correlation (r) in the soil moisture comparison were selected to give the best results for the simulation of hydrological and energy balance at KBU and FOR site. Figs. 36 and 37 show calibration of saturated hydraulic conductivity. These soil parameters are indicated in the look-up table for according to soil map (See Table 16).

In order to verify, calibrated soil properties parameters were compared with weighted average of soil properties parameters for various soil types of different region given by Raws et al. (1982) and all calibrated values were fallen within the range of prescribed soil properties parameters except for the pore size. However, our calibrated pore size index was similar to the study of Debruyckere et al. (1996), which was for sandy loam soil. The quartz content was assumed equivalent to the sand percentage of KBU site, which is similar as the study of Bashford et al. (2002), who assumed in their study.

Table 16 Soil look-up table of FOR and KBU site.

| Site | B | ψ_c (m) | θ_s (m ³ m ⁻³) | θ_r (m ³ m ⁻³) | K_s (m s ⁻¹) | DSL (m) | DST (K) | MSL (m) | MST (K) | C_s (J K ⁻¹ kg ⁻¹) | Q |
|------|------|-----------------|---|---|-------------------------------|--------------|--------------|--------------|--------------|--|------|
| FOR | 0.51 | 0.30 | 0.35 | 0.02 | 6.05×10^{-6} | 0.85 | 268.97 | 0.5 | 270.15 | 2.26×10^{-6} | 0.54 |
| KBU | 0.65 | 0.35 | 0.38 | 0.01 | 7.05×10^{-6} | 0.85 | 270.35 | 0.5 | 273.54 | 1.34×10^{-6} | 0.60 |

DSL: soil layer-2, DST: soil temperature for DSL, MSL: soil layer-1, MST: soil temperature for MSL, other parameters definition are cited in Table B-2-2 in Appendix B.

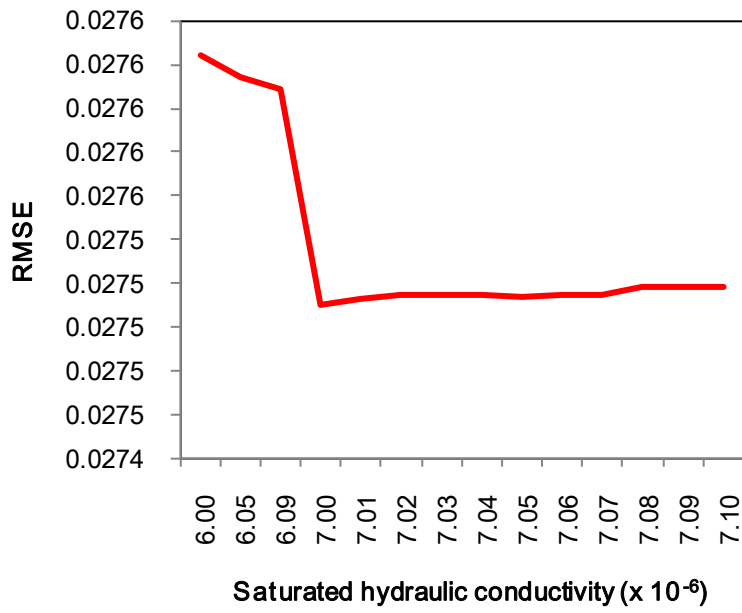


Fig. 36 Changes of the RMSE (root mean square error) Unit is $m s^{-1}$.

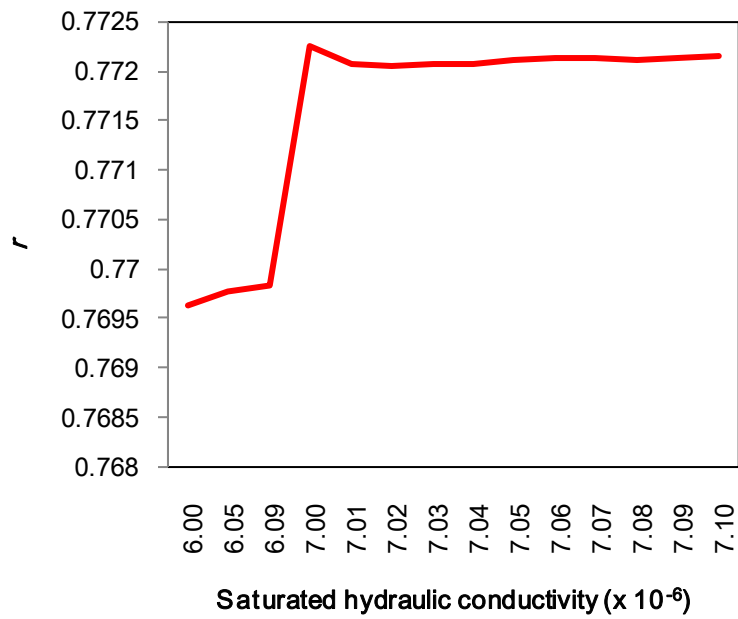


Fig. 37 Changes of the r (correlation coefficient). Unit is $m s^{-1}$.

3.2.1.2 Surface and plant parameters

Leaf-area index (LAI), roughness length and land aerodynamic characteristics, including roughness length for $z_{o,m}$ and for $z_{o,h}$ as well as zero-plane displacement height (d), are often set proportional to the canopy height (h_c). In this study, however, those parameters were prescribed as a function of leaf area index (LAI) and h_c based on intensive field survey at KBU site in 2003 summer (Table 8). The value of d is 0.66 of h_c (Li et al., 2005a) and instead of prescribing $z_{o,m}$ and $z_{o,h}$ for each land cover, non-linear equations (Eqs. (5)- (6)) by Kotani (2007) were used to compute those parameters using measured LAI, as given in Table 18 for nongrazing and grazing site, respectively.

$$z_{o,m} = 10^{(0.17 \ln(LAI) - 2.13)} \quad (5)$$

$$z_{o,h} = 10^{(-0.35 \ln(LAI) - 7.78)} \quad (6)$$

According to vegetation phenological data from the IMH meteorological station in KBU site, the vegetation growth started on around 23 April (DOY of 113) and stopped around on 21 October (DOY of 294) and LAI increased rapidly from end of April to late of July. The LAI reached to peak in July with a value of 0.66 in nongrazing site, whereas the maximum LAI was observed on August 24th with a value of 0.57 in grazing site. The value of d ranged between 0.024 and 0.091 for nongrazing site and from 0.016 and 0.069 for grazing site. The value of $z_{o,m}$ varied between 0.0038 and 0.0068 for nongrazing site and from 0.0032 and 0.0058 for grazing site, whereas $z_{o,h}$ varies between 2.31×10^{-8} and 6.31×10^{-8} for nongrazing site and from 2.85×10^{-8} and 8.55×10^{-8} for grazing site (See Table 18). In non-growing season, we assumed that LAI equal to 0.01 and then value of $z_{o,m}$ and $z_{o,h}$ were computed by means of Eqs. (5)- (6) (See Table 17). Calculated values of $z_{o,m}$ and $z_{o,h}$ agree with theoretical estimates for bluff-rough surface (e.g., Fig. 4.24 of Brutsaert (1982)). These vegetation parameters were inserted in the look-up table for according to vegetation map (See Table 18).

3.2.1.3 Vegetation root and soil layers

In the present application, vegetation root distribution in TOPLATS hydrological model was divided into three zones (Asano et al., 2007), whereas soil layers were subdivided into four layers, including root zone from (0-10 cm), surface zone-1(10-50 cm), surface zone-2 (50-100 cm) and transmission zone (100-300 cm).

Table 17 LAI, roughness length and zero-plane displacement at two different surface conditions in KBU site.

| Month | LAI ($\text{m}^2 \text{m}^{-2}$) | $z_{o,m}$ (m) | $z_{o,h}$ (m) | d_0 (m) | LAI ($\text{m}^2 \text{m}^{-2}$) | $z_{o,m}$ (m) | $z_{o,h}$ (m) | d_0 (m) |
|-----------|------------------------------------|---------------|-----------------------|-----------|------------------------------------|---------------|-----------------------|-----------|
| | Non-grazing condition | | | | Grazing condition | | | |
| April | 0.1 | 0.0029 | 1.1×10^{-7} | 0.001 | 0.1 | 0.0029 | 1.1×10^{-7} | 0.001 |
| May | 0.12 | 0.0024 | 6.14×10^{-8} | 0.001 | 0.12 | 0.0024 | 6.14×10^{-8} | 0.001 |
| June | 0.22 | 0.0039 | 5.74×10^{-8} | 0.042 | 0.25 | 0.0041 | 5.11×10^{-8} | 0.039 |
| July | 0.66 | 0.0061 | 2.31×10^{-8} | 0.084 | 0.50 | 0.0055 | 2.87×10^{-8} | 0.066 |
| August | 0.63 | 0.0052 | 3.29×10^{-8} | 0.091 | 0.57 | 0.0058 | 2.58×10^{-8} | 0.069 |
| September | 0.29 | 0.0045 | 4.46×10^{-8} | 0.049 | 0.19 | 0.0037 | 6.31×10^{-8} | 0.034 |

Table 18 Vegetation look-up table of FOR and KBU site.

| Month | LAI | α_d | α_w | ε | Heigth1 | Heigth2 | $z_{0,m}$ | $z_{0,h}$ | d_0 | r_{stmin} | r_{stmax} | R_{pl} | β | B | T_r |
|-----------|------|------------|------------|---------------|---------|---------|----------------------|----------------------|-------|-------------|-------------|----------|---------|--------|-------|
| FOR site | | | | | | | | | | | | | | | |
| April | 0.11 | 0.047 | 0.039 | 0.98 | 30 | 30 | 3×10^{-3} | 9.9×10^{-8} | 13.3 | 10 | 5000 | 30 | 0.06 | 0.0016 | 298 |
| May | 0.21 | 0.047 | 0.039 | 0.98 | 30 | 30 | 3.9×10^{-3} | 5.9×10^{-8} | 13.3 | 10 | 5000 | 30 | 0.06 | 0.0016 | 298 |
| Jun | 0.48 | 0.0502 | 0.0562 | 0.98 | 30 | 30 | 5.4×10^{-3} | 3.1×10^{-8} | 13.33 | 40 | 5000 | 30 | 0.06 | 0.0016 | 298 |
| July | 1.54 | 0.0576 | 0.0489 | 0.98 | 30 | 30 | 8.8×10^{-3} | 1.1×10^{-8} | 13.33 | 50 | 5000 | 30 | 0.06 | 0.0016 | 298 |
| August | 2.24 | 0.0554 | 0.0277 | 0.98 | 30 | 30 | 1.0×10^{-2} | 8.4×10^{-9} | 13.33 | 70 | 5000 | 30 | 0.06 | 0.0016 | 298 |
| September | 1.97 | 0.0603 | 0.0319 | 0.98 | 30 | 30 | 9.7×10^{-3} | 9.4×10^{-9} | 13.33 | 65 | 5000 | 30 | 0.06 | 0.0016 | 298 |
| October | 0.95 | 0.0414 | 0.032 | 0.98 | 30 | 30 | 7.2×10^{-3} | 1.7×10^{-8} | 13.33 | 55 | 5000 | 30 | 0.06 | 0.0016 | 298 |
| November | 0.49 | 0.0474 | 0.0452 | 0.98 | 30 | 30 | 5.5×10^{-3} | 2.9×10^{-8} | 13.33 | 15 | 5000 | 30 | 0.06 | 0.0016 | 298 |
| December | 0.10 | 0.0562 | 0.051 | 0.98 | 30 | 30 | 2.9×10^{-3} | 1.1×10^{-7} | 13.33 | 35 | 5000 | 30 | 0.06 | 0.0016 | 298 |
| KBU site | | | | | | | | | | | | | | | |
| April | 0.10 | 0.196 | 0.168 | 0.96 | 2.35 | 3.5 | 2.9×10^{-3} | 1.1×10^{-7} | 0.001 | 50 | 5000 | 30 | 0.06 | 0.0016 | 298 |
| May | 0.12 | 0.248 | 0.225 | 0.96 | 2.35 | 3.5 | 3.1×10^{-3} | 9.3×10^{-8} | 0.001 | 50 | 5000 | 30 | 0.06 | 0.0016 | 298 |
| Jun | 0.25 | 0.248 | 0.225 | 0.96 | 2.35 | 3.5 | 4.2×10^{-3} | 5.1×10^{-8} | 0.037 | 70 | 5000 | 30 | 0.06 | 0.0016 | 298 |
| July | 0.50 | 0.203 | 0.2081 | 0.98 | 2.35 | 3.5 | 5.5×10^{-3} | 2.9×10^{-8} | 0.067 | 50 | 5000 | 30 | 0.06 | 0.0016 | 298 |
| Aug | 0.57 | 0.219 | 0.195 | 0.98 | 2.35 | 3.5 | 5.9×10^{-3} | 2.6×10^{-8} | 0.069 | 45 | 5000 | 30 | 0.06 | 0.0016 | 298 |
| September | 0.19 | 0.2011 | 0.201 | 0.96 | 2.35 | 3.5 | 3.7×10^{-3} | 6.4×10^{-8} | 0.034 | 30 | 5000 | 30 | 0.06 | 0.0016 | 298 |
| October | 0.35 | 0.2011 | 0.201 | 0.96 | 2.35 | 3.5 | 4.8×10^{-3} | 3.9×10^{-8} | 0.025 | 20 | 5000 | 30 | 0.06 | 0.0016 | 298 |
| November | 0.01 | 0.6011 | 0.601 | 0.96 | 2.35 | 3.5 | 1.1×10^{-3} | 7.2×10^{-7} | 0.001 | 20 | 5000 | 30 | 0.06 | 0.0016 | 298 |
| December | 0.01 | 0.6011 | 0.601 | 0.96 | 2.35 | 3.5 | 1.1×10^{-3} | 7.2×10^{-7} | 0.001 | 20 | 5000 | 30 | 0.06 | 0.0016 | 298 |

Heigth1 is meteorological data height (m); Heigth2 is wind data height (m) (Note that refers to Table B-2-2 in Appendix B for definition for each parameter.)

3.2.2 Application at point scale

3.2.2.1 Daily and seasonal patterns of energy partitions

We assessed how grazing pressure and precipitation affects energy fluxes partitions. For this purpose, the measurements of energy fluxes of net radiation (R_n), sensible heat flux (H), latent heat flux (LE), ground heat flux (G), the ratios of H/R_n , LE/R_n , G/R_n , Bowen ratio (H/LE), precipitation (PPT), evapotranspiration (ET) as well as the ratio of ET/PPT were used to account for the difference in energy fluxes partition between two distinctive site conditions. Fig. 38 show diurnal change of R_n and its components H , LE and G of grazing and nongrazing site from April to December of 2003. At both of the sites, PPT increased from May to September of 2003, whereas LAI was increased from May and reached to peak in August, 2003 with the value of 0.57 at grazing site and in July with the value of 0.66 for nongrazing site.

As shown in Tables 19 and 20, PPT influenced monthly pattern of energy fluxes and their ratios. However, PPT did not influence the flux of R_n compared to G flux, but affected fluxes of H and LE . Energy partition were (i.e the ratios of H/R_n , LE/R_n , G/R_n) changes due to canopy development. The ratio of H/R_n and G/R_n decreased in increase of LAI, whereas the ratio of LE/R_n increased in an increase of LAI.

The ratio of H/R_n showed always larger values for grazing site than nongrazing site. It was mainly caused by smaller measured values for G of grazing site when similar values were measured for R_n and LE at both of grazing and nongrazing site. This was caused by various factors. For example, there are differences of $z_{o,m}$, $z_{o,h}$ and also of wind speed. Wind speed of grazing site was always larger than that of nongrazing site for every month (Table 21).

In both of sites, LE/R_n ratio increased or decreased when PPT was increased or decreased. This change in monthly ratio of LE/R_n is also due to changes in monthly LAI. However, increase or decrease of LE/R_n did not change much in energy partitioning of H and G . This is also reflected in the ratio of H/LE at both of sites. The comparison of available energy (R_n-G) and LE from grazing and nongrazing site is shown in Fig. 38. The regression lines between LE and R_n-G were obtained with high values of R^2 as 0.73 for grazing and 0.87 for nongrazing site, respectively. These results confirmed the strong dependency of evapotranspiration on the amount of available energy at both of sites.

Table 19 Monthly mean of energy fluxes and derived ratios of H/R_n , LE/R_n , G/R_n , H/LE (i.e. Bowen ratio), PPT , ET and ratio of ET/PPT (grazing condition, 2003)

| Month | R_n ($W\ m^{-2}$) | H ($W\ m^{-2}$) | LE ($W\ m^{-2}$) | G ($W\ m^{-2}$) | H/R_n | LE/R_n | G/R_n | H/LE | PPT ($mm\ month^{-1}$) | ET ($mm\ month^{-1}$) | ET/PPT |
|-----------|-----------------------|---------------------|----------------------|---------------------|---------|----------|---------|--------|----------------------------|---------------------------|----------|
| April | 77.45 | 57.57 | 16.07 | 7.22 | 0.74 | 0.21 | 0.09 | 3.58 | 0.00 | 6.92 | 0.00 |
| May | 83.87 | 59.49 | 24.48 | -0.10 | 0.70 | 0.29 | -0.001 | 2.42 | 28.41 | 13.11 | 0.46 |
| June | 88.80 | 57.29 | 33.60 | -2.08 | 0.64 | 0.37 | -0.023 | 1.70 | 44.01 | 17.44 | 0.39 |
| July | 95.51 | 38.52 | 52.72 | 4.27 | 0.40 | 0.55 | 0.044 | 0.73 | 54.41 | 28.27 | 0.52 |
| August | 85.12 | 51.23 | 33.24 | 0.65 | 0.60 | 0.39 | 0.007 | 1.54 | 40.63 | 17.83 | 0.42 |
| September | 56.41 | 32.94 | 30.76 | -7.29 | 0.58 | 0.54 | -0.129 | 1.07 | 65.76 | 15.35 | 0.22 |
| October | 19.79 | 21.87 | 4.76 | -5.17 | 1.11 | 0.24 | -0.26 | 4.59 | 0.00 | 5.41 | 0.00 |

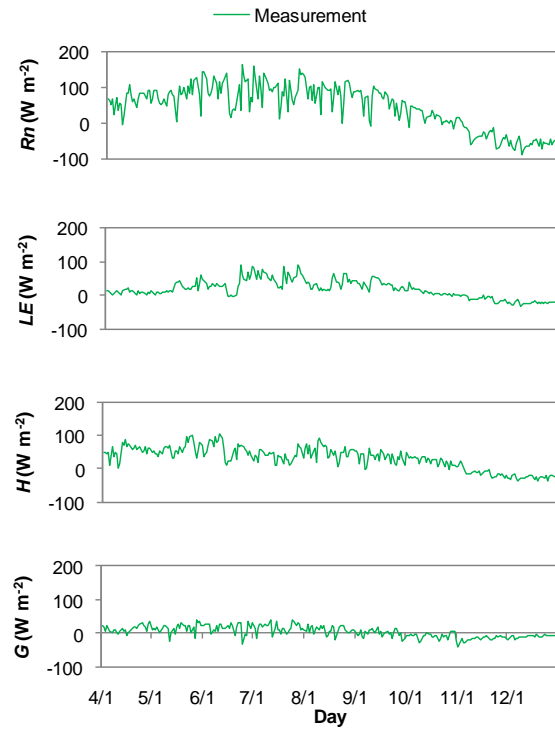
Table 20 Monthly mean of energy fluxes and derived ratios of H/R_n , LE/R_n , G/R_n , H/LE (i.e. Bowen ratio), PPT , ET and ratio of ET/PPT (nongrazing condition, 2003)

| Month | R_n ($W\ m^{-2}$) | H ($W\ m^{-2}$) | LE ($W\ m^{-2}$) | G ($W\ m^{-2}$) | H/R_n | LE/R_n | G/R_n | H/LE | PPT ($mm\ month^{-1}$) | ET ($mm\ month^{-1}$) | ET/PPT |
|-----------|-----------------------|---------------------|----------------------|---------------------|---------|----------|---------|--------|----------------------------|---------------------------|----------|
| April | 65.92 | 54.37 | 9.66 | 12.80 | 0.82 | 0.15 | 0.19 | 5.63 | 0.00 | 4.92 | 0.00 |
| May | 84.71 | 55.80 | 24.28 | 4.62 | 0.65 | 0.28 | 0.05 | 2.29 | 28.41 | 13.12 | 0.45 |
| June | 85.95 | 50.97 | 29.02 | 6.12 | 0.59 | 0.33 | 0.07 | 1.75 | 44.01 | 15.07 | 0.34 |
| July | 93.43 | 34.17 | 55.09 | 4.16 | 0.36 | 0.58 | 0.04 | 0.62 | 54.41 | 29.55 | 0.54 |
| August | 86.35 | 52.84 | 32.73 | 0.75 | 0.61 | 0.37 | 0.008 | 1.61 | 40.63 | 17.55 | 0.43 |
| September | 57.68 | 32.50 | 29.11 | -3.93 | 0.56 | 0.50 | -0.068 | 1.11 | 65.76 | 14.52 | 0.20 |
| October | 17.46 | 22.64 | 7.48 | -8.04 | 1.30 | 0.43 | -0.46 | 3.03 | 0.00 | 6.43 | 0.00 |

Table 21 Monthly mean wind speed at grazing and nongrazing condition, 2003

| Surface | April | May | Jun | July | August | September | October | November | December |
|------------|-------|-----|-----|------|--------|-----------|---------|----------|----------|
| Grazing | 7.5 | 4.8 | 3.7 | 3.5 | 3.9 | 2.7 | 3.3 | 2.6 | 2.3 |
| Nongrazing | 7.3 | 4.1 | 3.6 | 2.5 | 3.4 | 2.4 | 3.0 | 2.3 | 2.1 |

a)



b)

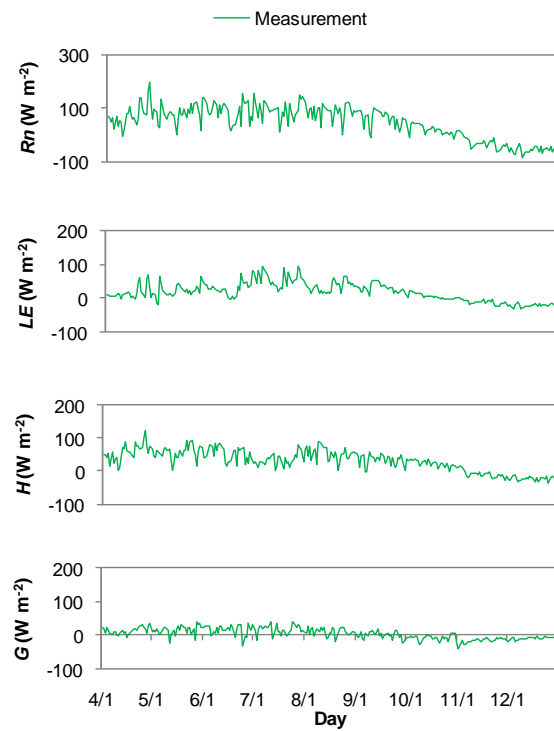


Fig. 38 Diurnal change of measured energy fluxes at grazing (panel a) and nongrazing (panel b) condition in KBU site from April to December of 2003.

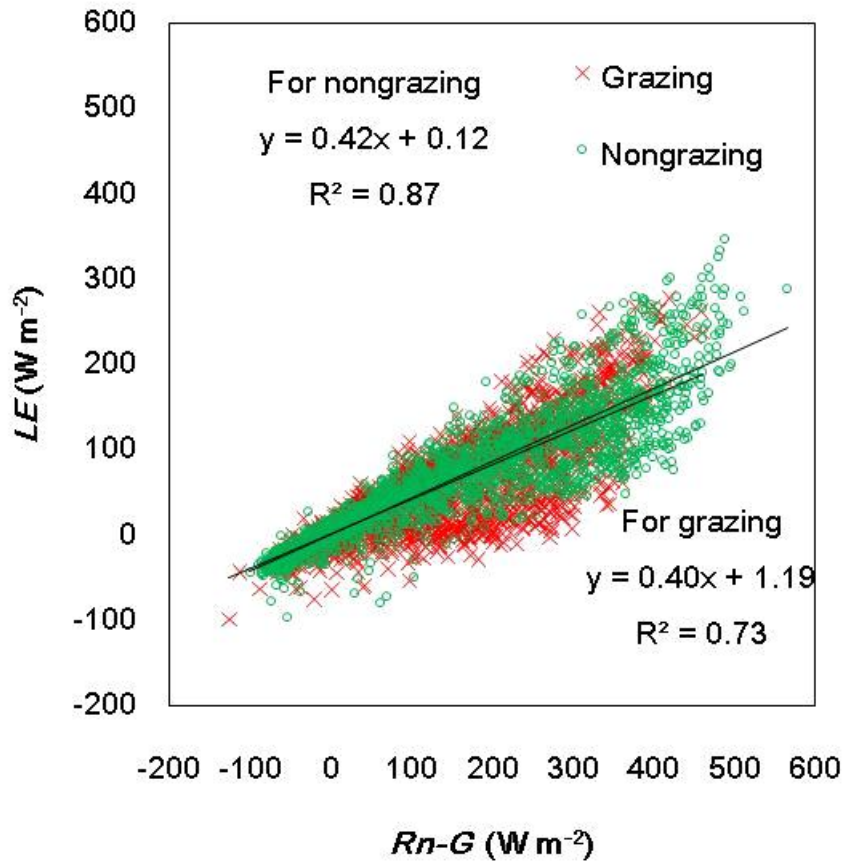


Fig. 39 Available energy (R_n-G) and LE for grazing and nongrazing condition in KBU site. (May to September, 2003)

3.2.2.2 Validation of TOPLATS at point scale (without coupling)

To validate the TOPLATS hydrological model applicability at point scale in our study, extensive comparisons have been performed for hydrological and energy fluxes using flux measurement data from grassland and forest site. Summary for time series of simulated energy and hydrological fluxes versus measured fluxes from KBU site are shown in Figs. 40-42 for grazing and Figs. 43-45 for nongrazing surface condition.

A quite good agreement was found between the measured and simulated energy fluxes at grazing and nongrazing surface condition as shown in Figs. 40 and 43. The simulated energy fluxes captures seasonal variation and magnitude of measured energy fluxes at both surface condition for the validation period from April to December of 2003. RMSE of net radiation was 11.74 W m^{-2} . The regression coefficients of linear equation $\hat{y} = ax + b$ were $a=0.99$ and $b=16.79$, with $r=0.98$ for grazing surface condition. For nongrazing surface condition, RMSE was 11.37 W m^{-2} , regression coefficients of linear equation $\hat{y} = ax + b$ were $a=1.11$ and $b=14.12$, and $r=0.95$ (See Table 22). This good agreement for the net radiation resulted from reasonable prescribed of albedo (See Table 19), reflected solar radiation and upwelling long-wave radiations in the model calculations.

The simulation of the latent heat flux showed a good agreement with the observations in both the magnitudes and temporal patterns at grazing and nongrazing surface condition. RMSE of latent heat flux was 16.52 W m^{-2} . The regression coefficients of linear equation $\hat{y} = ax + b$ were $a=0.56$ and $b=14.57$, with an $r=0.72$ for grazing surface condition, whereas those were obtained RMSE was 18.71 W m^{-2} , regression coefficients of linear equation $\hat{y} = ax + b$ were $a=0.62$ and $b=16.34$, and $r=0.71$ for nongrazing surface condition (See Table 22). However, the simulated latent heat fluxes were overestimated; they were higher than the observed latent heat fluxes during the rainfall events. These patterns were not due to infiltration of moisture to soils but due to immediate evapotranspiration into the atmosphere.

The simulated sensible heat flux had a similar temporal pattern of the observed sensible heat flux, and the error statistics for the TOPLATS hydrological model can be summarized as RMSE of 14.58 W m^{-2} , regression coefficients of linear equation $\hat{y} = ax + b$ were $a=0.62$ and $b=3.65$, and $r=0.83$ for grazing surface condition, whereas RMSE of 12.12 W m^{-2} , regression coefficients of linear equation $\hat{y} = ax + b$ were $a=0.85$ and $b=-4.99$, and $r=0.89$ for nongrazing surface condition (See Table 22).

For ground heat flux comparisons, corrected ground heat flux was used by Kato (2007), who observed ground heat flux with 10 heat flux plates at grazing and nongrazing surface condition in KBU site. However, there were differences between the simulated and the observed

ground heat flux at both of grazing and nongrazing surface condition. In the TOPLATS hydrological model, the ground heat flux was computed as a function of soil temperature and soil thermal conductivity. Since TOPLATS hydrological model gives quite good simulation for soil temperature, this difference during the comparison of measured and simulated ground heat flux is thought to come from mainly measurement error during the observation. In general, annual measured ground heat flux should be zero (Kato, 2007), but he found that even after correction of measured ground heat flux was not equal to zero. This means that corrected ground heat flux at grazing and nongrazing surface condition were still not quite satisfactory. However, simulated ground heat fluxes at grazing and nongrazing surface condition captures seasonal variation and magnitude of measured ground heat fluxes for the validation period from Apr to Dec of 2003. RMSE of ground heat flux was 13.74 W m^{-2} . The regression coefficients of linear equation $\hat{y} = ax + b$ were $a=1.56$ and $b=9.56$, with $r=0.73$ for grazing surface condition. For nongrazing surface condition, RMSE was 16.72 W m^{-2} , regression coefficients of linear equation $\hat{y} = ax + b$ were $a=0.84$ and $b=10.68$, and $r=0.65$ (See Table 22). During winter period, comparison of ground heat flux was not good due to worth comparison of soil moisture (see below). This is not surprising as the TDR sensors are incapable of detecting accurate soil moisture when it is frozen (Watanabe and Wake, 2009).

For hydrological fluxes, observed soil moisture at a depth of 10 and 30 cm was compared with simulated moisture at depth of 10 cm and for 10-50 cm respectively at different surface condition of grazing and nongrazing site (Figs. 41 and 44). In all cases, calibrated soil parameters were used with measured LAI data for grazing and non-grazing site in KBU site for 2003. From result it can be found that simulated values gave better correspondence with observed ones at the depth of 10 cm in comparison to at those 30 cm depth for both grazing and non-grazing condition. RMSE of soil moisture comparison was $0.029 \text{ cm}^3 \text{ cm}^{-3}$. The regression coefficients of linear equation $\hat{y} = ax + b$ were $a=0.55$ and $b=0.02$, with r value of 0.69 for grazing surface condition. For nongrazing surface condition, RMSE was $0.017 \text{ cm}^3 \text{ cm}^{-3}$, regression coefficients of linear equation $\hat{y} = ax + b$ were $a=0.61$ and $b=0.03$, and $r=0.82$ (See Table 22).

For hydrological fluxes, another property i.e. evapotranspiration was compared between observed and simulated one at grazing and nongrazing surface condition (Figs. 41 and 44). These comparisons gave good agreement of simulated and measured in both of grazing and nongrazing surface condition. The error statistics for the TOPLATS hydrological model can be summarized as RMSE of $0.011 \text{ mm hour}^{-1}$, regression coefficients of linear equation $\hat{y} = ax + b$ were $a=0.56$ and $b=0.01$, and $r=0.72$ for grazing surface condition, whereas RMSE of 0.013 mm

hour⁻¹, regression coefficients of linear equation $\hat{y} = ax + b$ were $a=0.62$ and $b=0.01$, and $r=0.71$ for nongrazing surface condition (See Table 21). Figs. 42 and 45 show simulated evaporation and transpiration at grazing and nongrazing surface condition. The most of evapotranspiration was mainly transpiration part with 89%, whereas it was contributed by 11% of evaporation at both of grazing and nongrazing surface condition.

From the TOPLATS hydrological application at forest site, we also found quite good agreement for energy and hydrological fluxes as shown in Fig. 46. RMSE of net radiation was 9.58 W m^{-2} . The regression coefficients of linear equation $\hat{y} = ax + b$ were $a=0.95$ and $b=12.49$, with $r=0.98$ (See Table 22). This was again resulted from reasonable prescribed of albedo (See Table 19), reflected solar radiation, and upgoing longwave radiations in the model calculations.

Simulated sensible and latent heat fluxes captured seasonal variation and magnitude of those measured from FOR site. The statistics values of RMSE=11.24, regression coefficients of linear equation $\hat{y} = ax + b$ were $a=1.02$ and $b=-0.44$ and r value of 0.89 were found for sensible heat flux, whereas RMSE=11.58, regression coefficients of linear equation $\hat{y} = ax + b$ were $a=0.56$ and $b=14.57$ and $r=0.87$ were found for latent heat flux. Also good agreement was found for comparison of the simulated and the measured ground heat flux with $r=0.81$, RMSE = 7.1 W m^{-2} and regression coefficients of linear equation $\hat{y} = ax + b$ were $a=1.56$ and $b=9.56$.

For hydrological fluxes, evapotranspiration and observed soil moisture at a depth of 10 and 30 cm was also compared with simulated moisture at depth of 10 cm and for 10-50 cm respectively at forest site (Fig. 47). The error statistics for the TOPLATS hydrological model can be summarized for evapotranspiration with RMSE of $0.008 \text{ mm hour}^{-1}$, regression coefficients of linear equation $\hat{y} = ax + b$ were $a=0.56$ and $b=0.01$, and $r=0.87$, whereas RMSE= $0.021 \text{ cm}^3 \text{ cm}^{-3}$, the regression coefficients of linear equation $\hat{y} = ax + b$ were $a=0.71$ and $b=0.01$ and $r=0.69$ found for soil moisture (See Table 22).

Application and validation of TOPLATS hydrological model with calibrated soil and vegetation parameters captured of diurnal fluctuation pattern of energy and hydrological components in both of grazing and nongrazing surface condition at KBU site as well as at FOR site. This signifies that TOPLATS hydrological model works well in Mongolian semi-arid region.

Table 22 Comparison of statistics between simulated and measured energy and hydrological fluxes at KBU and FOR site (from 2003/04 to 2003/12)

| Variables | Grazing surface condition at KBU site | | | | Nongrazing surface condition at KBU site | | | | FOR site | | | |
|--------------------|---------------------------------------|----------|----------|----------|--|----------|----------|----------|----------|----------|----------|----------|
| | RMSE | <i>a</i> | <i>b</i> | <i>r</i> | RMSE | <i>a</i> | <i>b</i> | <i>r</i> | RMSE | <i>a</i> | <i>b</i> | <i>r</i> |
| Net radiation | 11.74 | 0.99 | 16.79 | 0.98 | 11.37 | 1.11 | 14.12 | 0.95 | 9.58 | 0.95 | 12.49 | 0.98 |
| Latent heat | 16.52 | 0.56 | 14.57 | 0.72 | 18.71 | 0.62 | 16.34 | 0.71 | 11.24 | 0.56 | 14.57 | 0.87 |
| Sensible heat | 14.58 | 0.62 | 3.65 | 0.83 | 12.12 | 0.85 | -4.99 | 0.89 | 11.58 | 1.02 | -0.44 | 0.89 |
| Ground heat | 15.74 | 1.56 | 9.56 | 0.73 | 16.72 | 0.84 | 10.68 | 0.65 | 6.64 | 1.56 | 9.56 | 0.81 |
| Soil temperature | 3.36 | 0.98 | 1.77 | 0.97 | 2.47 | 0.94 | 14.61 | 0.96 | 2.34 | 0.97 | 0.77 | 0.99 |
| Soil moisture | 0.029 | 0.55 | 0.02 | 0.69 | 0.017 | 0.61 | 0.03 | 0.82 | 0.021 | 0.71 | 0.01 | 0.69 |
| Evapotranspiration | 0.011 | 0.56 | 0.01 | 0.72 | 0.013 | 0.62 | 0.01 | 0.71 | 0.008 | 0.56 | 0.01 | 0.87 |

RMSE is root mean square error, *a* and *b* are coefficients of linear equation of $\hat{y} = ax + b$, *r* is correlation coefficient. Unit of the variables are (W m^{-2}) for net radiation, latent heat, sensible heat and ground heat flux, (K) for soil temperature, (mm hour^{-1}) for evapotranspiration and ($\text{cm}^3 \text{ cm}^{-3}$) for soil moisture

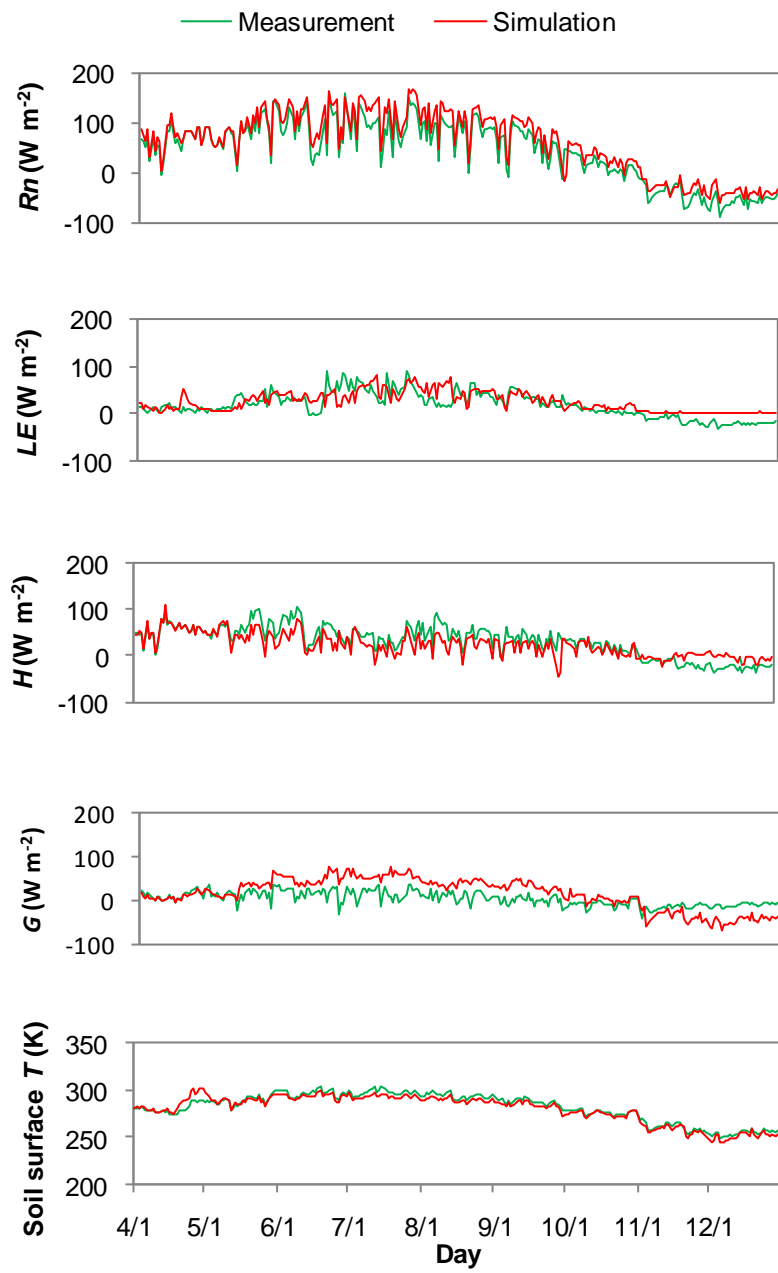


Fig. 40 Comparison of simulated and measured energy fluxes at grazing condition in KBU site from April to December of 2003.

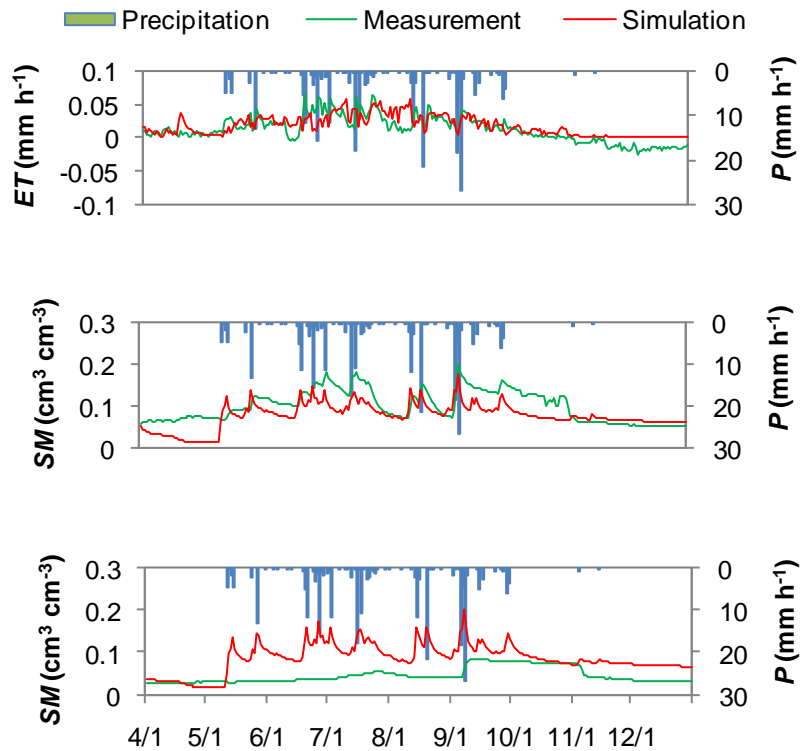


Fig. 41 Comparison of simulated and measured hydrological fluxes at grazing condition in KBU site from April to December of 2003. (Note: Top panel represents evapotranspiration, middle for soil moisture content at 10 and bottom for 30 cm depth)

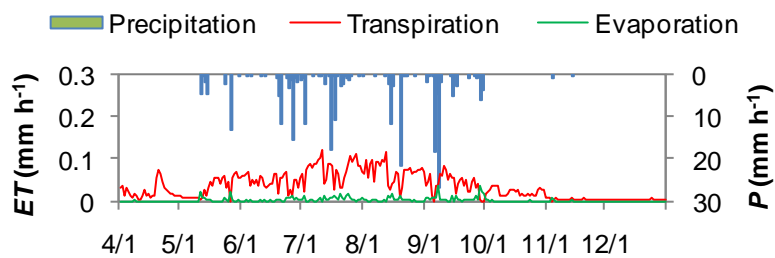


Fig. 42 Transpiration and evaporation at grazing condition in KBU site from April to December of 2003.

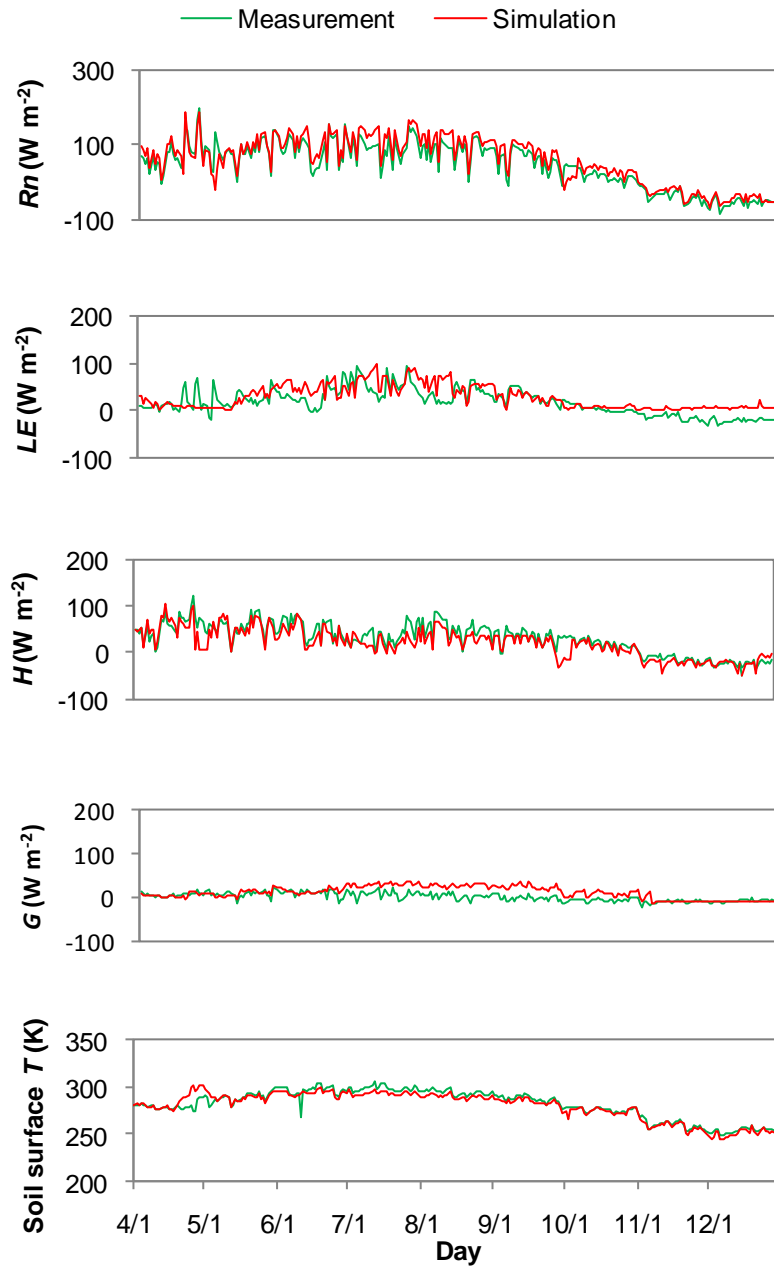


Fig. 43 Comparison of simulated and measured energy fluxes at nongrazing condition in KBU site from April to December of 2003.

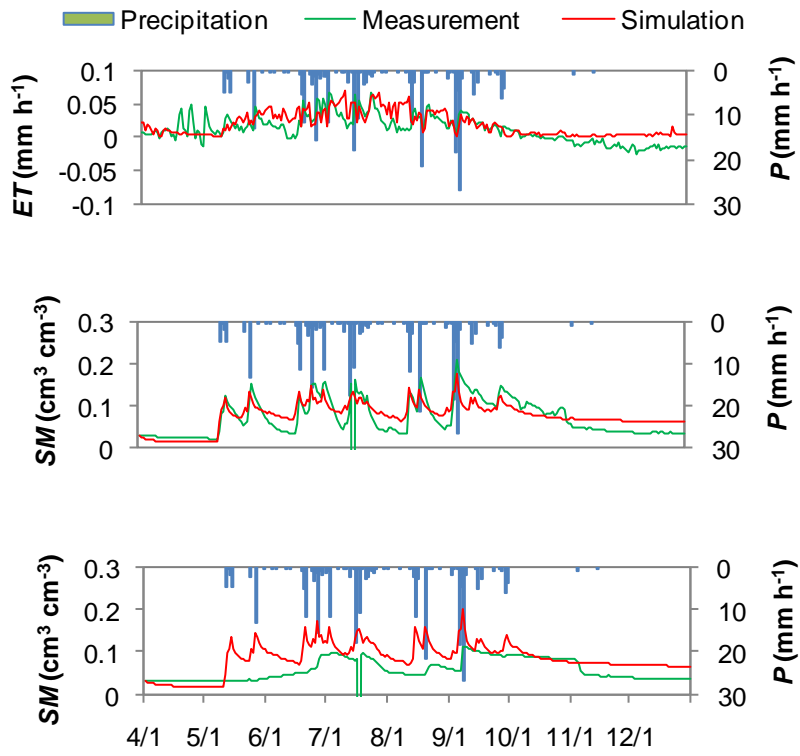


Fig. 44 Comparison of simulated and measured hydrological fluxes at grazing condition in KBU site from April to December of 2003. (Note: Top panel represents evapotranspiration, middle for soil moisture content at 10 and bottom for 30 cm depth)

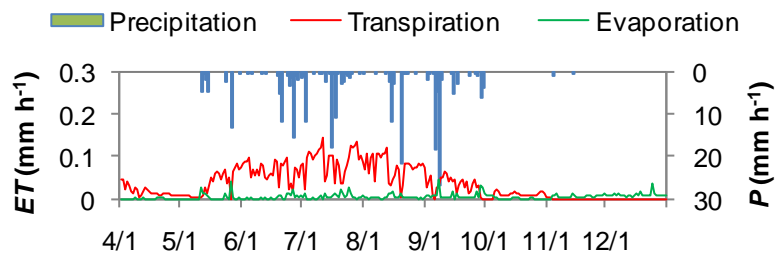


Fig. 45 Transpiration and evaporation at grazing condition in KBU site from April to December of 2003.

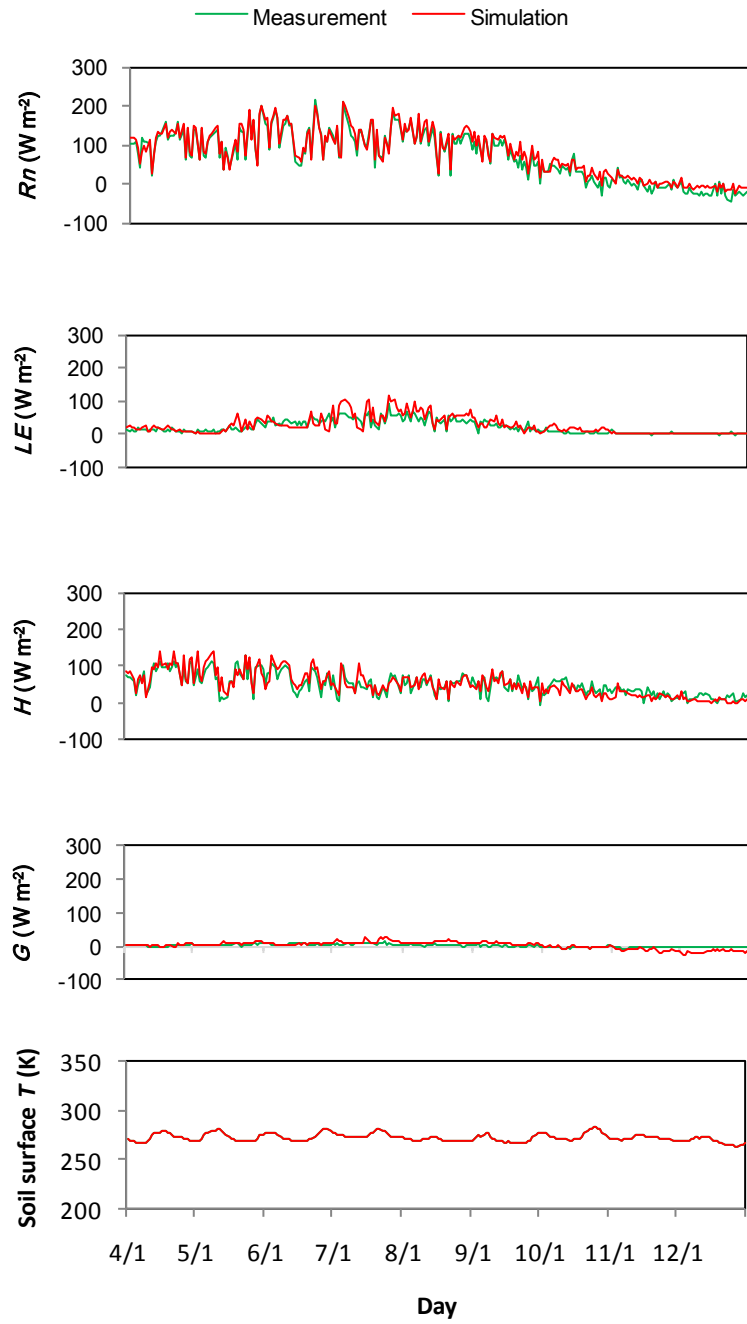


Fig. 46 Comparison of daily simulated and measured energy fluxes at FOR site from April to December, 2003.

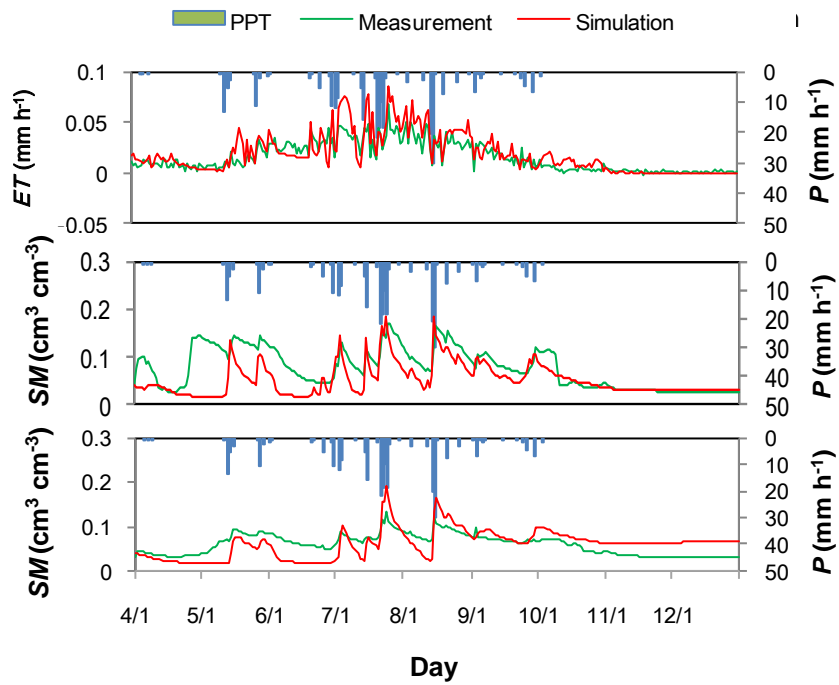


Fig. 47 Comparison of simulated and measured hydrological fluxes at forest site from April to December, 2003. (Note: Top panel represents evapotranspiration, soil moisture content at 10 and 30 cm depth)

3.3 Coupled environmental modeling approach on ecohydrological processes

As we discussed above, there are potentially many parameters which can be used for coupling between ecosystem model and land surface hydrological model. However, parameter selection depends on structures and outputs of those models. In addition, prior to coupling the two environmental models, it is important to demonstrate that the two models are sensitive to the output of the other. In the present study, LAI was selected as the linkage parameter as discussed in method section.

3.3.1 Coupling methodology for environmental modeling system

The primary purpose of coupling century ecosystem model with TOPLATS land surface hydrologic model is to provide TOPLATS hydrological model with dynamic values of LAI. Once coupling parameter and methodology has been decided, the coupling procedure was designed and adopted in this study to gain insight into various environmental issues. The coupling has been performed as follows: first, the century ecosystem model was configured to run at a monthly time step in the KBU site for driving observed monthly averaged atmosphere forcing of maximum and minimum air temperature, precipitation to get simulated aboveground biomass. A simple algorithm based on Mariko et al. (2004) was then employed to convert aboveground biomass to LAI. This simple equation was developed based on measured aboveground biomass and LAI data derived from KBU site. The algorithm equation is formulated as follow:

$$Y = 0.057 + 0.006X \quad (7)$$

LAI thus calculated by means of above equation was used as inputs to TOPLATS hydrological model to simulate energy fluxes and hydrological components at one hour time step. Thus, at every monthly time step, TOPLATS hydrological model is updated by realistic LAI estimates. Fig. 48 shows comparison of calculated LAI by means of Eq. (7) and measured LAI (Sugita et al., 2003) at grazing and nongraing surface condition at KBU site for 2003. This approach is acceptable because the difference in calculated and measured LAI determined for each surface condition was found small in the study site.

To see the efficiency of coupling two environmental models, hydrological fluxes and energy flux were compared through various measured and simulated parameters.

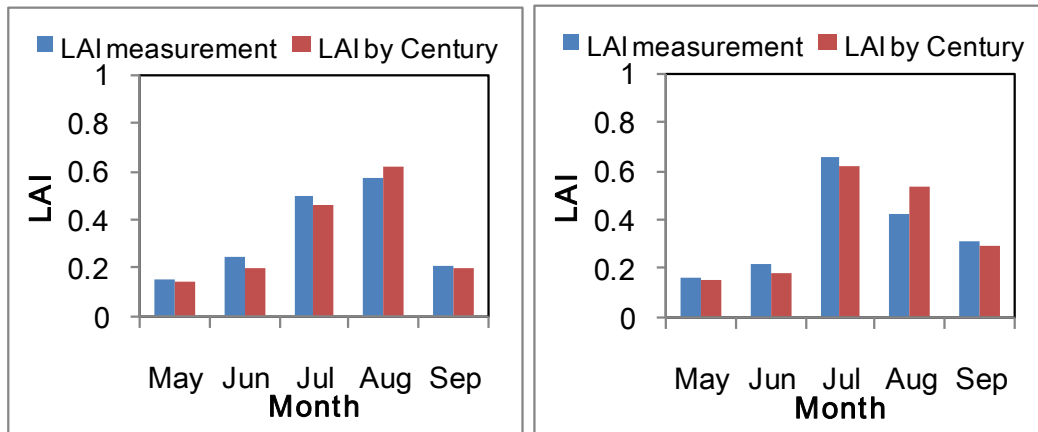


Fig. 48 Comparison between measured LAI and those obtained from simulated aboveground biomass by century ecosystem model. Left hand side panel represents the grazing condition and right hand side panel represents nongrazing condition (KBU site, 2003).

3.3.2 Parameter selection and sensitivity test

In the sensitivity test, LAI was selected as 0.3, 0.6 and 0.9, when other parameters were kept constant, except for surface albedo and roughness length for heat transfer and momentum. The selection was based on the fact that mean LAI at KBU in July was 0.66. Those parameters should change according to changes in LAI. Also, two distinctive days of no rain and rainy day were selected, which are shown in Fig. 49. No rain day was selected on June 6th, 2003, whereas rainy day was selected on June 26th, 2003. On that day, precipitation occurred before noon and the total amount of precipitation was 10 mm day⁻¹. TOPLATS land surface hydrological model was used to investigate the hydrological model's sensitivities to changes in LAI forcing. The model was configured to run over the KBU site.

Fig. 50 shows the sensitivity test of daily soil moisture content at 10 cm to LAI and precipitation as well. In no rainy day, soil moisture contents were decreased with an increase of LAI by 1% (LAI=0.6) and 2% (LAI=0.9), whereas soil moisture were also decreased by 1.5% (LAI=0.6) and 2.5% (LAI=0.9) in rainy day.

Fig. 51 shows that change of evapotranspiration (ET) under different LAI values. When LAI=0.69 and LAI=0.9, ET were increased by 39.5% and 62.5% in no rainy day. In rainy day, ET were increased by 84.6% (LAI=0.6) and 152.1% (LAI=0.9).

Transpiration (Tr) change were shown in Fig. 52. In no rainy day, Tr were increased by 57.4% (LAI=0.6) and 81.6% (LAI=0.9), whereas Tr were also increased by 84.6% (LAI=0.6) and 152.9% (LAI=0.9) in rainy day.

Fig. 53 shows that evaporation (E) change based on different LAI values. E were increased by 32.15% when LAI=0.6, whereas it also increased by 54.5% (LAI=0.9) in no rainy day. In rainy day, E were increased by 67.4% (LAI=0.6) and 121.6% (LAI=0.9).

Fig. 54 shows change of infiltration (IN) under the different LAI values. Its value did not change in no rainy day, while there is decrease in with LAI by 0.15% (LAI=0.6) and 0.25% (LAI=0.9) in rainy day.

Fig. 55 shows net radiation (R_n) change under the different LAI values. In no rainy day, R_n were increased by 4.2% (LAI=0.6) and 6.2% (LAI=0.9), whereas R_n were also increased by 2.6% (LAI=0.6) and 4.9% (LAI=0.9) in rainy day.

The changes of ground heat flux (G) are shown in Fig. 56. In no rainy day, G were decreased by 14.2% (LAI=0.6) and 20.2% (LAI=0.9), whereas G were also decreased by 20.6% (LAI=0.6) and 31.9% (LAI=0.9) in rainy day.

Fig. 57 shows sensible heat flux (H) change under the different LAI values. In no rainy

day, H were decreased by 10.1% (LAI=0.6) and 12.2% (LAI=0.9), whereas H were also decreased by 6.4% (LAI=0.6) and 8.9% (LAI=0.9) in rainy day.

Fig. 58 shows latent heat flux (LE) change under the different LAI values. In no rainy day, LE were increased by 40.1% (LAI=0.6) and 64.2% (LAI=0.9), whereas LE were also increased by 84.4% (LAI=0.6) and 153.1% (LAI=0.9) in rainy day.

The changes of soil surface temperature are shown in Fig. 59. In no rainy day, soil surface temperature were decreased by 0.12% (LAI=0.6) and 0.18% (LAI=0.9), whereas soil surface temperature were also decreased by 0.13% (LAI=0.6) and 0.25% (LAI=0.9) in rainy day.

Throughout this sensitivities analysis, several features can be noted. First, the combination of precipitation and LAI change has larger effect on hydrological components than that in energy components. Second, overall performance of this sensitivity test shows that LAI is acceptable to couple century ecosystem model and TOPLATS hydrological model.

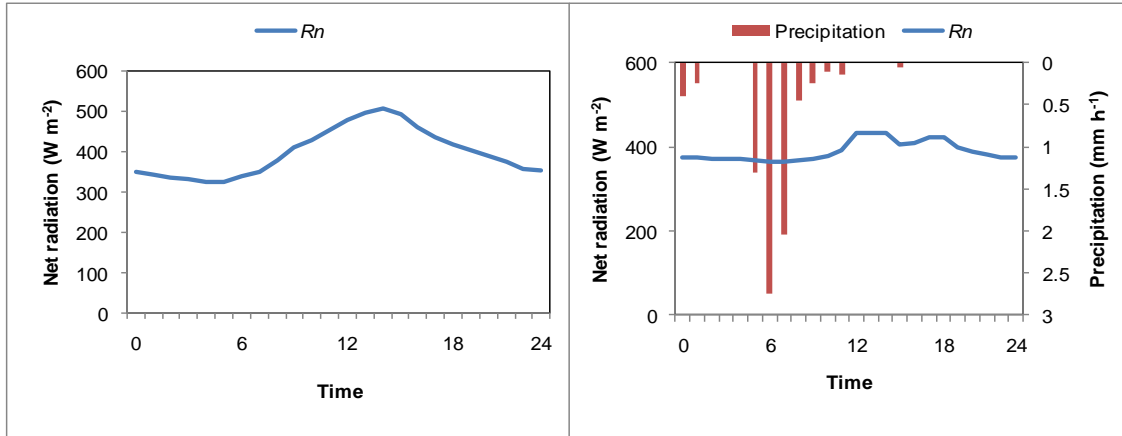


Fig. 49 Condition on two selected days. Left hand side represents no rain day (2003/ 06/08) and right hand side represents rainy day (2003/ 06/26)

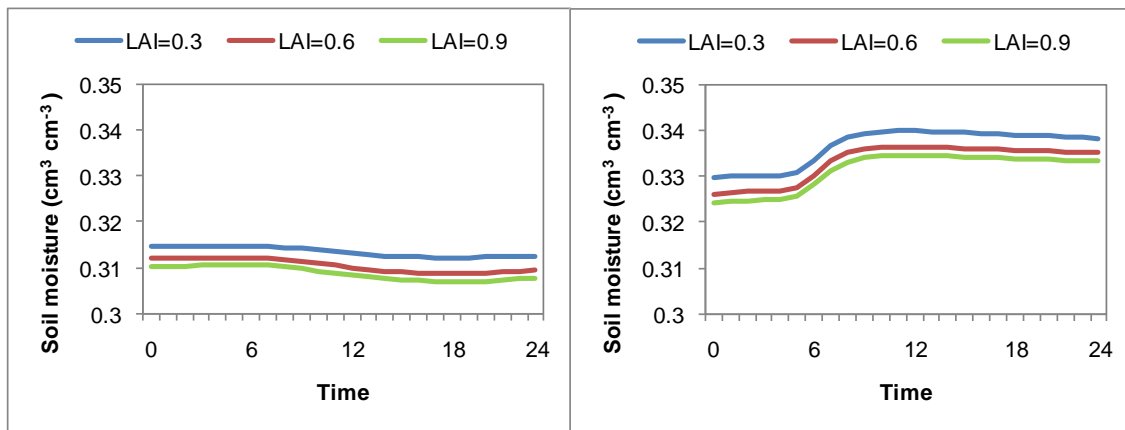


Fig. 50 Comparison of simulated soil moisture content at 10 cm depth. Left hand side panel represents the results showing no rain day and effect of adopting different LAI of 0.3, 0.6, and 0.9. Right hand side panel represents the results showing rainy day and effect of using different LAI of 0.3, 0.6, and 0.9.

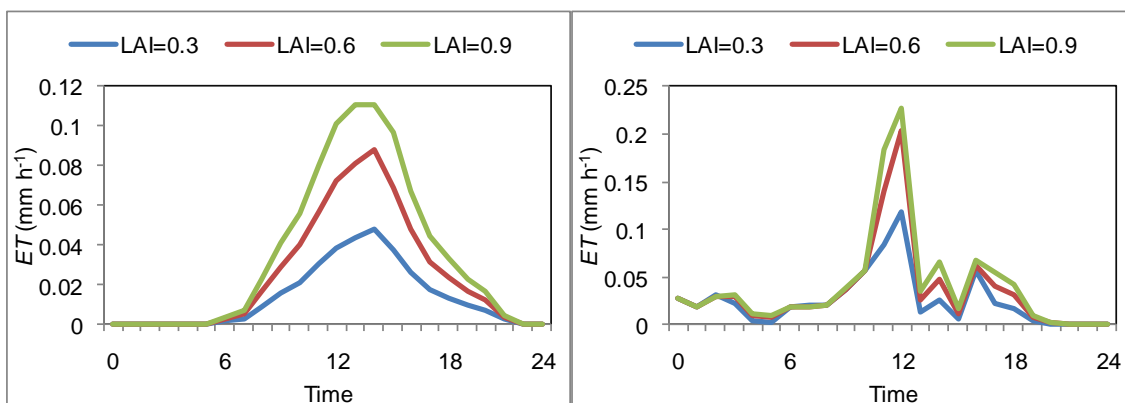


Fig. 51 Same as in Fig. 50, but for evapotranspiration

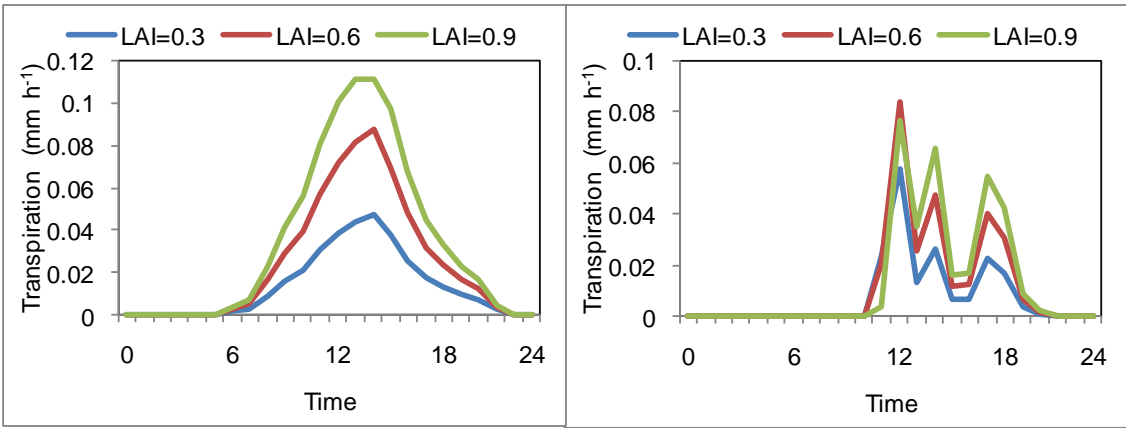


Fig. 52 Same as in Fig. 50, but for transpiration

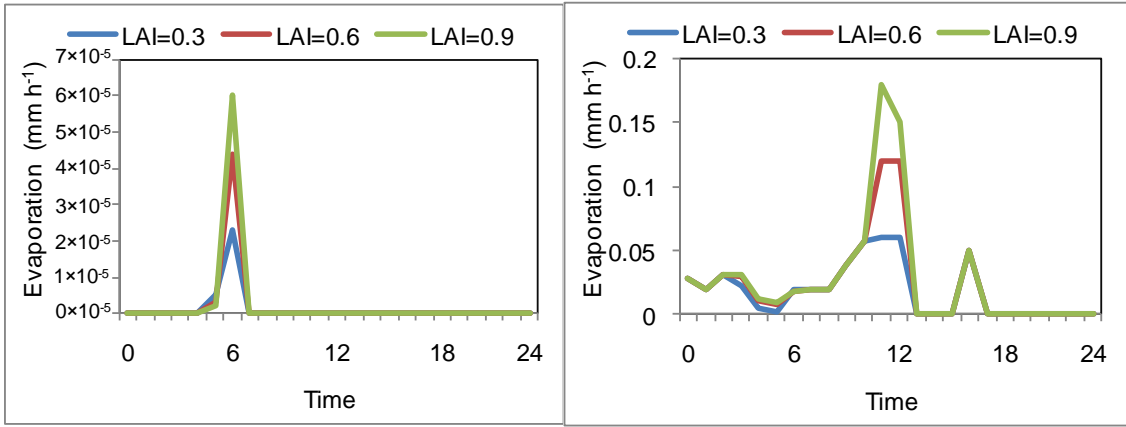


Fig. 53 Same as in Fig. 50, but for evaporation

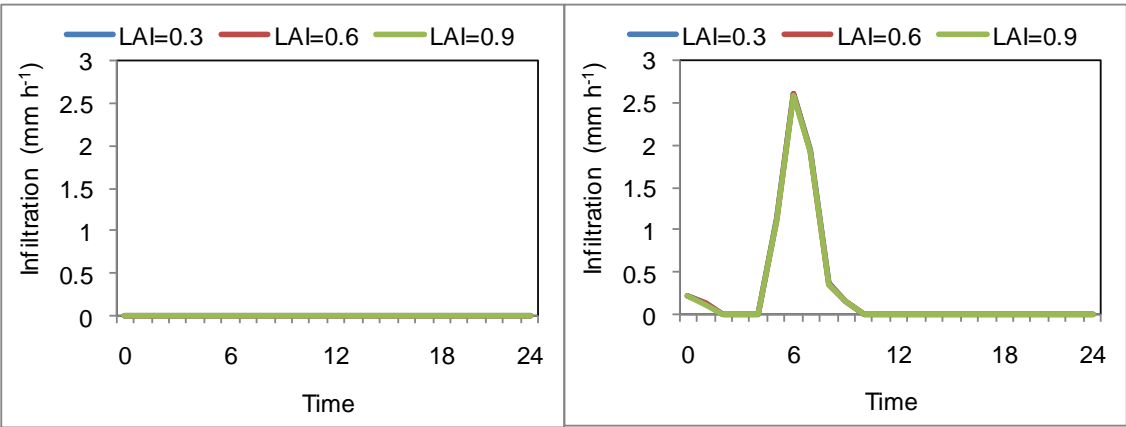


Fig. 54 Same as in Fig. 50, but for infiltration

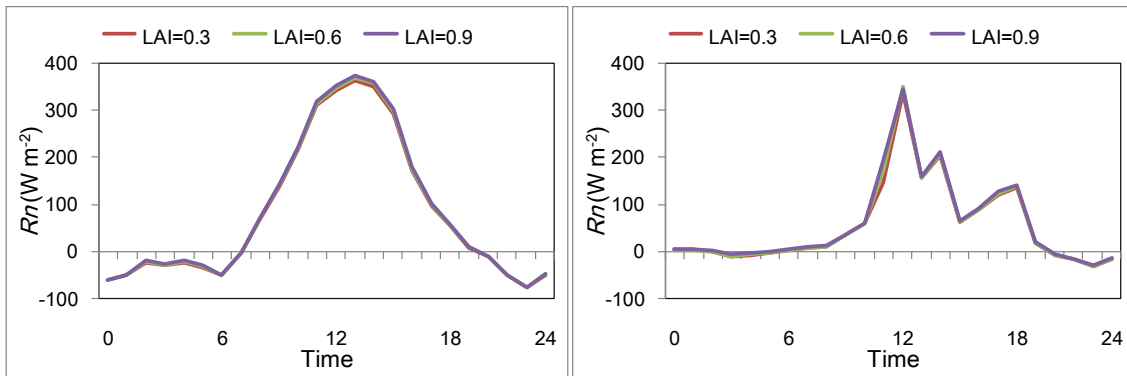


Fig. 55 Same as in Fig. 50, but for net radiation.

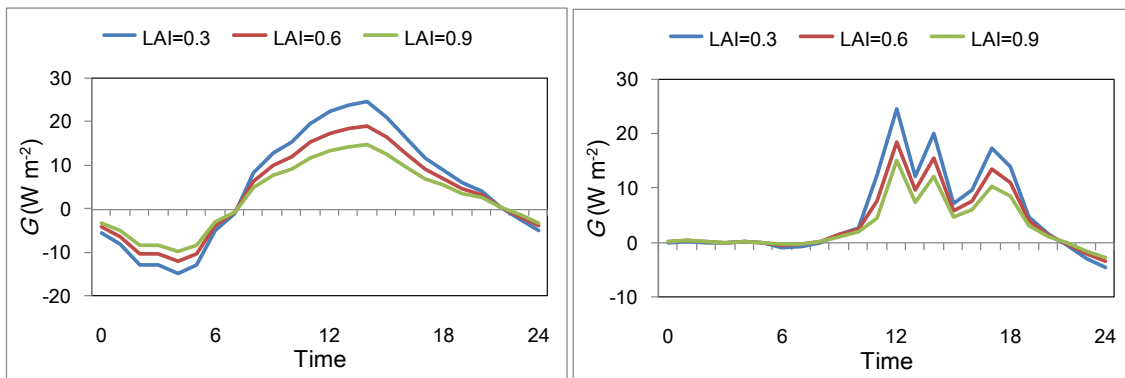


Fig. 56 Same as in Fig. 50, but for ground heat flux.

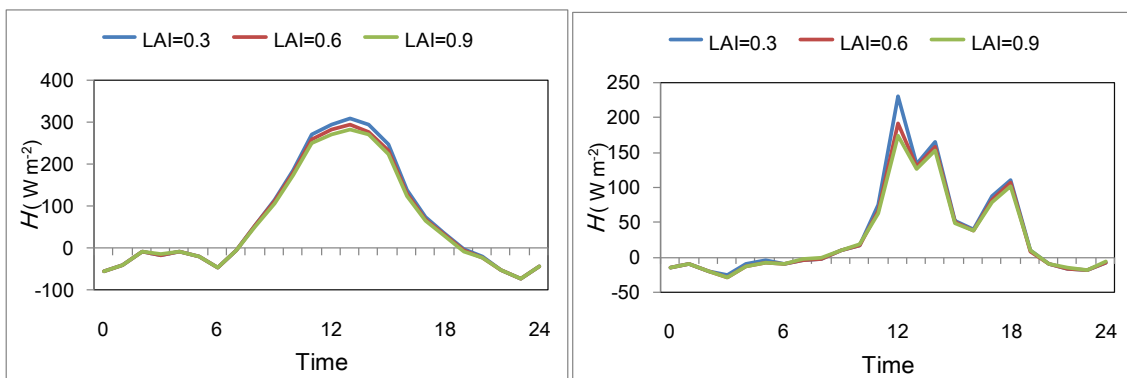


Fig. 57 Same as in Fig. 50, but for sensible heat flux.

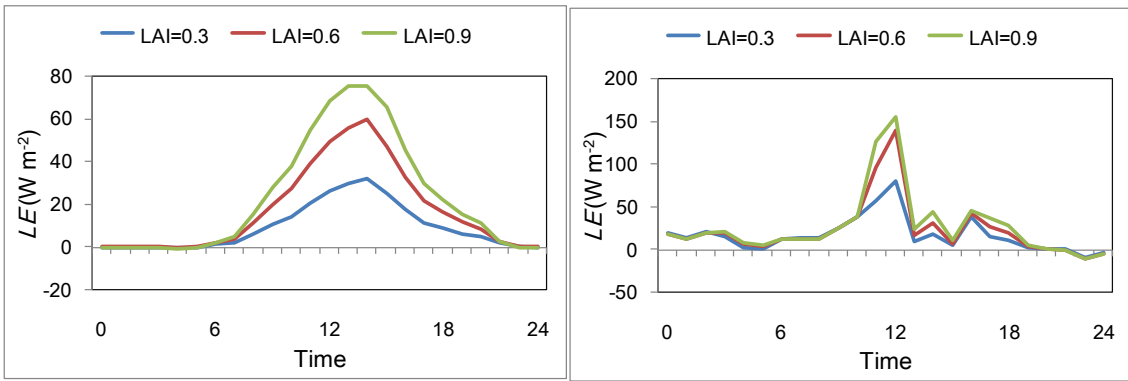


Fig. 58 Same as in Fig. 50, but for latent heat flux.

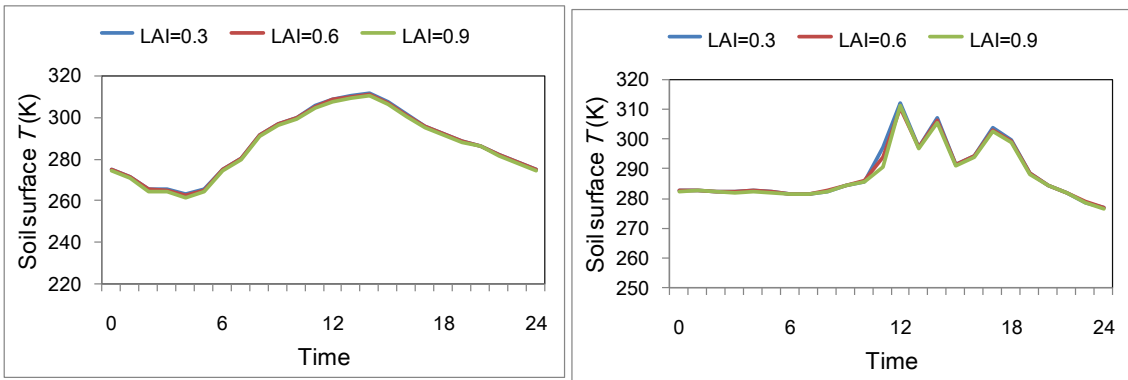


Fig. 59 Same as in Fig. 50, but for soil temperature

3.3.3 Validation of coupled modeling approach (century ecosystem model and TOPLATS hydrological model)

To validate the applicability of coupled modeling approach in our study, extensive comparisons have been performed for hydrological and energy fluxes using flux measurements data from 2004 to 2005 in grassland. As stated in method section, one-way data transferring methodology was used for coupling between century ecosystem model and TOPLATS hydrological model using LAI value as a linkage parameter. LAI values were calculated by means of Eq. (7) from simulated aboveground biomass at grazing and nongrazing surface condition by the century ecosystem model. The values of roughness lengths for momentum ($z_{o,m}$) and heat transfer ($z_{o,h}$) were calculated by employing Eqs. (5)-(6). Summarized time series of simulated energy and hydrological fluxes versus measured fluxes from KBU site are shown in Figs. 60-62 for grazing and Figs. 63-65 for nongrazing surface condition.

A quite good agreement was found between the measured and simulated energy fluxes at grazing and nongrazing surface condition as shown in Figs. 60 and 63. The simulated energy fluxes captures seasonal variation and magnitude of measured energy fluxes at both surface condition for the validation period of coupled modeling approach between 2004 and 2005. RMSE of net radiation was 8.94 W m^{-2} . The regression coefficients of linear equation $\hat{y} = ax + b$ were $a=1.06$ and $b=19.41$, with $r=0.95$ for grazing surface condition. For nongrazing surface condition, RMSE was 9.38 W m^{-2} , regression coefficients of linear equation $\hat{y} = ax + b$ were $a=1.02$ and $b=17.68$, and $r=0.95$ (See Table 23).

The simulation of the latent heat flux showed a good agreement with the observations in both the magnitudes and temporal patterns at grazing and nongrazing surface condition. RMSE of latent heat flux was 16.57 W m^{-2} . The regression coefficients of linear equation $\hat{y} = ax + b$ were $a=0.66$ and $b=16.32$, with an $r=0.70$ for grazing surface condition, whereas those were obtained RMSE was 19.18 W m^{-2} , regression coefficients of linear equation $\hat{y} = ax + b$ were $a=1.01$ and $b=20.06$, and $r=0.68$ for nongrazing surface condition (See Table 23).

The simulated sensible heat flux had a similar temporal pattern as that seen in the observed sensible heat flux. The error statistics for the TOPLATS hydrological model can be summarized as RMSE of 10.95 W m^{-2} , regression coefficients of linear equation $\hat{y} = ax + b$ were $a=0.79$ and $b=8.08$, and $r=0.80$ for grazing surface condition, whereas RMSE of 12.67 W m^{-2} , regression coefficients of linear equation $\hat{y} = ax + b$ were $a=0.88$ and $b=-4.61$, and $r=0.80$ for nongrazing surface condition (See Table 23).

The simulated ground heat fluxes at grazing and nongrazing surface condition captures seasonal variation and magnitude of measured ground heat fluxes. RMSE of ground heat flux was 14.41 W m^{-2} . The regression coefficients of linear equation $\hat{y} = ax + b$ were $a=1.36$ and $b=9.65$, with $r=0.64$ for grazing surface condition. For nongrazing surface condition, RMSE was 11.57 W m^{-2} , regression coefficients of linear equation $\hat{y} = ax + b$ were $a=0.88$ and $b=11.88$, and $r=0.69$ (See Table 23). During winter period, comparison of ground heat flux was not good due to worth comparison of soil moisture (see below). This is not surprising as the TDR sensors are incapable of detecting accurate soil moisture when it is frozen (Watanabe and Wake, 2009).

For hydrological fluxes, observed soil moisture at a depth of 10 and 30 cm was compared with simulated moisture at depth of 10 cm and for 10-50 cm respectively at different surface conditions of grazing and nongrazing site (Figs. 61 and 64). In both of grazing and non-grazing conditions, simulated soil moisture gave better correspondence with observation at the depth of 10 cm in comparison to at 30 cm depth. This was because for 30 cm comparison, simulation was available only for 10-50 cm, and exact match with the observation was not possible. RMSE of soil moisture was $0.021 \text{ cm}^3 \text{ cm}^{-3}$. The regression coefficients of linear equation $\hat{y} = ax + b$ were $a=0.32$ and $b=0.04$, with $r=0.77$ for grazing surface condition. For nongrazing surface condition, RMSE was $0.016 \text{ cm}^3 \text{ cm}^{-3}$, regression coefficients of linear equation $\hat{y} = ax + b$ were $a=0.35$ and $b=0.05$, and $r=0.76$ (See Table 23).

For hydrological fluxes, another property i.e. evapotranspiration was compared between observation and simulation at grazing and nongrazing surface conditions (Figs. 61 and 64). These comparisons gave good agreement of simulated and measured fluxes in both of grazing and nongrazing surface condition. The error statistics for the TOPLATS hydrological model can be summarized as RMSE of $0.0009 \text{ mm hour}^{-1}$, regression coefficients of linear equation $\hat{y} = ax + b$ were $a=0.58$ and $b=0.05$, and $r=0.70$ for grazing surface condition, whereas RMSE of $0.018 \text{ mm hour}^{-1}$, regression coefficients of linear equation $\hat{y} = ax + b$ were $a=0.92$ and $b=0.03$, and $r=0.68$ for nongrazing surface condition (See Table 23). Figs. 62 and 65 show simulated evaporation and transpiration at grazing and nongrazing surface condition. Evapotranspiration was mainly contributed by transpiration with 91%, whereas 9% was contributed by evaporation at both of grazing and nongrazing surface conditions.

Coupled modeling approach with calibrated soil and vegetation parameters and calculated LAI captured diurnal fluctuation pattern of measured energy and hydrological components in both of grazing and nongrazing surface condition. This signifies that this coupled model works well and calculated LAI value was judged acceptable for coupling between these two models in Mongolian semi-arid region.

Table 23 Comparison of statistics between simulated and measured energy and hydrological fluxes at KBU based on coupled modeling approach (from 2004/01 to 2005/12)

| Variables | Grazing surface condition at KBU site | | | | Nongrazing surface condition at KBU site | | | |
|--------------------|---------------------------------------|----------|----------|----------|--|----------|----------|----------|
| | RMSE | <i>a</i> | <i>b</i> | <i>r</i> | RMSE | <i>a</i> | <i>b</i> | <i>r</i> |
| Net radiation | 9.94 | 1.06 | 19.41 | 0.97 | 9.38 | 1.02 | 17.68 | 0.95 |
| Latent heat | 16.57 | 0.66 | 16.32 | 0.70 | 19.18 | 1.01 | 20.06 | 0.68 |
| Sensible heat | 10.05 | 0.79 | 8.08 | 0.80 | 12.67 | 0.88 | -4.61 | 0.81 |
| Ground heat | 12.41 | 1.36 | 9.65 | 0.64 | 11.57 | 0.88 | 11.88 | 0.69 |
| Soil temperature | 2.25 | 0.9 | 25.13 | 0.98 | 2.94 | 1.36 | 14.24 | 0.99 |
| Soil moisture | 0.021 | 0.32 | 0.04 | 0.77 | 0.016 | 0.32 | 0.05 | 0.76 |
| Evapotranspiration | 0.0009 | 0.58 | 0.05 | 0.70 | 0.018 | 0.92 | 0.03 | 0.68 |

RMSE is root mean square error, *a* and *b* are coefficients of linear equation of $\hat{y} = ax + b$, *r* is correlation coefficient. Unit of the variables are (W m^{-2}) for net radiation, latent heat, sensible heat and ground heat flux, (K) for soil temperature, (mm hour^{-1}) for evapotranspiration and ($\text{cm}^3 \text{ cm}^{-3}$) for soil moisture

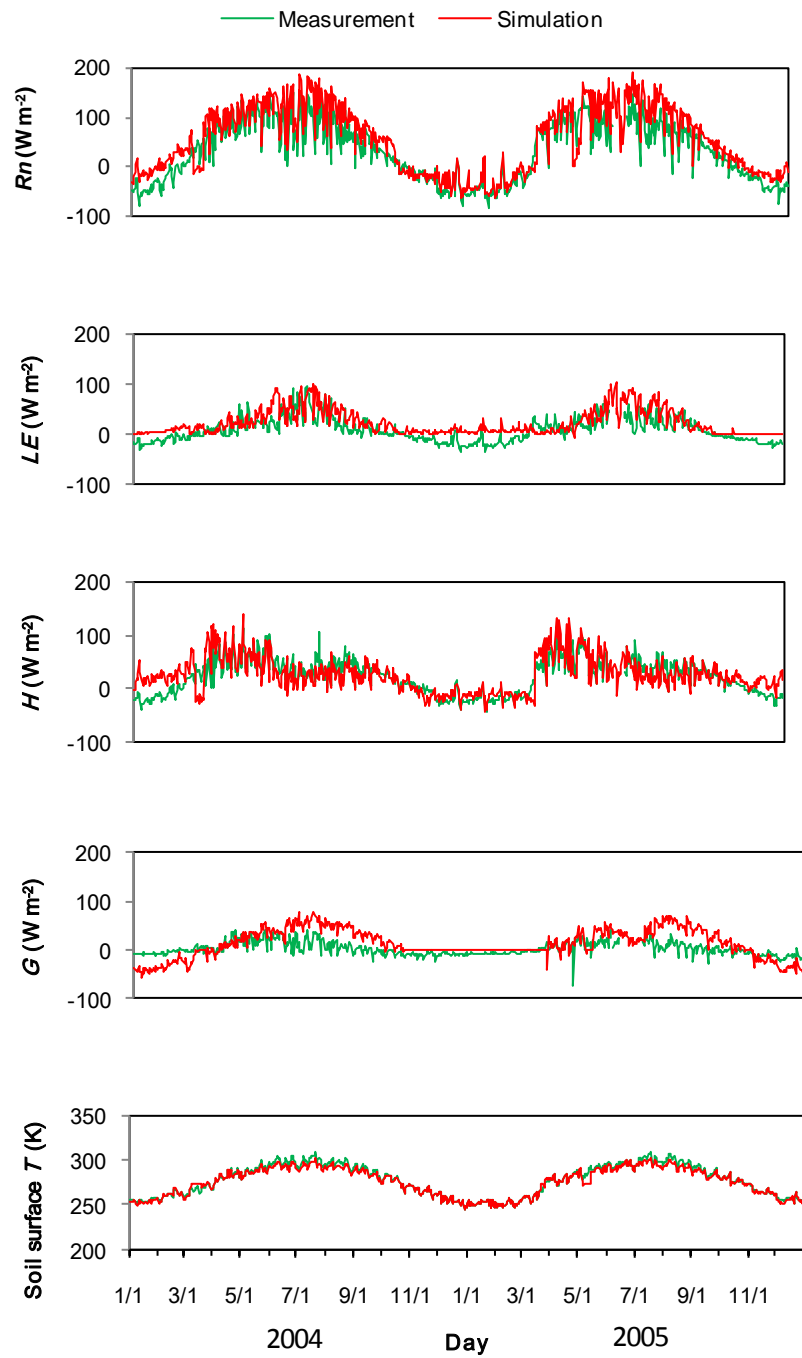


Fig. 60 Comparison of simulated and measured energy fluxes at grazing condition in KBU site from 2004 to 2005.

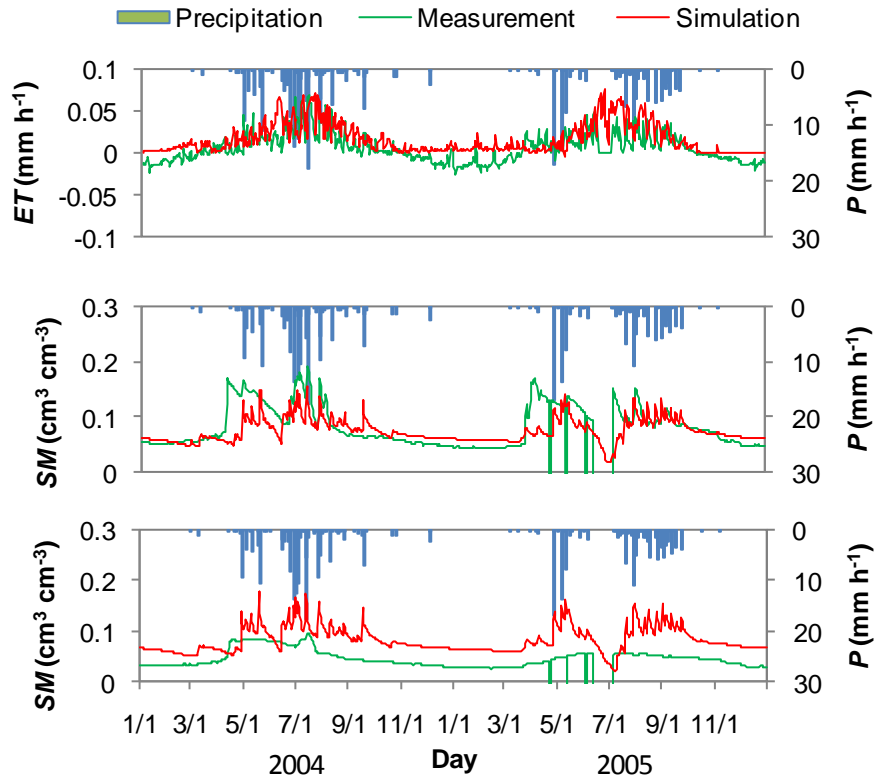


Fig. 61 Comparison of simulated and measured hydrological fluxes at grazing condition in KBU site from 2004 to 2005. (Note: Top panel represents evapotranspiration, middle for soil moisture content at 10 and bottom for 30 cm depth)

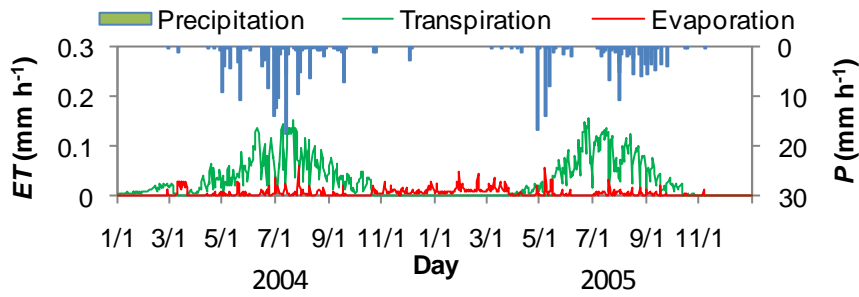


Fig. 62 Transpiration and evaporation at grazing condition in KBU site from 2004 to 2005.

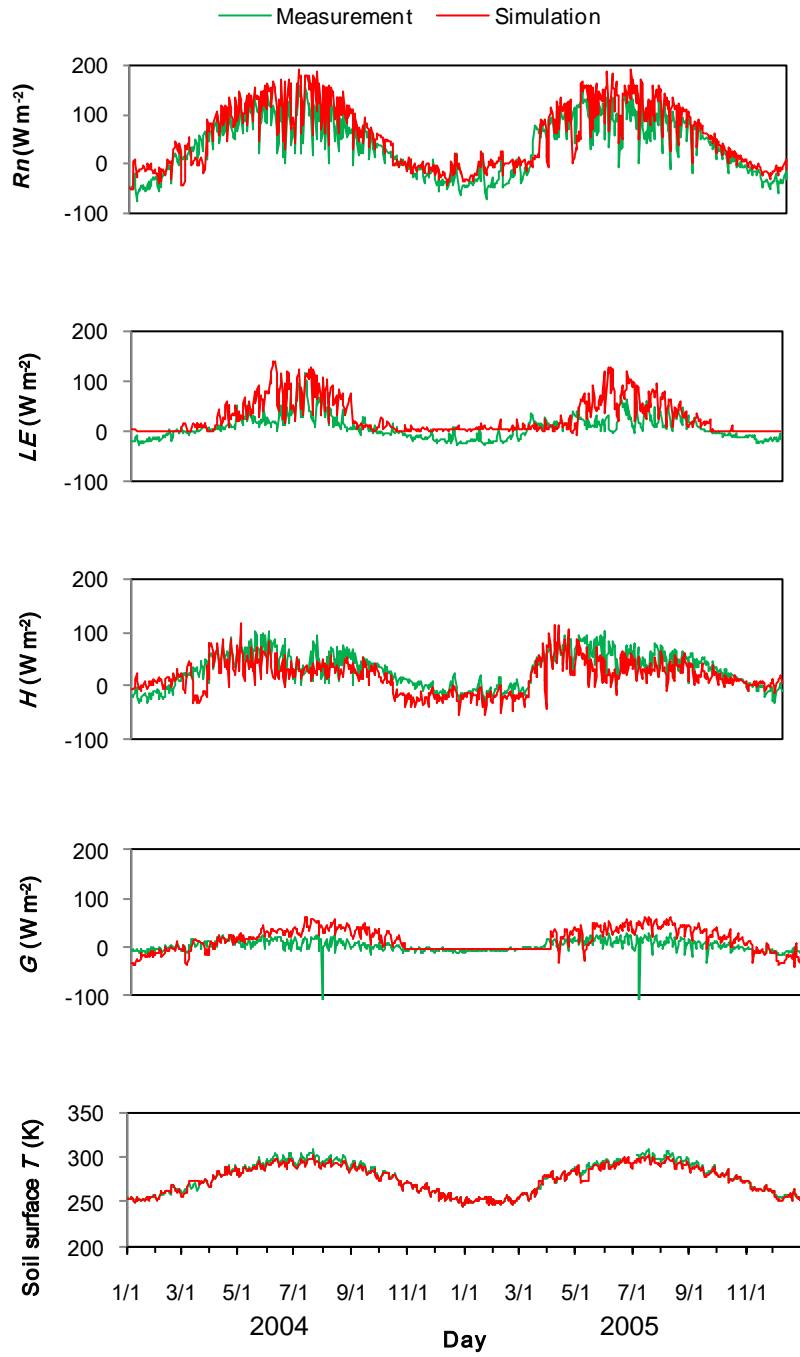


Fig. 63 Comparison of simulated and measured energy fluxes at nongrazing condition in KBU site from 2004 to 2005.

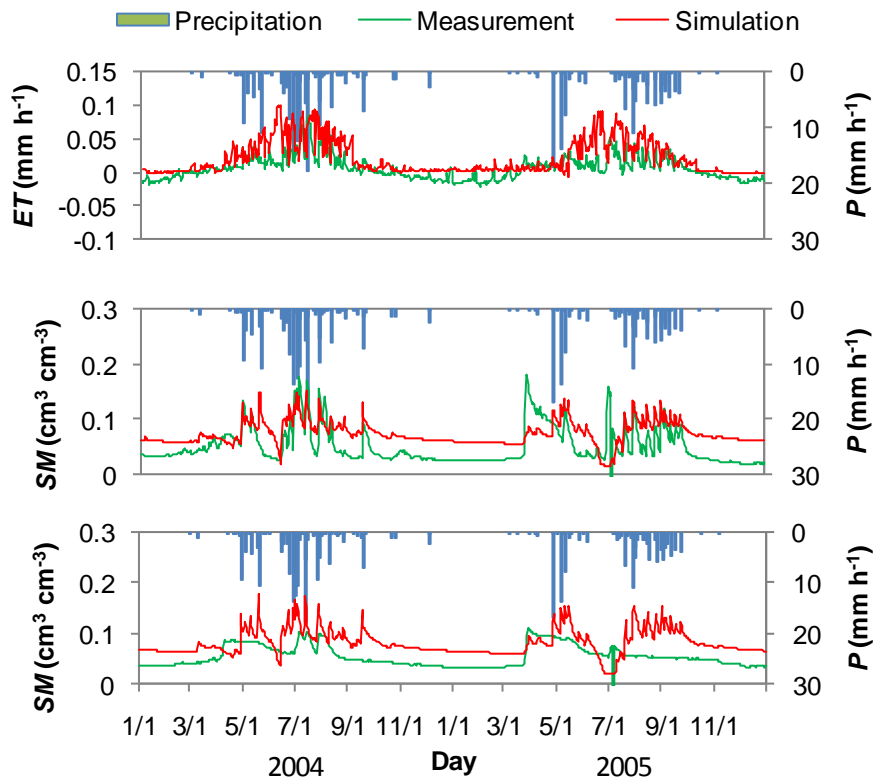


Fig. 64 Comparison of simulated and measured hydrological fluxes at grazing condition in KBU site from 2004 to 2005. (Note: Top panel represents evapotranspiration, middle for soil moisture content at 10 and bottom for 30 cm depth)

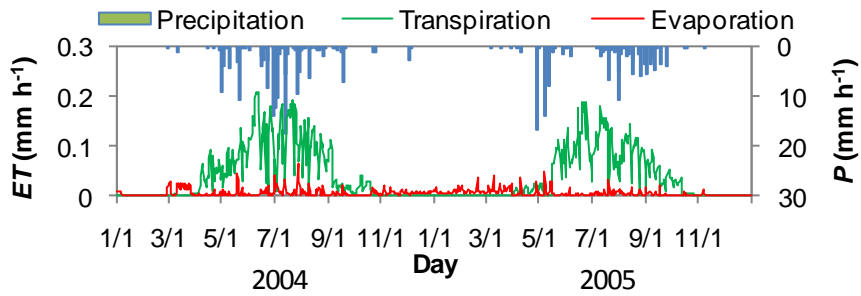


Fig. 65 Transpiration and evaporation at grazing condition in KBU site from 2004 to 2005.

3.4 Spatial application of TOPLATS hydrological model.

For a long time, hydrologists have been interested in how spatially complex terrain affects computed hydrological and energy fluxes. Soil moisture, in turn, influences watershed hydrology by determining how rainfall inputs are partitioned into surface runoff or infiltration and how radiation inputs are also partitioned into latent, sensible heat fluxes and soil heat fluxes.

Soil transmissivity is a spatially heterogeneous property that also influences soil water balances and is incorporated in TOPLATS hydrological model with the topographic index to represent runoff tendency. The topographic index was computed from DEM data. We used ASTER GDEM data (Earth Remote Sensing Data Analysis Center, 2009). Original ASTER GDEM had a 30 m resolution, so that we changed it to 1 km by Kriging interpolation method in ArcGIS 9.3. After changing the grid size of ASTER GDEM, topographic index was calculated by using Eq. (3) for the upper part of Kherlen river basin as shown in Fig. 66. Figs. 67 and 68 show vegetation and soil distribution map based on Saandar and Sugita (2004). These maps were used in order to give vegetation and soil parameters to TOPLATS hydrological model. In the Kherlen river basin, vegetation and soil type were divided into forest and steppe area. Therefore, each grid of forest and grassland area in vegetation and soil map were separately assigned with different dummy variable, i.e., 1 for forest and 2 for steppe area. These different numbers were recognized by the each look-up table of them (Table 17 for soil look-up table and Table 19 for vegetation look-up table). Concerning the most important input of rainfall, the spatial and temporal variability is high in the upper Kherlen river watershed. This is due to the topographic effect of rainfall enhancement in our study area. Therefore, in addition to these time constant map, seven time series (hourly) of spatial forcing data were generated that includes air temperature, air pressure, relative humidity, wind speed, downward long-wave and shortwave, and precipitation data. Also four initial soil moisture data at four different soil layers were used to run spatial application of TOPLATS hydrological model in order to understand the basin scale hydrological and energy processes.

For spatial application TOPLATS hydrological model, basin average saturated hydraulic conductivity was used and it was computed by following equation (8) based on the method of Brutsaert and Lopez (1998). The rate of decrease in groundwater flow from a watershed is much slower than that the other runoff components. This means that the flows resulting only from groundwater storage can be assumed to be those that correspondence to the lowest dQ/dt at a given Q where Q is the observed discharge and dQ/dt is the time change of Q . This was incorporated in Eq. (8).

$$k_0 = 0.5757 \left(\frac{a_3}{a_1} \right)^{\frac{1}{2}} A(LD)^{-2} \quad (8)$$

where k_0 is basin average hydraulic conductivity, a_1 and a_3 are parameters, L is total length of all stream network which was determined based on IMH of river network data (see Fig. 69), D is thickness of aquifer which was assumed to be 12 m based on ground well measurement along Kherlen river basin (see Fig. 70).

The parameters of a_1 and a_3 were determined based on long term observed discharge at UDN site (Fig. 4) in upper Kherlen river watershed. In more detail, those parameters can be obtained at the lower envelopes with slopes 1 and 3 on log-log plot of dQ/dt and Q as shown in Fig. 71. After determination of each parameter, we computed basin average saturated hydraulic conductivity as $5.8 \times 10^{-4} \text{ m s}^{-1}$. In order to verify, calculated basin average saturated hydraulic conductivity was compared with other study values given by Brutsaert (2005) and our calculated value falls within the range of saturated hydraulic conductivity of geology of the watershed. Also basin average groundwater level was assumed to be 2 m representing shallow groundwater depth of the Kherlen river basin.

After these parameters had been fixed, pore size index and exponential decay parameter were further calibrated to obtain agreement of discharge with measurements on average. Thus, pore size index was changed from 0.65 to 0.3 and exponential decay parameter from 4 to 7. Model simulations were done at an hourly time-step, using the prepared meteorological data set as described earlier. The same vegetation and soil parameters used for calibration at point application (Table 17 for soil parameters) of TOPLATS hydrological model were also used here. Spatial application of TOPLATS hydrological model was carried out from 2004 to 2005 to simulate spatial distribution of energy and hydrological fluxes.

Fig. 72 shows the spatial distribution of simulated daily energy and hydrological fluxes. These spatially distributed patterns show clear difference of each variable at forest and grassland site. Thus, TOPLATS hydrological model can consider both of vegetation heterogeneity for energy fluxes and topographic index for hydrological fluxes. In other word, the vegetation input map together with their parameters reflected in energy fluxes clearly whereas topographic index map derived from DEM strongly affected hydrological fluxes such as spatial distribution of soil moisture. However, validation of spatially distributed simulated energy and water fluxes is not possible due to non availability of distributed measured fluxes. Thus only the discharge hydrograph at the catchment outlet can be used for validation purpose.

Application of TOPLATS hydrological model to the spatial datasets together with vegetation and soil parameters produced discharge and results were found acceptable for simulation of discharge of the Kherlen river as shown in Fig. 73. Fig. 73 (a) shows the comparison of simulated and measured discharge using spatial average precipitation based on Thiessen polygon method (Fig. 74). However, the comparison was not very good with $r=0.61$ and $RMSE=10.23 \text{ m}^3 \text{ s}^{-1}$ because spatial average precipitation gives large amount of precipitation at lower part of Kherlen river basin that resulted larger discharge value. This also suggests the need to use spatial distribution of precipitation to simulate discharge, because of inconsistent relation between precipitation and discharge at larger watershed area. Thus, distribution of precipitation was also determined based on Kriging interpolation method with 1 km resolution based on 4 AWSs and 2 flux stations data. Although seasonality of simulated discharge is acceptable, individual peaks of the reproduced hydrograph did not correspond well. The main reasons for the individual peaks discrepancy can be explained by (1) the coarse spatial and temporal resolution of precipitation data. The poor coverage with rainfall gauges in large study area makes an appropriate regional estimation of precipitation difficult, since only 6 station data were used to spatial distribution: density of rain gauge network is approximately equal to 0.00015 km^{-2} . (2) The insufficient availability of information on soil hydrological parameters since many different soil types lies in the larger watershed. (3) The difficulty to calibrate a spatial distributed process based hydrological model in a reasonable way. Even if a limited number of model parameters could be selected for calibration, it is not feasible to calibrate them for all of 104,232 simulation grids in our study area. However, the total amount of simulated discharge was very close to observed one in 2004 with $r=0.91$ and $RMSE=2.21 \text{ m}^3 \text{ s}^{-1}$, whereas $r=0.90$ and $RMSE=5.67 \text{ m}^3 \text{ s}^{-1}$ for 2005. The correlation coefficients further confirm that the model simulates the base flow adequately, although the RMSE of the results indicate that individual peaks can be over or underestimated. This simulation has verified the results of earlier studies of Bormann and Diekkruger (2003) for subhumid region in West Africa, Bormann (2006) in mountainous region in Germany, Endreny et al. (2000) for semi-humid region in America, and Pauwels and Gabrielle (2006) for Zwalm catchment in Belgium. They all found very good seasonality of simulated discharge, but individual peaks of observed discharge did not well represented. Again, this is one of difficulties to derive realistic and physically sound parameter sets of any environmental modeling system. Furthermore, one has to keep in mind that a calibration of model parameters also implies a calibration of all errors occurring e.g. errors in input data. Overall performance of TOPLAST hydrological model shows that it can work with century ecosystem model for future projection of ecohydrological components in the study area.

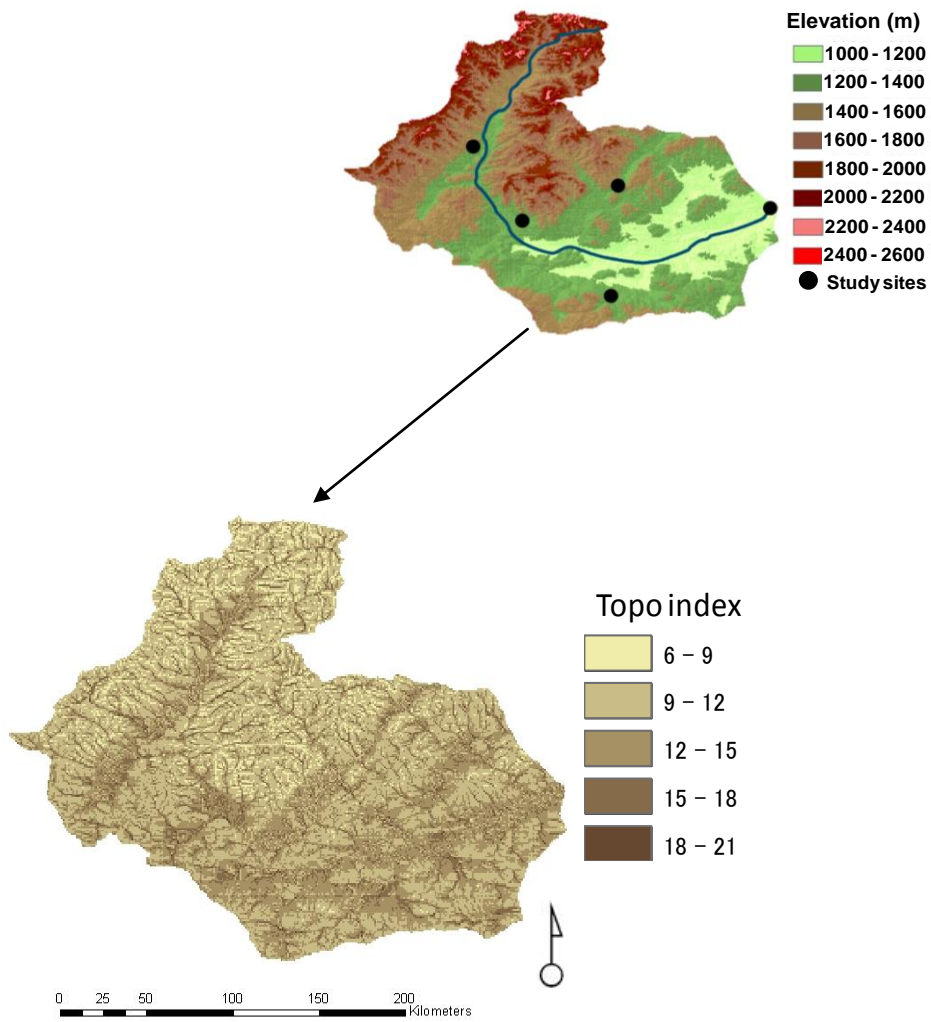


Fig. 66 Upper Kherlen river basin map of topographic index calculated from (a) ASTER GDEM data.

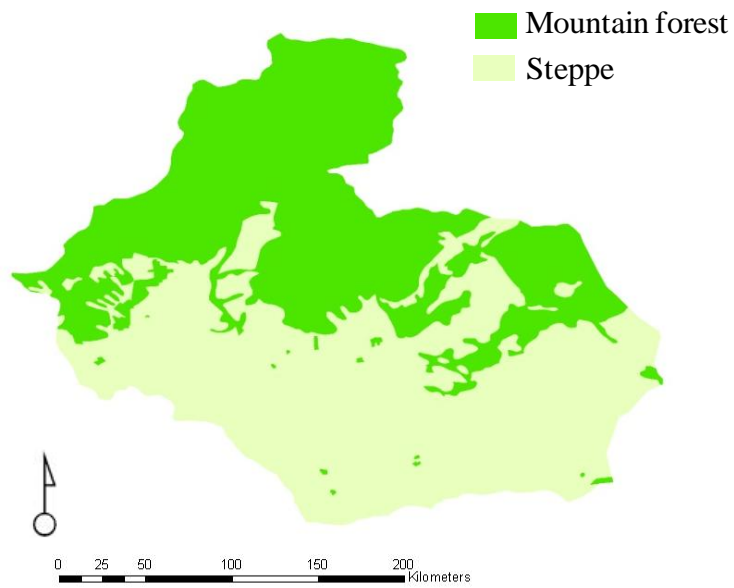


Fig. 67 Upper Kherlen river basin map of vegetation, derived from Mongolian digital atlas (Saandar and Sugita, 2004).

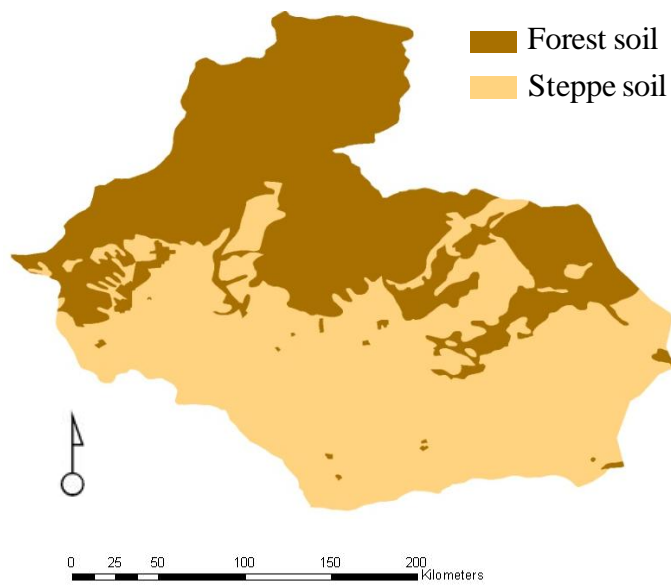


Fig. 68 Upper Kherlen river basin map of soil, derived from Mongolian digital atlas (Saandar and Sugita, 2004).

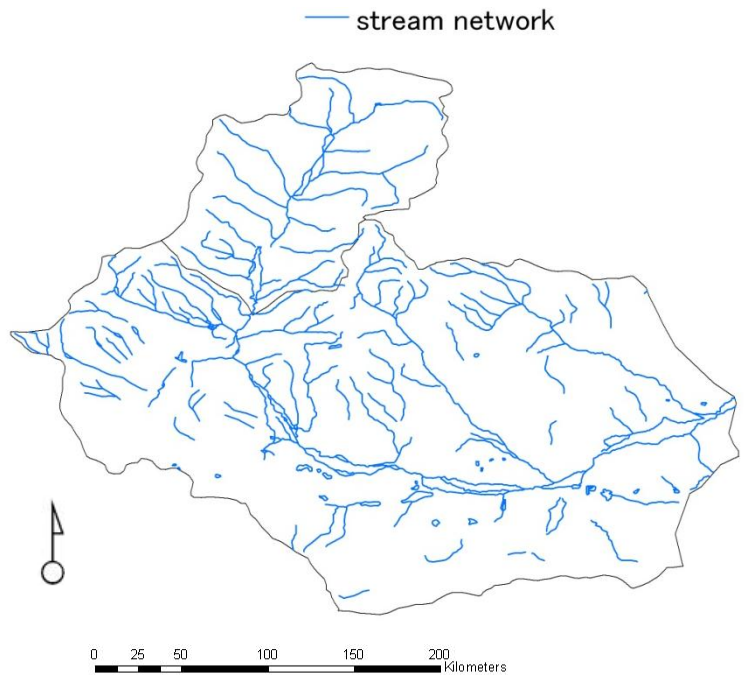


Fig. 69 Stream network of the upper part of Kherlen river basin which was determined based on IMH of river network data.

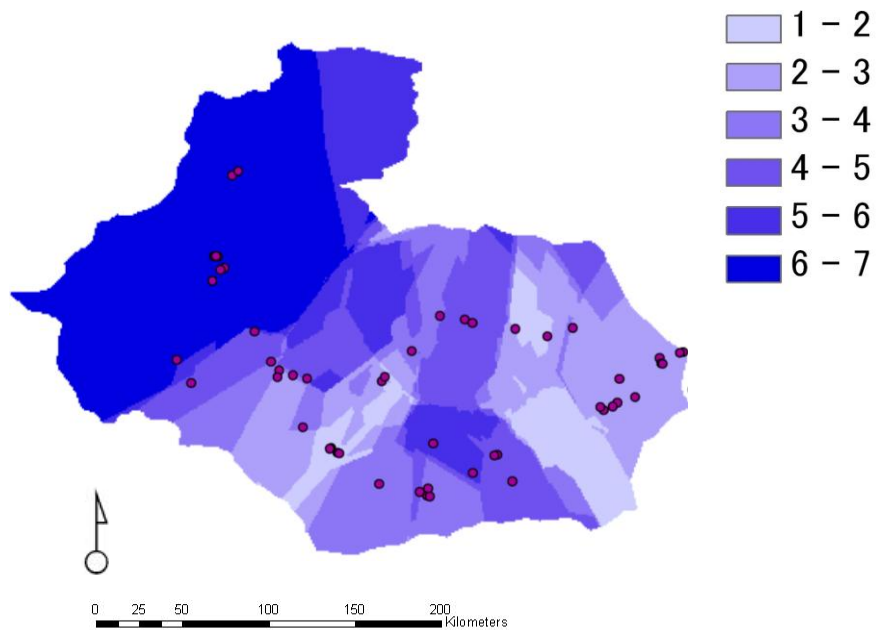


Fig. 70 Water table of the upper part of Kherlen river basin based on groundwater measurements (Red circles) in the Kherlen river basin. (Unit is m)

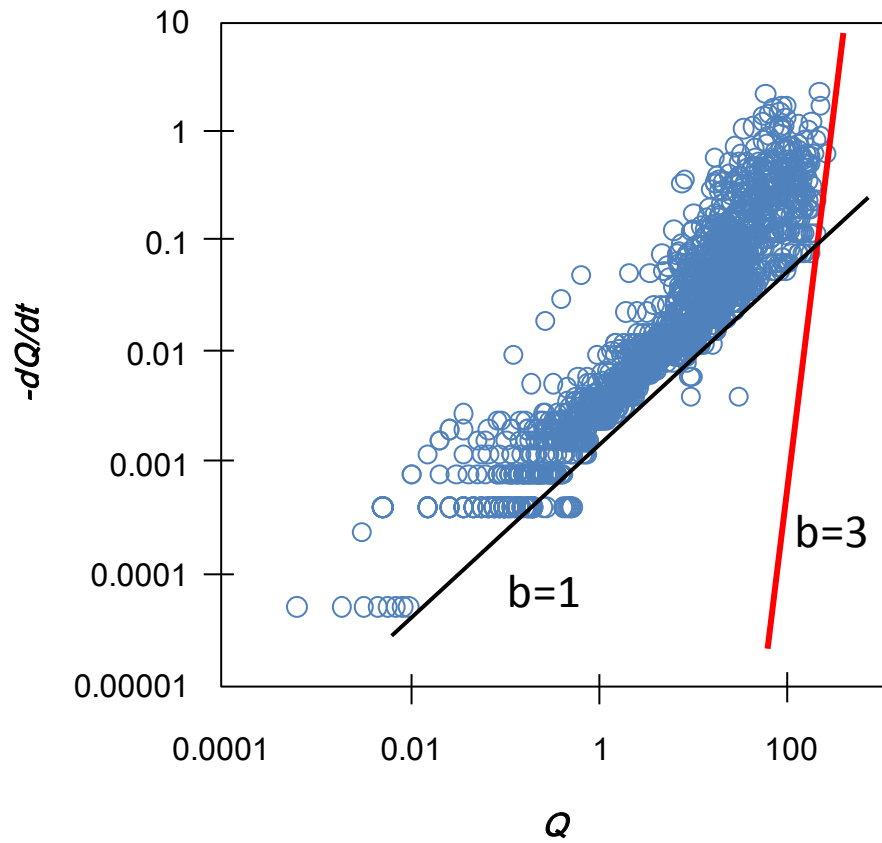


Fig. 71 Data points dQ/dt plotted against Q observed during 1959-2005 of upper part of Kherlen river basin, with lower envelope lines with slopes 1 and 3, respectively.

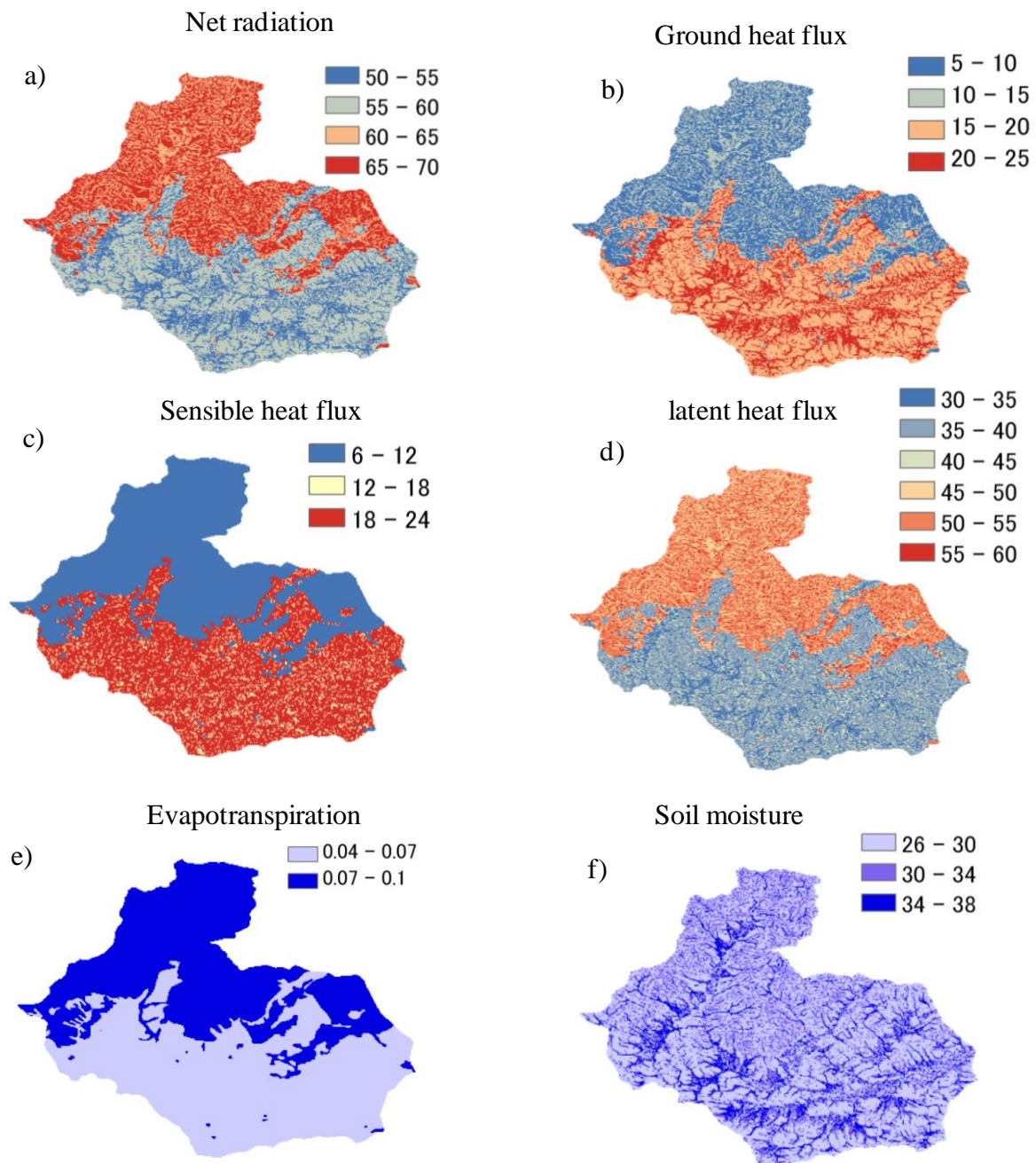
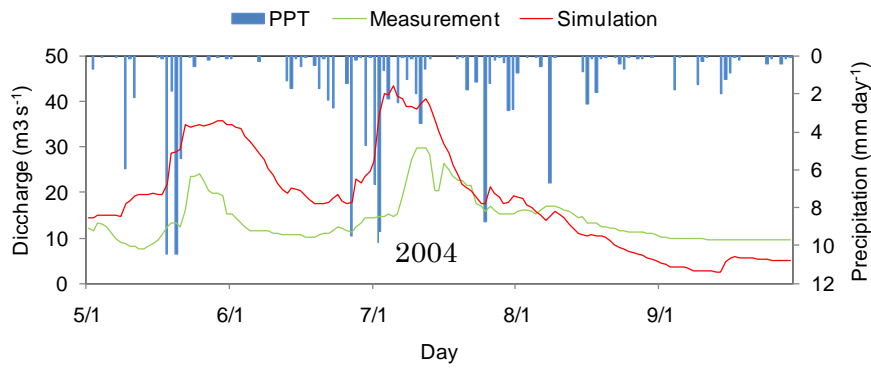
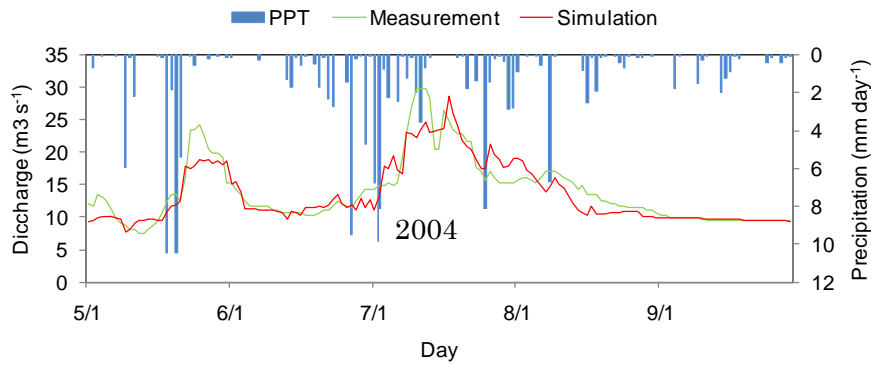


Fig. 72 Spatial distribution of model-simulated average daily average energy and hydrological fluxes. (2005/04/01). (Unit $W m^{-2}$ and $mm h^{-1}$)

a)



b)



c)

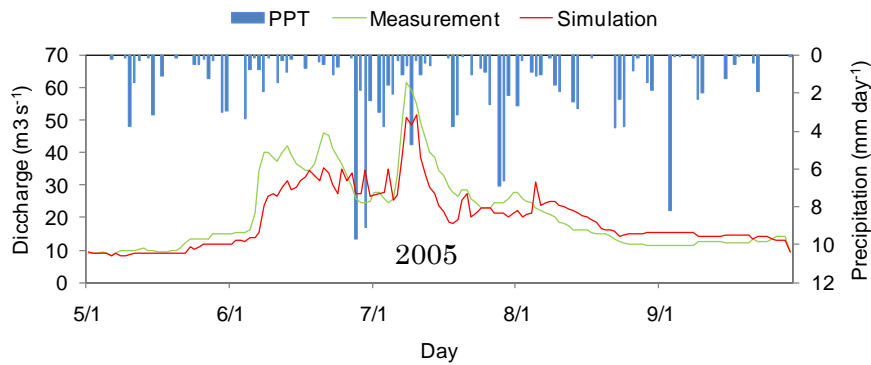


Fig. 73 Comparison of modeled and measured discharge at UDN discharge station in upper part of Kherlen river watershed. The panel (a) shows comparison of discharge of 2004 (Precipitation: Thiessen method), panel (b) for 2004 (Precipitation: Spatial forcing) and panel (c) for 2005 (Precipitation: Spatial forcing).

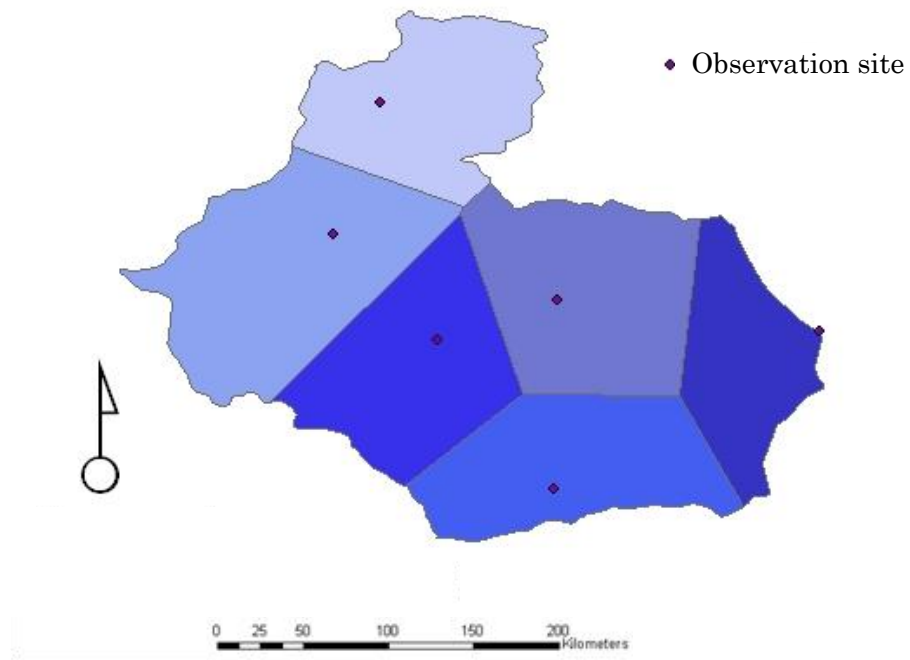


Fig. 74 Thiessen polygon determined for each rain gauge at observation sites

3.5 Future projection of ecohydrology under environmental changes

As addressed in the introduction, main interest in studying ecohydrological response of ranges from basic understanding of ecohydrological processes to its prediction under global warming and grazing pressure changes. We used models for each purpose to see how well we can simulate measured responses (i.e. to test how well our conceptual understanding and its manifestation via model reproduces reality) and to predict what might happen in the future. These models are the results of our understanding of natural complex system observations of the system. Even if we were able to measure every aspect of the carbon-hydrological-energy cycles that occurs in an interested area of study, we would still have an image only of what is happening under current conditions and could not determine what would occur under changed conditions in the future without some sort of extrapolation. In order to make a sense out of our observations or to extrapolate beyond what we actually observed, we need to make use of our basic understanding of physical systems and a convenient way to do that is with models.

Therefore, an integrated environmental modeling approach was adopted dealing with future projection of ecohydrological processes in this region. To shed some light on these remaining issues in this region, particularly on the influence of global warming and grazing pressure changes to the ecohydrological study, first, century ecosystem model and TOPLATS hydrological model were employed in the study area to simulate ecohydrological components and validated them using observational data. Second, an attempt was made to use one-way data transfer methodology for coupling those environmental models to simulate and validate ecohydrological components at point scale as well as spatial scale. Then finally, in this section outputs of the regional climate model were applied together with this coupled environmental modeling approach to make future projection of ecohydrological processes.

As stated in the method section, the outputs of TERC-RAMS were used as present climate condition and future global warming scenario. Different grazing scenarios will also be used for future projection of ecohydrological components. In this way, the study of ecohydrological processes under the influence of global warming and grazing pressure change can be studied in a consistent manner. The future projections were done between 2070 and 2080. Base runs were done in present period from 1994 to 2004. The future projection of ecohydrological components and their processes in our study area were performed based on one global warming scenario (GW), four different grazing pressure change scenarios (GP1-GP4) and combination of the two (GWP1-GWP2) as shown in Table 24. All future projections were

compared with the base line scenario (B).

Note that, grazing pressure was increased by 3% - 94% in Kherlen river basin during last two decades (Sugita et al., 2007). Before 1990, grazing pressure remained about same in this area as shown in Fig. 6 (after, Sugita et al., 2007). This was reflected in different grazing pressure scenarios that help to separate evaluation of global warming and grazing pressure effects on ecohydrological components in the study area. Statistical variables (i.e. mean, standard deviation and coefficient of variation) were used to explain comprehensive comparison and assessment of the possible impact of global warming and grazing pressure change on regional ecohydrological processes.

Table 23 Future scenarios

| Category | Scenario | Abbreviation of scenario |
|----------|--|--------------------------|
| 0 | Baseline | |
| | Present climate with current grazing pressure | B |
| 1 | Climate change only | |
| | Global warming with current grazing pressure | GW |
| 2 | Grazing pressure changes only | |
| | Present climate + Grazing pressure increase (50%) | GP1 |
| | Present climate + Grazing pressure increase (100%) | GP2 |
| | Present climate + Grazing pressure decrease (50%) | GP3 |
| | Present climate + Grazing pressure decrease (nongrazing) | GP4 |
| 3 | Climate change + grazing pressure changes | |
| | Global warming + Grazing pressure increase (50%) | GWP1 |
| | Global warming + Grazing pressure increase (100%) | GWP2 |
| | Global warming + Grazing pressure decrease (50%) | GWP3 |
| | Global warming + Grazing pressure decrease (nongrazing) | GWP4 |

Over Kherlen river basin, annual mean precipitation ranges from 190 mm y^{-1} to 310 mm y^{-1} in current condition as shown in Fig. 75a) whereas it decreased by 10% in future condition in Fig. 75c). Geographically, annual mean precipitation decreases gradually from northwest (forest area) to southeast (grassland area) in both of current and future condition, according to elevation changes. A closer look at the difference of current and future precipitation distribution in Fig. 75e), reveals that precipitation distribution decreased from 15 to 20 mm y^{-1} around upper to middle of the Kherlen river basin, but it was increased by 5 to 10 mm y^{-1} in lower part in the Kherlen river basin. Figs. 75c) and 75f) show that larger change in grassland area than that of forest area.

Upper part of Kherlen river basin has lower value of mean air temperature both at present (Fig. 76a) and future condition (Fig. 76d), because of higher elevation. The difference of air temperature between present and future condition shows that air temperature increased by about 5°C throughout Kherlen river basin.

Ideally the simulation under the global warming scenario should be made with increased level of CO₂ under A2 scenario from which future climate projection was obtained. However, as shown in Fig. 77, the change of aboveground biomass due to CO₂ level increase from 350 ppm to 700 ppm (the maximum level allowed to in century ecosystem model) is small. Thus, it was decided to keep current level of CO₂ even for global warming scenario in what follows.

Fig. 78a) shows spatially estimated aboveground biomass under B scenario in present condition. The estimated aboveground biomass ranged from 4 to 8 g C m⁻² in forest area, whereas it was between 2 and 4 g C m⁻² in grassland area. Aboveground biomass was decreased under GW scenario from B scenario as shown in Fig. 78d). Under GW scenario, simulated aboveground biomass was decreased from B scenario by about 2 to 2.5 g C m⁻² in middle of the Kherlen river basin (Fig. 78g). In the forest area, aboveground biomass was decreased by 0.5 to 2 g C m⁻², whereas it was decreased by 0.5 to 2.5 g C m⁻² in grassland area. However, aboveground biomass was increased by 0.5 to 1.4 g C m⁻² in the grassland area (Fig. 78g), where precipitation was increased in the future condition (Fig. 75g). The difference of coefficient of variation of GW scenario and B scenario shows larger change in grassland site than forest site in Fig. 78i).

Under GP1 scenario (Fig. 79g), simulated aboveground biomass was decreased by 1.5 to 2.5 g C m⁻² in forest area. In grassland area it decreased also by 0.5 to 1 g C m⁻². Fig. 80g) shows simulated aboveground biomass under GP2 scenario and it was decreased by about 2 to 2.5 g C m⁻² over the Kherlen river basin. Under GP3 scenario (Fig. 81g), simulated aboveground

biomass was increased by 1 to 1.4 g C m⁻² over the Kherlen river basin, whereas it increased by 1.4 g C m⁻² over the Kherlen river basin under GP4 scenario (Fig 82).

Simulated aboveground biomass under GWP1 scenario and GWP2 scenario was decreased by about 2 to 2.5 g C m⁻² over the Kherlen river basin as shown in Figs. 83g) and 84g), whereas it was increased by 1 to 1.4 g C m⁻² over the Kherlen river basin under GWP3 and GWP4 scenarios (Figs. 85g and 86g). Geographically, simulated annual mean aboveground biomass decreased from west-north to south-east under all scenarios over Kherlen river basin.

Figs. 87a) and 87d) show simulated belowground biomass under B scenario and GW scenario. Spatial distribution of simulated belowground biomass ranged from 120 to 140 g C m⁻² in forest area, whereas it was between 100 and 120 g C m⁻² in grassland area. Fig. 87d), simulated belowground biomass was decreased under GW scenario from 30 g C m⁻² in forest area under GW scenario, whereas it was also decreased by 10 g C m⁻² at grassland area. Fig. 87g) shows the difference of simulated belowground biomass of GW scenario and B scenario and belowground biomass was reduced from 10 to 25 g C m⁻² in forest area, whereas in grassland area, simulated belowground biomass decreased by 5 to 20 g C m⁻². Figs. 88g), 89g), 90g and 91g)) show that simulated belowground biomass was increased by 0 to 5 g C m⁻² under GP1, GP2 GP3 and GP4 scenarios. Under GWP1 and GWP2 scenarios, simulated belowground biomass was decreased by 20 to 25 g C m⁻² in forest area, whereas it decreased by 5 to 20 g C m⁻² in grassland area (Fig. 92g) and 93g). Figs. 94g) and 95g) show belowground biomass was reduced from 10 to 25 g C m⁻² in forest area and it was decreased by 5 to 20 g C m⁻² under GWP3 and GWP4 scenarios.

Once simulation under all scenarios had been done, simulated aboveground biomass of each run was converted into LAI by Eq. (7). Also roughness lengths of heat and momentum were calculated from those LAI values by means of Eqs. (5)-(6). Then all vegetation parameters were inserted in loop-up table of TOPLATS hydrological model that were used for current and future projection of fluxes data.

Figs. 96a) and 96d) show simulated evapotranspiration under B and GW scenarios. Spatial distribution of simulated evapotranspiration under B scenario ranged between 150 and 170 mm y⁻¹ in forest area whereas it ranged from 120 to 140 mm y⁻¹ in grassland area. Evapotranspiration was decreased by 30 to 50 mm y⁻¹ in forest area whereas it was increased 10 to 30 mm y⁻¹ in grassland area in Fig. 96g). Under GP1 scenario, evapotranspiration was decreased by 0 -10 mm y⁻¹ in forest area whereas it was decreased 10 to 30 mm y⁻¹ in grassland area (Fig. 97g). Under GP2 scenario, evapotranspiration was decreased by 0 -10 mm y⁻¹ in forest area whereas it was decreased 30 to 50 mm y⁻¹ in grassland area (Fig. 98g). Under GP3 and GP4

scenarios, evapotranspiration was increased by 10 to 30 mm y⁻¹ in forest area whereas it was increased 30 to 50 mm y⁻¹ in grassland area (Figs. 99g) and 100g)). Figs. 101g) and 102g) show that evapotranspiration was decreased by 30 to 50 mm y⁻¹ in forest area whereas it was decreased 10 to 30 mm y⁻¹ in grassland area under GWP1 and GWP2 scenarios. As shown in Fig. 103g) and 104g), evapotranspiration was decreased by 10 to 30 mm y⁻¹ in forest area whereas it was increased 30 to 50 mm y⁻¹ in grassland area under GWP3 and GWP4 scenarios.

Spatial distribution of simulated soil moisture was ranged from 26 and 40 % over the Kherlen river basin as shown in Figs. 105 -113 under all scenarios.

We investigated the difference of precipitation and evapotranspiration of each scenario in order to determine the water consumption. Figs. 114a), 114b), 114c), 114d) and 114e) show the difference of annual mean precipitation of present condition and evapotranspiration under B, GP1, GP2, GP3 and GP4 scenarios. Under B scenario, infiltration ranged from 80 to 120 mm y⁻¹ whereas 120 – 160 mm y⁻¹ for GP1 scenario, 120 – 160 mm y⁻¹ for GP2 scenario, 40 – 140 mm y⁻¹ for GP1 scenario and 38 – 130 mm y⁻¹ for GP4 scenario. Figs. 114f), 114g), 114h), 114k) and 114l) show the difference of annual mean precipitation at different future conditions and evapotranspiration under GW, GWP1, GWP2, GWP3 and GWP4 scenarios. Spatial distribution of infiltration rate ranged from 40 - 160 mm y⁻¹ under GW scenario. Under GWP1 and GWP2 scenarios, infiltration rate ranged between 120 and 160 mm y⁻¹ whereas 40 – 160 mm y⁻¹ for GWP3 and GWP4 scenarios.

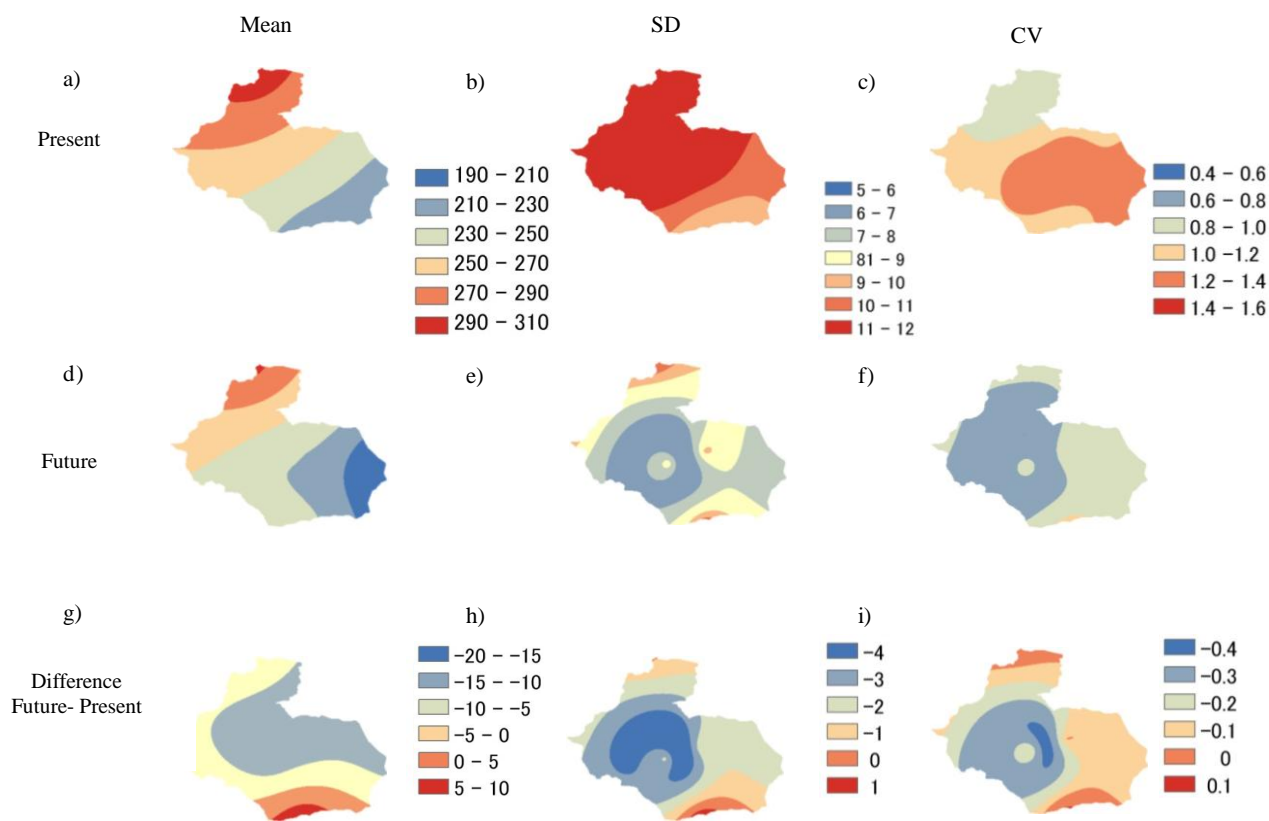


Fig. 75 Annual mean, standard deviation (SD) and coefficient of variation (CV) of precipitation in current and future condition. The panels a), b) and c) represent mean, SD and CV of precipitation in current condition. The panels d), e) and f) represent mean, SD and CV of precipitation in future condition. The panels g), e) and i) represent the difference mean, SD and CV of precipitation between future and current condition.

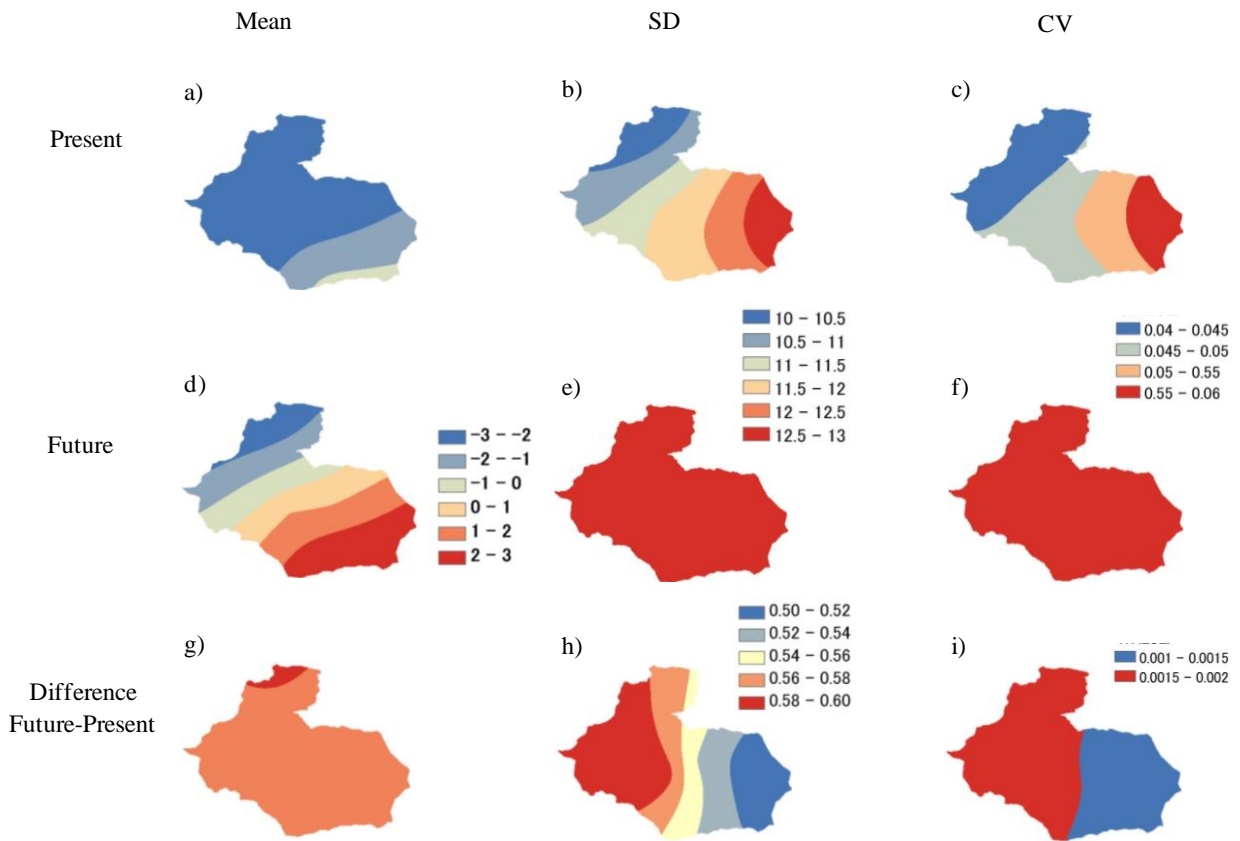


Fig. 76 Annual mean, standard deviation (SD) and coefficient of variation (CV) of air temperature in current and future condition. The panels a), b) and c) represent mean, SD and CV of air temperature in current condition. The panels d), e) and f) represent mean, SD and CV of air temperature in future condition. The panels g), h) and i) represent the difference mean, SD and CV of air temperature between future and current condition.

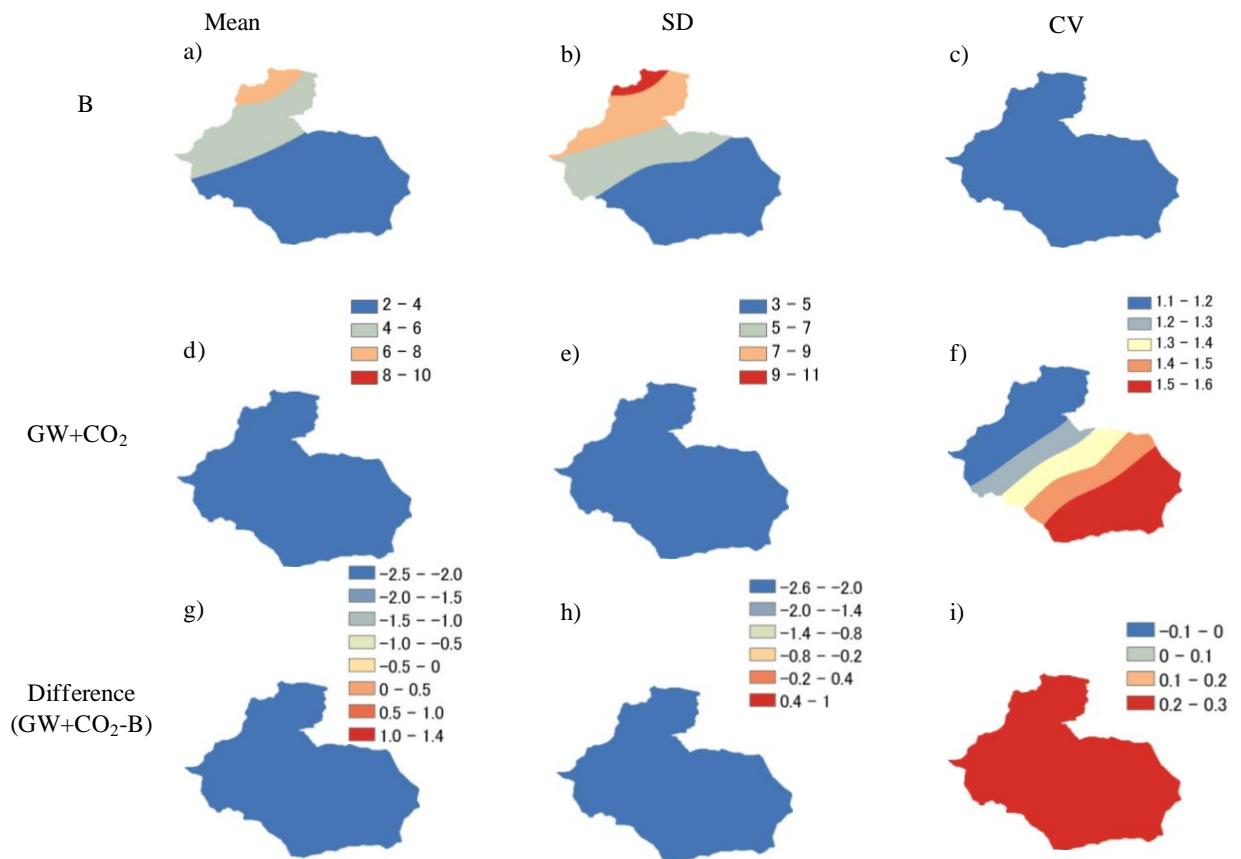


Fig. 77 Annual mean, standard deviation (SD) and coefficient of variation (CV) of aboveground biomass (*AB*) under B and GW scenarios + CO₂. The panels a), b) and c) represent mean, SD and CV of *AB* in B scenario. The panels d), e) and f) represent mean, SD and CV of *AB* under GW+CO₂ scenario. The panels g), h) and i) represent the difference of mean, SD and CV of *AB* between GW+ CO₂ and B scenarios. (Unit is g C m⁻²)

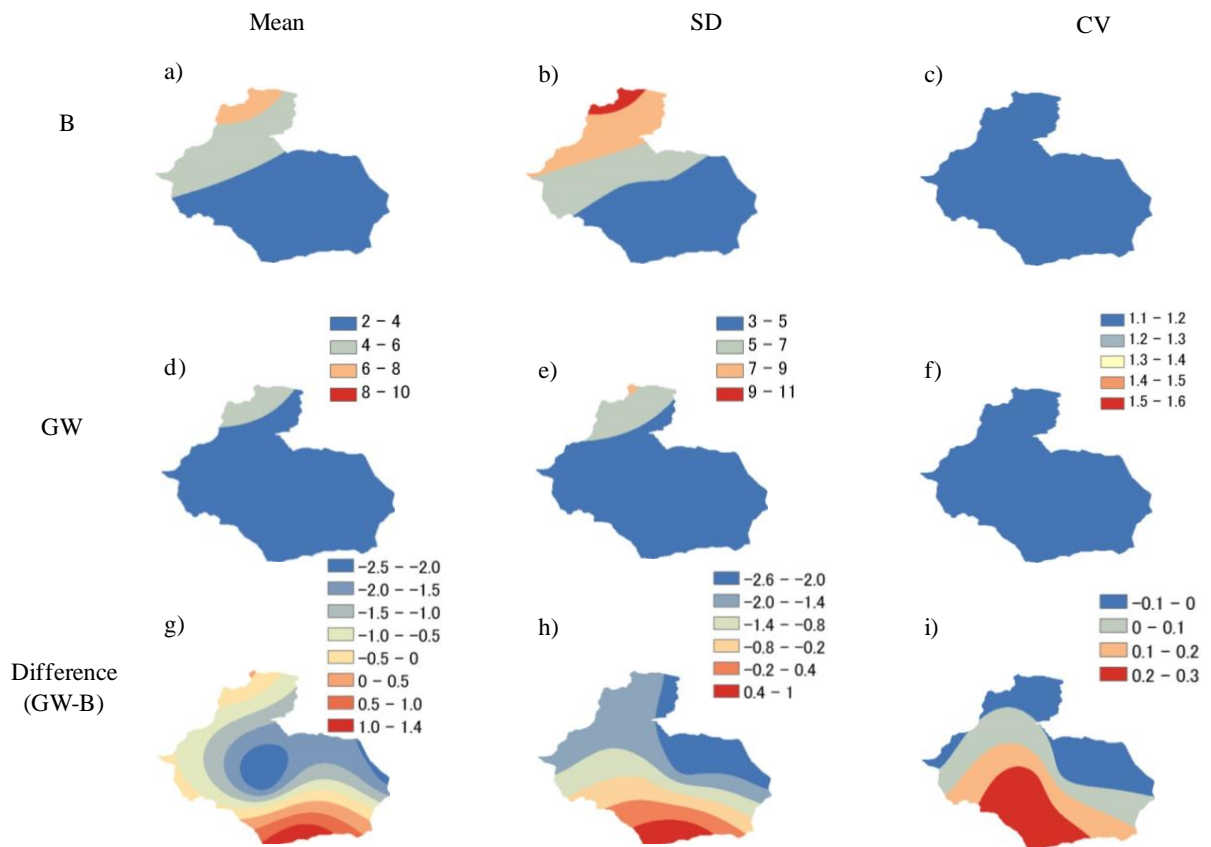


Fig. 78 Annual mean, standard deviation (SD) and coefficient of variation (CV) of aboveground biomass (*AB*) under B and GW scenarios. The panels a), b) and c) represent mean, SD and CV of *AB* in B scenario. The panels d), e) and f) represent mean, SD and CV of *AB* under GW scenario. The panels g), h) and i) represent the difference of mean, SD and CV of *AB* between GW and B scenarios. (Unit is g C m^{-2})

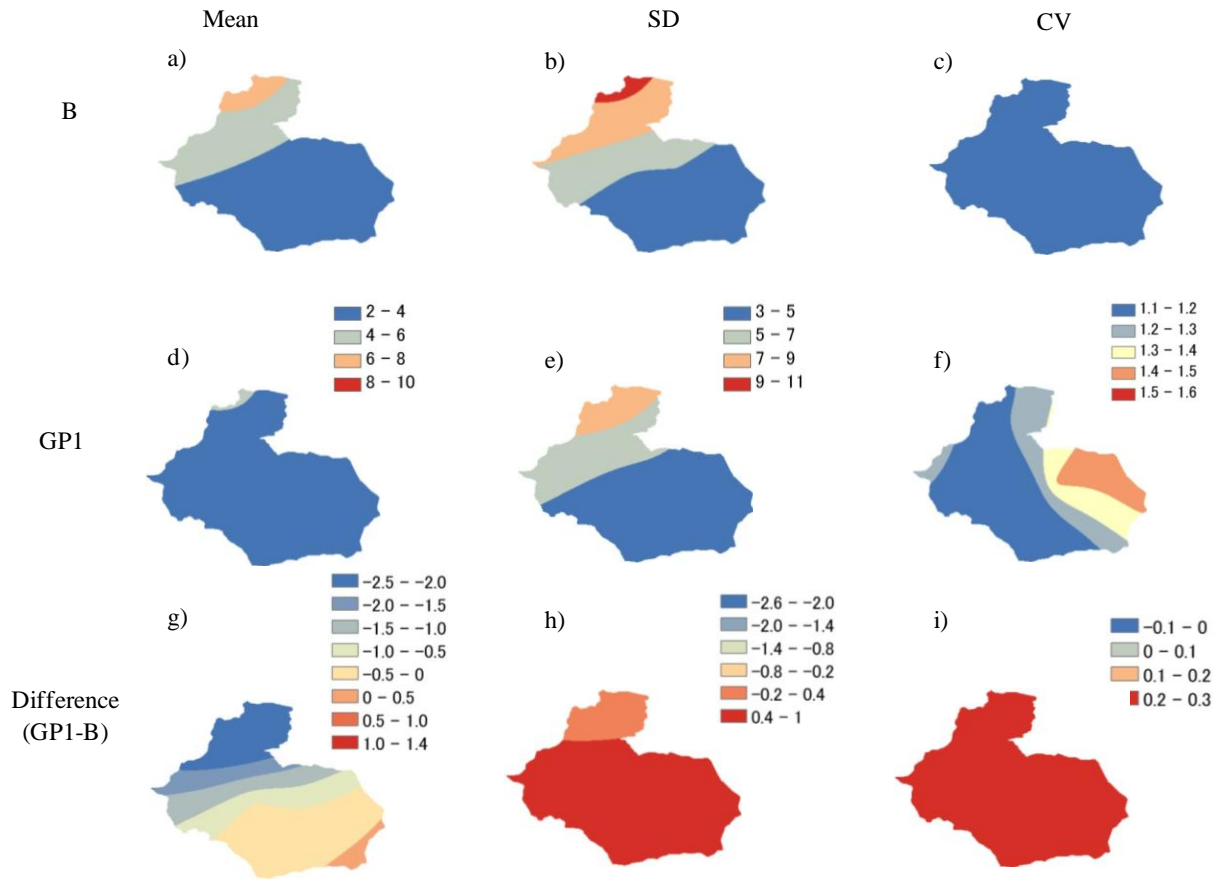


Fig. 79 Annual mean, standard deviation (SD) and coefficient of variation (CV) of aboveground biomass (*AB*) under B and GP1 scenarios. The panels a), b) and c) represent mean, SD and CV of *AB* in B scenario. The panels d), e) and f) represent mean, SD and CV of *AB* under GP1 scenario. The panels g), h) and i) represent the difference of mean, SD and CV of *AB* between GP1 and B scenarios. (Unit is $g C m^{-2}$)

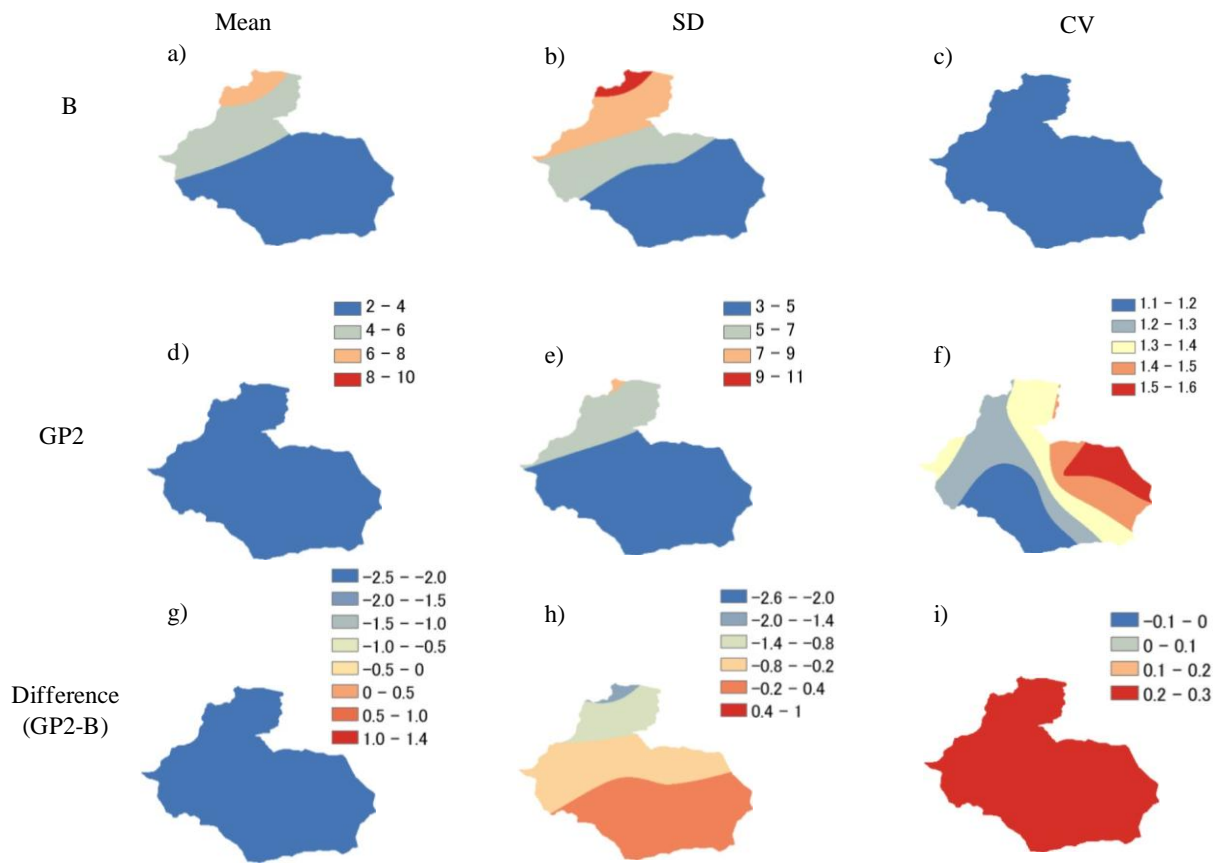


Fig. 80 Annual mean, standard deviation (SD) and coefficient of variation (CV) of aboveground biomass (*AB*) under B and GP2 scenarios. The panels a), b) and c) represent mean, SD and CV of *AB* in B scenario. The panels d), e) and f) represent mean, SD and CV of *AB* under GP2 scenario. The panels g), h) and i) represent the difference of mean, SD and CV of *AB* between GP2 and B scenarios. (Unit is g C m^{-2})

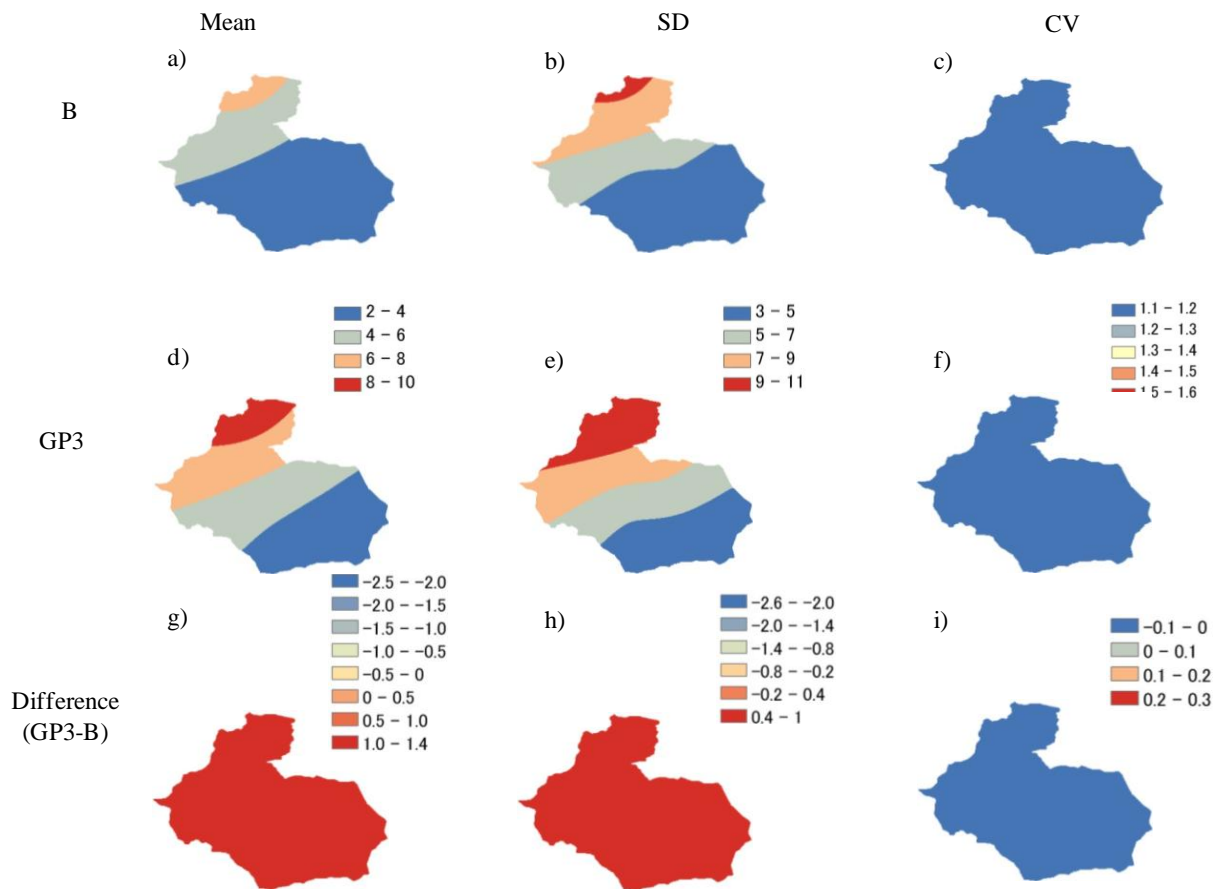


Fig. 81 Annual mean, standard deviation (SD) and coefficient of variation (CV) of aboveground biomass (*AB*) under B and GP3 scenarios. The panels a), b) and c) represent mean, SD and CV of *AB* in B scenario. The panels d), e) and f) represent mean, SD and CV of *AB* under GP3 scenario. The panels g), h) and i) represent the difference of mean, SD and CV of *AB* between GP3 and B scenarios. (Unit is $g C m^{-2}$)

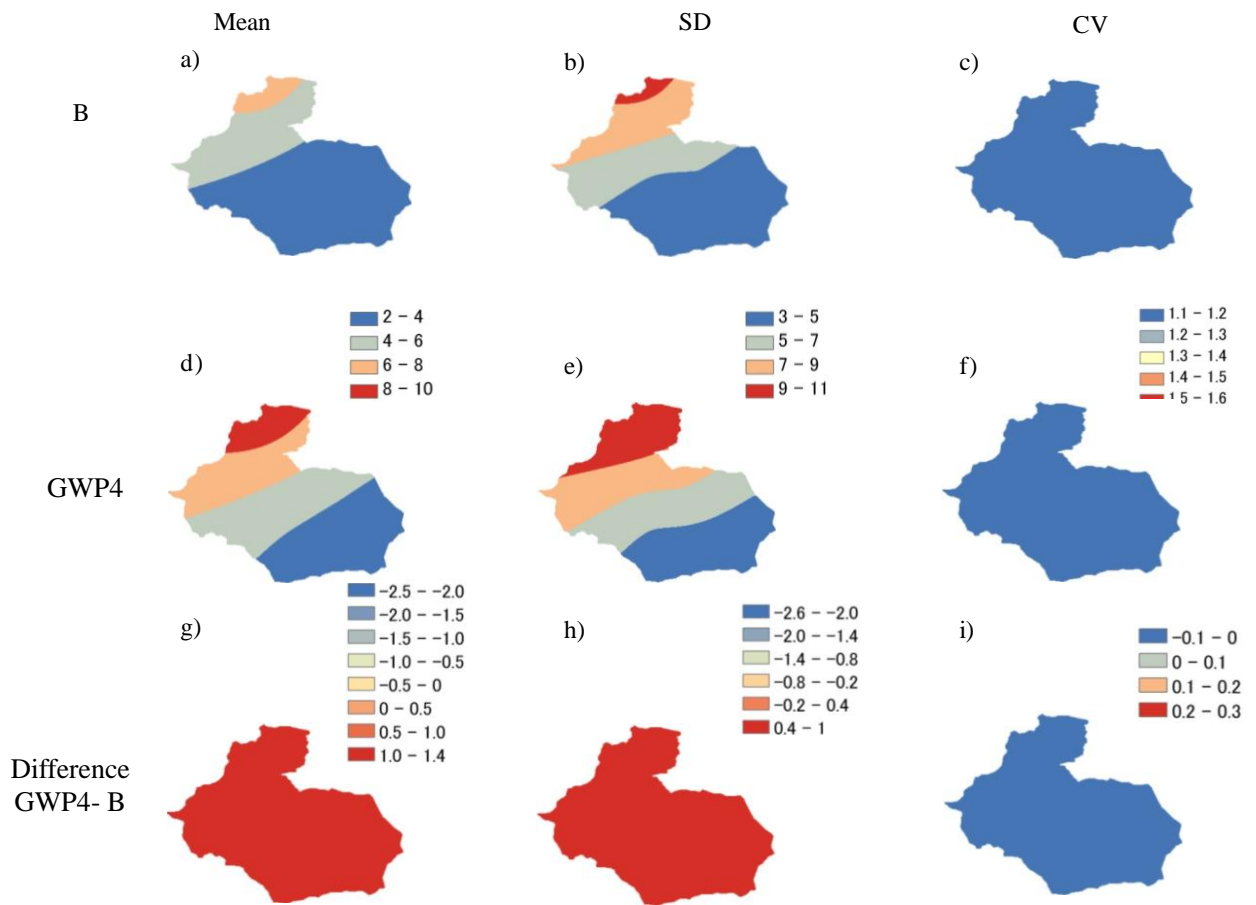


Fig. 82 Annual mean, standard deviation (SD) and coefficient of variation (CV) of aboveground biomass (*AB*) under B and GP4 scenarios. The panels a), b) and c) represent mean, SD and CV of *AB* in B scenario. The panels d), e) and f) represent mean, SD and CV of *AB* under GP4 scenario. The panels g), h) and i) represent the difference of mean, SD and CV of *AB* between GP4 and B scenarios. (Unit is g C m^{-2})

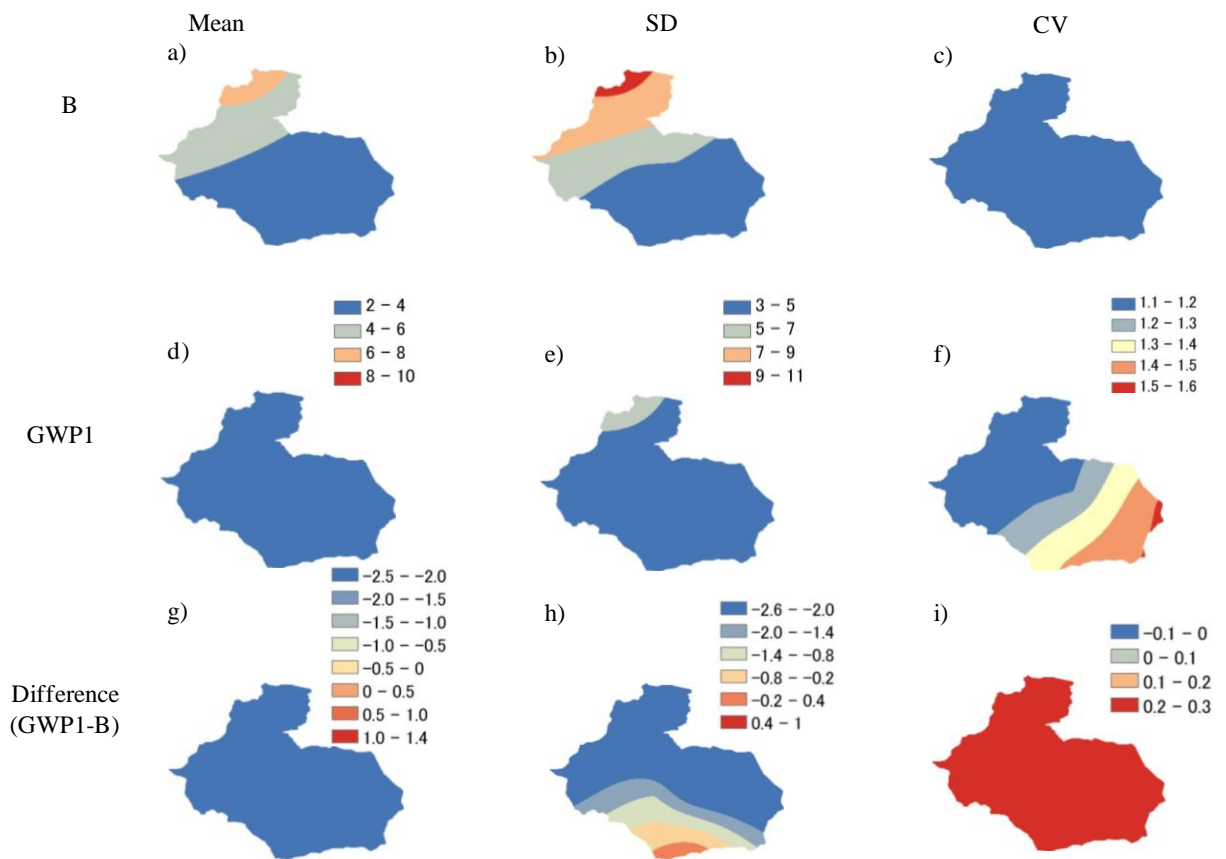


Fig. 83 Annual mean, standard deviation (SD) and coefficient of variation (CV) of aboveground biomass (*AB*) under B and GWP1 scenarios. The panels a), b) and c) represent mean, SD and CV of *AB* in B scenario. The panels d), e) and f) represent mean, SD and CV of *AB* under GWP1 scenario. The panels g), h) and i) represent the difference of mean, SD and CV of *AB* between GWP1 and B scenarios. (Unit is $g\ C\ m^{-2}$)

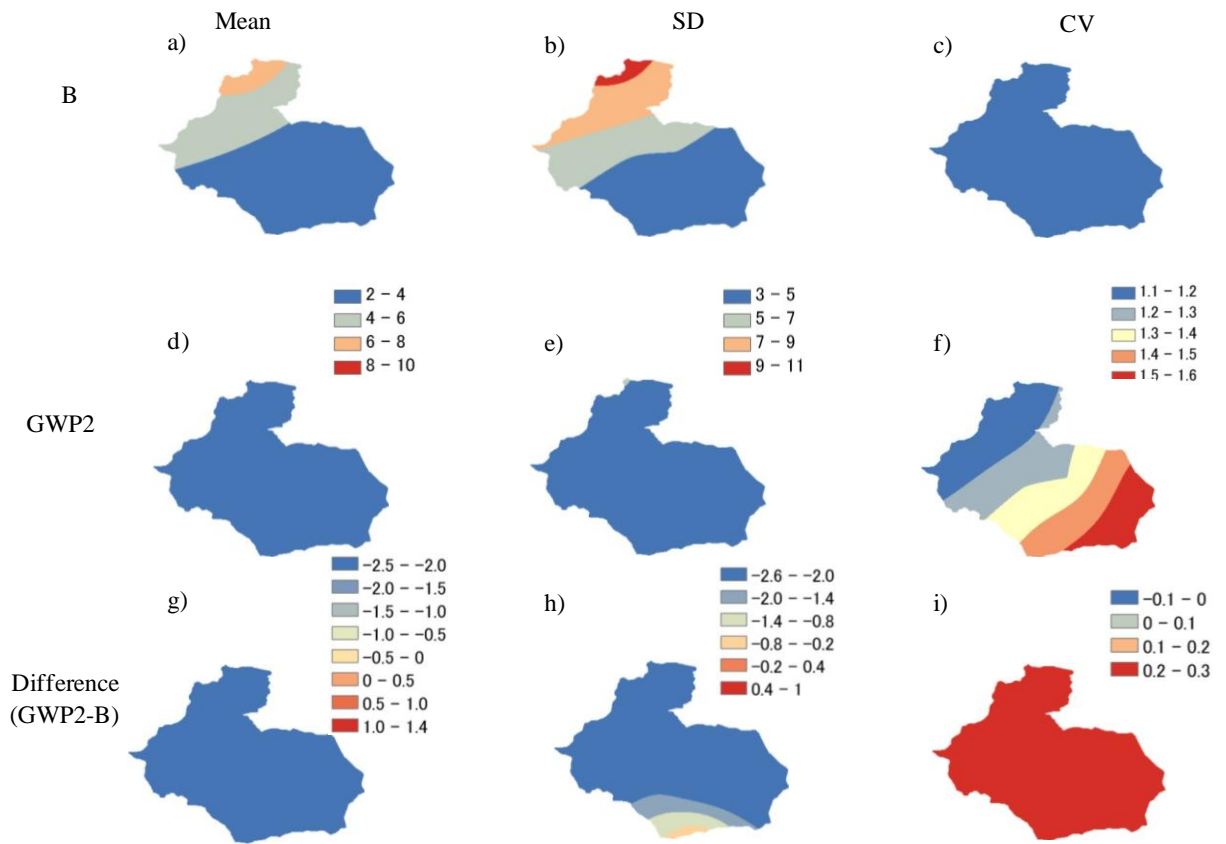


Fig. 84 Annual mean, standard deviation (SD) and coefficient of variation (CV) of aboveground biomass (*AB*) under B and GWP2 scenarios. The panels a), b) and c) represent mean, SD and CV of *AB* in B scenario. The panels d), e) and f) represent mean, SD and CV of *AB* under GWP2 scenario. The panels g), h) and i) represent the difference of mean, SD and CV of *AB* between GWP2 and B scenarios. (Unit is $g\ C\ m^{-2}$)

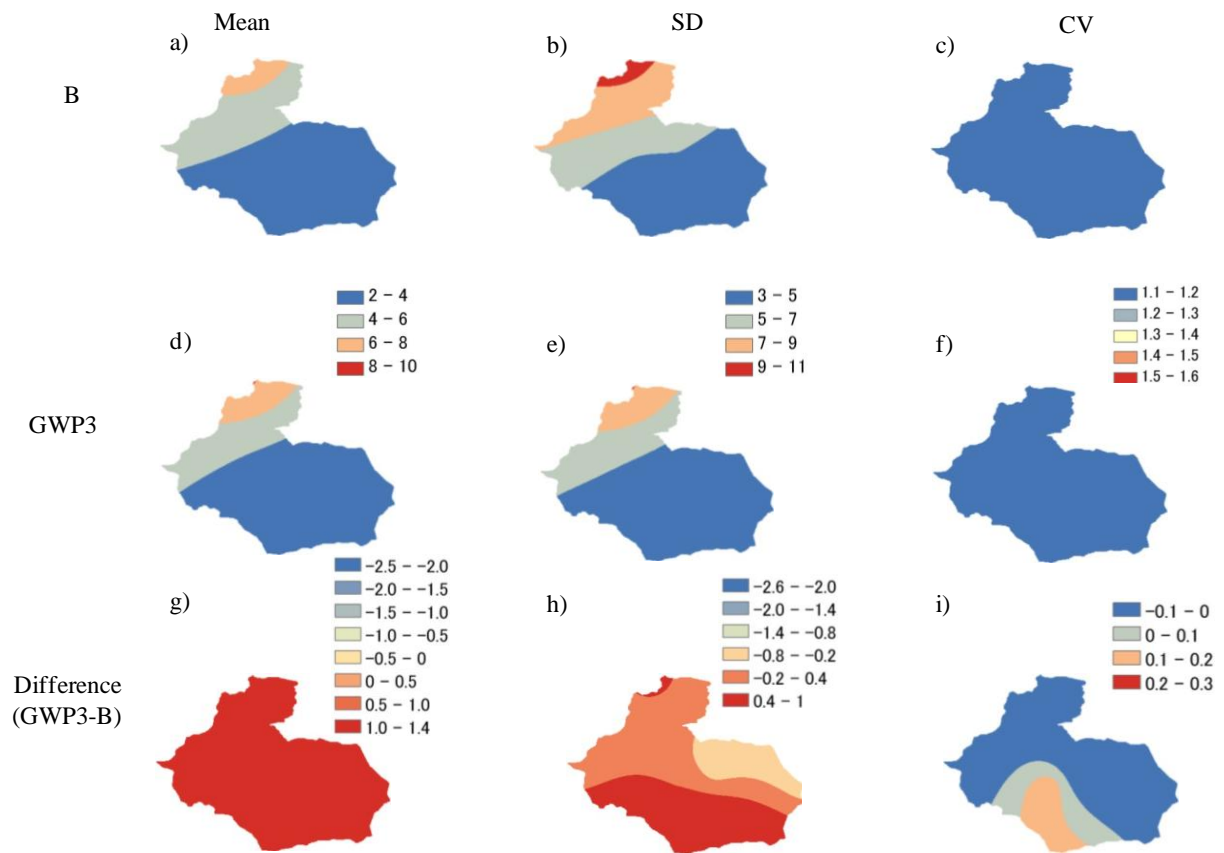


Fig. 85 Annual mean, standard deviation (SD) and coefficient of variation (CV) of aboveground biomass (*AB*) under B and GWP3 scenarios. The panels a), b) and c) represent mean, SD and CV of *AB* in B scenario. The panels d), e) and f) represent mean, SD and CV of *AB* under GWP3 scenario. The panels g), h) and i) represent the difference of mean, SD and CV of *AB* between GWP3 and B scenarios. (Unit is $g C m^{-2}$)

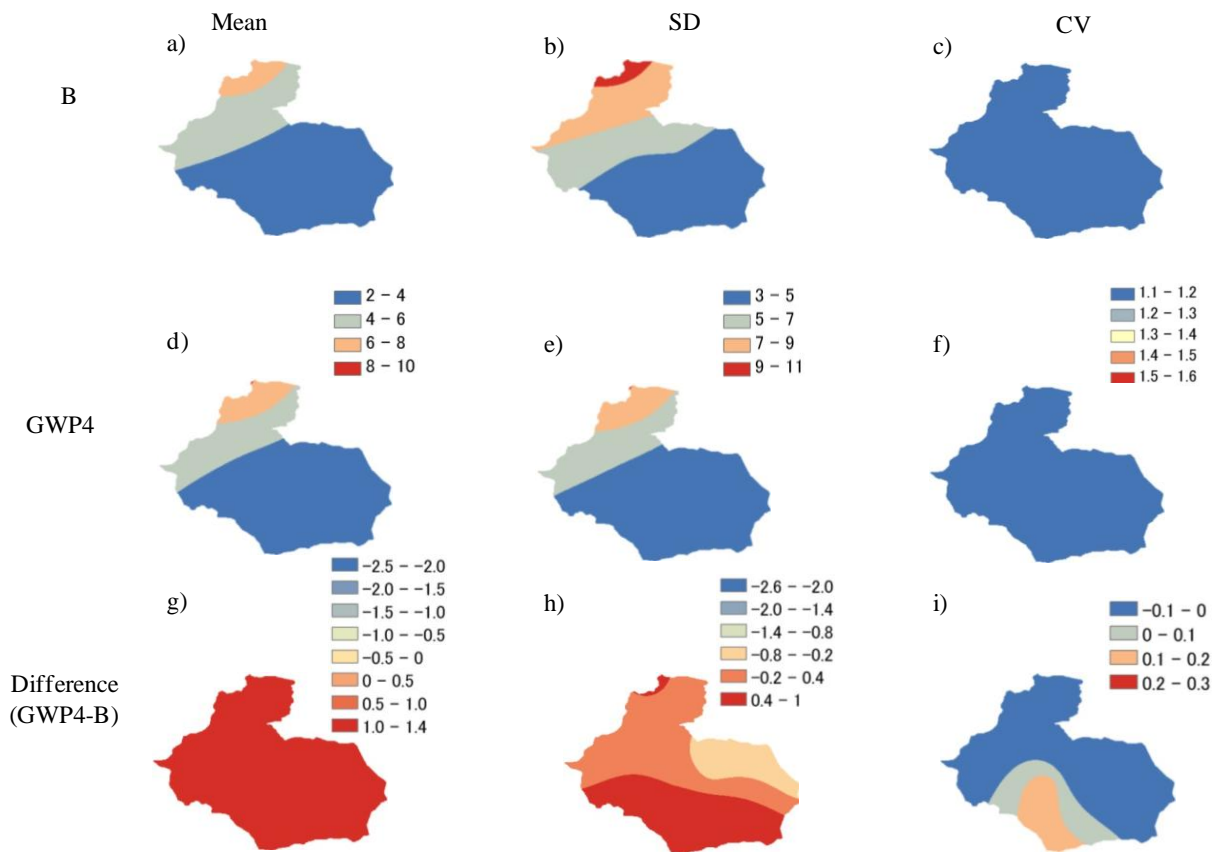


Fig. 86 Annual mean, standard deviation (SD) and coefficient of variation (CV) of aboveground biomass (*AB*) under B and GWP4 scenarios. The panels a), b) and c) represent mean, SD and CV of *AB* in B scenario. The panels d), e) and f) represent mean, SD and CV of *AB* under GWP4 scenario. The panels g), h) and i) represent the difference of mean, SD and CV of *AB* between GWP4 and B scenarios. (Unit is $g C m^{-2}$)

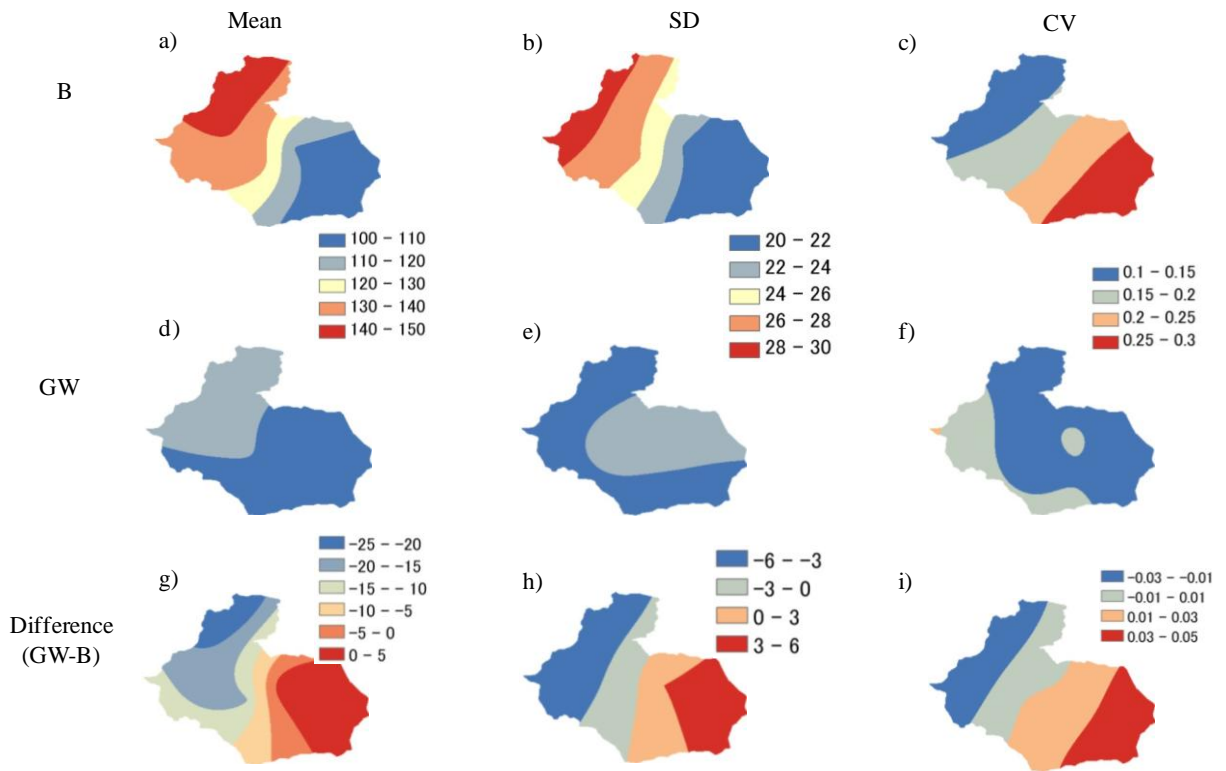


Fig. 87 Annual mean, standard deviation (SD) and coefficient of variation (CV) of belowground biomass (*BB*) under B and GW scenarios. The panels a), b) and c) represent mean, SD and CV of *BB* in B scenario. The panels d), e) and f) represent mean, SD and CV of *BB* under GW scenario. The panels g), h) and i) represent the difference of mean, SD and CV of *BB* between GW and B scenarios. (Unit is g C m^{-2})

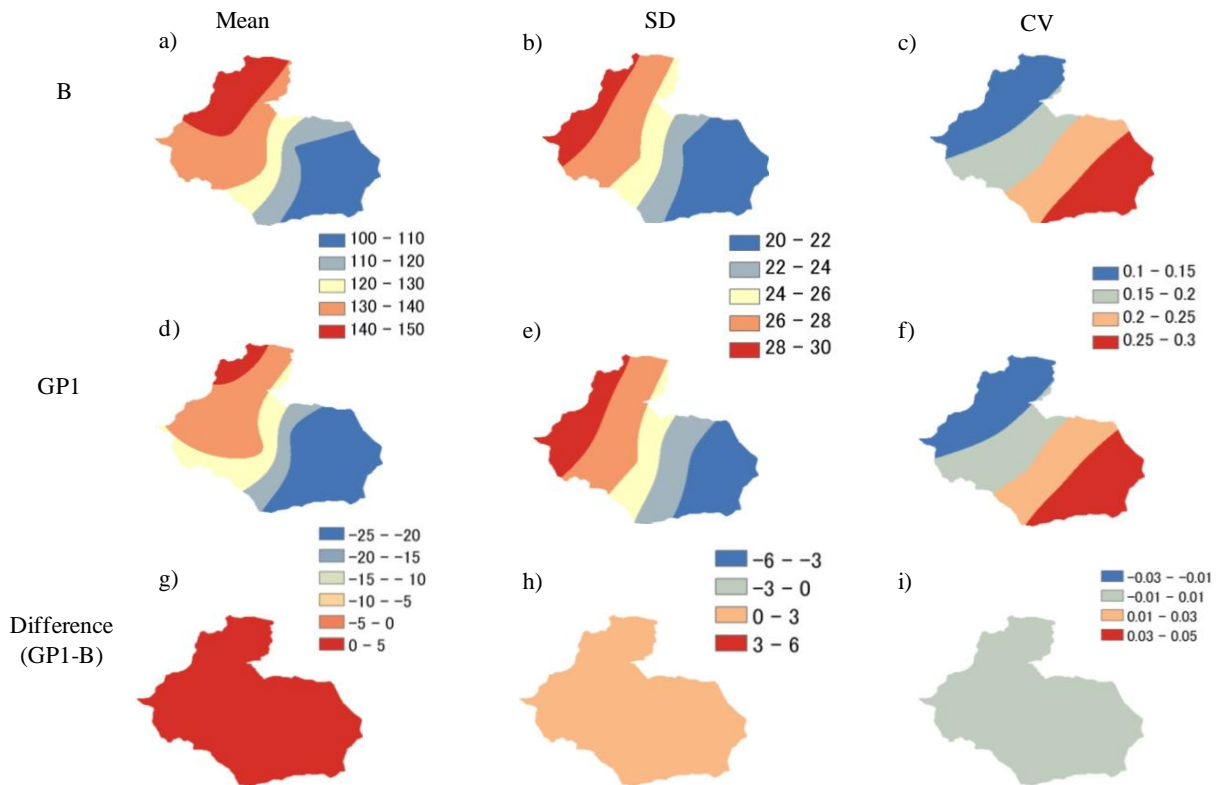


Fig. 88 Annual mean, standard deviation (SD) and coefficient of variation (CV) of belowground biomass (*BB*) under B and GP1 scenarios. The panels a), b) and c) represent mean, SD and CV of *BB* in B scenario. The panels d), e) and f) represent mean, SD and CV of *BB* under GP1 scenario. The panels g), h) and i) represent the difference of mean, SD and CV of *BB* between GP1 and B scenarios. (Unit is g C m^{-2})

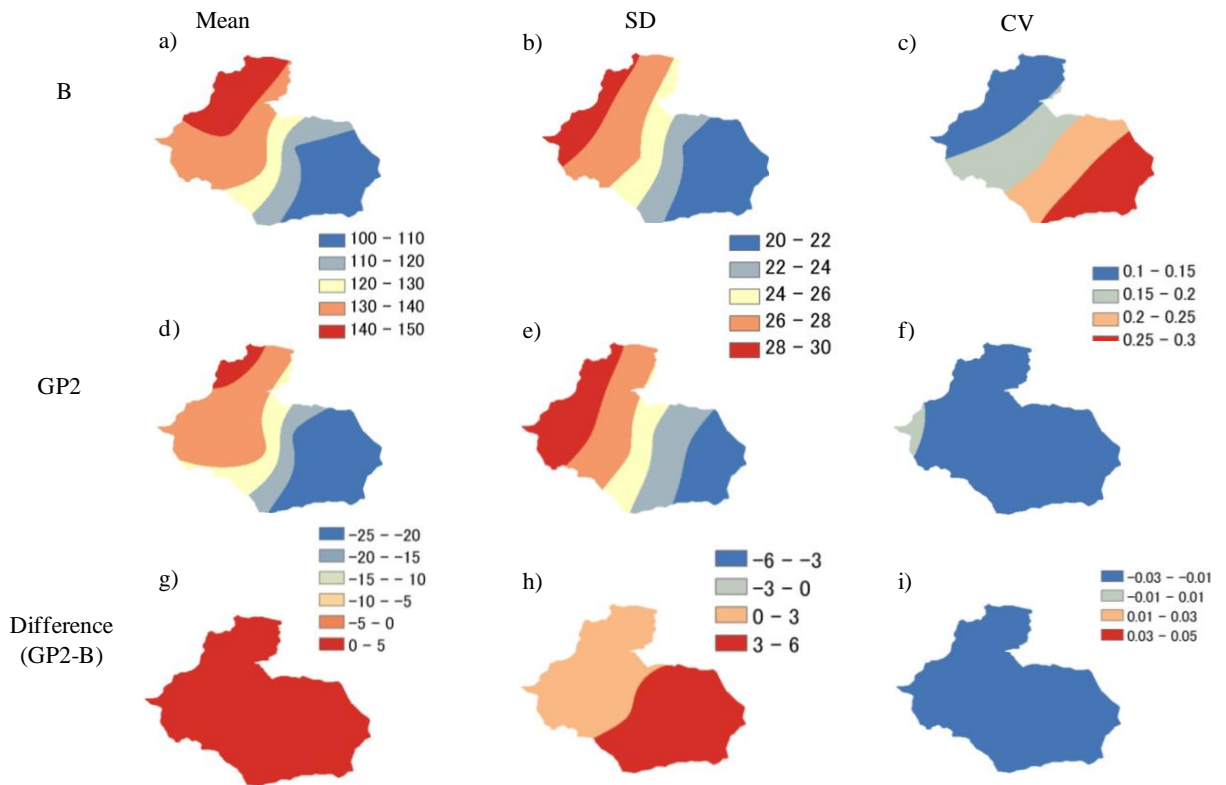


Fig. 89 Annual mean, standard deviation (SD) and coefficient of variation (CV) of belowground biomass (BB) under B and GP2 scenarios. The panels a), b) and c) represent mean, SD and CV of BB in B scenario. The panels d), e) and f) represent mean, SD and CV of BB under GP2 scenario. The panels g), h) and i) represent the difference of mean, SD and CV of BB between GP2 and B scenarios. (Unit is $C\ m^{-2}$)

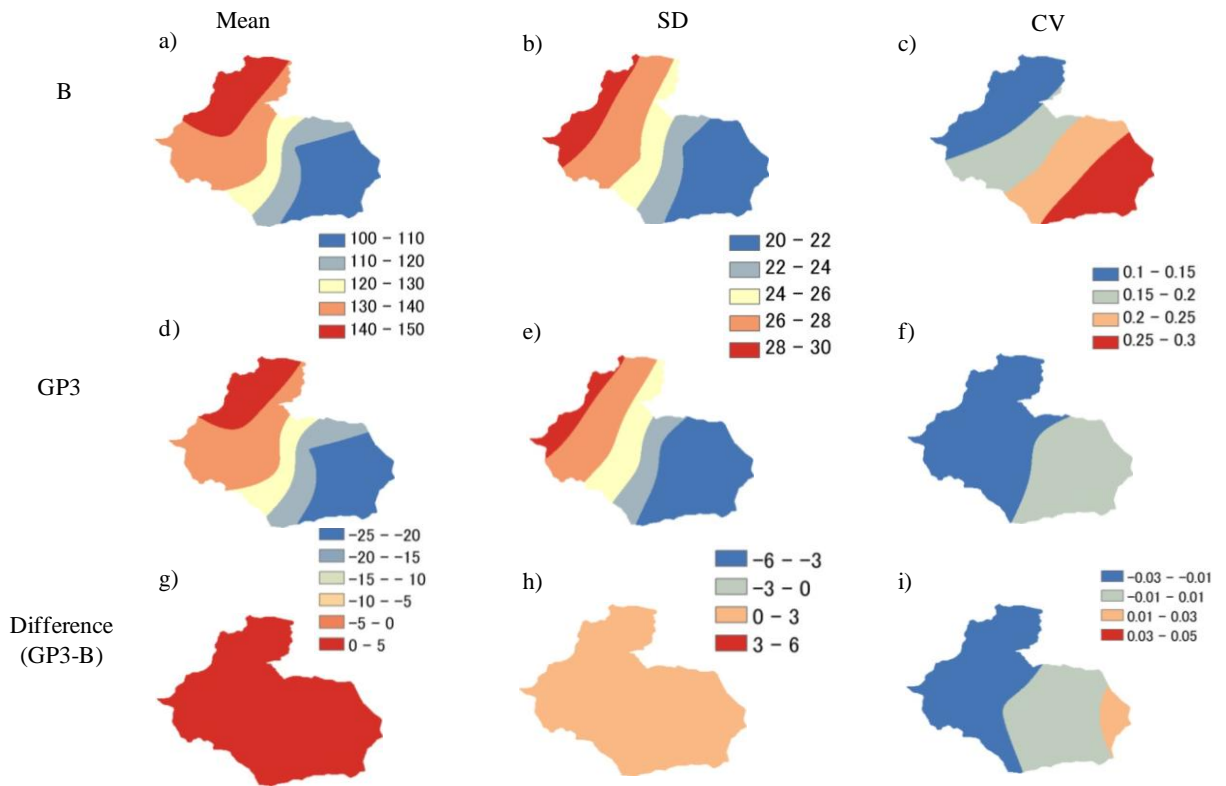


Fig. 90 Annual mean, standard deviation (SD) and coefficient of variation (CV) of belowground biomass (BB) under B and GP3 scenarios. The panels a), b) and c) represent mean, SD and CV of BB in B scenario. The panels d), e) and f) represent mean, SD and CV of BB under GP3 scenario. The panels g), h) and i) represent the difference of mean, SD and CV of BB between GP3 and B scenarios. (Unit is g C m^{-2})

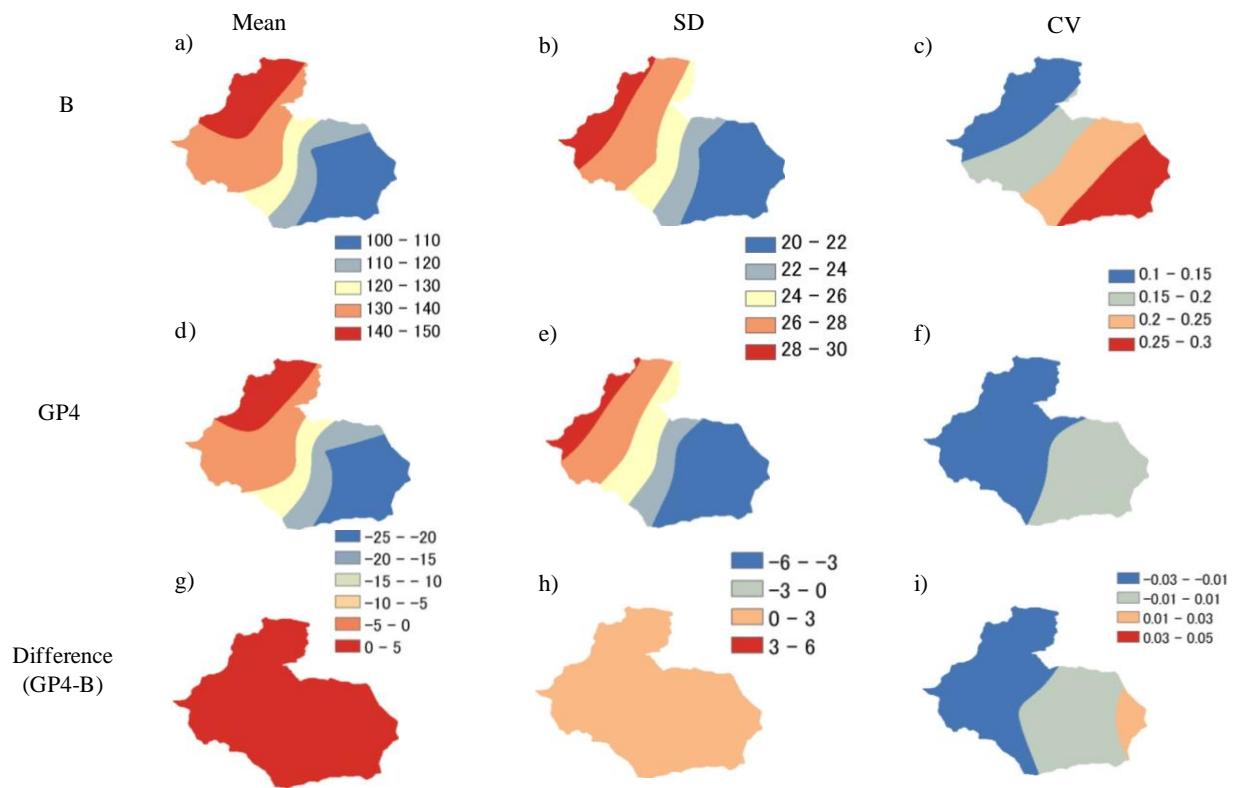


Fig. 91 Annual mean, standard deviation (SD) and coefficient of variation (CV) of belowground biomass (*BB*) under B and GP4 scenarios. The panels a), b) and c) represent mean, SD and CV of *BB* in B scenario. The panels d), e) and f) represent mean, SD and CV of *BB* under GP4 scenario. The panels g), h) and i) represent the difference of mean, SD and CV of *BB* between GP4 and B scenarios. (Unit is g C m^{-2})

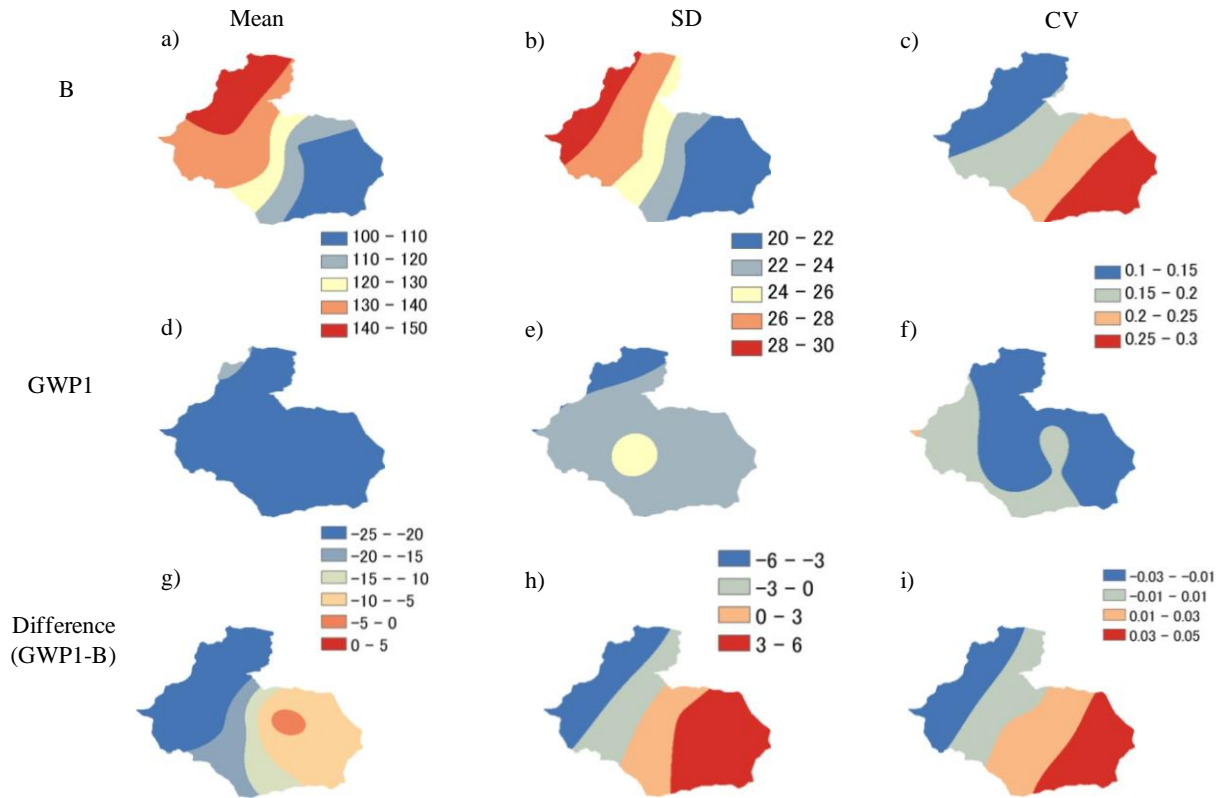


Fig. 92 Annual mean, standard deviation (SD) and coefficient of variation (CV) of belowground biomass (*BB*) under B and GWP1 scenarios. The panels a), b) and c) represent mean, SD and CV of *BB* in B scenario. The panels d), e) and f) represent mean, SD and CV of *BB* under GWP1 scenario. The panels g), h) and i) represent the difference of mean, SD and CV of *BB* between GWP1 and B scenarios. (Unit is $g\ C\ m^{-2}$)

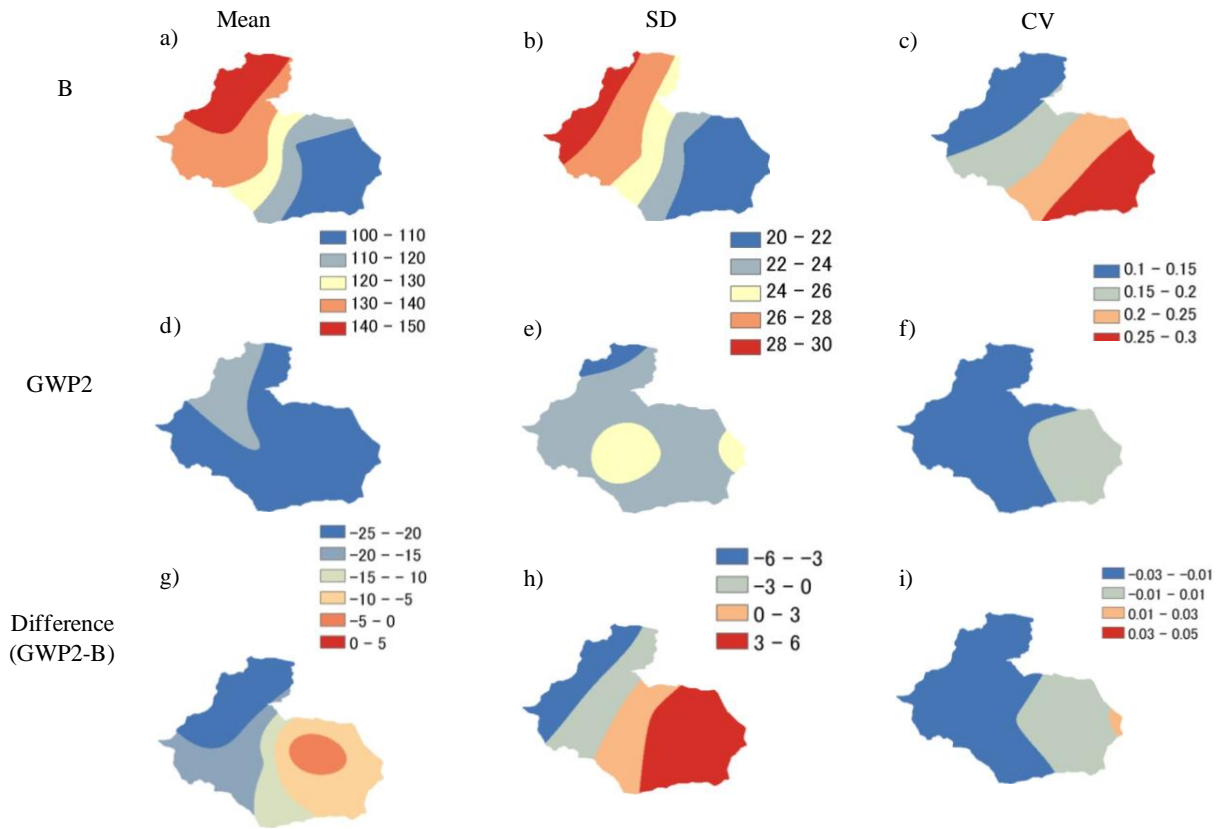


Fig. 93 Annual mean, standard deviation (SD) and coefficient of variation (CV) of belowground biomass (*BB*) under B and GWP2 scenarios. The panels a), b) and c) represent mean, SD and CV of *BB* in B scenario. The panels d), e) and f) represent mean, SD and CV of *BB* under GWP2 scenario. The panels g), h) and i) represent the difference of mean, SD and CV of *BB* between GWP2 and B scenarios. (Unit is $g C m^{-2}$)

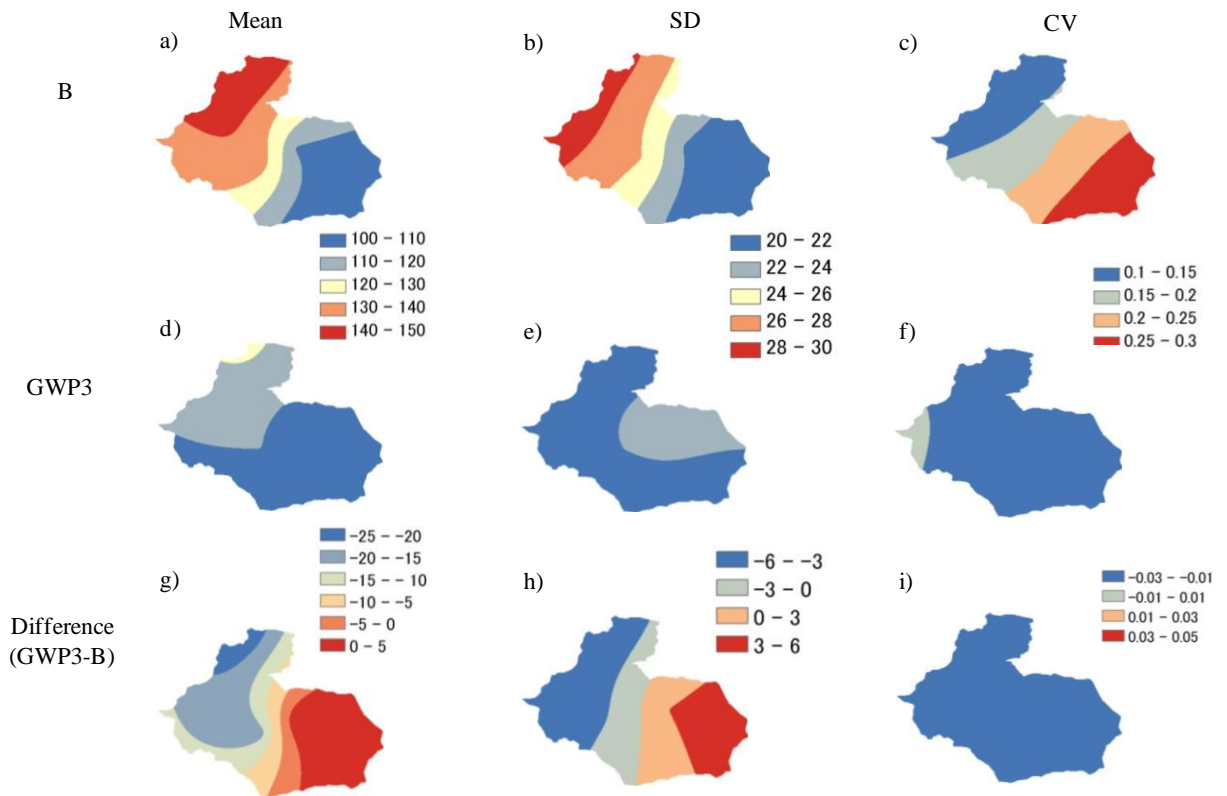


Fig. 94 Annual mean, standard deviation (SD) and coefficient of variation (CV) of belowground biomass (*BB*) under B and GWP3 scenarios. The panels a), b) and c) represent mean, SD and CV of *BB* in B scenario. The panels d), e) and f) represent mean, SD and CV of *BB* under GWP3 scenario. The panels g), h) and i) represent the difference of mean, SD and CV of *BB* between GWP3 and B scenarios. (Unit is $g\ C\ m^{-2}$)

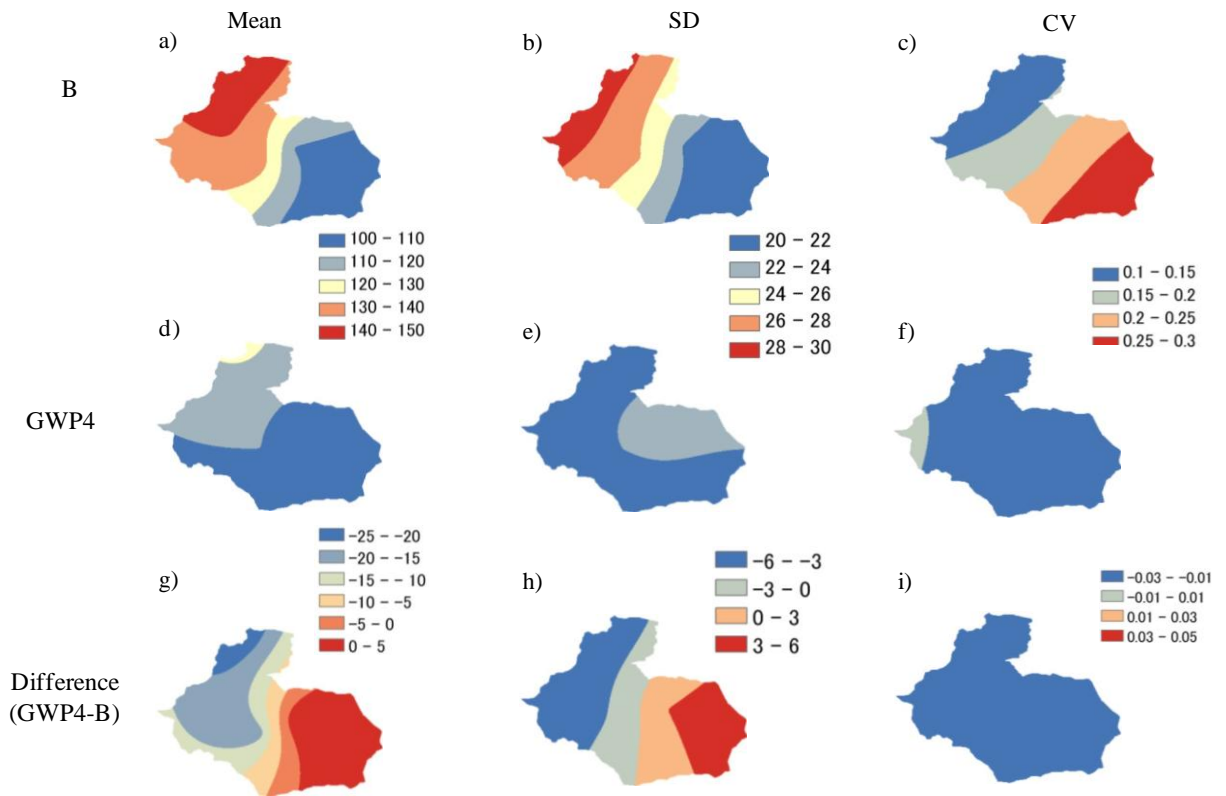


Fig. 95 Annual mean, standard deviation (SD) and coefficient of variation (CV) of belowground biomass (*BB*) under B and GWP4 scenarios. The panels a), b) and c) represent mean, SD and CV of *BB* in B scenario. The panels d), e) and f) represent mean, SD and CV of *BB* under GWP4 scenario. The panels g), h) and i) represent the difference of mean, SD and CV of *BB* between GWP4 and B scenarios. (Unit is $g\ C\ m^{-2}$)

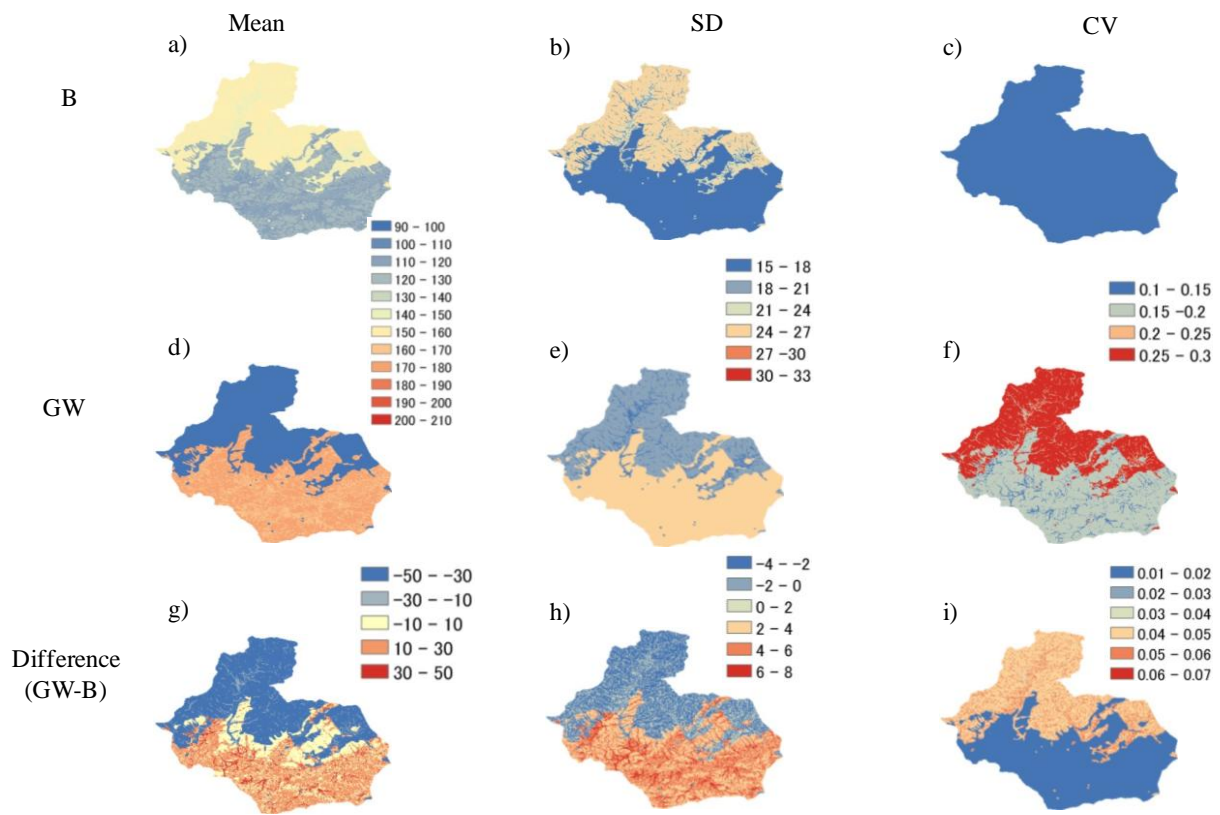


Fig. 96 Annual mean, standard deviation (SD) and coefficient of variation (CV) of evapotranspiration (ET) under B and GW scenarios. The panels a), b) and c) represent mean, SD and CV of ET in B scenario. The panels d), e) and f) represent mean, SD and CV of ET under GW scenario. The panels g), h) and i) represent the difference of mean, SD and CV of ET between GW and B scenarios. (Unit is mm y^{-1})

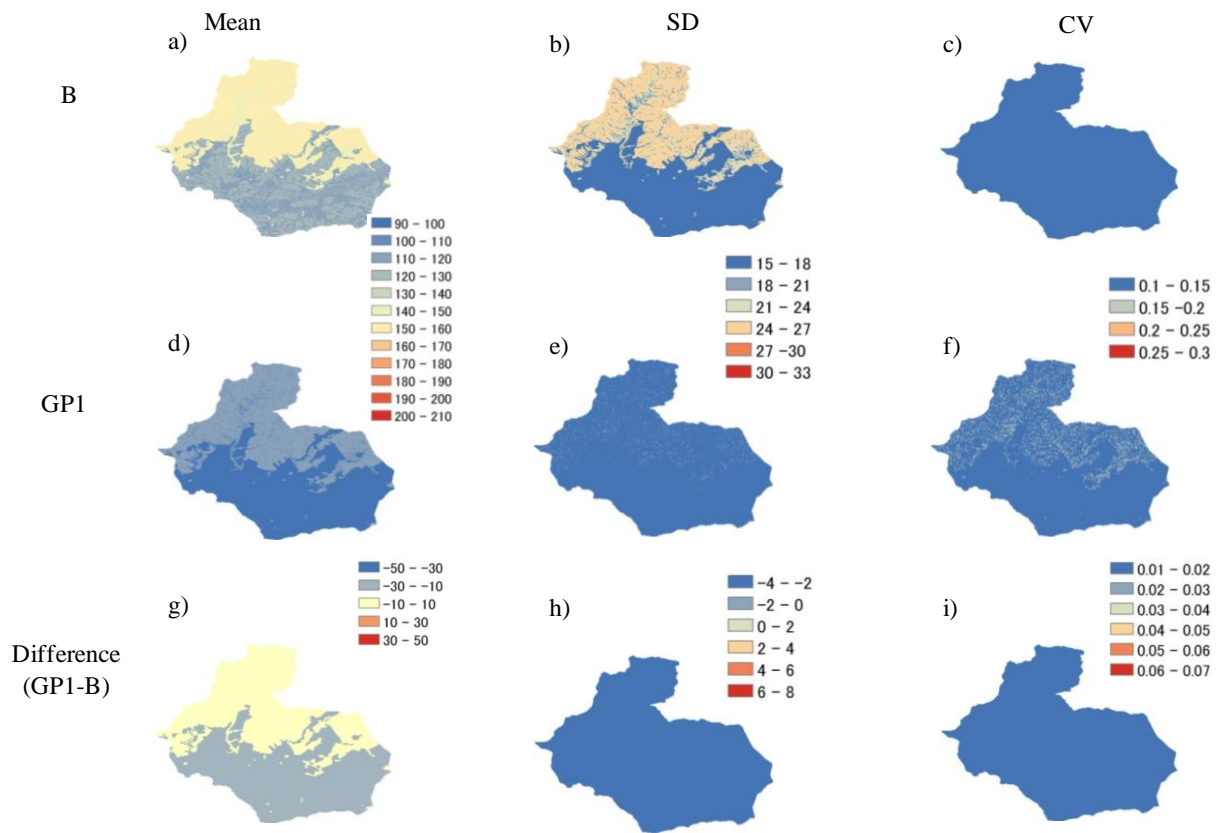


Fig. 97 Annual mean, standard deviation (SD) and coefficient of variation (CV) of evapotranspiration (ET) under B and GP1 scenarios. The panels a), b) and c) represent mean, SD and CV of ET in B scenario. The panels d), e) and f) represent mean, SD and CV of ET under GP1 scenario. The panels g), h) and i) represent the difference of mean, SD and CV of ET between GP1 and B scenarios. (Unit is mm y^{-1})

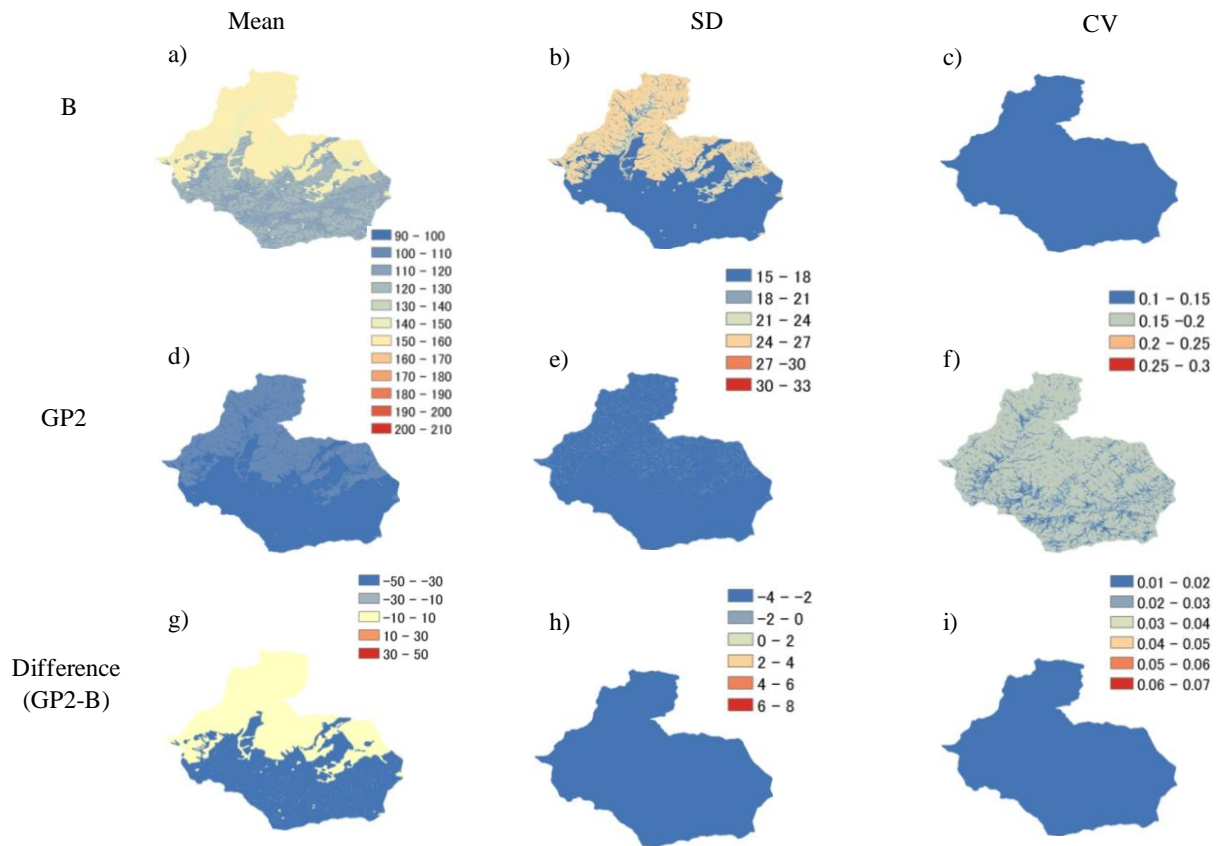


Fig. 98 Annual mean, standard deviation (SD) and coefficient of variation (CV) of evapotranspiration (ET) under B and GP2 scenarios. The panels a), b) and c) represent mean, SD and CV of ET in B scenario. The panels d), e) and f) represent mean, SD and CV of ET under GP2 scenario. The panels g), h) and i) represent the difference of mean, SD and CV of ET between GP2 and B scenarios. (Unit is mm y^{-1})

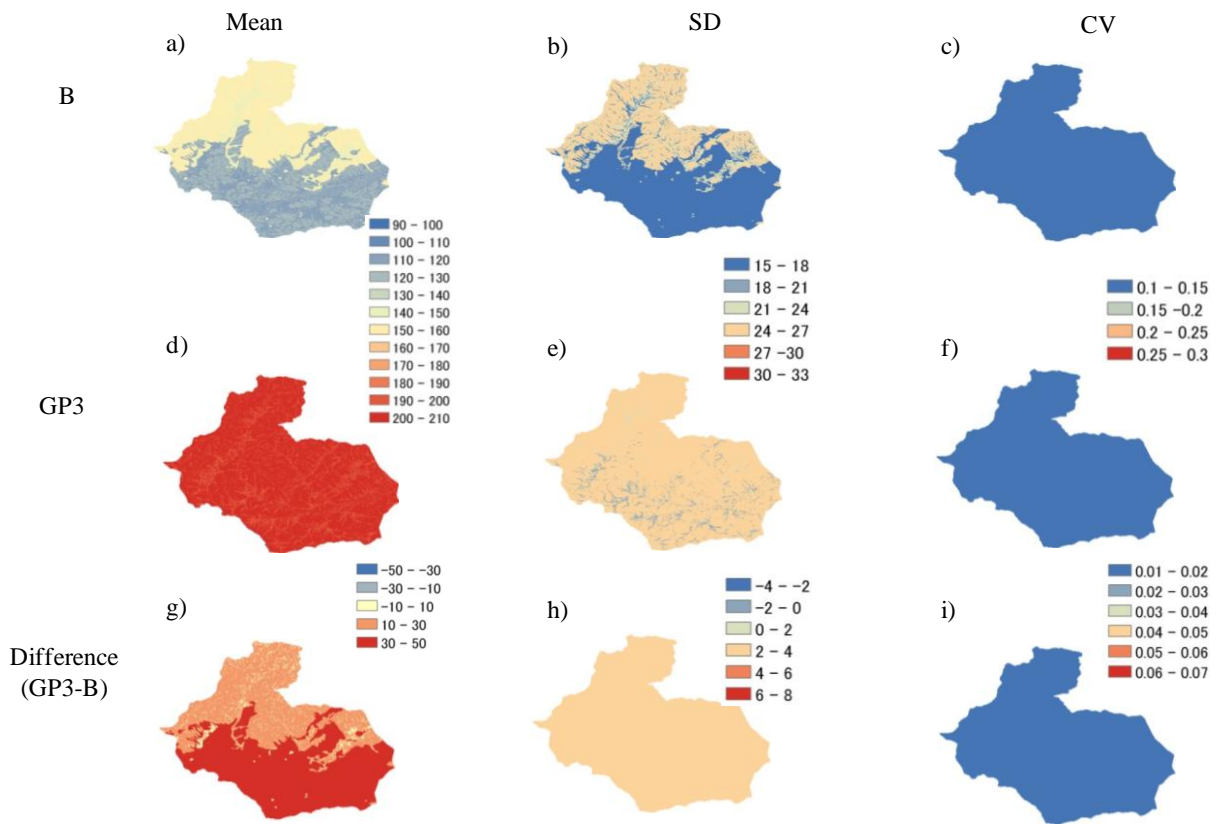


Fig. 99 Annual mean, standard deviation (SD) and coefficient of variation (CV) of evapotranspiration (ET) under B and GP3 scenarios. The panels a), b) and c) represent mean, SD and CV of ET in B scenario. The panels d), e) and f) represent mean, SD and CV of ET under GP3 scenario. The panels g), h) and i) represent the difference of mean, SD and CV of ET between GP3 and B scenarios. (Unit is mm y^{-1})

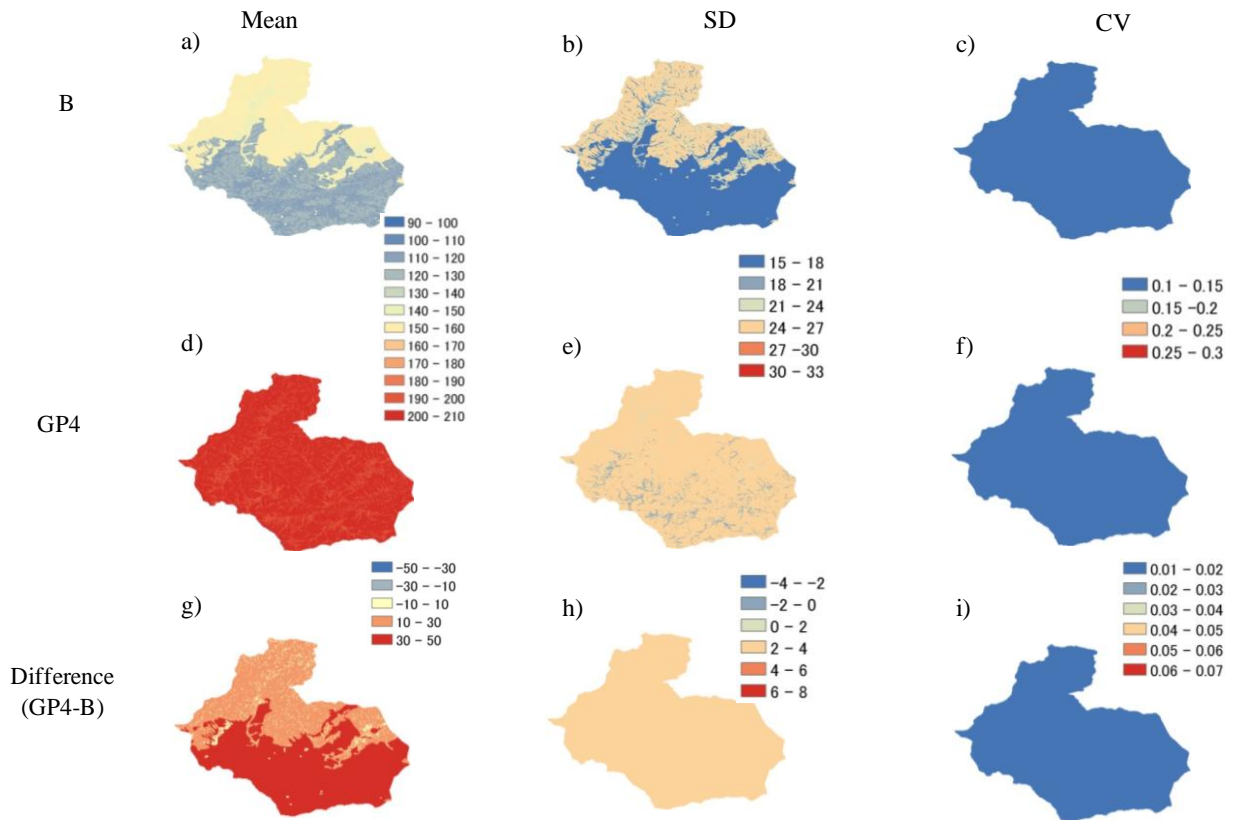


Fig. 100 Annual mean, standard deviation (SD) and coefficient of variation (CV) of evapotranspiration (ET) under B and GP4 scenarios. The panels a), b) and c) represent mean, SD and CV of ET in B scenario. The panels d), e) and f) represent mean, SD and CV of ET under GP4 scenario. The panels g), h) and i) represent the difference of mean, SD and CV of ET between GP4 and B scenarios. (Unit is mm y^{-1})

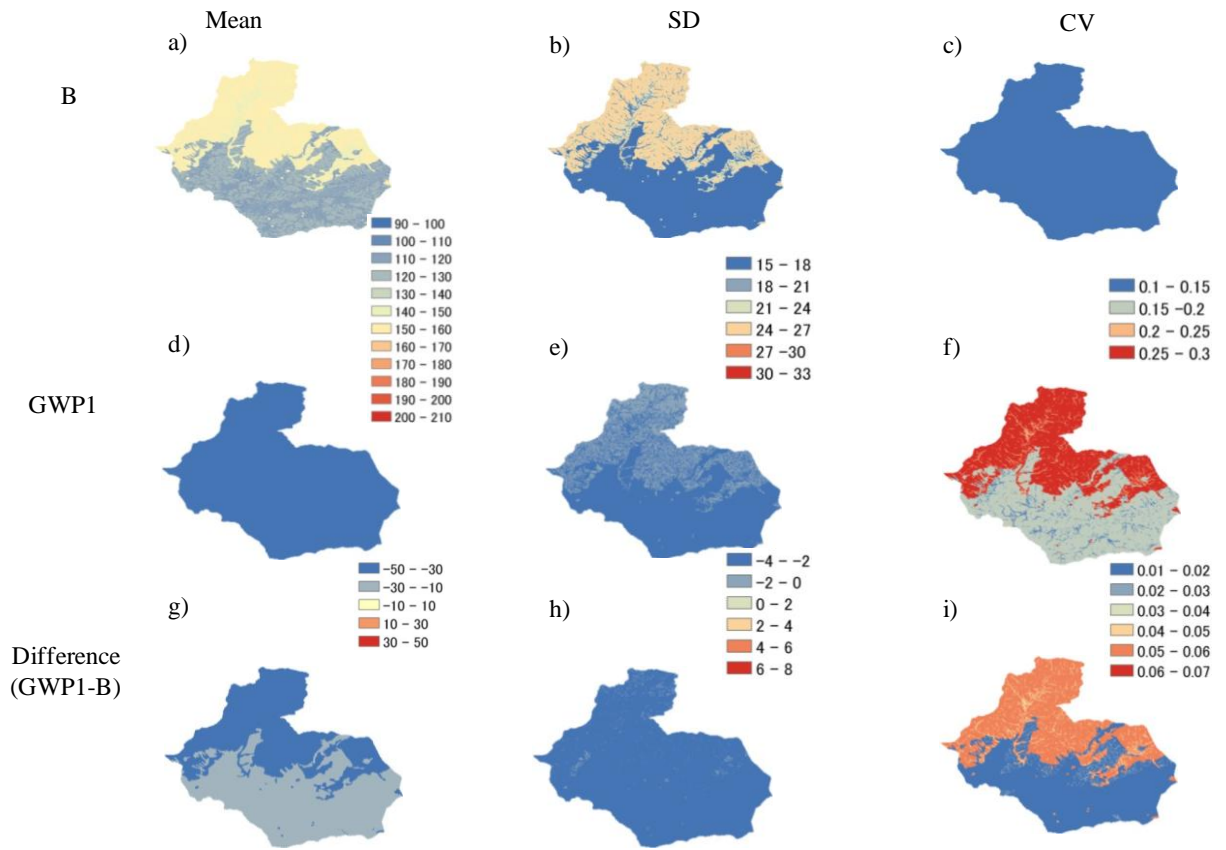


Fig. 101 Annual mean, standard deviation (SD) and coefficient of variation (CV) of evapotranspiration (ET) under B and GWP1 scenarios. The panels a), b) and c) represent mean, SD and CV of ET in B scenario. The panels d), e) and f) represent mean, SD and CV of ET under GWP1 scenario. The panels g), h) and i) represent the difference of mean, SD and CV of ET between GWP1 and B scenarios. (Unit is mm y^{-1})

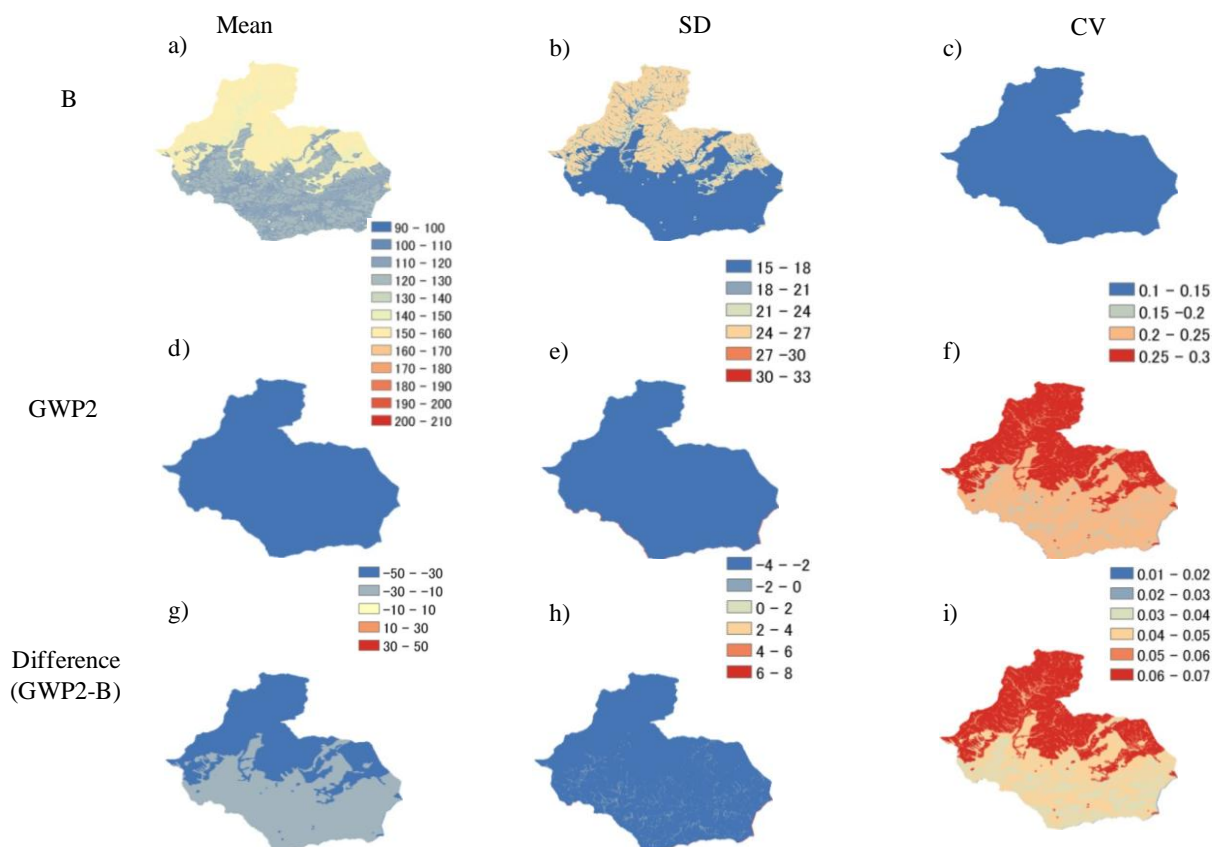


Fig. 102 Annual mean, standard deviation (SD) and coefficient of variation (CV) of evapotranspiration (*ET*) under B and GWP2 scenarios. The panels a), b) and c) represent mean, SD and CV of *ET* in B scenario. The panels d), e) and f) represent mean, SD and CV of *ET* under GWP2 scenario. The panels g), h) and i) represent the difference of mean, SD and CV of *ET* between GWP2 and B scenarios. (Unit is mm y⁻¹)

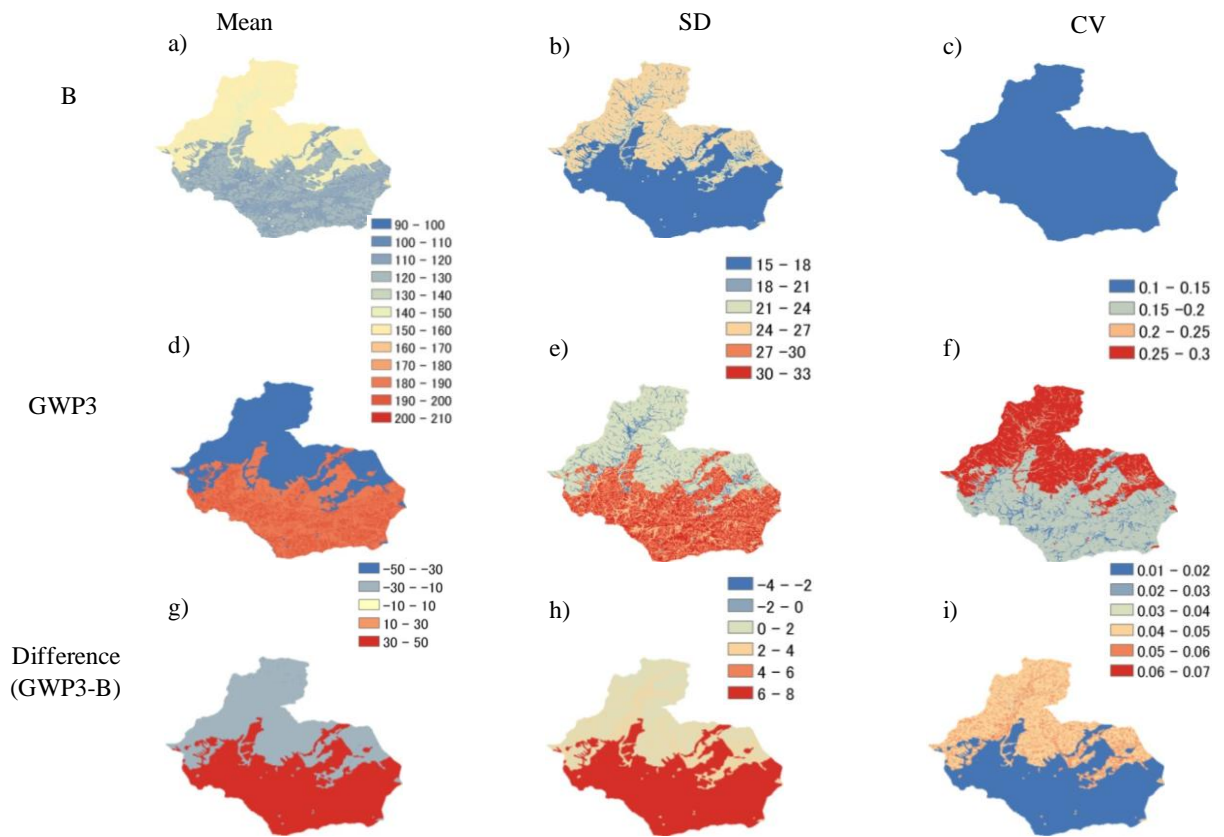


Fig. 103 Annual mean, standard deviation (SD) and coefficient of variation (CV) of evapotranspiration (ET) under B and GWP3 scenarios. The panels a), b) and c) represent mean, SD and CV of ET in B scenario. The panels d), e) and f) represent mean, SD and CV of ET under GWP3 scenario. The panels g), h) and i) represent the difference of mean, SD and CV of ET between GWP3 and B scenarios. (Unit is mm y^{-1})

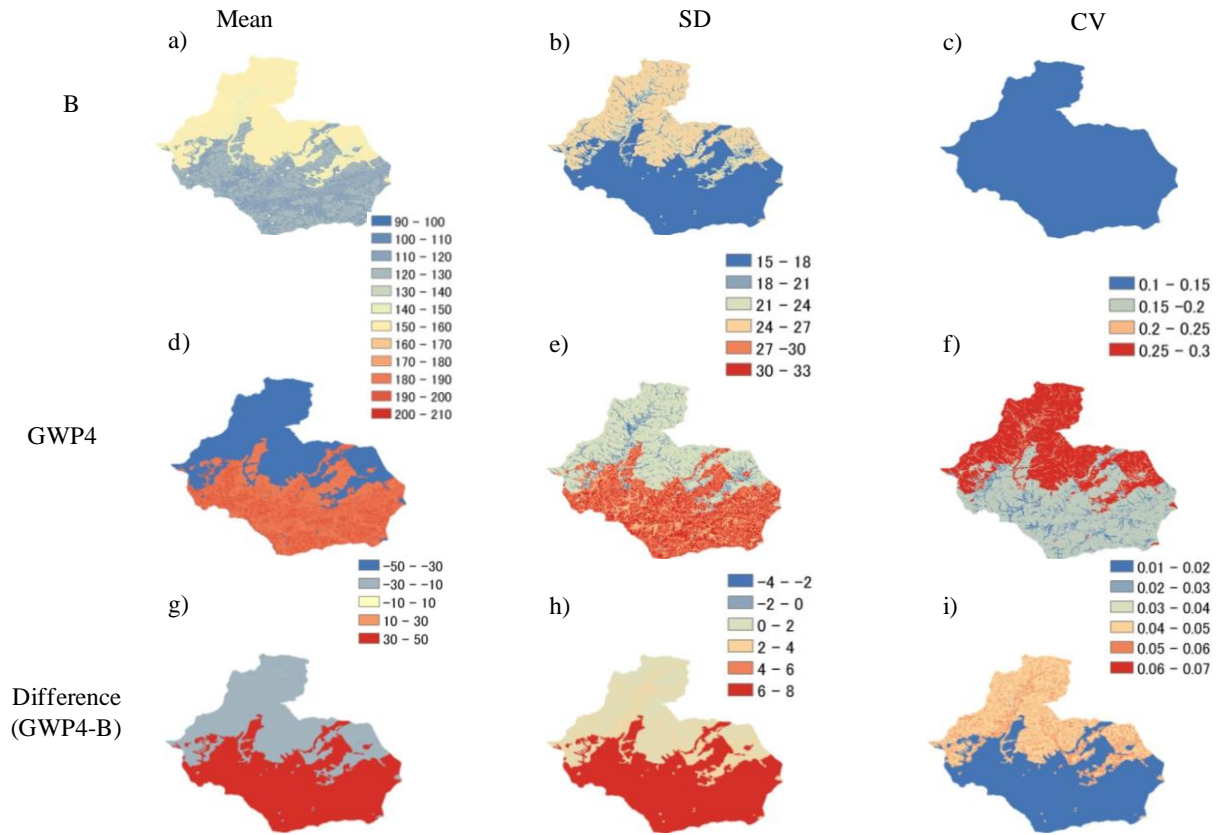


Fig. 104 Annual mean, standard deviation (SD) and coefficient of variation (CV) of evapotranspiration (ET) under B and GWP4 scenarios. The panels a), b) and c) represent mean, SD and CV of ET in B scenario. The panels d), e) and f) represent mean, SD and CV of ET under GWP4 scenario. The panels g), h) and i) represent the difference of mean, SD and CV of ET between GWP4 and B scenarios. (Unit is mm y^{-1})

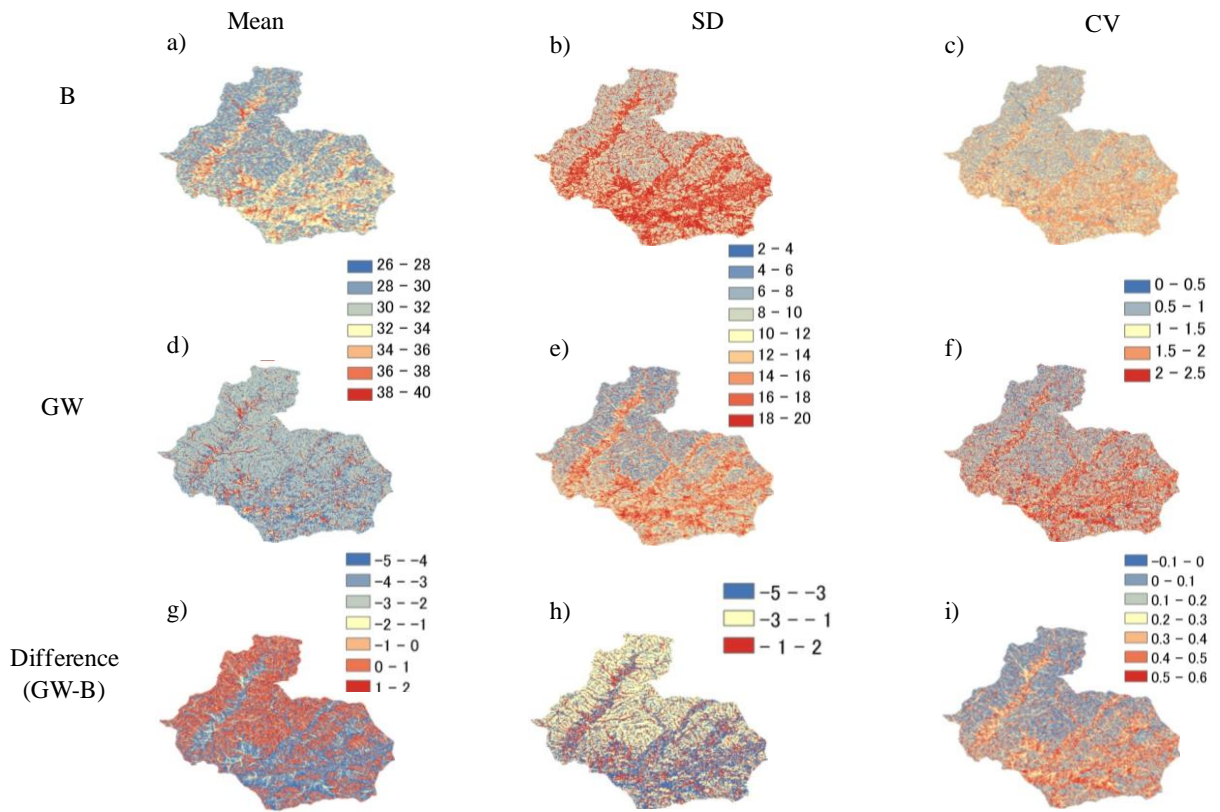


Fig. 105 Annual mean, standard deviation (SD) and coefficient of variation (CV) of soil moisture (SM) under B and GW scenarios. The panels a), b) and c) represent mean, SD and CV of SM in B scenario. The panels d), e) and f) represent mean, SD and CV of SM under GW scenario. The panels g), h) and i) represent the difference of mean, SD and CV of SM between GW and B scenarios. (Unit is %)

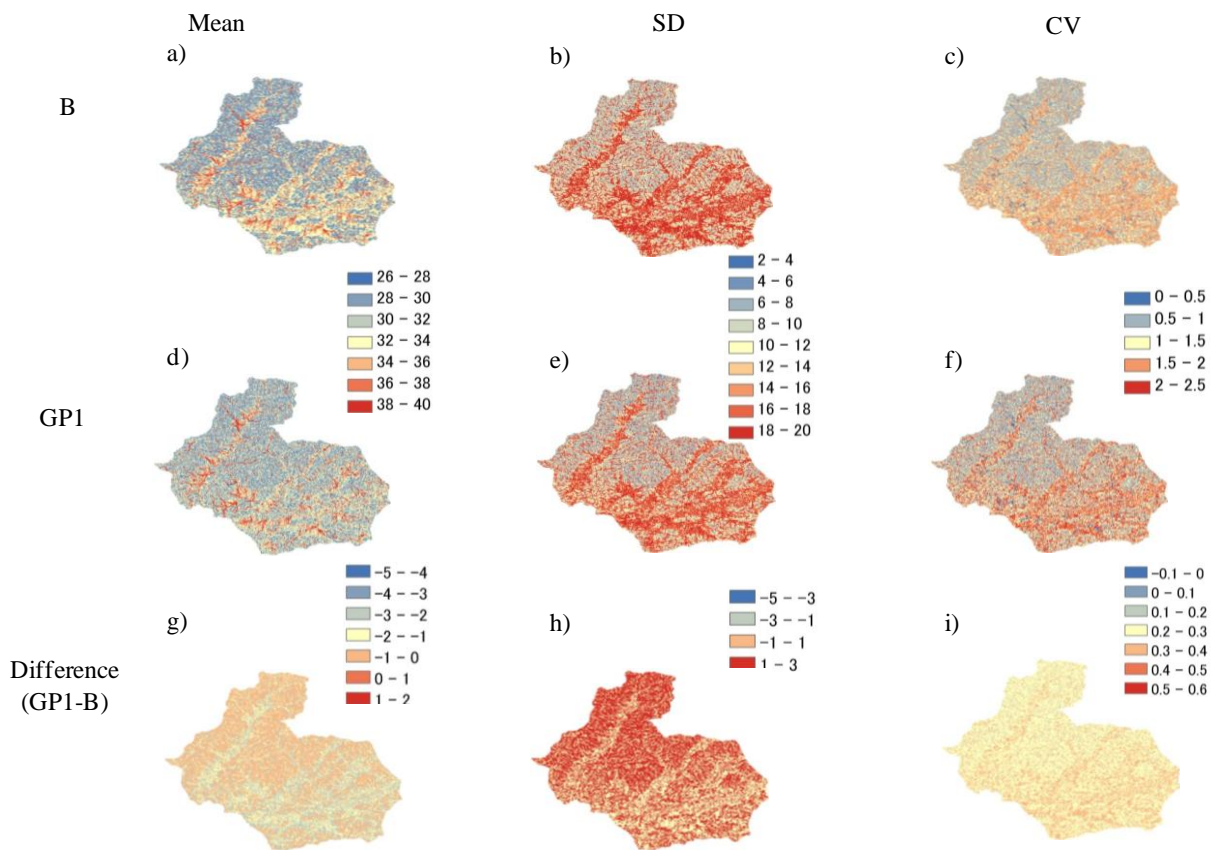


Fig. 106 Annual mean, standard deviation (SD) and coefficient of variation (CV) of soil moisture (*SM*) under B and GP1 scenarios. The panels a), b) and c) represent mean, SD and CV of *SM* in B scenario. The panels d), e) and f) represent mean, SD and CV of *SM* under GP1 scenario. The panels g), h) and i) represent the difference of mean, SD and CV of *SM* between GP1 and B scenarios. (Unit is %)

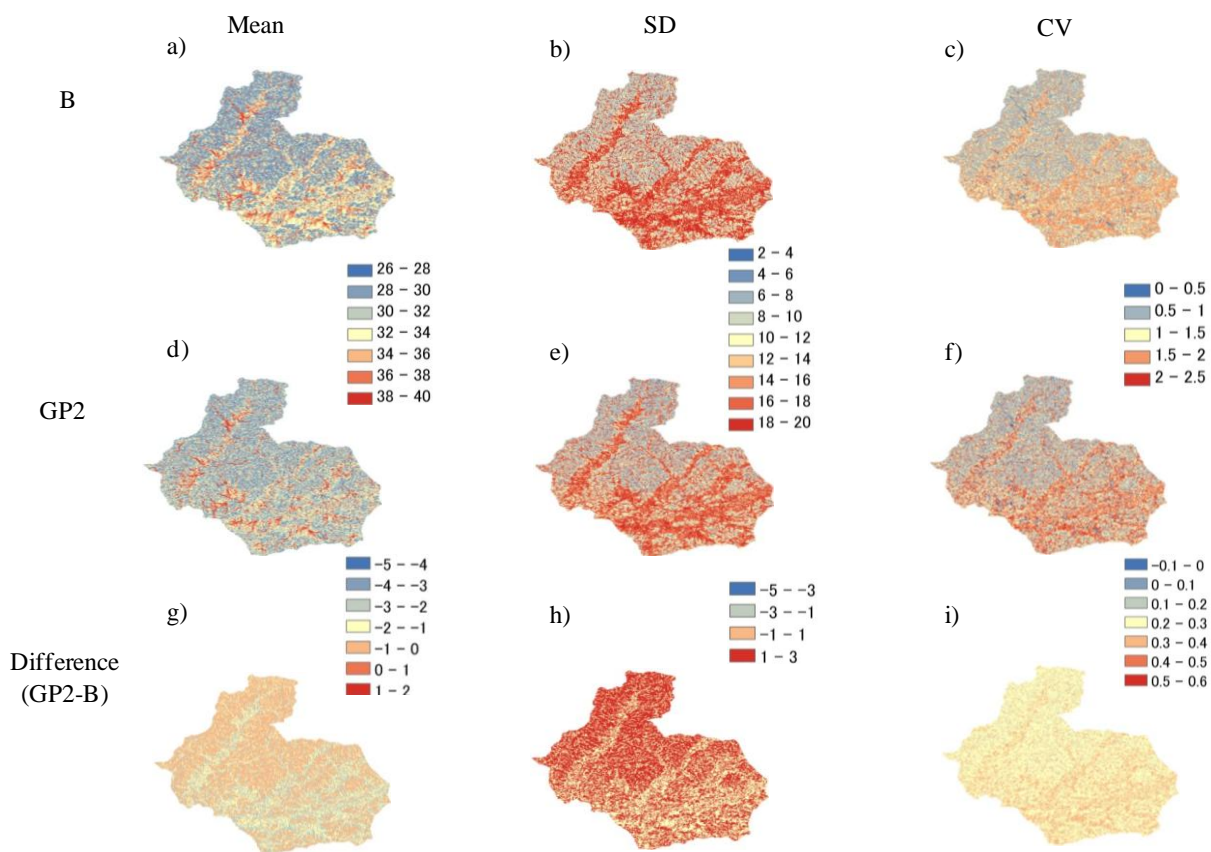


Fig. 107 Annual mean, standard deviation (SD) and coefficient of variation (CV) of soil moisture (SM) under B and GP2 scenarios. The panels a), b) and c) represent mean, SD and CV of SM in B scenario. The panels d), e) and f) represent mean, SD and CV of SM under GP2 scenario. The panels g), h) and i) represent the difference of mean, SD and CV of SM between GP2 and B scenarios. (Unit is %)

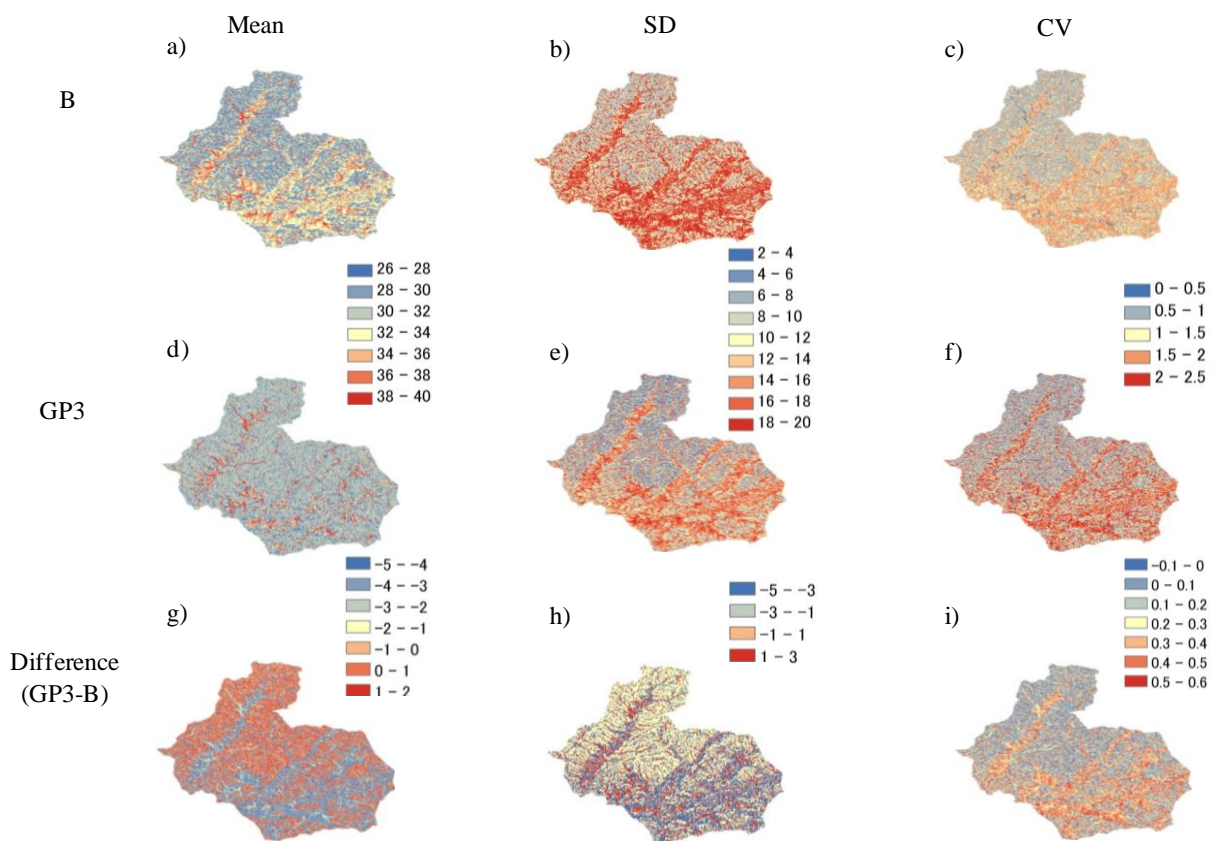


Fig. 108 Annual mean, standard deviation (SD) and coefficient of variation (CV) of soil moisture (*SM*) under B and GP3 scenarios. The panels a), b) and c) represent mean, SD and CV of *SM* in B scenario. The panels d), e) and f) represent mean, SD and CV of *SM* under GP3 scenario. The panels g), h) and i) represent the difference of mean, SD and CV of *SM* between GP3 and B scenarios. (Unit is %)

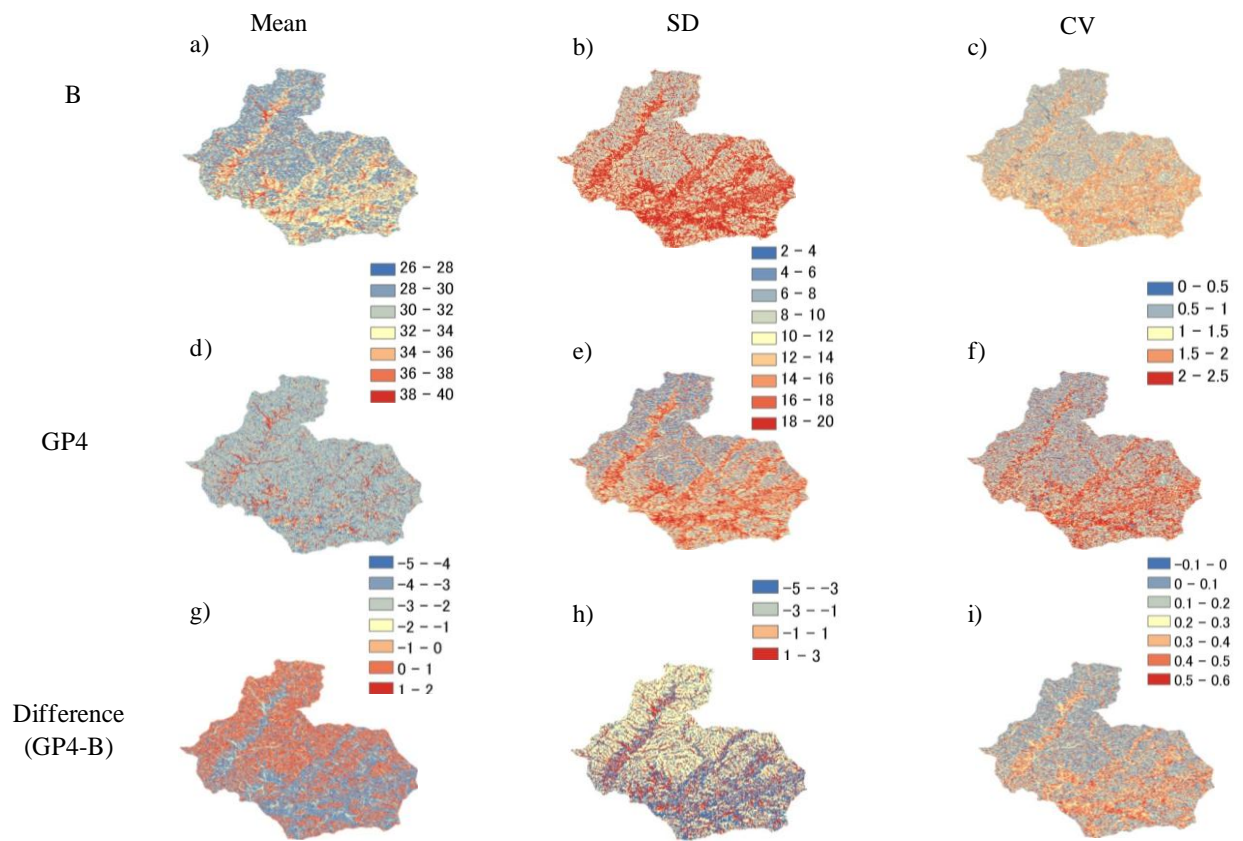


Fig. 109 Annual mean, standard deviation (SD) and coefficient of variation (CV) of soil moisture (SM) under B and GP4 scenarios. The panels a), b) and c) represent mean, SD and CV of SM in B scenario. The panels d), e) and f) represent mean, SD and CV of SM under GP4 scenario. The panels g), h) and i) represent the difference of mean, SD and CV of SM between GP4 and B scenarios. (Unit is %)

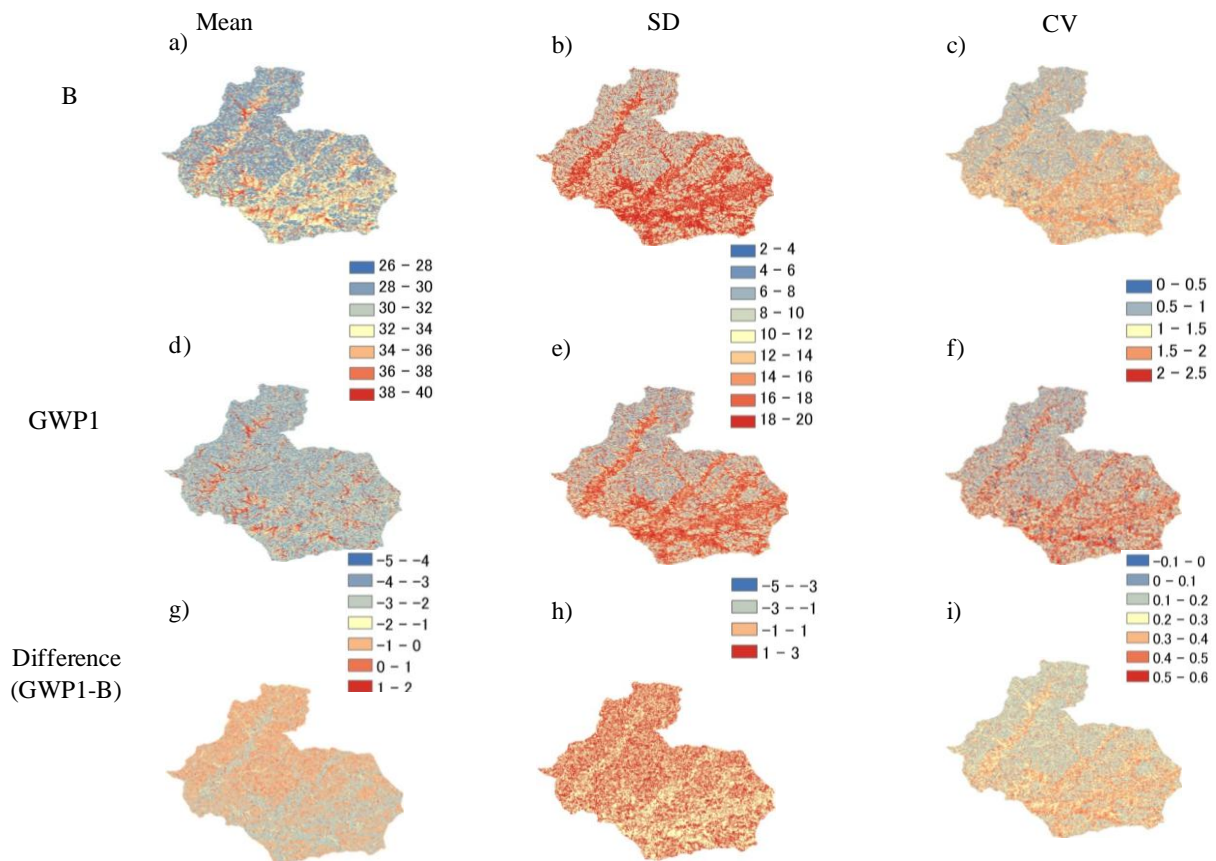


Fig. 110 Annual mean, standard deviation (SD) and coefficient of variation (CV) of soil moisture (SM) under B and GWP1 scenarios. The panels a), b) and c) represent mean, SD and CV of SM in B scenario. The panels d), e) and f) represent mean, SD and CV of SM under GWP1 scenario. The panels g), h) and i) represent the difference of mean, SD and CV of SM between GWP1 and B scenarios. (Unit is %)

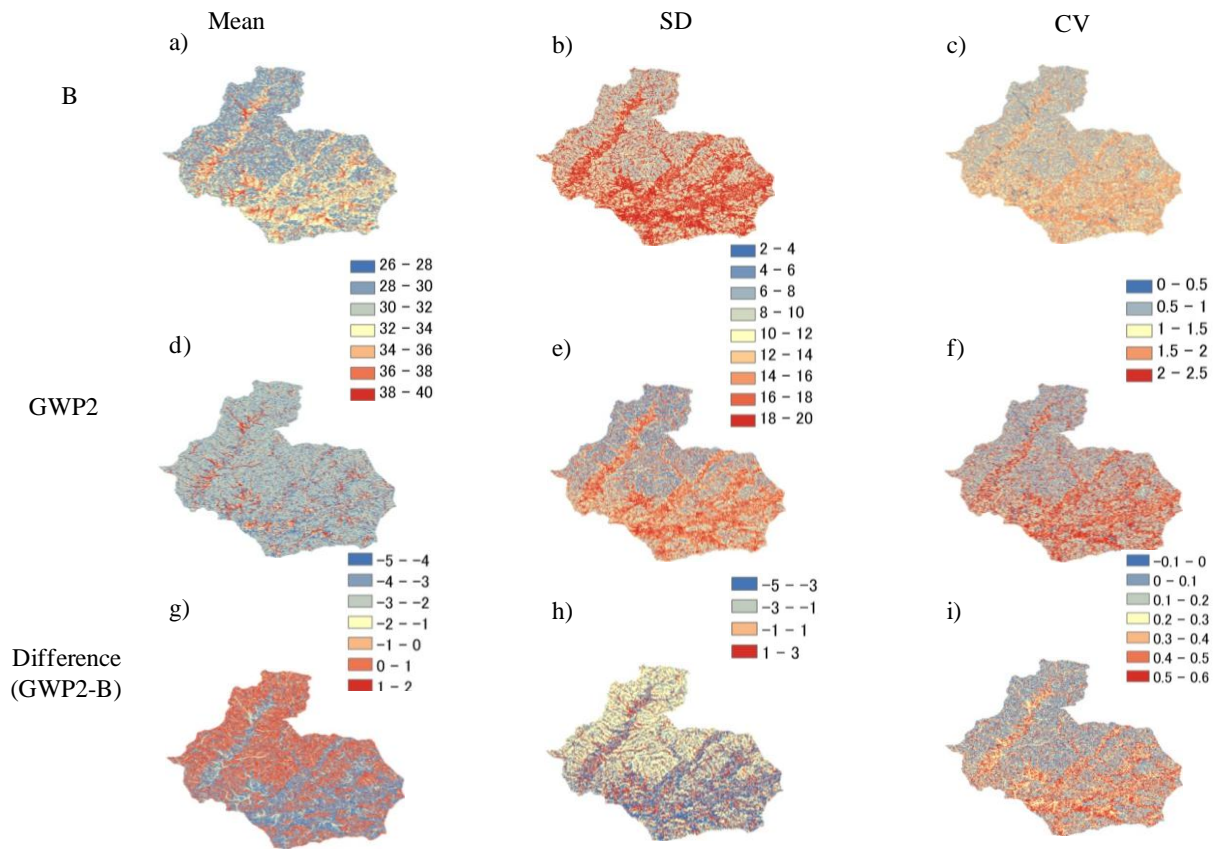


Fig. 111 Annual mean, standard deviation (SD) and coefficient of variation (CV) of soil moisture (*SM*) under B and GWP2 scenarios. The panels a), b) and c) represent mean, SD and CV of *SM* in B scenario. The panels d), e) and f) represent mean, SD and CV of *SM* under GWP2 scenario. The panels g), h) and i) represent the difference of mean, SD and CV of *SM* between GWP2 and B scenarios. (Unit is %)

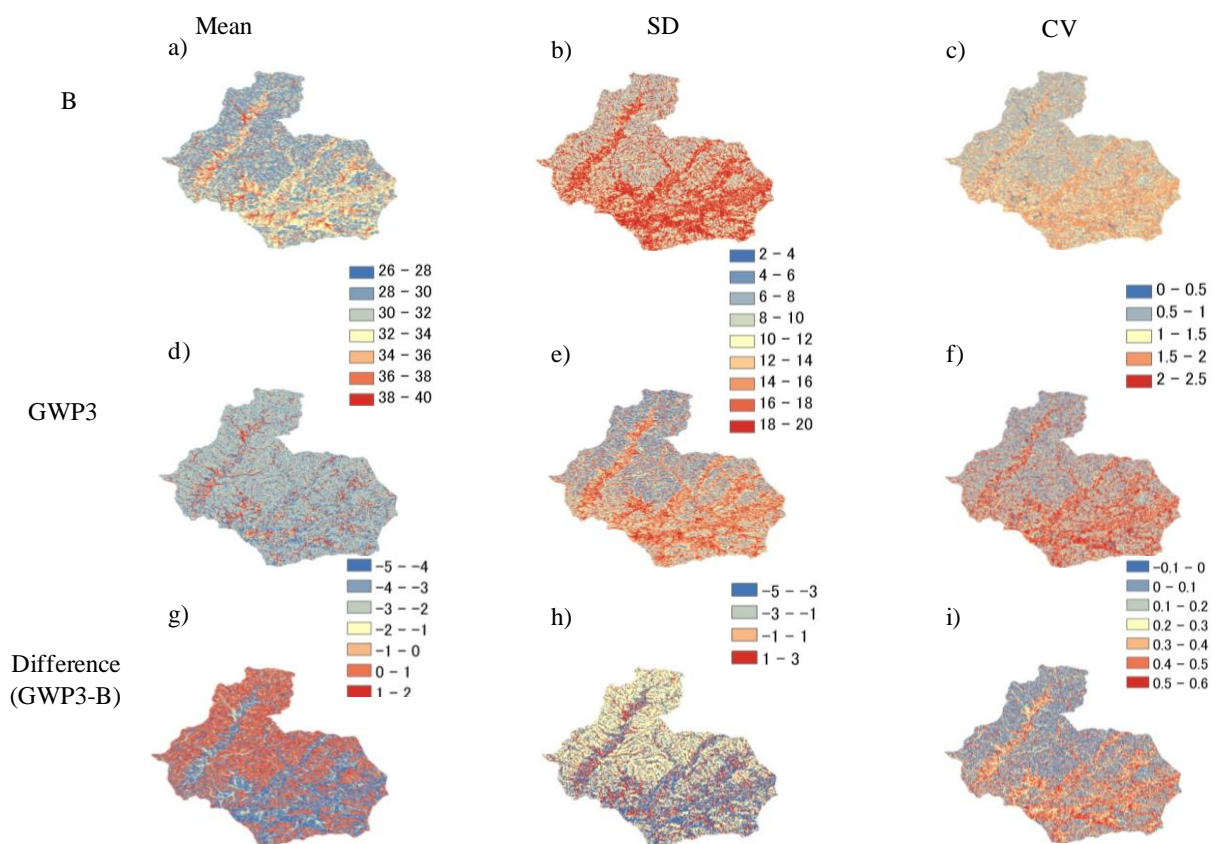


Fig. 112 Annual mean, standard deviation (SD) and coefficient of variation (CV) of soil moisture (*SM*) under B and GWP3 scenarios. The panels a), b) and c) represent mean, SD and CV of *SM* in B scenario. The panels d), e) and f) represent mean, SD and CV of *SM* under GWP3 scenario. The panels g), h) and i) represent the difference of mean, SD and CV of *SM* between GWP3 and B scenarios. (Unit is %)

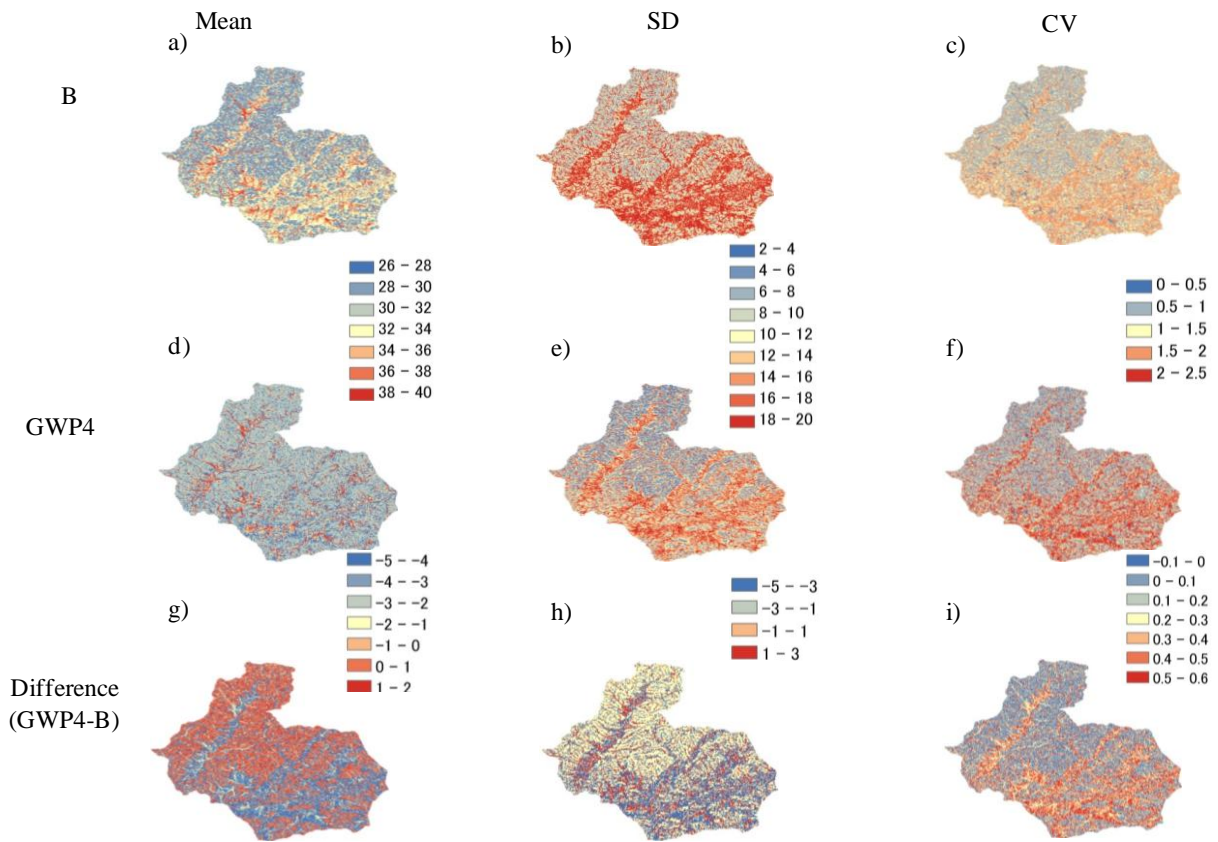


Fig. 113 Annual mean, standard deviation (SD) and coefficient of variation (CV) of soil moisture (*SM*) under B and GWP4 scenarios. The panels a), b) and c) represent mean, SD and CV of *SM* in B scenario. The panels d), e) and f) represent mean, SD and CV of *SM* under GWP4 scenario. The panels g), h) and i) represent the difference of mean, SD and CV of *SM* between GWP4 and B scenarios. (Unit is %)

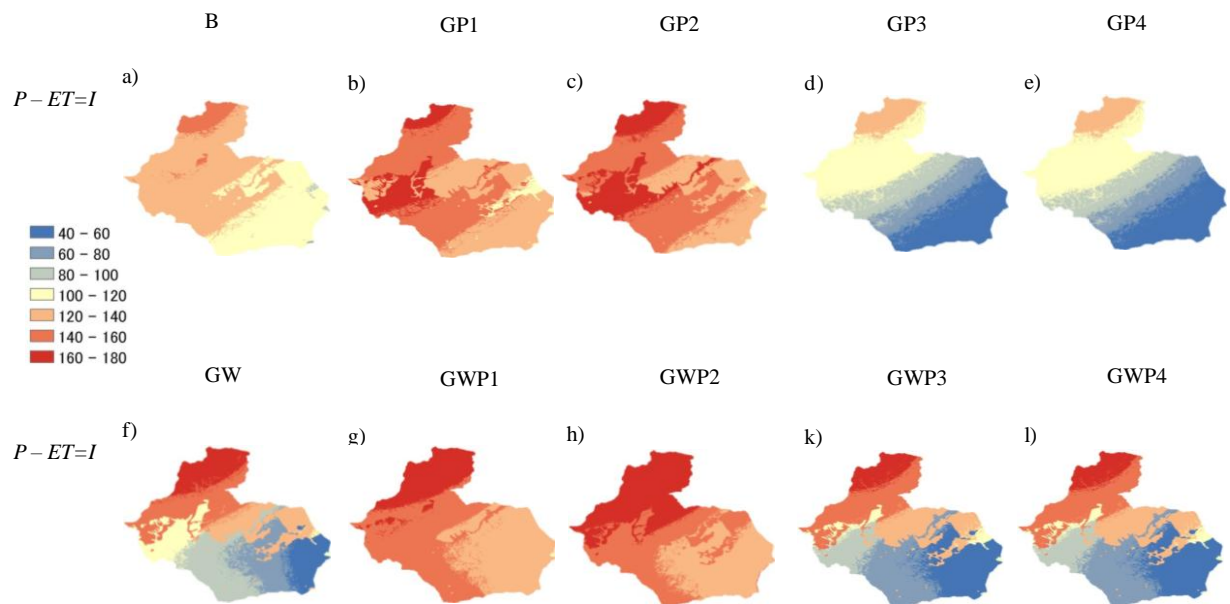


Fig. 114 Difference of annual mean precipitation (P) and evapotranspiration (ET). Panel a) for B scenario, b) for GP1 scenario, c) for GP2 scenario, d) for GP3 scenario, e) for GP4 scenario, f) for GW scenario, g) for GWP1 scenario, h) for GWP2 scenario, k) for GWP3 scenario and l) for GWP4 scenario. (Unit is mm y^{-1})

The summaries of different scenarios of ecohydrological components are shown in Figs. 115-124. The changes under GW, GP1, GP2, GP3, GP4, GWP1, GWP2, GWP3 and GWP4 scenarios from B scenario can be summarized as follows. In GW scenario, aboveground biomass, belowground biomass, evaporation, transpiration, soil moisture, infiltration and discharge were decreased by 23.9, 10.3, 23.5, 1.6, 7.9, 0.9 and 20.2% as compared with those of the B scenario. Evaporation and aboveground and belowground biomass were mainly decreased due to decrease of precipitation amount. In general, transpiration from vegetation is controlled by number of factors, including humidity in atmosphere, soil moisture, net radiation, ground heat flux, wind speed, air pressure and so on. Under GW scenario, soil moisture, net radiation and wind speed were decreased by 7.9, 0.84 and 13.8%, whereas air pressure, ground heat flux and vapor pressure were increased by 0.13, 15.4, and 36.13% from B scenario. These detailed calculations help us to determine which variables lead to reduction of transpiration under the GW scenario. From these results, transpiration was decreased mainly by the increase of ground heat flux and vapor pressure. On the other hand, decrease of infiltration resulted in decrease of soil moisture and discharge.

In GP1 scenario, aboveground biomass, belowground biomass, evaporation, transpiration, soil moisture, infiltration and discharge were decreased by 17.7, 3.2, 21.3, 7.5, 34.2, 2.4 and 0.9% as compared with those of the B scenario. Under this scenario, decrease of simulated aboveground biomass lead to decrease of evaporation and transpiration. Transpiration was also influenced by decrease of soil moisture. Discharge was decreased by 0.9% which was resulted from infiltration. Under GP1 scenario, soil moisture, net radiation and ground heat flux were decreased by 34.2, 3.02, and 1.12% from B scenario.

In GP2 scenario, aboveground biomass, belowground biomass, evaporation, transpiration, soil moisture, infiltration and discharge were decreased by 25.3, 2.4, 18.7, 9.3, 34.2, 1.7 and 0.4% as compared with those of the B scenario. Evaporation and transpiration decreased mainly due to aboveground biomass reduction. Infiltration also affected soil moisture and discharge under this scenario. Decrease in soil moisture reduced transpiration. Soil moisture and ground heat flux were decreased by 34.2 and 22.4%, whereas net radiation was increased by 5.4% from B scenario under GP2 scenario.

In GP3 scenario, aboveground biomass, belowground biomass, evaporation, transpiration and soil moisture were increased by 17.8, 0.2, 8.7, 7.2 and 2.9%, whereas infiltration and discharge were decreased by 4.3 and 5.7% as compared with those of the B scenario. Net radiation and ground heat flux were decreased by 3.4 and 36.4%, whereas soil moisture was increased by 2.9% from B scenario under GP3 scenario.

In GP4 scenario, aboveground biomass, belowground biomass, evaporation, transpiration and soil moisture were increased by 18.1, 0.9, 9.1, 8.2 and 3.9%, whereas infiltration and discharge were decreased by 4.4 and 2.7% as compared with those of the B scenario. Net radiation and ground heat flux were decreased by 5.4 and 37.4% from B scenario under GP4 scenario.

In GWP1 scenario, aboveground biomass, belowground biomass, evaporation, transpiration, soil moisture, infiltration and discharge was decreased by 32.3, 14.1, 34.1, 4.9, 31.1, 2.9 and 20.1% as compared with those of the B scenario. Aboveground and belowground biomass decreased due to precipitation and grazing pressure changes. Under this scenario, evaporation decreased by 34.1% due to increase of vapor pressure and decrease of precipitation, whereas transpiration was also decreased because of precipitation, aboveground biomass, soil moisture and vapor pressure. Discharge was decreased by 20.1% which was resulted from decrease of infiltration. Net radiation and ground heat flux were increased by 3.84 and 21.4% from B scenario.

In GWP2 scenario, aboveground biomass, belowground biomass, evaporation, transpiration, soil moisture, infiltration, discharge was decreased by 38.3, 14.4, 19.7, 7.9, 31.5, 2.3 and 15.4% as compared with those of the B scenario. Here, again aboveground and belowground biomass decreased due to precipitation and grazing pressure changes. Evaporation was decreased due to increase of vapor pressure and decrease of precipitation, whereas transpiration was also decreased by because of precipitation, aboveground biomass, soil moisture and vapor pressure. Decrease of infiltration lead into discharge reduction under this scenario. In case of GWP2 scenario, net radiation and ground heat flux were increased by 5.74 and 13.4% from B scenario.

In GWP3 scenario, aboveground biomass was increased by 1.96% from the B scenario because of grazing pressure, whereas belowground biomass, evaporation, transpiration, soil moisture, infiltration and discharge were decreased by 9.6, 15.3, 0.1, 18.2, 2.6 and 21.4%, as compared with those of the B scenario. Net radiation and ground heat flux were increased by 8.4 and 23.4% from B scenario under GWP3 scenario.

In GWP4 scenario, aboveground biomass was increased by 2.6% from the B scenario because of grazing pressure, whereas belowground biomass, evaporation, transpiration, soil moisture, infiltration and discharge were decreased by 5.6, 18.3, 0.5, 19.4, 3.6 and 22.4% as compared with those of the B scenario. Net radiation and ground heat flux were increased by 9.1 and 23.4% from B scenario under GWP4 scenario.

From the projection of aboveground biomass under different scenarios, aboveground biomass is most sensitive to change in the combination of precipitation and grazing pressure. Therefore, global warming had much influence on aboveground biomass due to water and temperature stress to plant whereas grazing pressure also brought large effects on aboveground biomass by resulting from plant consumption by livestock. These results suggest that aboveground biomass will decrease due to the cumulative effect of both grazing pressure and global warming in Mongolian semi-arid region. Belowground biomass was also reduced because decrease of aboveground biomass by global warming and grazing pressure changes.

Simulated evaporation and transpiration were decreased under GP1 and GP2 scenarios, whereas those were increased under GP3 and GP4 scenarios. Reduction of evaporation and transpiration was mainly caused by decrease of aboveground biomass and soil moisture content. Simulated evaporation under GW, GWP1, GWP2, GWP3 and GWP4 scenarios was decreased due to decrease of precipitation. On the other hand, transpiration was also decreased, which was mainly caused by vapor pressure, soil moisture, ground heat flux and net radiation.

Moreover, precipitation intensity in future condition was found smaller than present condition because precipitation amount was decreased in the future condition. Also it should be noted that the precipitation intensity changed according to different scenarios in the present and future condition. This is mainly caused by evaporation of intercepted rainfall by canopy. Different value of precipitation intensity also affected saturated excess runoff amount. Thus, infiltration rate was decreased when aboveground biomass were increased under different scenarios, which also effected discharge. These results suggest that surface runoff and infiltration rate were also controlled by land cover in Mongolian semi-arid region.

Figs. 125 and 126 show the variation changes of ecological and hydrological components. Fig. 125 shows the variation changes of simulated aboveground biomass and below ground biomass under all scenarios from baseline (B scenario). From these results, we found that simulated aboveground and belowground biomass under grazing pressure changes scenarios was larger than that of combination of climate changes and grazing pressure changes scenarios. These results suggest that global warming has larger effect than grazing pressure changes on aboveground and belowground biomass. Fig. 126 shows the variation changes of hydrological components, including evapotranspiration, difference of precipitation and evapotranspiration, soil moisture, discharge, ground water storage and precipitation under all scenarios. From these results, we found that evapotranspiration and soil moisture are more sensitive than other hydrological components to global warming and grazing pressure changes.

The summary of percentage changes of ecohydrological components under all scenarios from baseline (B scenario) are shown in Table 25. We found that ecohydrological components were decreased under all scenarios. However, larger percentage changes were found in future condition for ecohydrological components. These results suggest that ecohydrological components were decreased due to global warming in Mongolian semi-arid region.

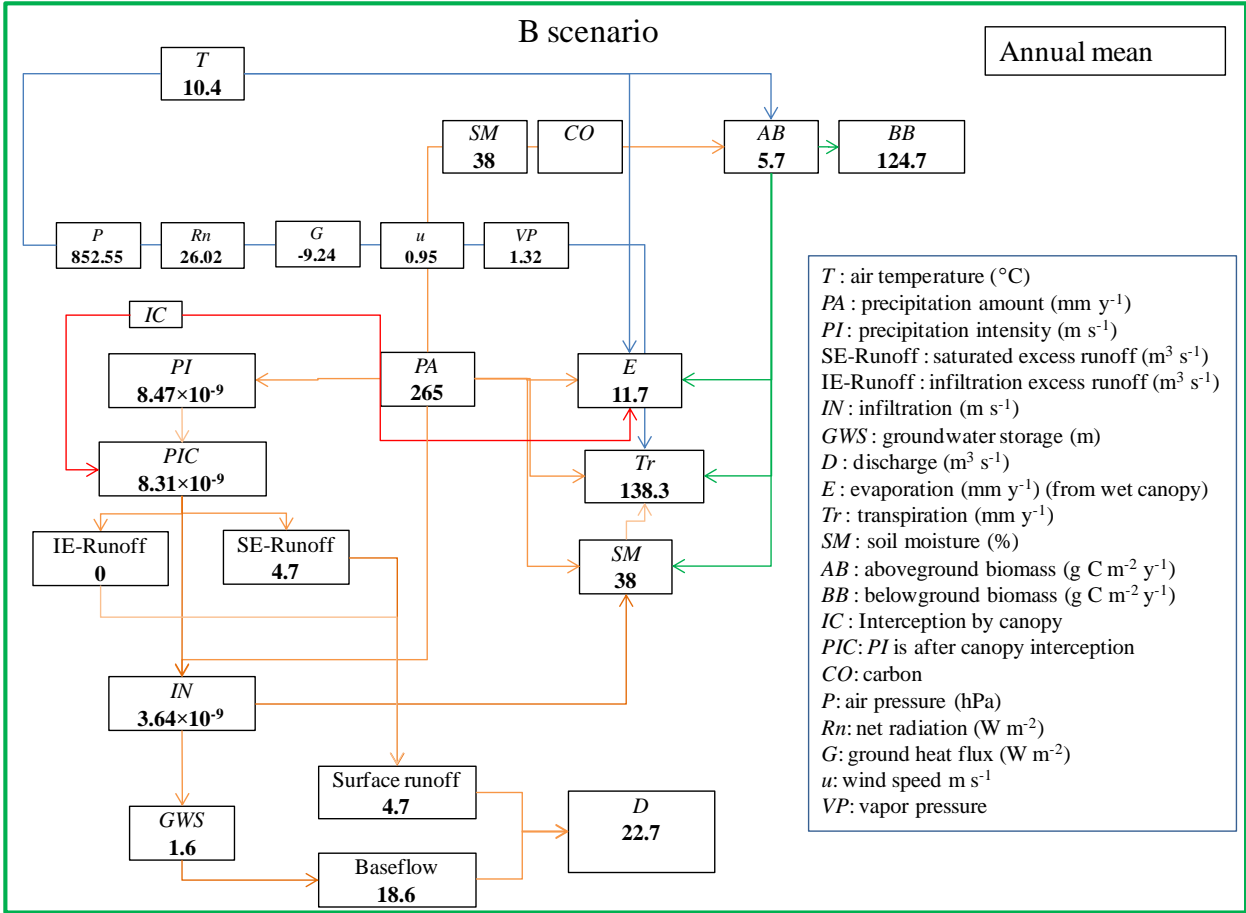


Fig. 115 Relation between ecohydrological components under B scenario

Red line: relation between *IC* and *PIC*
 Blue line: relation between *T* and *E* and *Tr*
 Green line: relation between *AB* and *E*, *Tr* and *SM*
 Orange line: relation between *P* and other variables

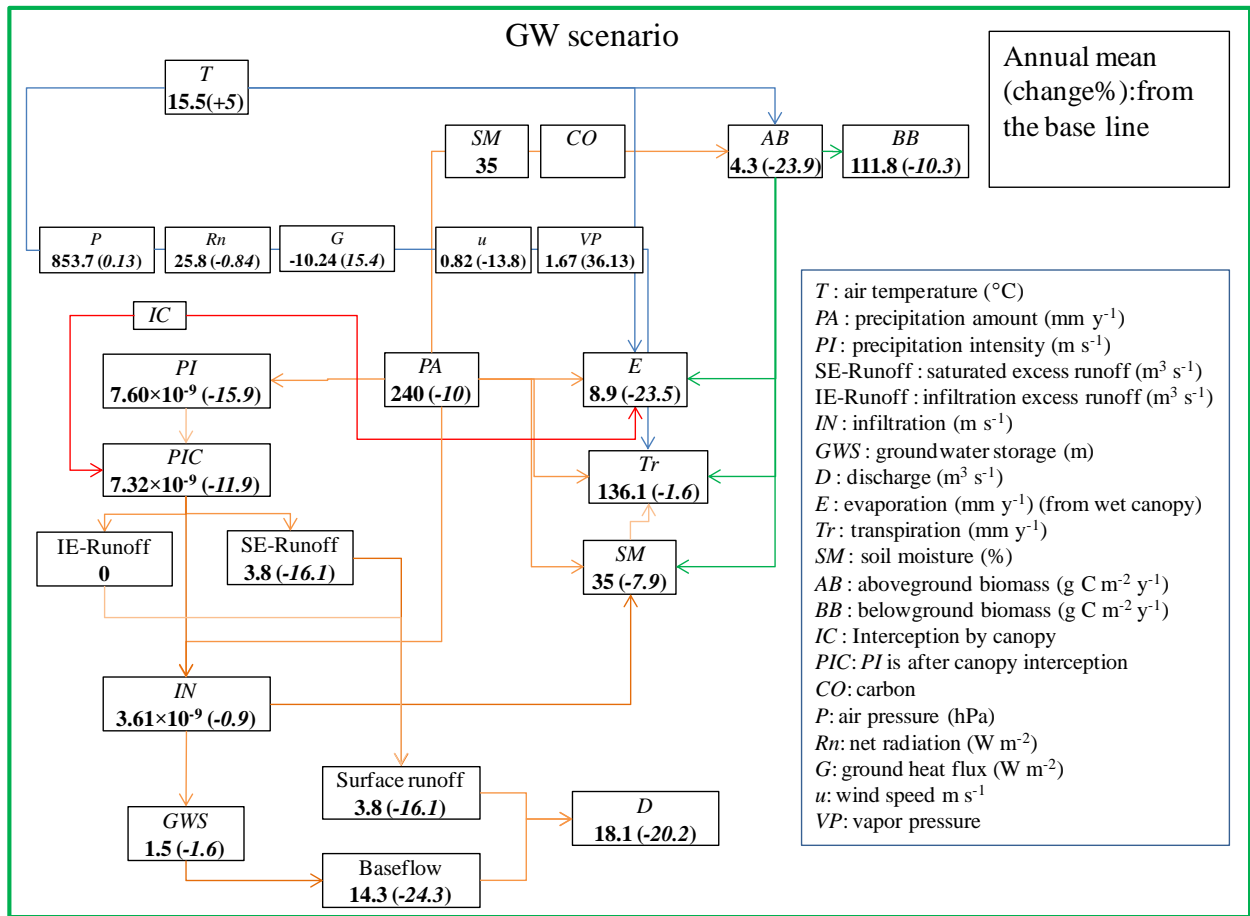


Fig. 116 Relation between ecohydrological components under GW scenario

- Red line: relation between *IC* and *PIC*
- Blue line: relation between *T* and *E* and *Tr*
- Green line: relation between *AB* and *E*, *Tr* and *SM*
- Orange line: relation between *P* and other variables

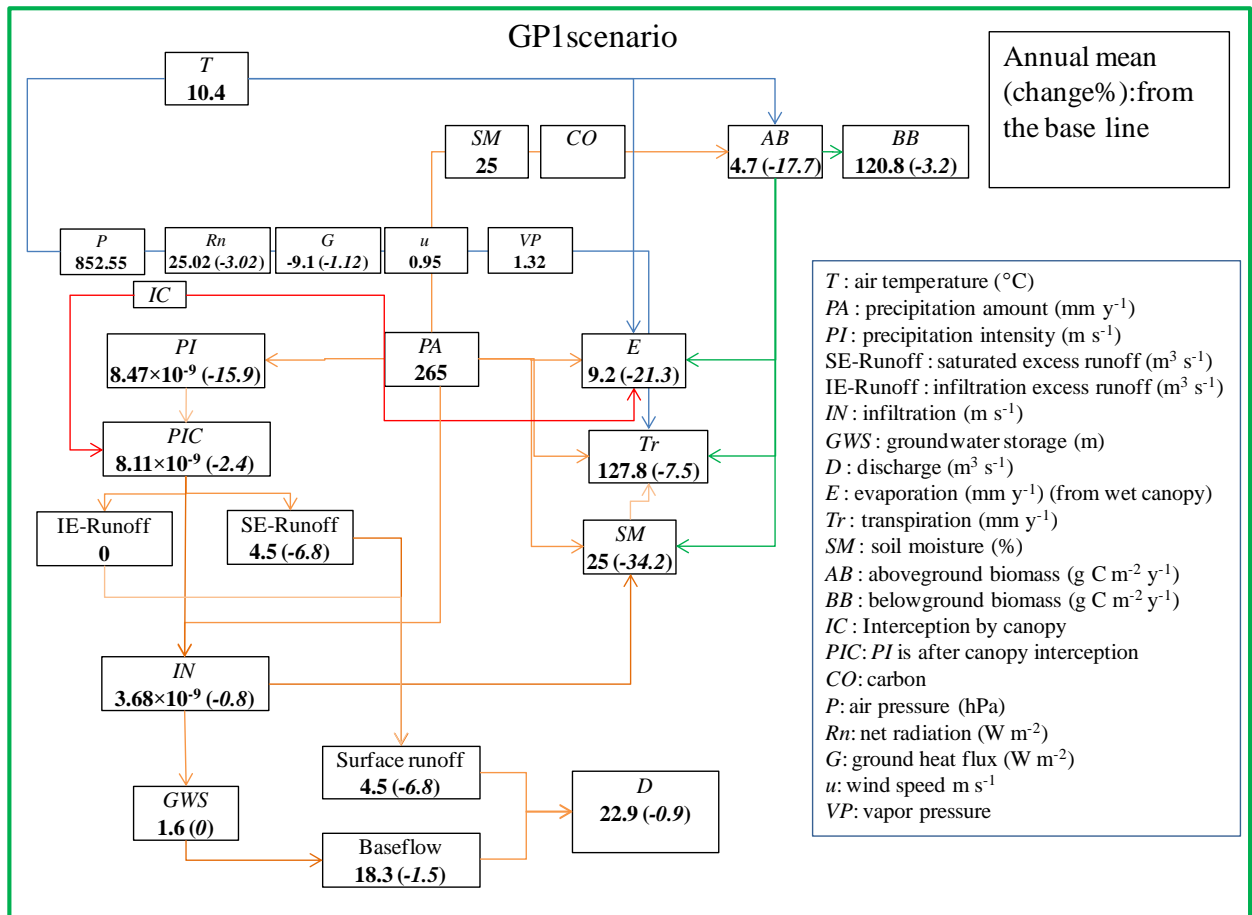


Fig. 117 Relation between ecohydrological components under GP1 scenario

- Red line: relation between *IC* and *PIC*
- Blue line: relation between *T* and *E* and *Tr*
- Green line: relation between *AB* and *E*, *Tr* and *SM*
- Orange line: relation between *P* and other variables

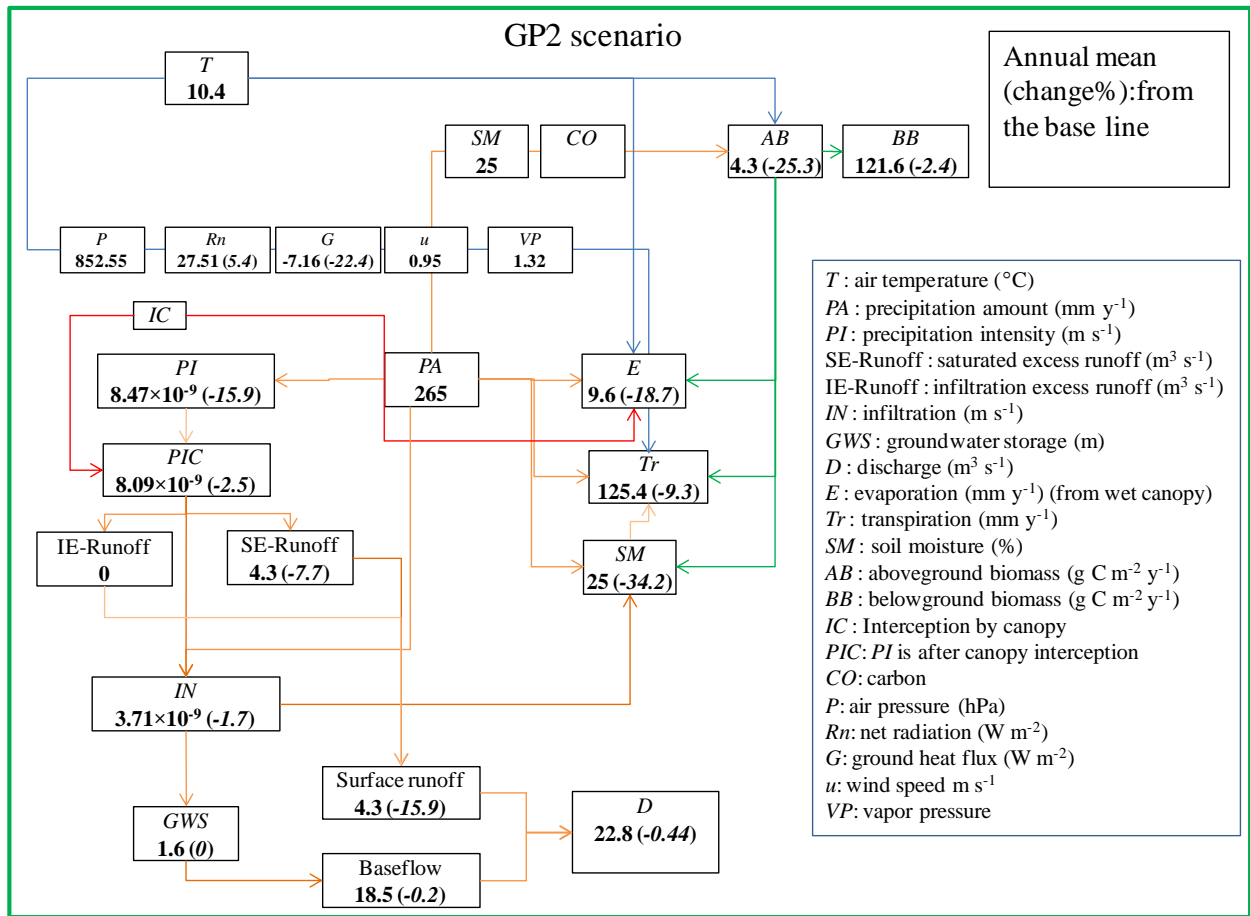


Fig. 118 Relation between ecohydrological components under GP2 scenario

Red line: relation between *IC* and *PIC*
 Blue line: relation between *T* and *E* and *Tr*
 Green line: relation between *AB* and *E*, *Tr* and *SM*
 Orange line: relation between *P* and other variables

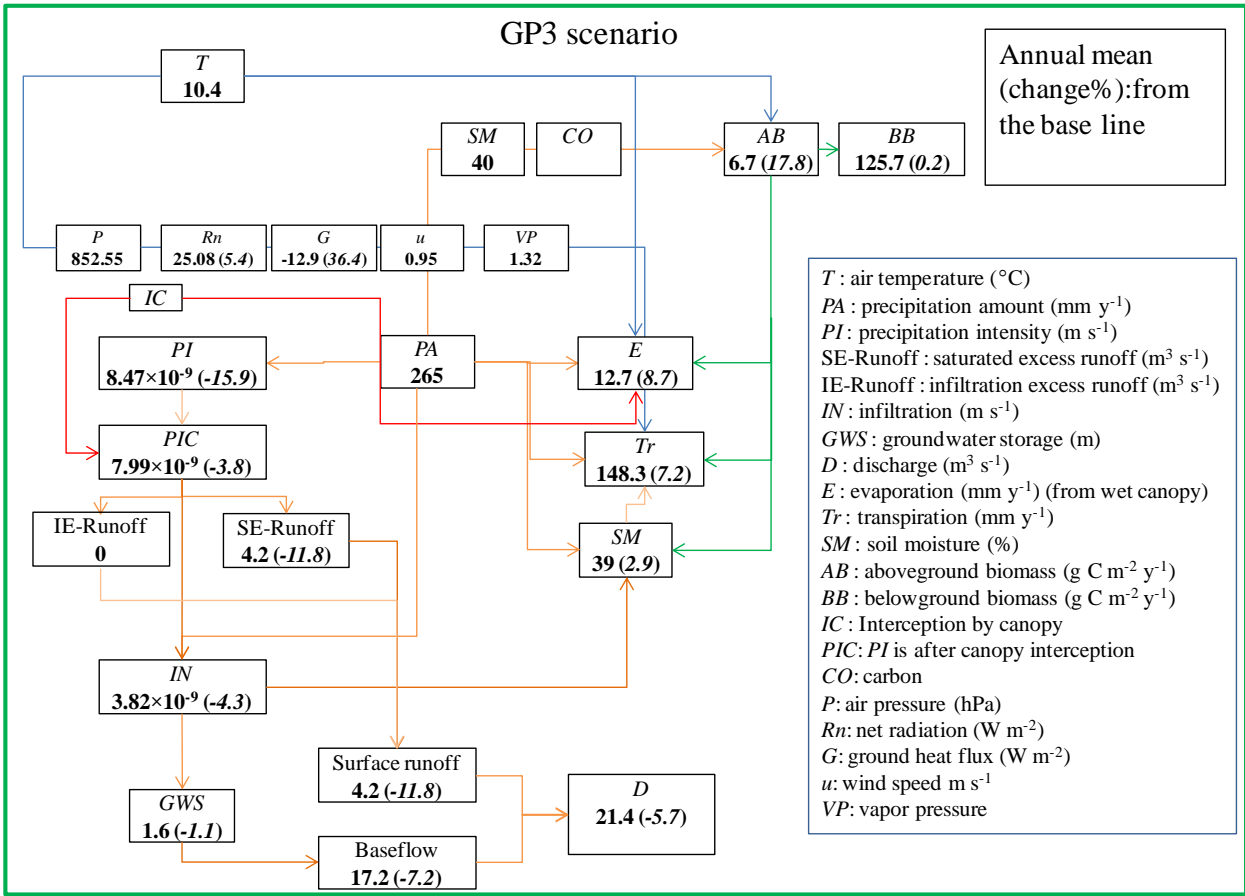


Fig. 119 Relation between ecohydrological components under GP3 scenario

- Red line: relation between *IC* and *PIC*
- Blue line: relation between *T* and *E* and *Tr*
- Green line: relation between *AB* and *E*, *Tr* and *SM*
- Orange line: relation between *P* and other variables

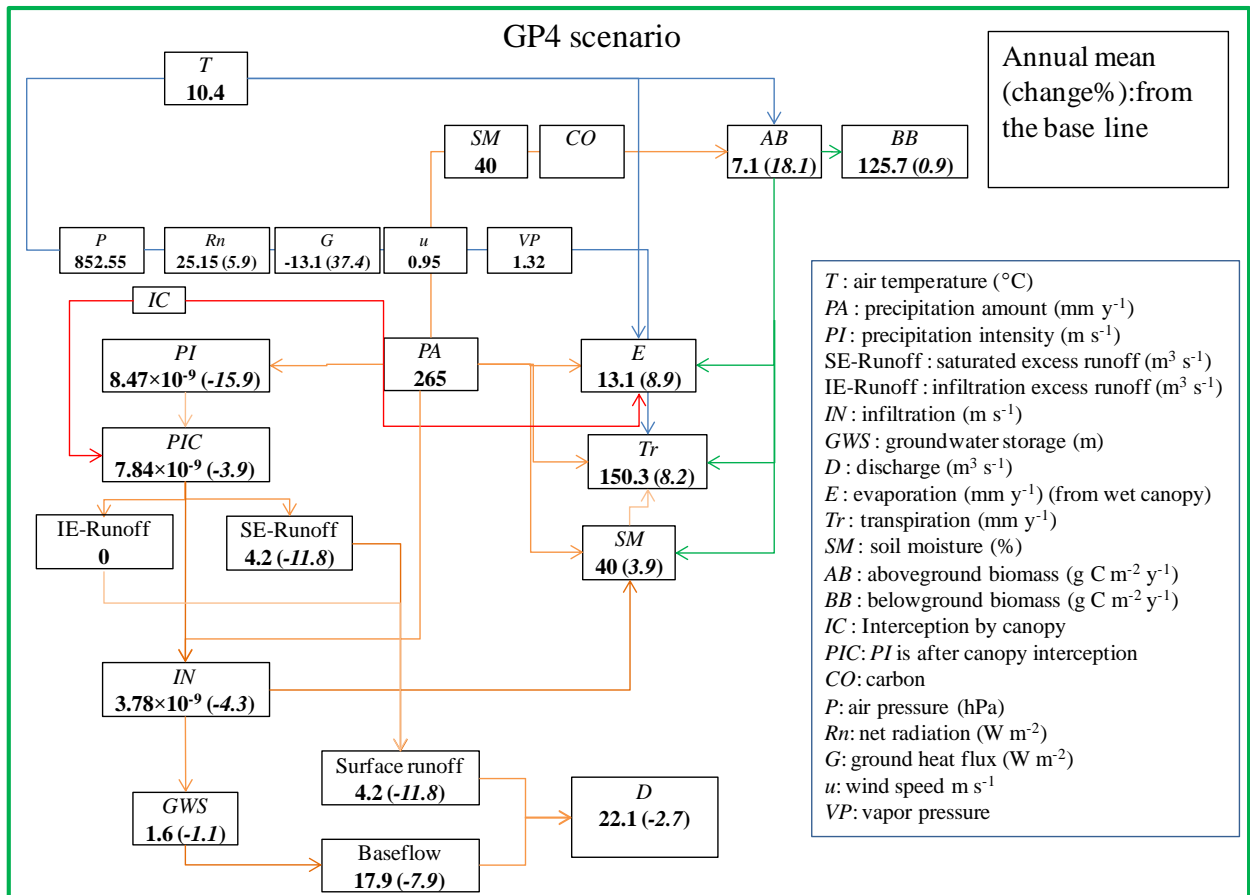


Fig. 120 Relation between ecohydrological components under GP4 scenario

- Red line: relation between *IC* and *PIC*
- Blue line: relation between *T* and *E* and *Tr*
- Green line: relation between *AB* and *E*, *Tr* and *SM*
- Orange line: relation between *P* and other variables

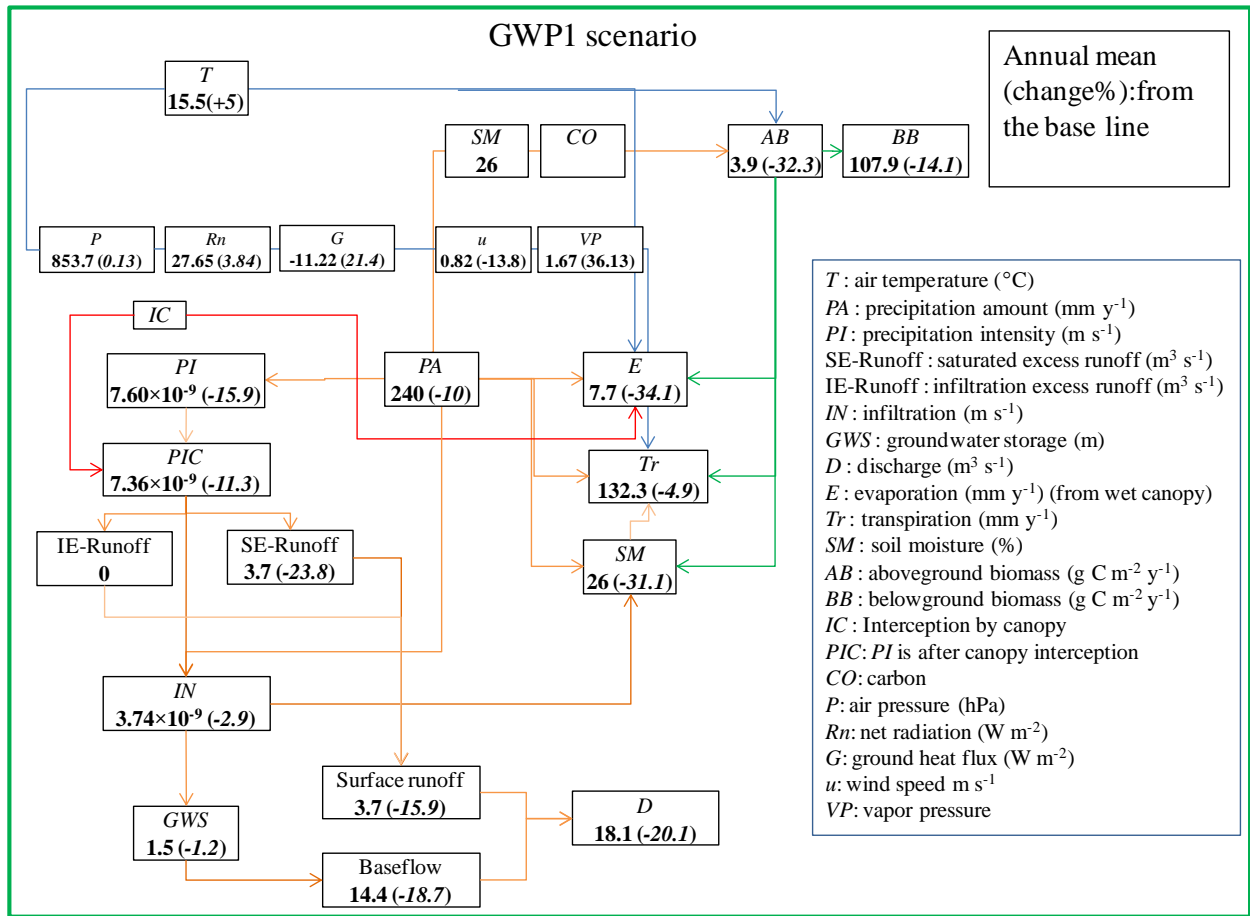


Fig. 121 Relation betweenecohydrological components under GWP1 scenario

Red line: relation between *IC* and *PIC*

Blue line: relation between *T* and *E* and *Tr*

Green line: relation between *AB* and *E*, *Tr* and *SM*

Orange line: relation between *P* and other variables

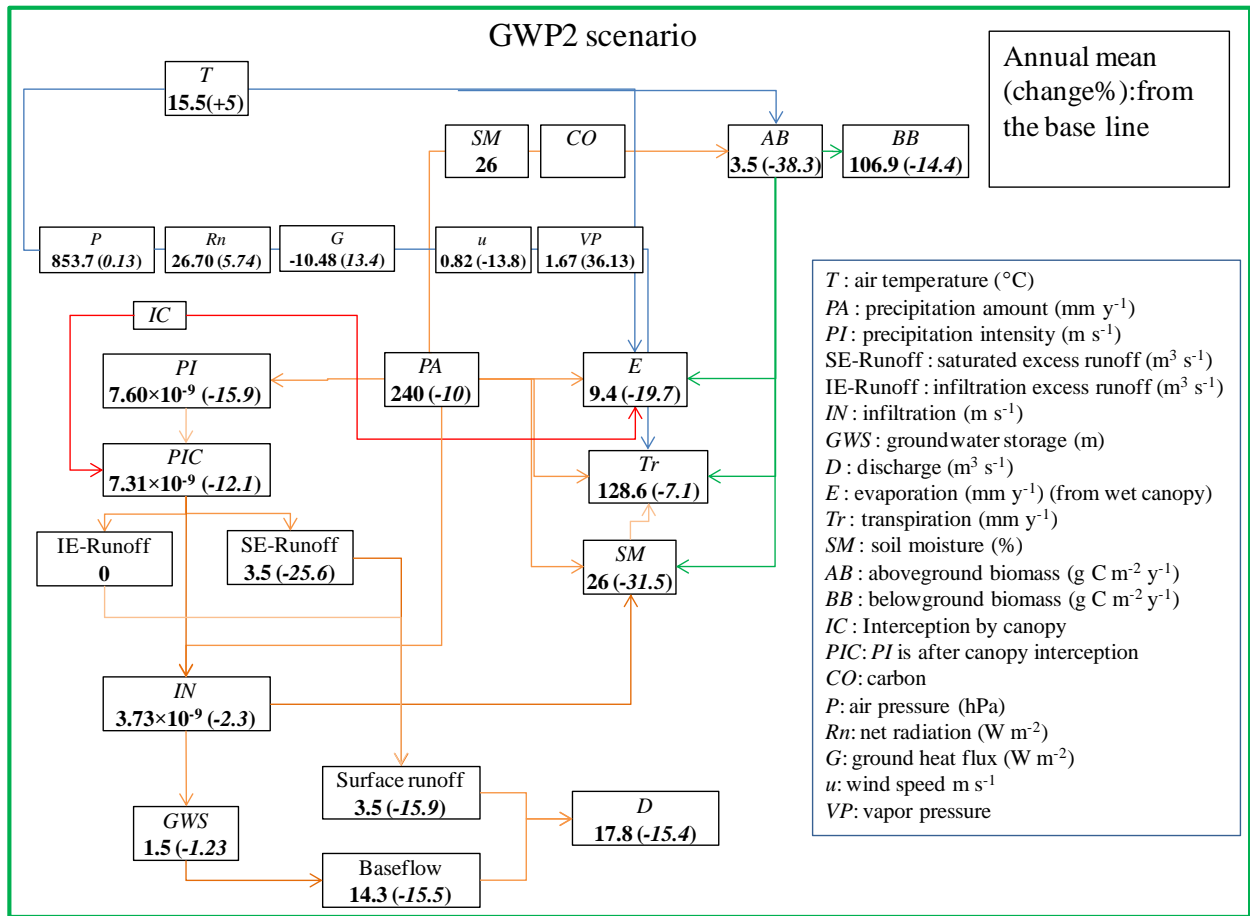


Fig. 122 Relation betweenecohydrological components under GWP2 scenario

Red line: relation between *IC* and *PIC*
 Blue line: relation between *T* and *E* and *Tr*
 Green line: relation between *AB* and *E*, *Tr* and *SM*
 Orange line: relation between *P* and other variables

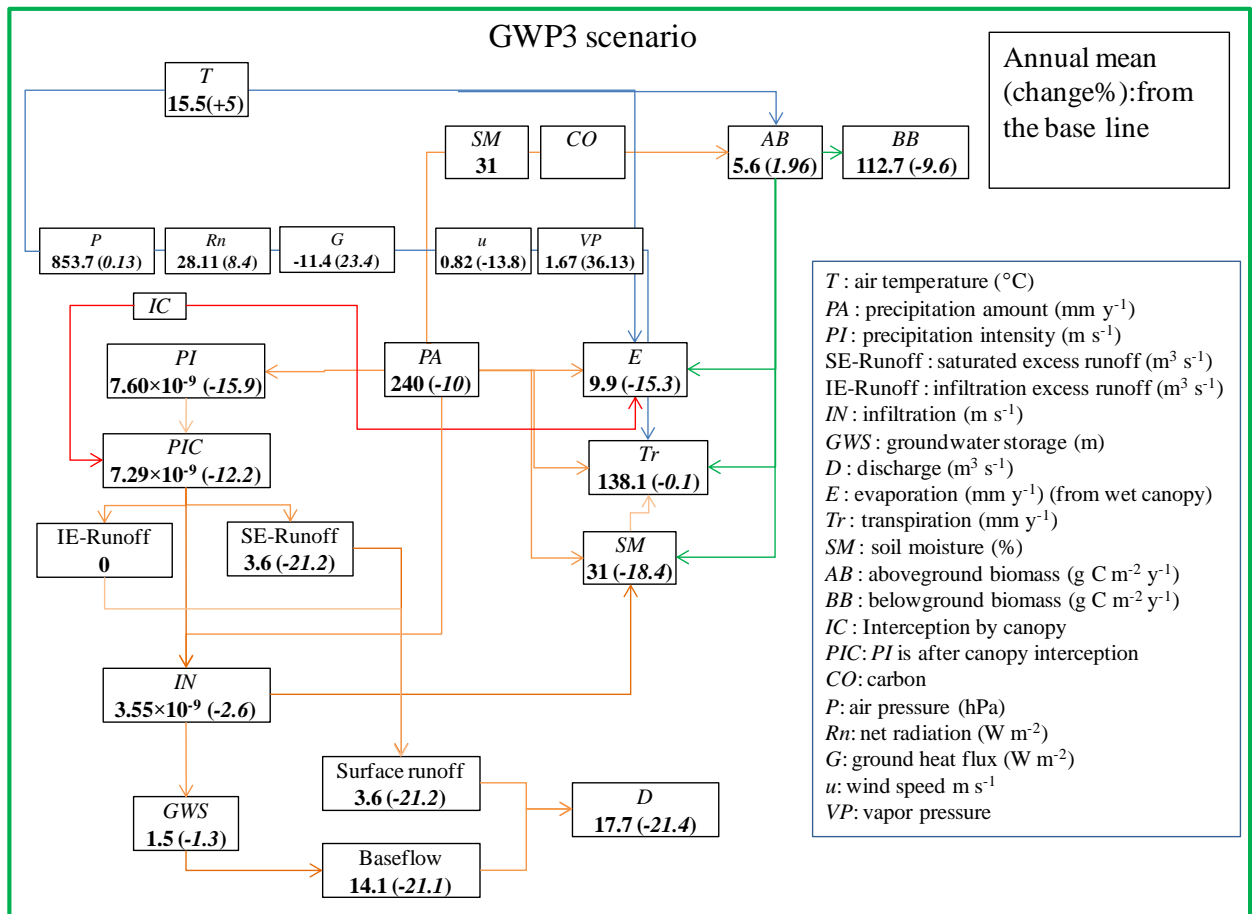


Fig. 123 Relation betweenecohydrological components under GWP3 scenario

- Red line: relation between *IC* and *PIC*
- Blue line: relation between *T* and *E* and *Tr*
- Green line: relation between *AB* and *E*, *Tr* and *SM*
- Orange line: relation between *P* and other variables

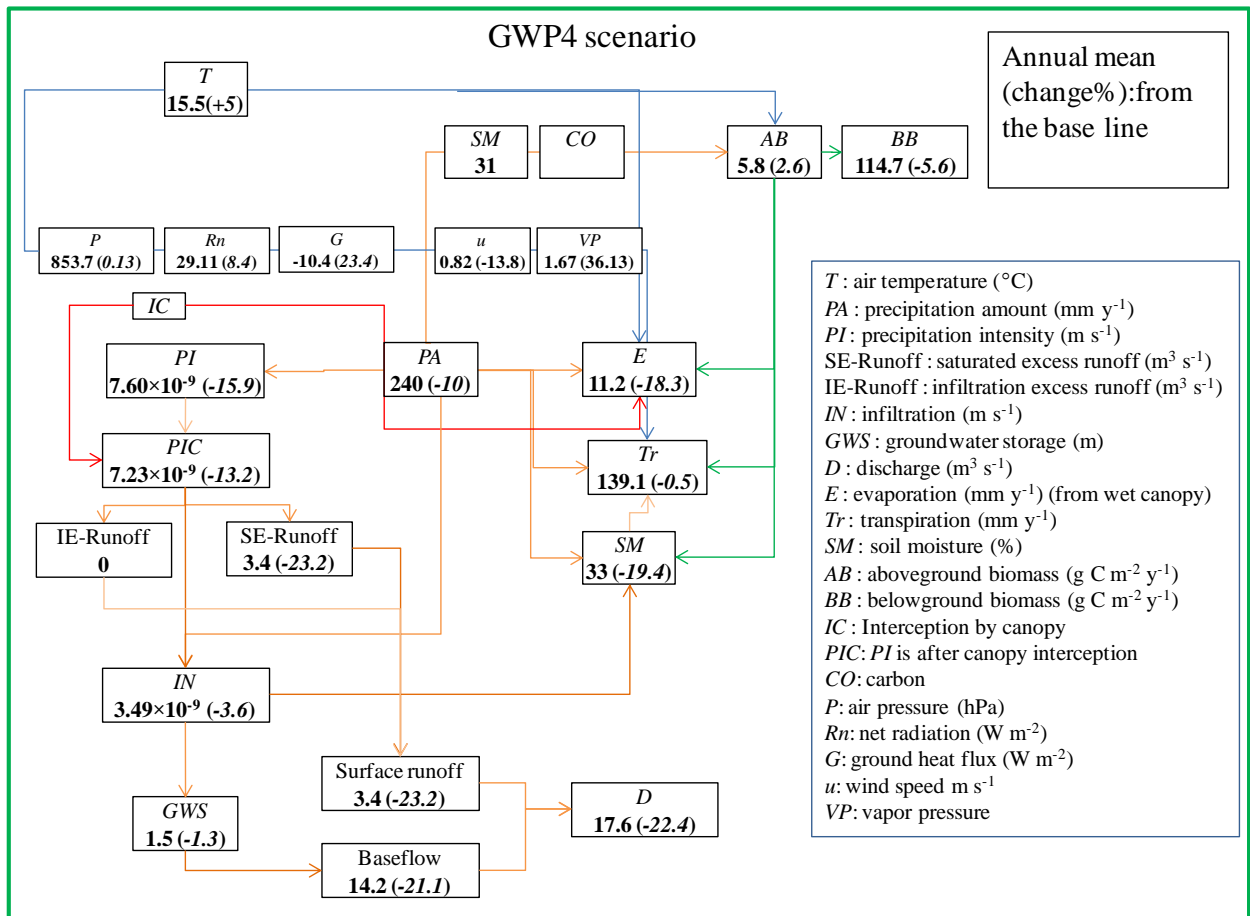


Fig. 124 Relation betweenecohydrological components under GWP4 scenario

- Red line: relation between *IC* and *PIC*
- Blue line: relation between *T* and *E* and *Tr*
- Green line: relation between *AB* and *E*, *Tr* and *SM*
- Orange line: relation between *P* and other variables

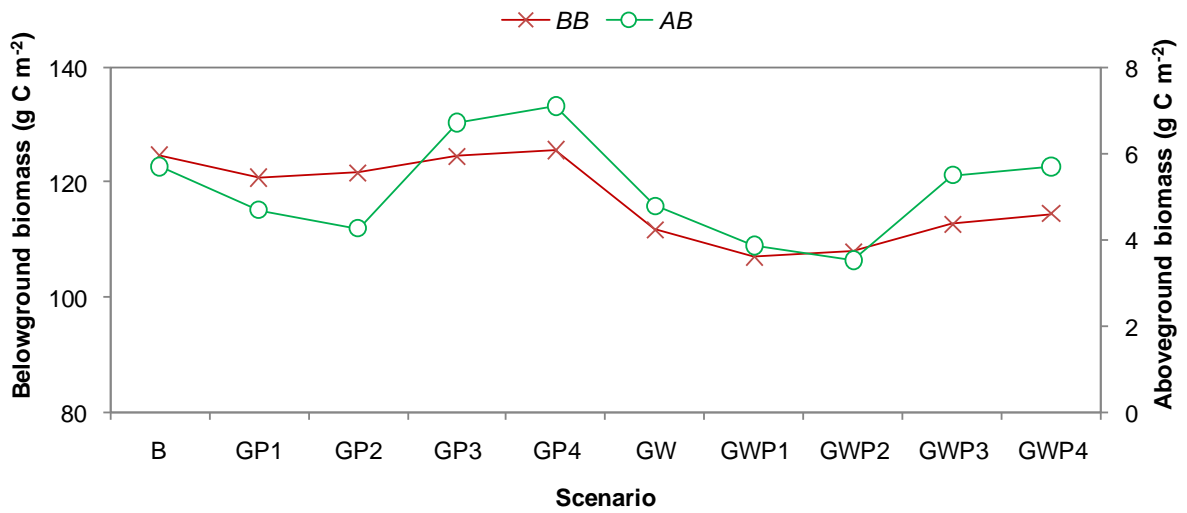


Fig. 125 Variation of aboveground biomass (g C m^{-2}) and belowground biomass (g C m^{-2}).

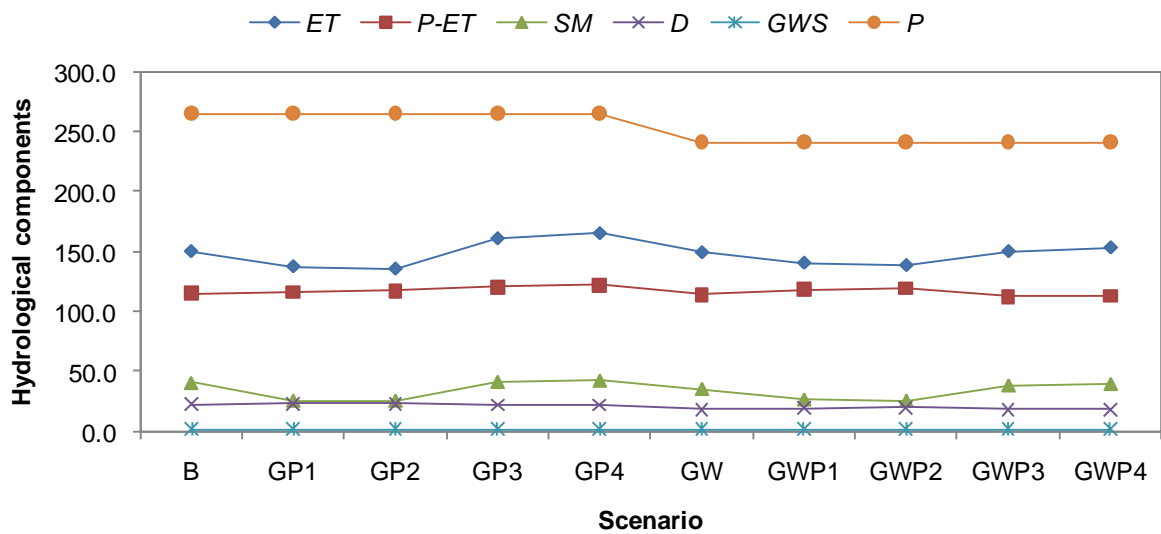


Fig. 126 Variation of evapotranspiration (ET : mm y^{-1}), difference of precipitation (P : mm y^{-1}) and ET ($P-ET$: mm y^{-1}) and soil moisture (SM : %), discharge (D : $\text{m}^3 \text{s}^{-1}$) ground water storage (GWS : m) and P under different scenarios.

Table 25 Percentage of ecohydrological components under different scenarios from B scenario.

| Scenarios | <i>AB</i> | <i>BB</i> | <i>ET</i> | <i>P-ET</i> | <i>SM</i> | <i>D</i> |
|-----------|-----------|-----------|-----------|-------------|-----------|----------|
| GW | -16.0 | -10.3 | -0.7 | -0.9 | -12.5 | -18.2 |
| GP1 | -17.8 | -3.1 | -8.7 | -0.9 | -37.5 | -3.2 |
| GP2 | -25.3 | -2.4 | -10.0 | -1.7 | -37.5 | -4.1 |
| GP3 | 17.9 | -0.1 | 7.3 | 4.3 | 2.5 | -2.7 |
| GP4 | 24.6 | 0.8 | 10.3 | 6.1 | 5.0 | -0.9 |
| GWP1 | -32.3 | -14.1 | -6.7 | -2.6 | -35.0 | -15.0 |
| GWP2 | -38.4 | -13.4 | -8.0 | -3.5 | -37.5 | -17.7 |
| GWP3 | 3.5 | -9.6 | 0.8 | -2.6 | -5.0 | -19.1 |
| GWP4 | 5.8 | -8.2 | 2.1 | -2.2 | -2.0 | -19.1 |

AB: aboveground biomass; *BB*: belowground biomass; *ET*: evapotranspiration; *P-ET*: difference of precipitation and; *SM*: soil moisture; *D*: discharge.

In order to look at the difference of spatial distribution of simulated ecohydrological components, we compared base line (B scenario) and GW scenario; grazing pressure change scenarios (GP1-GP4) and combination of two (GWP1-GWP2) scenarios.

Fig. 127a) shows spatially estimated aboveground biomass under B scenario in present condition. The estimated aboveground biomass ranged from 4 to 8 g C m² in forest site, whereas between 2 and 4 g C m² in grassland site. Spatial distribution of simulated aboveground biomass was decreased under GW scenario from 2 to 6 g C m² in Fig. 127d). Under GW scenario, simulated aboveground biomass was decreased by about 2 g C m² in grassland site (Fig. 127g). The small changes were also observed in forest area. Under GP1 (Fig. 128g), GWP1 (Fig. 128g), GP2 (Fig. 129g) and GWP2 (Fig. 129g) scenarios, simulated aboveground biomass was decreased by 0.3 to 0.6 g C m². However, coefficient of variation indicates larger changes were observed in grassland than forest area (Figs. 128i) and 128i)). Figs. 130a), 130d), 131a) and 131d) show simulated aboveground biomass under from GP3 to GP4 and from GWP3 to GWP4 scenarios. Under GWP3 and GPW4 scenarios, simulated aboveground biomass was decreased by about 0.3 to 1.5 g C m² in the Kherlen river basin (Figs. 130g and 131g).

Figs. 132g), 133g), 134g), 135g) and 136g) show simulated belowground biomass was decreased by 10 to 25 g C m² over the Kherlen river basin under all scenarios.

Figs. 137a) and 137d) show evapotranspiration under B and GW scenario. Evapotranspiration ranged between 150 and 170 mm y⁻¹ in forest area whereas it was ranged from 120 to 140 mm y⁻¹ in grassland area. Under GW scenario, simulated evapotranspiration ranged from 160 to 180 mm y⁻¹ in grassland area and 110 – 140 mm y⁻¹ for forest area. Evapotranspiration was decreased by 20 mm y⁻¹ in forest site whereas it was increased 15 mm y⁻¹ in grassland area in Fig. 137g).

Under GP1 (Fig. 138a), GWP1 (Fig. 138d), GP2 (Fig. 139a) and GWP2 (Fig. 139d) scenarios, spatial distribution of simulated evapotranspiration shows similar pattern of changes over the Kherlen river basin. However, coefficient of variation indicates larger changes observed in forest area than grassland area (Figs. 138i) and 139i)).

Figs. 140g) and 141g) show evapotranspiration changes in GP3-GP4 and GWP3-GWP4 scenarios. Under these scenarios, evapotranspiration decreased by 60 mm y⁻¹ in forest area, whereas it was decreased 10 mm y⁻¹ in grassland area as shown in Figs. 140g) and 141g).

Under all scenarios (Figs. 142 - 145), spatial distribution of simulated soil moisture was ranged from 26 and 40 % over the Kherlen river basin.

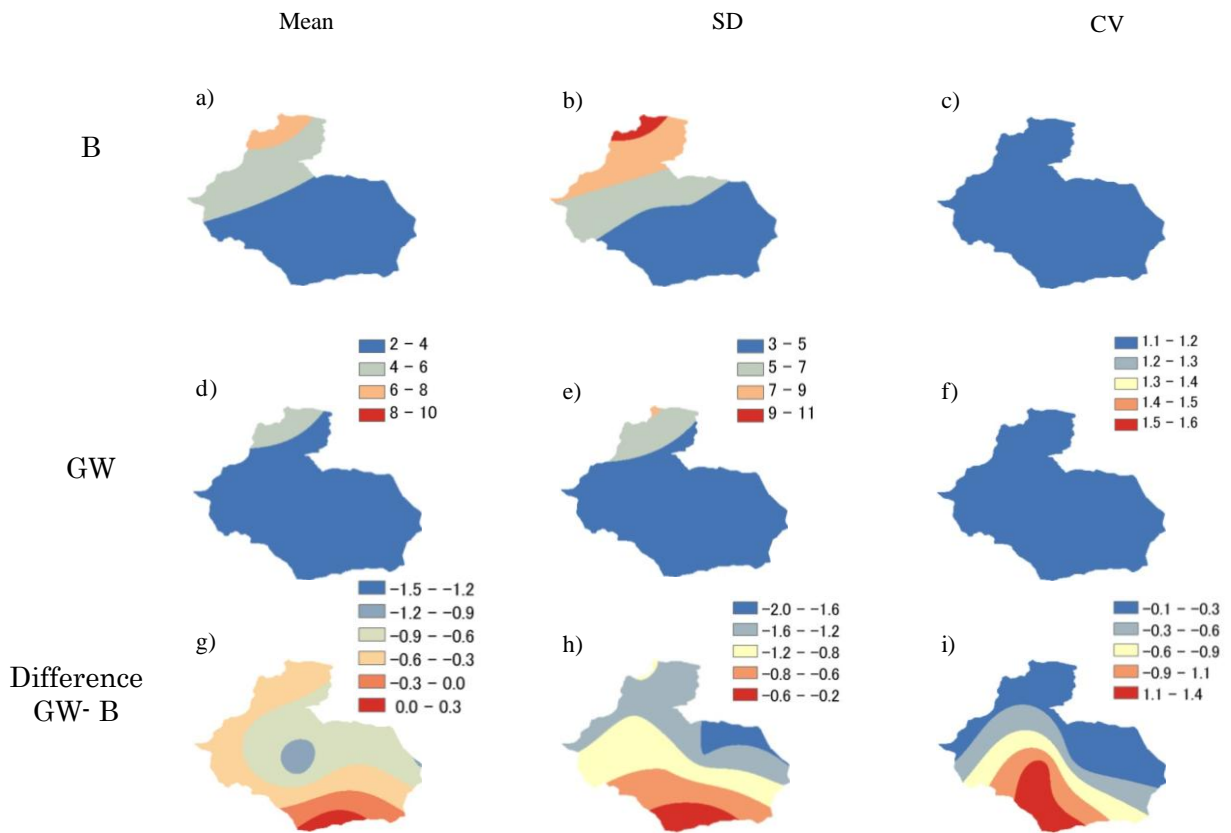


Fig. 127 Annual mean, standard deviation (SD) and coefficient of variation (CV) of aboveground biomass (*AB*) under B and GW scenarios. The panels a), b) and c) represent mean, SD and CV of *AB* in B scenario. The panels d), e) and f) represent mean, SD and CV of *AB* under GW scenario. The panels g), h) and i) represent the difference of mean, SD and CV of *AB* between GW and B scenarios. (Unit is g C m^{-2})

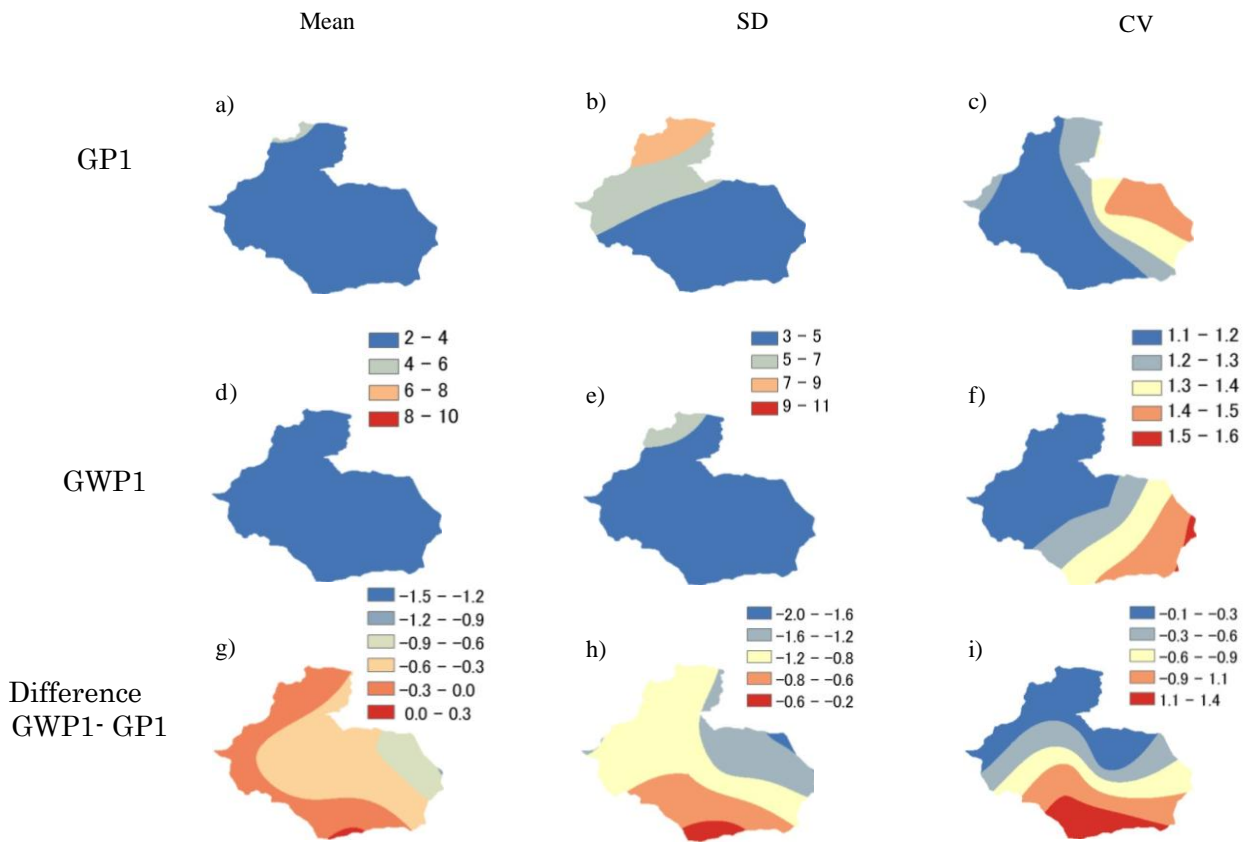


Fig. 128 Annual mean, standard deviation (SD) and coefficient of variation (CV) of aboveground biomass (*AB*) under GP1 and GWP1 scenarios. The panels a), b) and c) represent mean, SD and CV of *AB* in GP1 scenario. The panels d), e) and f) represent mean, SD and CV of *AB* under GWP1 scenario. The panels g), h) and i) represent the difference of mean, SD and CV of *AB* between GWP1 and GP1 scenarios. (Unit is g C m^{-2})

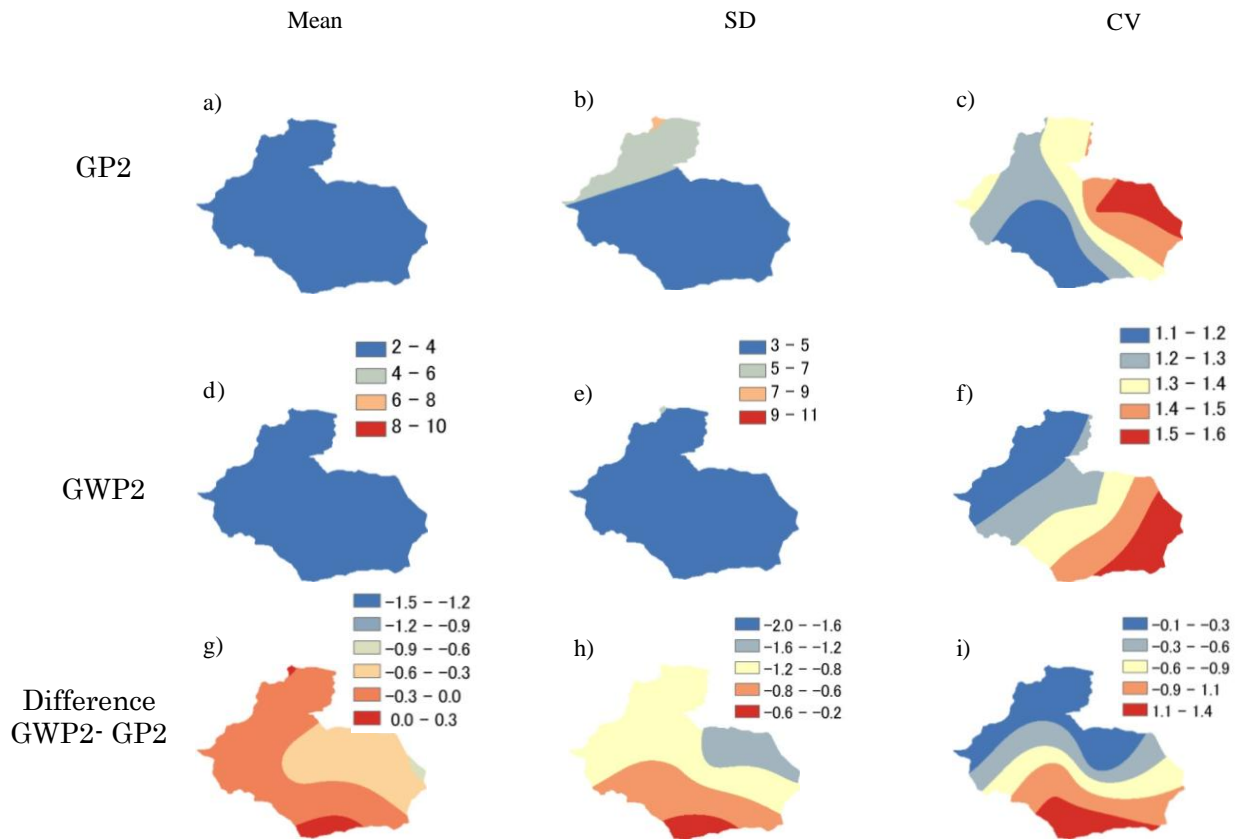


Fig. 129 Annual mean, standard deviation (SD) and coefficient of variation (CV) of aboveground biomass (*AB*) under GP2 and GWP2 scenarios. The panels a), b) and c) represent mean, SD and CV of *AB* in GP2 scenario. The panels d), e) and f) represent mean, SD and CV of *AB* under GWP2 scenario. The panels g), h) and i) represent the difference of mean, SD and CV of *AB* between GWP2 and GP2 scenarios. (Unit is g C m^{-2})

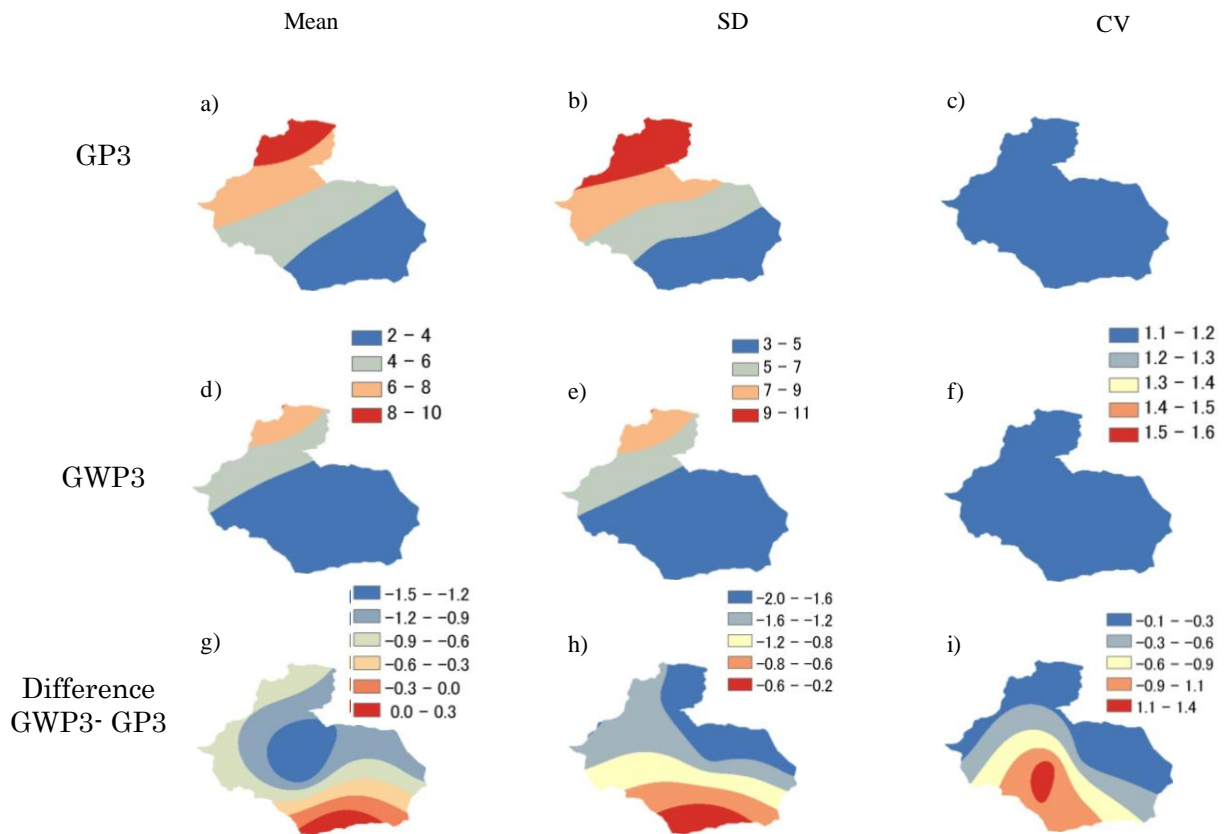


Fig. 130 Annual mean, standard deviation (SD) and coefficient of variation (CV) of aboveground biomass (*AB*) under GP3 and GWP3 scenarios. The panels a), b) and c) represent mean, SD and CV of *AB* in GP3 scenario. The panels d), e) and f) represent mean, SD and CV of *AB* under GWP3 scenario. The panels g), h) and i) represent the difference of mean, SD and CV of *AB* between GWP3 and GP3 scenarios. (Unit is g C m^{-2})

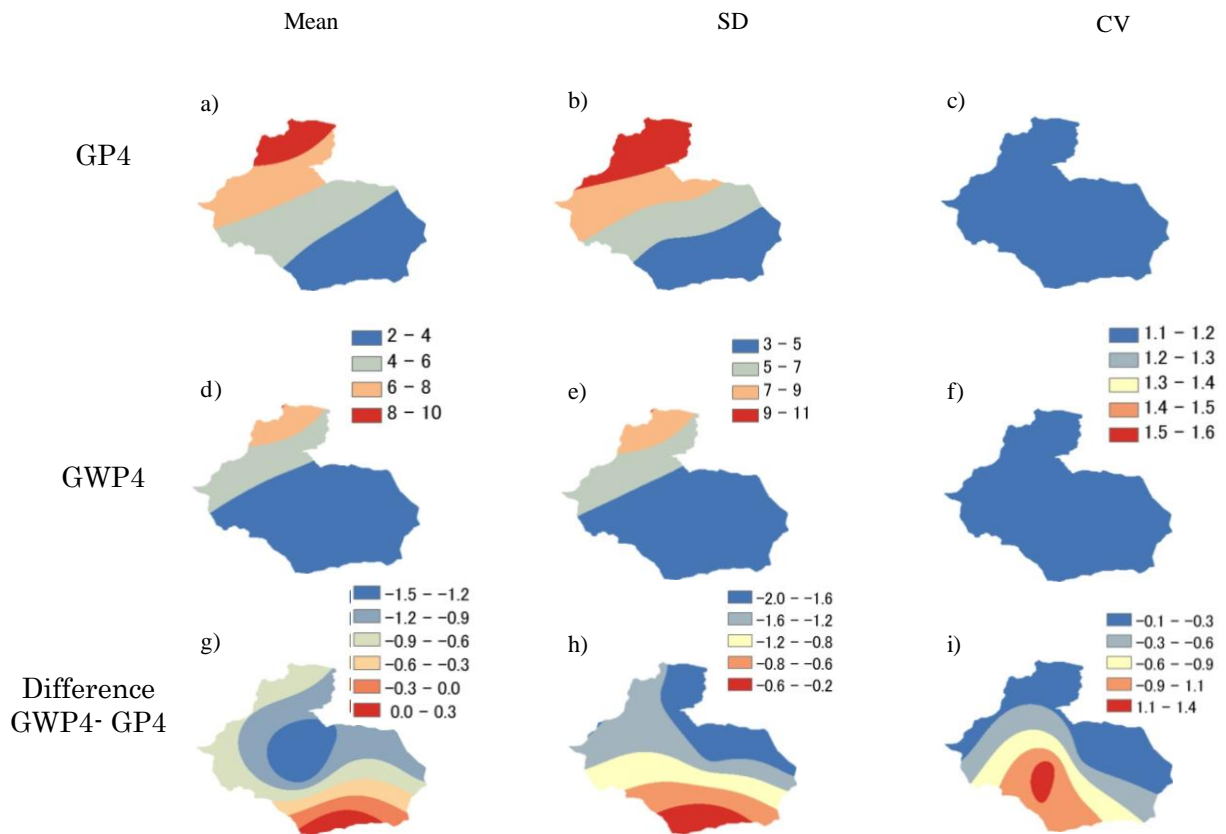


Fig. 131 Annual mean, standard deviation (SD) and coefficient of variation (CV) of aboveground biomass (*AB*) under GP4 and GWP4 scenarios. The panels a), b) and c) represent mean, SD and CV of *AB* in GP4 scenario. The panels d), e) and f) represent mean, SD and CV of *AB* under GWP3 scenario. The panels g), h) and i) represent the difference of mean, SD and CV of *AB* between GWP4 and GP4 scenarios. (Unit is g C m^{-2})

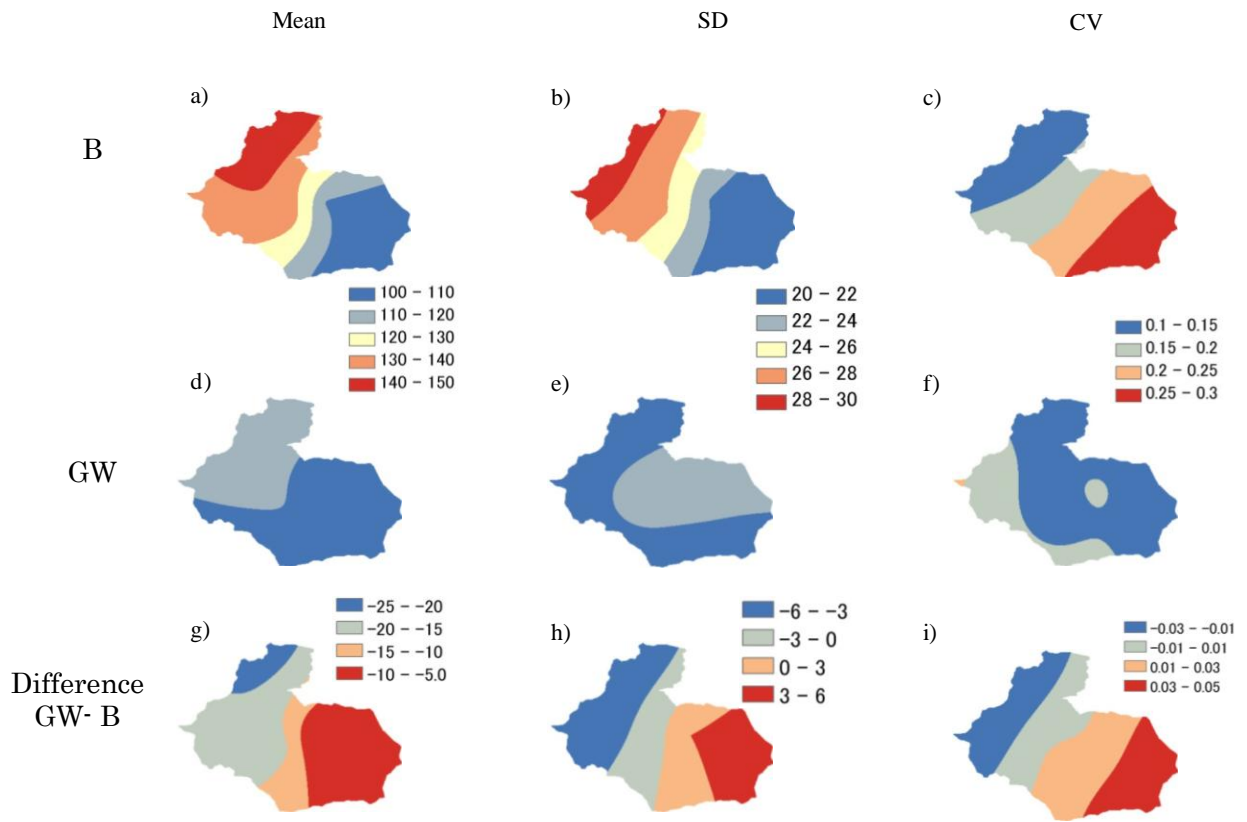


Fig. 132 Annual mean, standard deviation (SD) and coefficient of variation (CV) of belowground biomass (*BB*) under B and GW scenarios. The panels a), b) and c) represent mean, SD and CV of *BB* in B scenario. The panels d), e) and f) represent mean, SD and CV of *BB* under GW scenario. The panels g), h) and i) represent the difference of mean, SD and CV of *BB* between GW and B scenarios. (Unit is g C m^{-2})

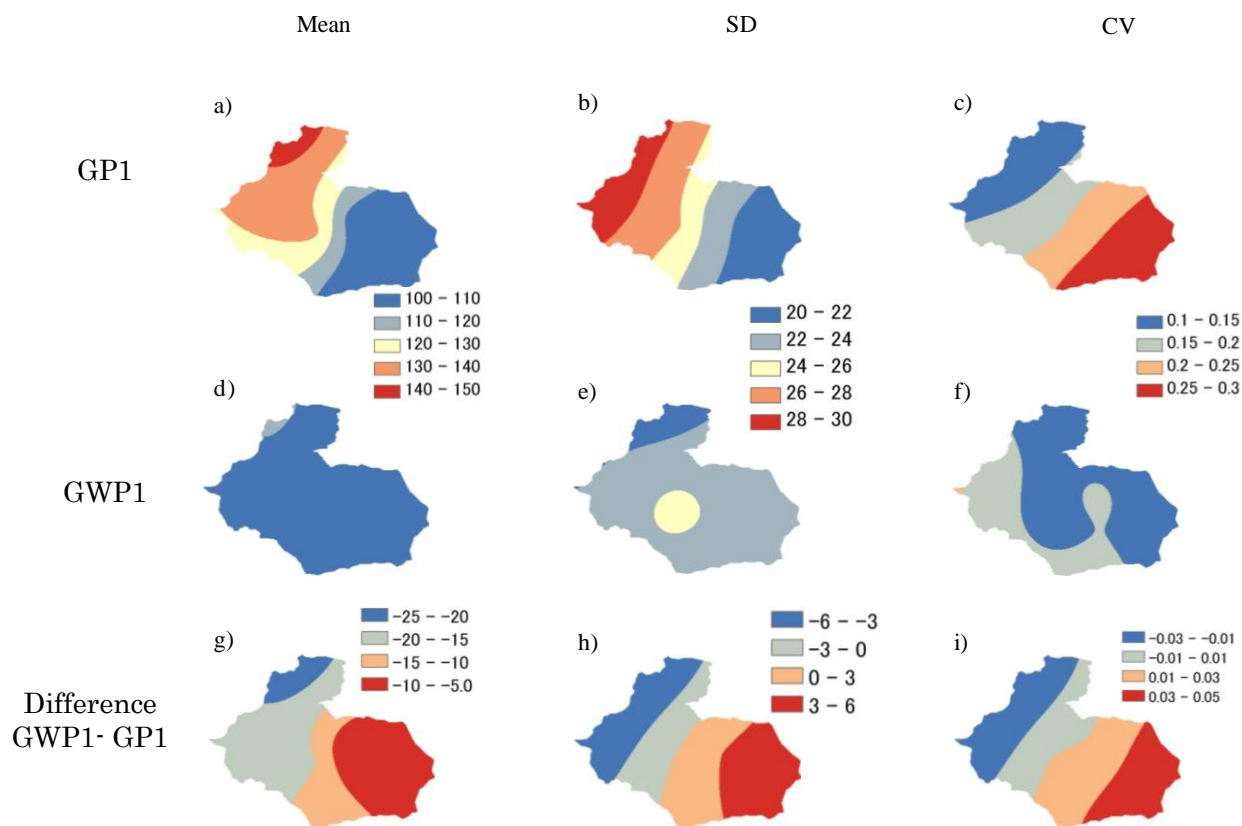


Fig. 133 Annual mean, standard deviation (SD) and coefficient of variation (CV) of belowground biomass (*BB*) under GP1 and GWP1 scenarios. The panels a), b) and c) represent mean, SD and CV of *BB* in GP1 scenario. The panels d), e) and f) represent mean, SD and CV of *BB* under GWP1 scenario. The panels g), h) and i) represent the difference of mean, SD and CV of *BB* between GWP1 and GP1 scenarios. (Unit is g C m^{-2})

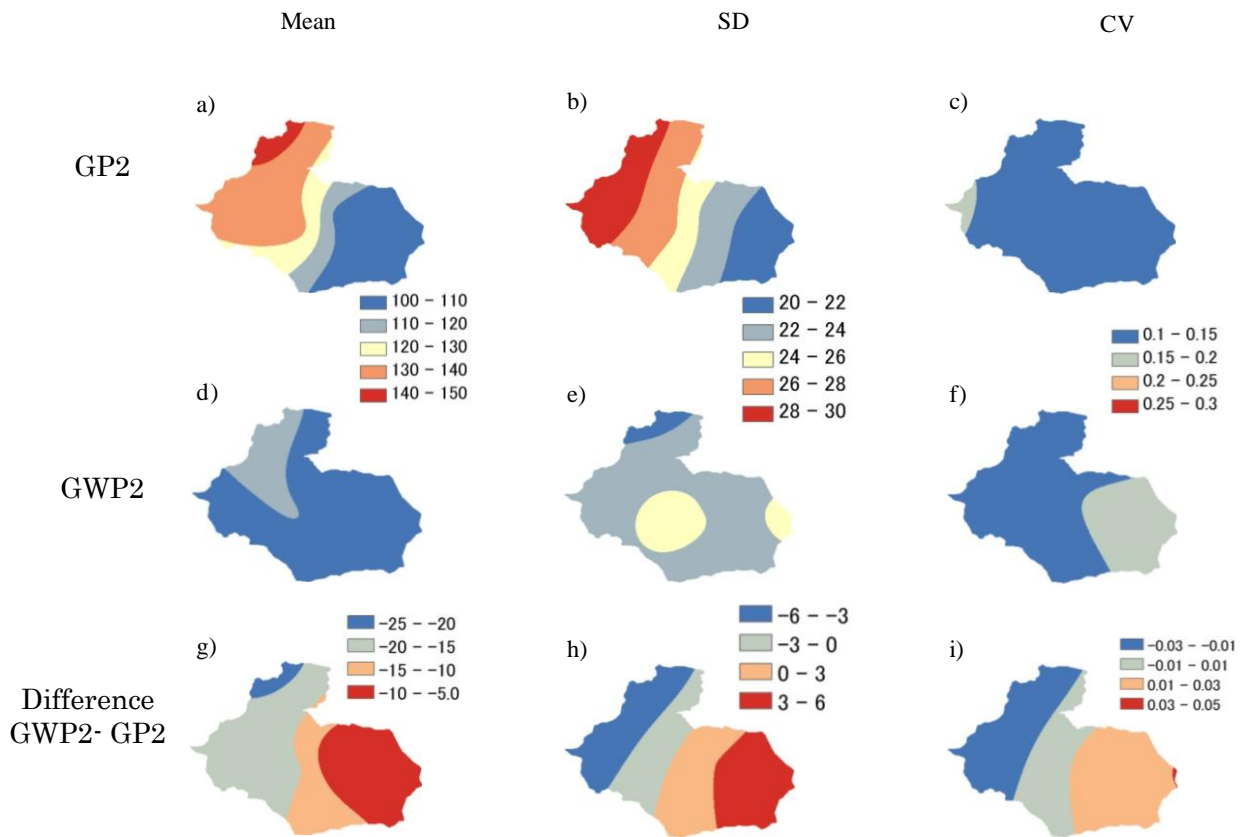


Fig. 134 Annual mean, standard deviation (SD) and coefficient of variation (CV) of belowground biomass (*BB*) under GP2 and GWP2 scenarios. The panels a), b) and c) represent mean, SD and CV of *BB* in GP2 scenario. The panels d), e) and f) represent mean, SD and CV of *BB* under GWP2 scenario. The panels g), h) and i) represent the difference of mean, SD and CV of *BB* between GWP2 and GP2 scenarios. (Unit is g C m^{-2})

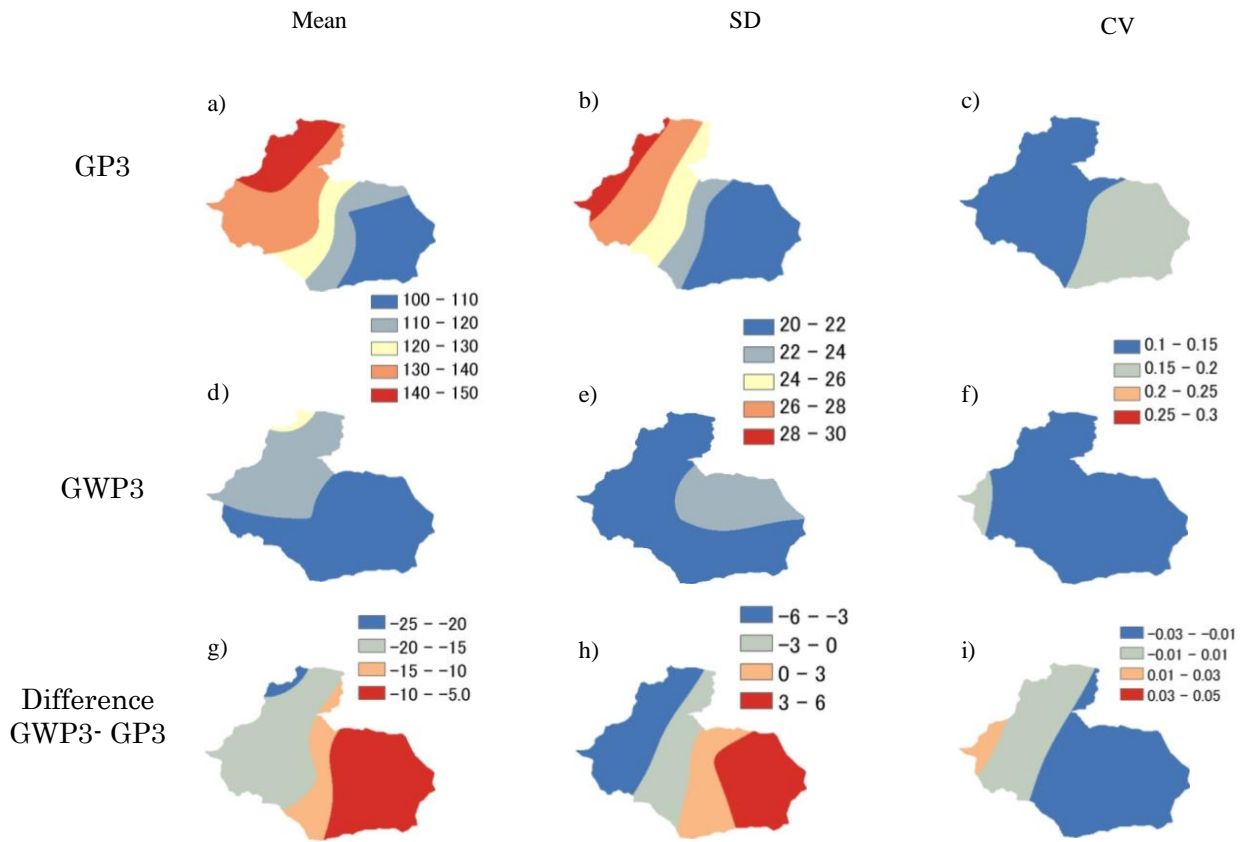


Fig. 135 Annual mean, standard deviation (SD) and coefficient of variation (CV) of belowground biomass (*BB*) under GP3 and GWP3 scenarios. The panels a), b) and c) represent mean, SD and CV of *BB* in GP3 scenario. The panels d), e) and f) represent mean, SD and CV of *BB* under GWP3 scenario. The panels g), h) and i) represent the difference of mean, SD and CV of *BB* between GWP3 and GP3 scenarios. (Unit is g C m^{-2})

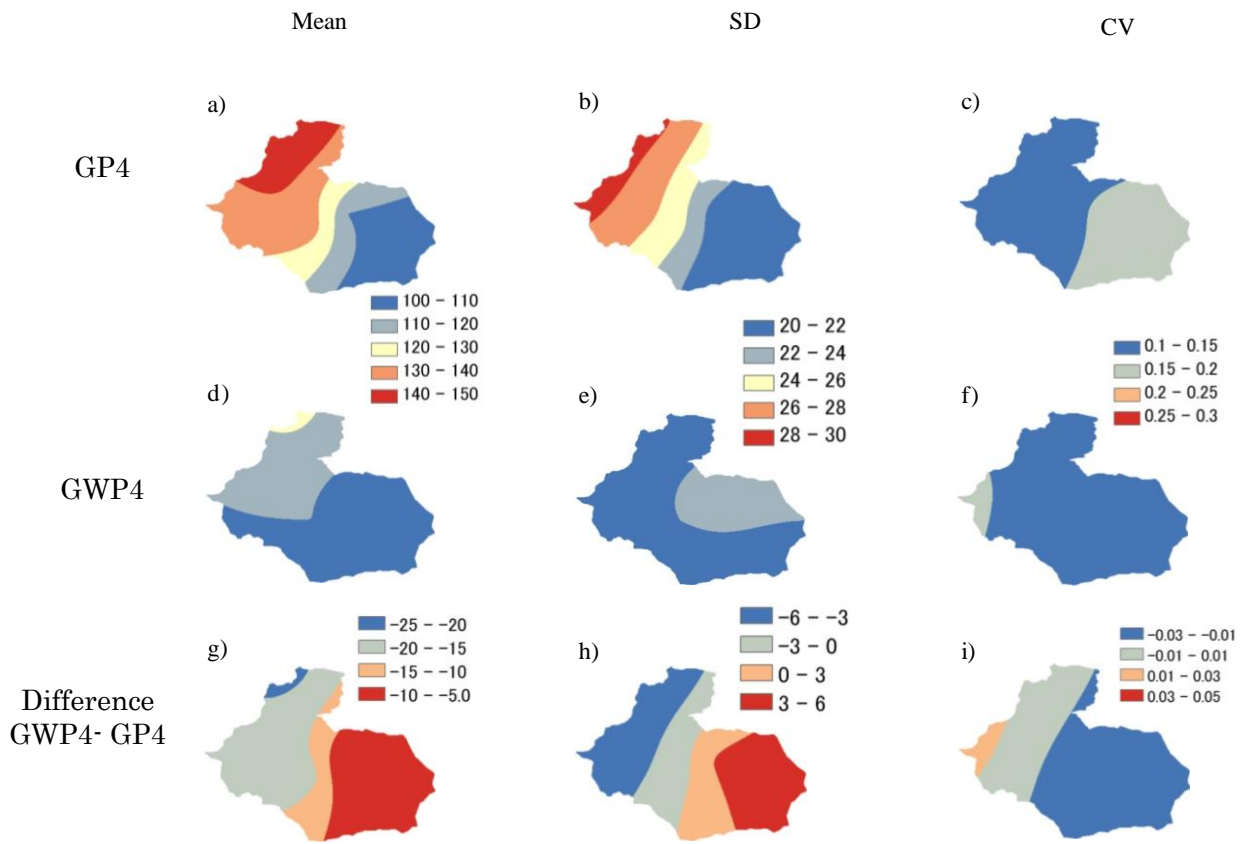


Fig. 136 Annual mean, standard deviation (SD) and coefficient of variation (CV) of belowground biomass (*BB*) under GP4 and GWP4 scenarios. The panels a), b) and c) represent mean, SD and CV of *BB* in GP4 scenario. The panels d), e) and f) represent mean, SD and CV of *BB* under GWP3 scenario. The panels g), h) and i) represent the difference of mean, SD and CV of *BB* between GWP4 and GP4 scenarios. (Unit is g C m^{-2})

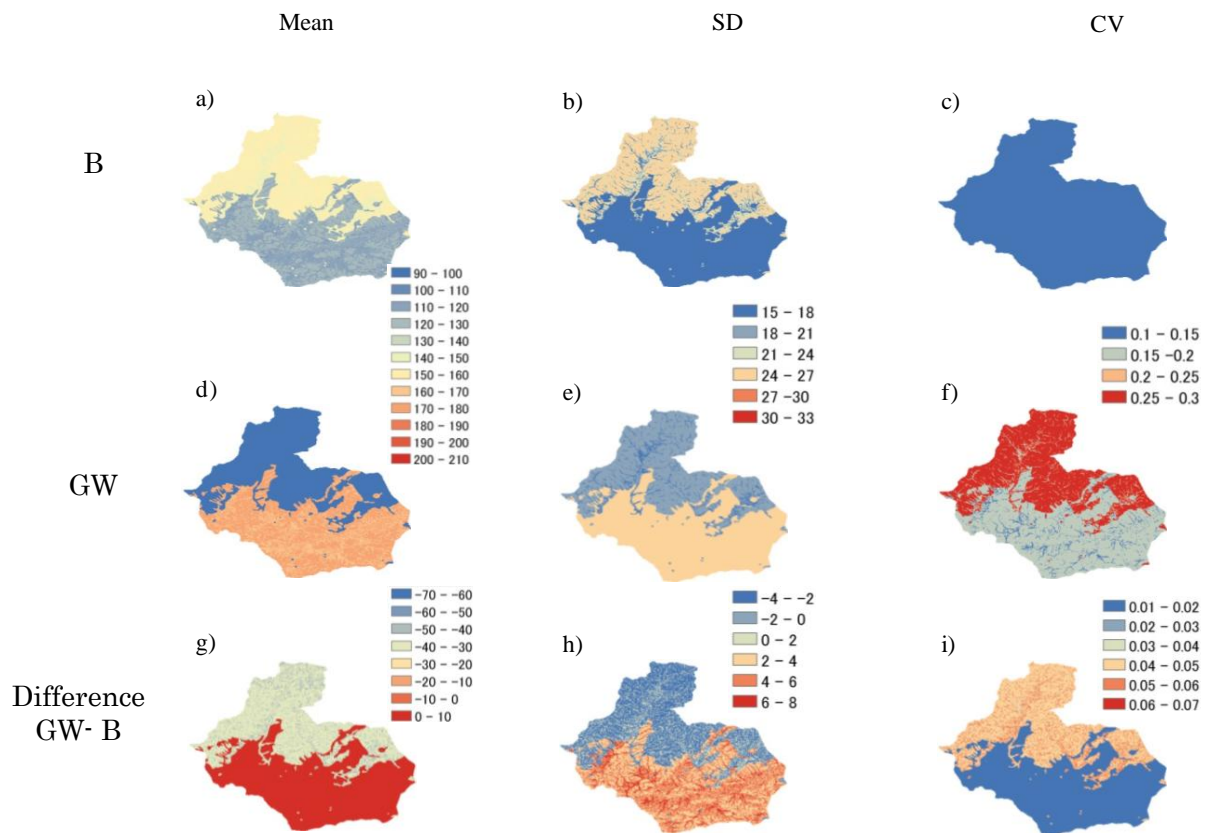


Fig. 137 Annual mean, standard deviation (SD) and coefficient of variation (CV) of evapotranspiration (ET) under B and GW scenarios. The panels a), b) and c) represent mean, SD and CV of ET in B scenario. The panels d), e) and f) represent mean, SD and CV of ET under GW scenario. The panels g), h) and i) represent the difference of mean, SD and CV of ET between GW and B scenarios. (Unit is mm y^{-1})

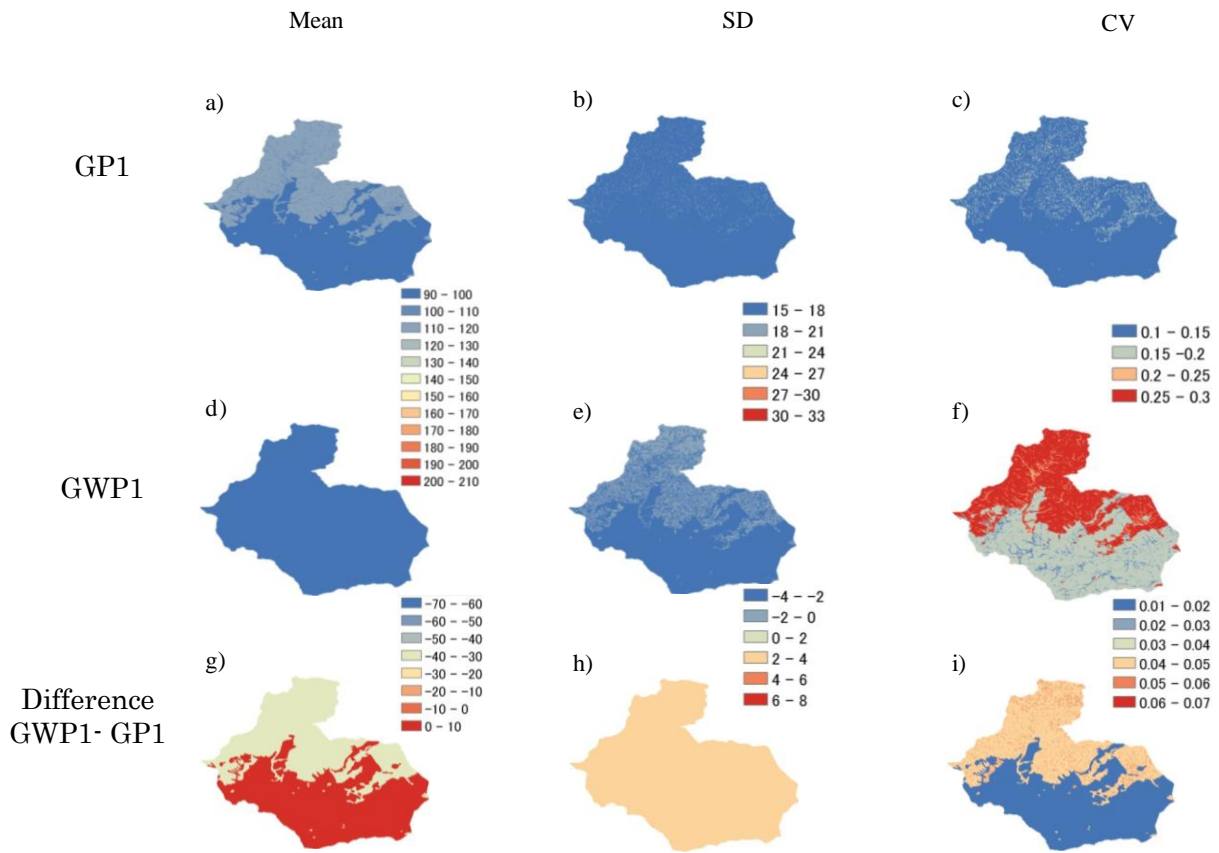


Fig. 138 Annual mean, standard deviation (SD) and coefficient of variation (CV) of evapotranspiration (*ET*) under GP1 and GWP1 scenarios. The panels a), b) and c) represent mean, SD and CV of *ET* in GP1 scenario. The panels d), e) and f) represent mean, SD and CV of *ET* under GWP1 scenario. The panels g), h) and i) represent the difference of mean, SD and CV of *ET* between GWP1 and GP1 scenarios. (Unit is mm y^{-1})

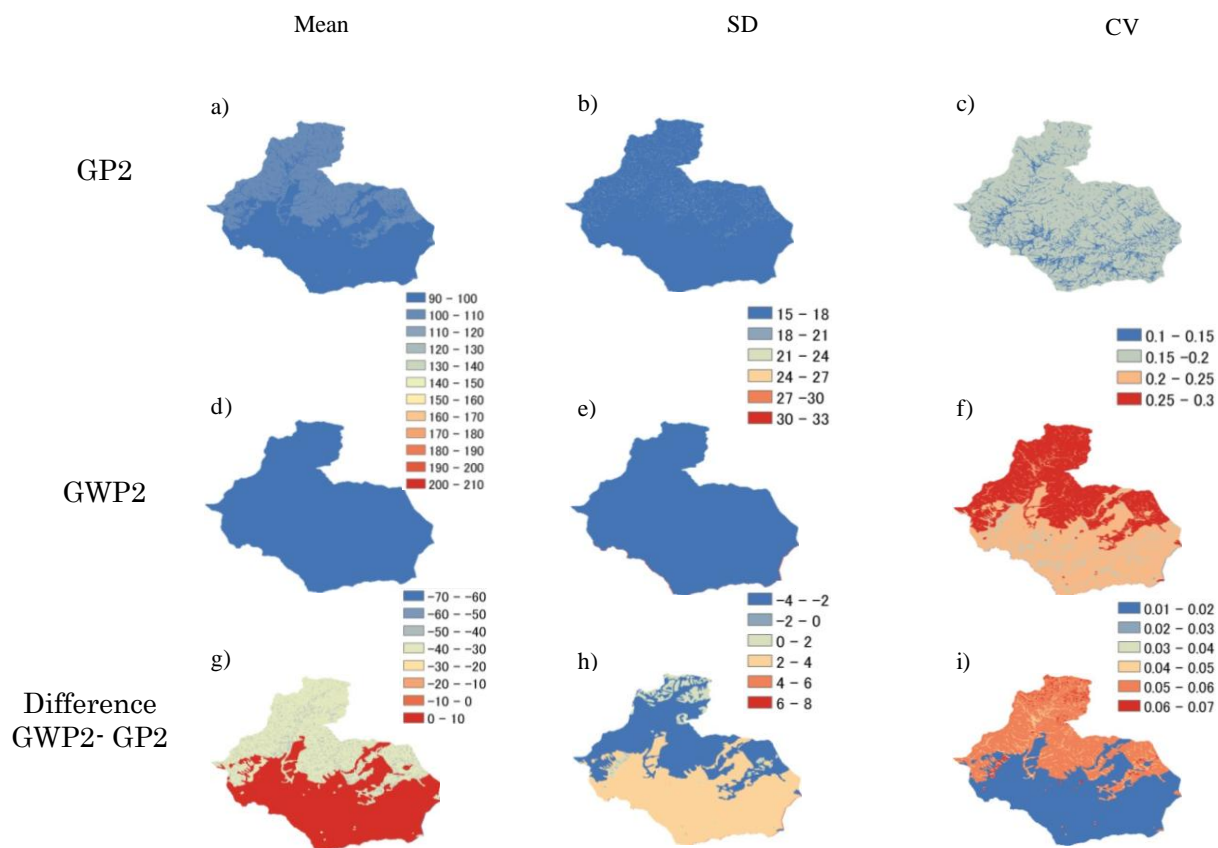


Fig. 139 Annual mean, standard deviation (SD) and coefficient of variation (CV) of evapotranspiration (ET) under GP2 and GWP2 scenarios. The panels a), b) and c) represent mean, SD and CV of ET in GP2 scenario. The panels d), e) and f) represent mean, SD and CV of ET under GWP2 scenario. The panels g), h) and i) represent the difference of mean, SD and CV of ET between GWP2 and GP2 scenarios. (Unit is mm y^{-1})

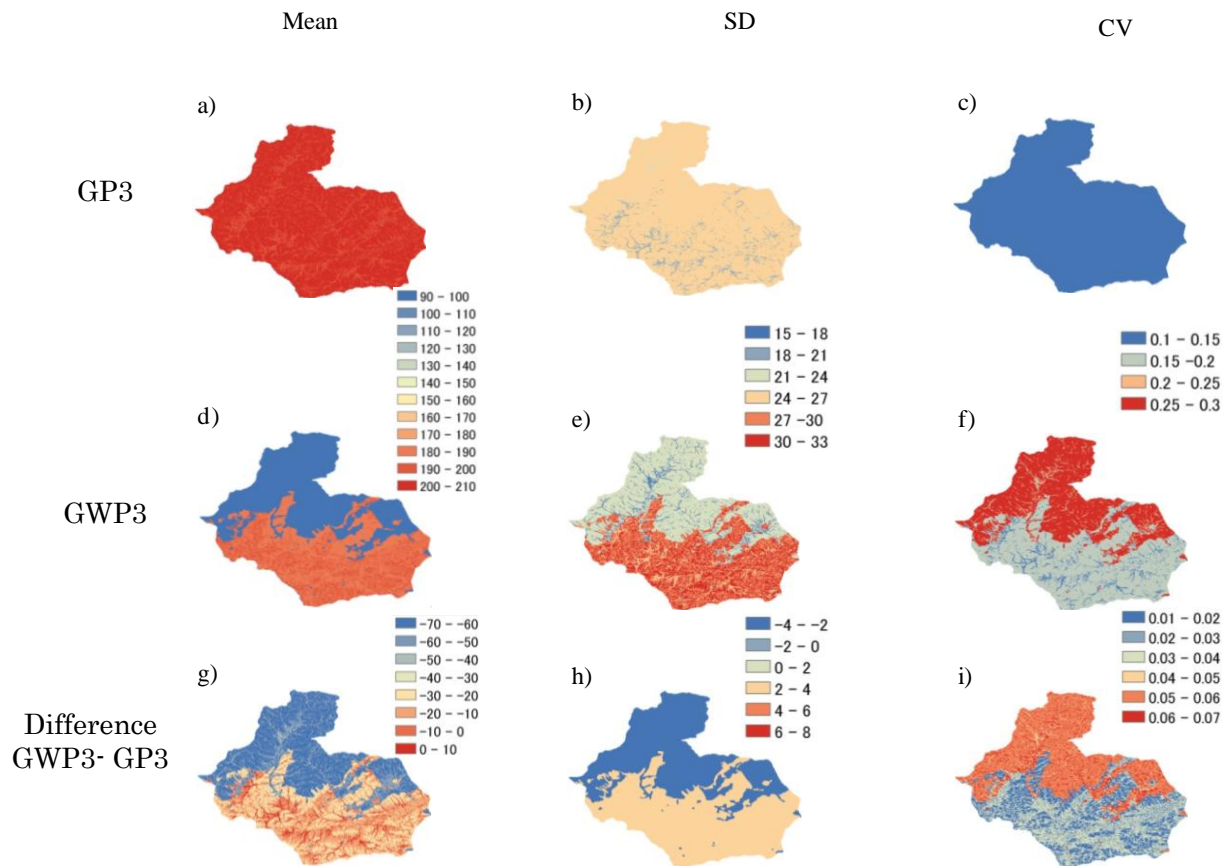


Fig. 140 Annual mean, standard deviation (SD) and coefficient of variation (CV) of evapotranspiration (ET) under GP3 and GWP3 scenarios. The panels a), b) and c) represent mean, SD and CV of ET in GP3 scenario. The panels d), e) and f) represent mean, SD and CV of ET under GWP3 scenario. The panels g), h) and i) represent the difference of mean, SD and CV of ET between GWP3 and GP3 scenarios. (Unit is mm y^{-1})

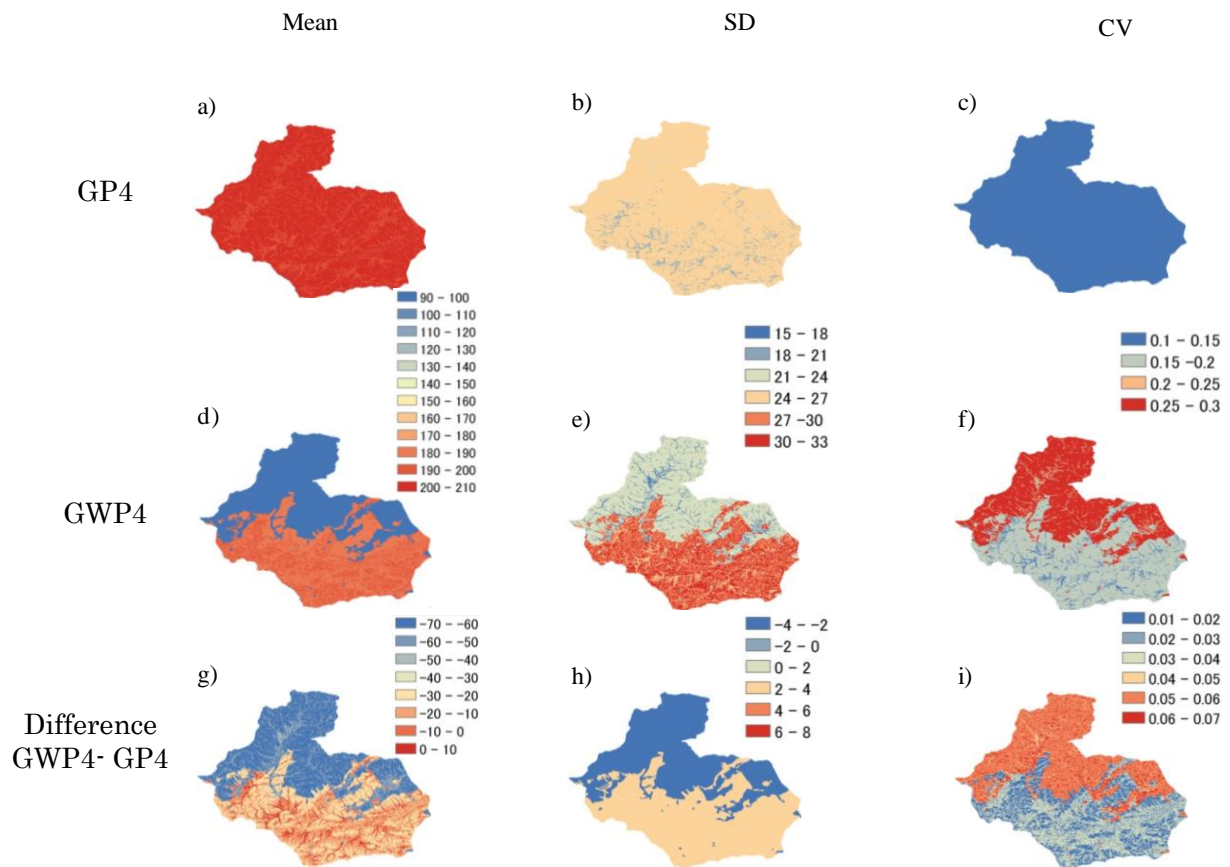


Fig. 141 Annual mean, standard deviation (SD) and coefficient of variation (CV) of evapotranspiration (ET) under GP4 and GWP4 scenarios. The panels a), b) and c) represent mean, SD and CV of ET in GP4 scenario. The panels d), e) and f) represent mean, SD and CV of ET under GWP4 scenario. The panels g), h) and i) represent the difference of mean, SD and CV of ET between GWP4 and GP4 scenarios. (Unit is mm y^{-1})

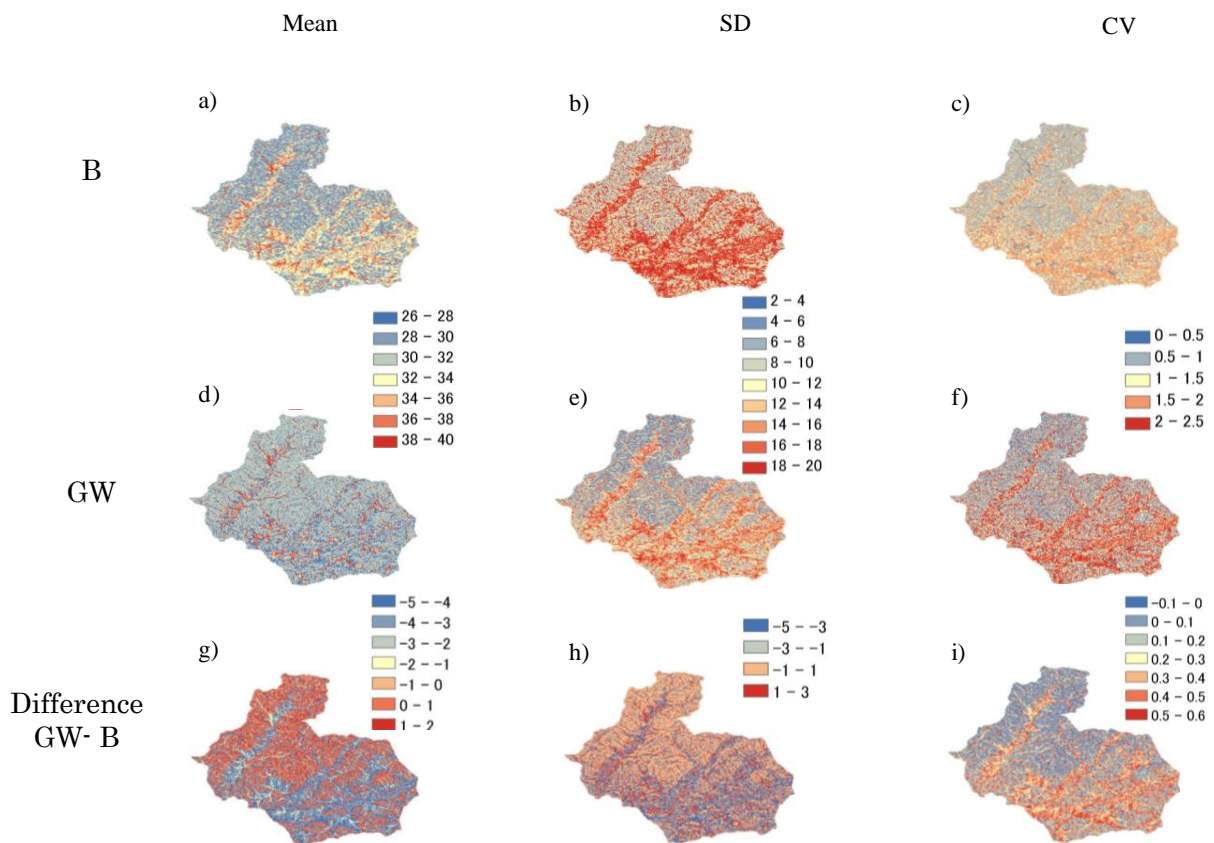


Fig. 142 Annual mean, standard deviation (SD) and coefficient of variation (CV) of soil moisture (SM) under B and GW scenarios. The panels a), b) and c) represent mean, SD and CV of SM in B scenario. The panels d), e) and f) represent mean, SD and CV of SM under GW scenario. The panels g), h) and i) represent the difference of mean, SD and CV of SM between GW and B scenarios. (Unit is %)

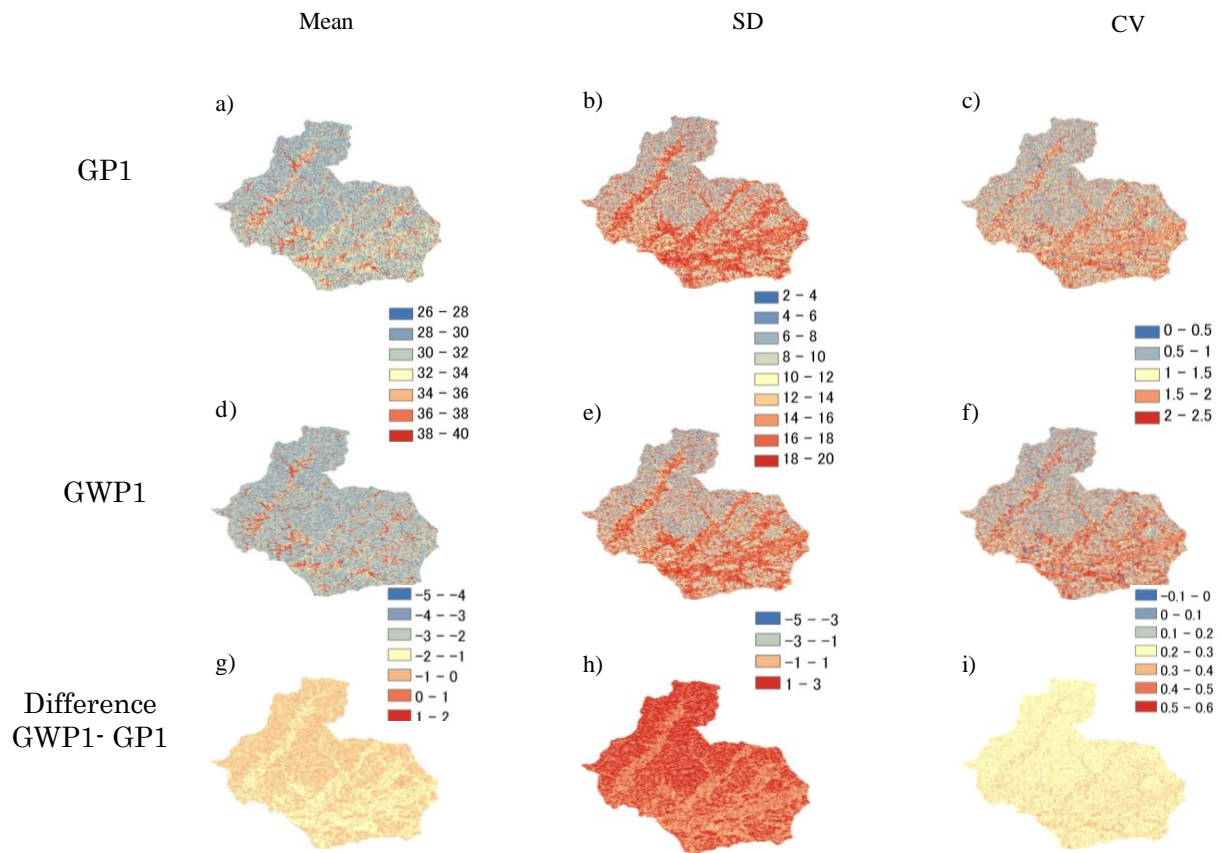


Fig. 143 Annual mean, standard deviation (SD) and coefficient of variation (CV) of soil moisture (*SM*) under GP1 and GWP1 scenarios. The panels a), b) and c) represent mean, SD and CV of *SM* in GP1 scenario. The panels d), e) and f) represent mean, SD and CV of *SM* under GWP1 scenario. The panels g), h) and i) represent the difference of mean, SD and CV of *SM* between GWP1 and GP1 scenarios. (Unit is %)

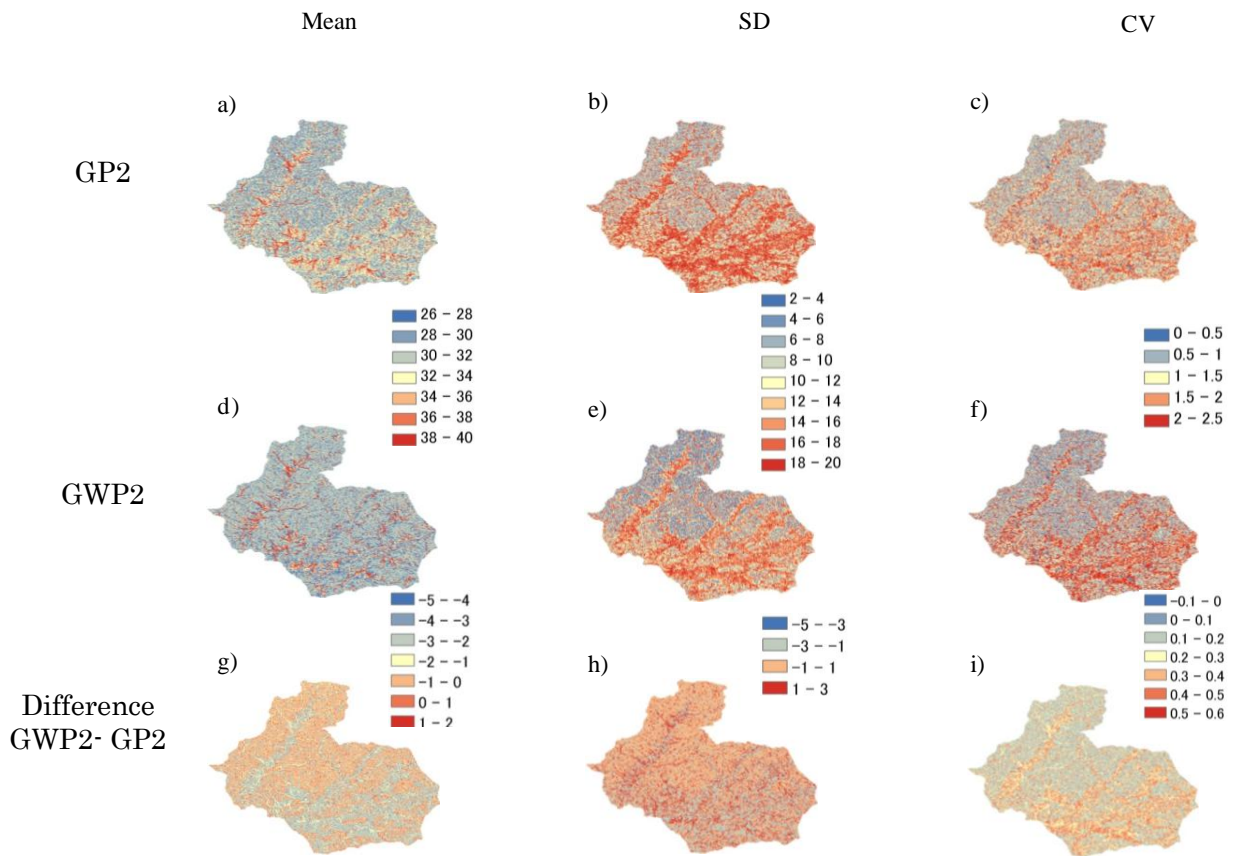


Fig. 144 Annual mean, standard deviation (SD) and coefficient of variation (CV) of soil moisture (*SM*) under GP2 and GWP2 scenarios. The panels a), b) and c) represent mean, SD and CV of *SM* in GP2 scenario. The panels d), e) and f) represent mean, SD and CV of *SM* under GWP2 scenario. The panels g), h) and i) represent the difference of mean, SD and CV of *SM* between GWP2 and GP2 scenarios. (Unit is %)

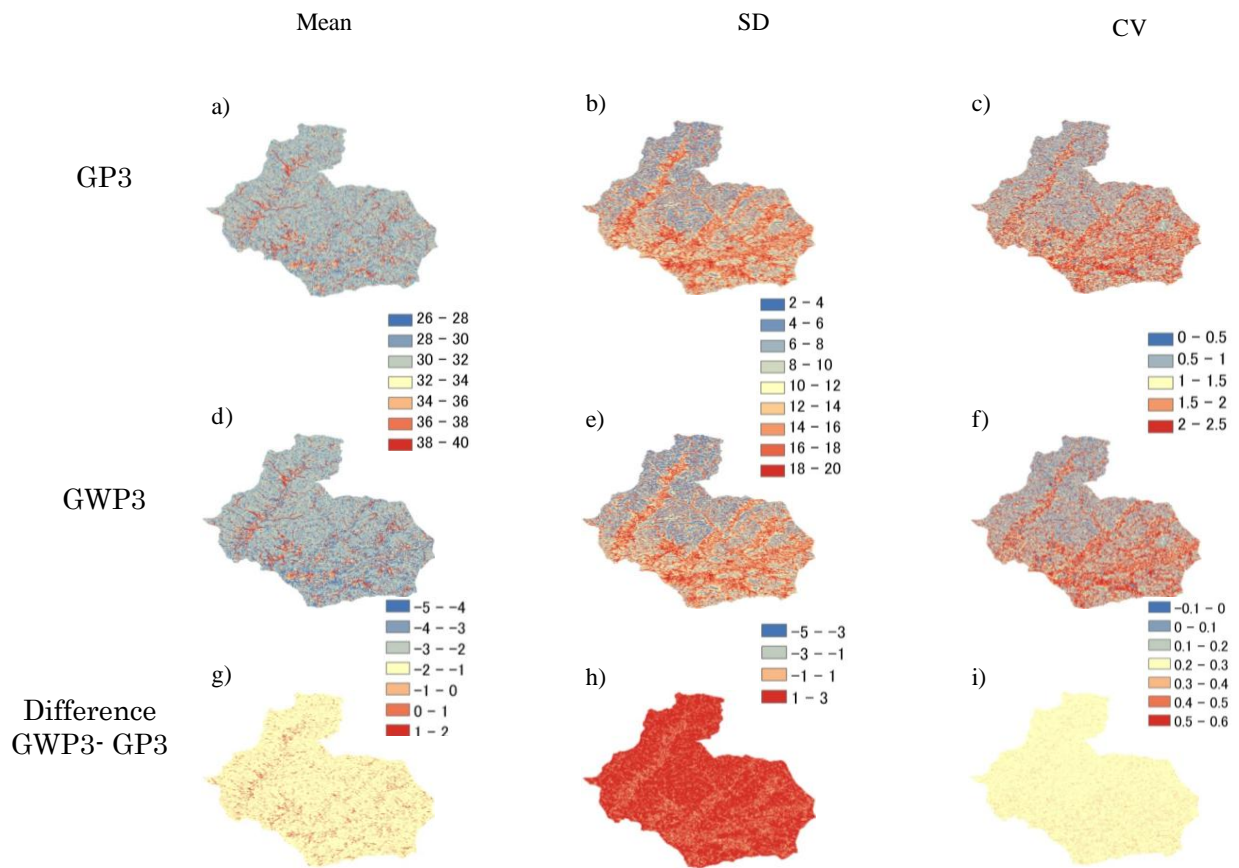


Fig. 145 Annual mean, standard deviation (SD) and coefficient of variation (CV) of soil moisture (*SM*) under GP3 and GWP3 scenarios. The panels a), b) and c) represent mean, SD and CV of *SM* in GP3 scenario. The panels d), e) and f) represent mean, SD and CV of *SM* under GWP3 scenario. The panels g), h) and i) represent the difference of mean, SD and CV of *SM* between GWP3 and GP3 scenarios. (Unit is %)

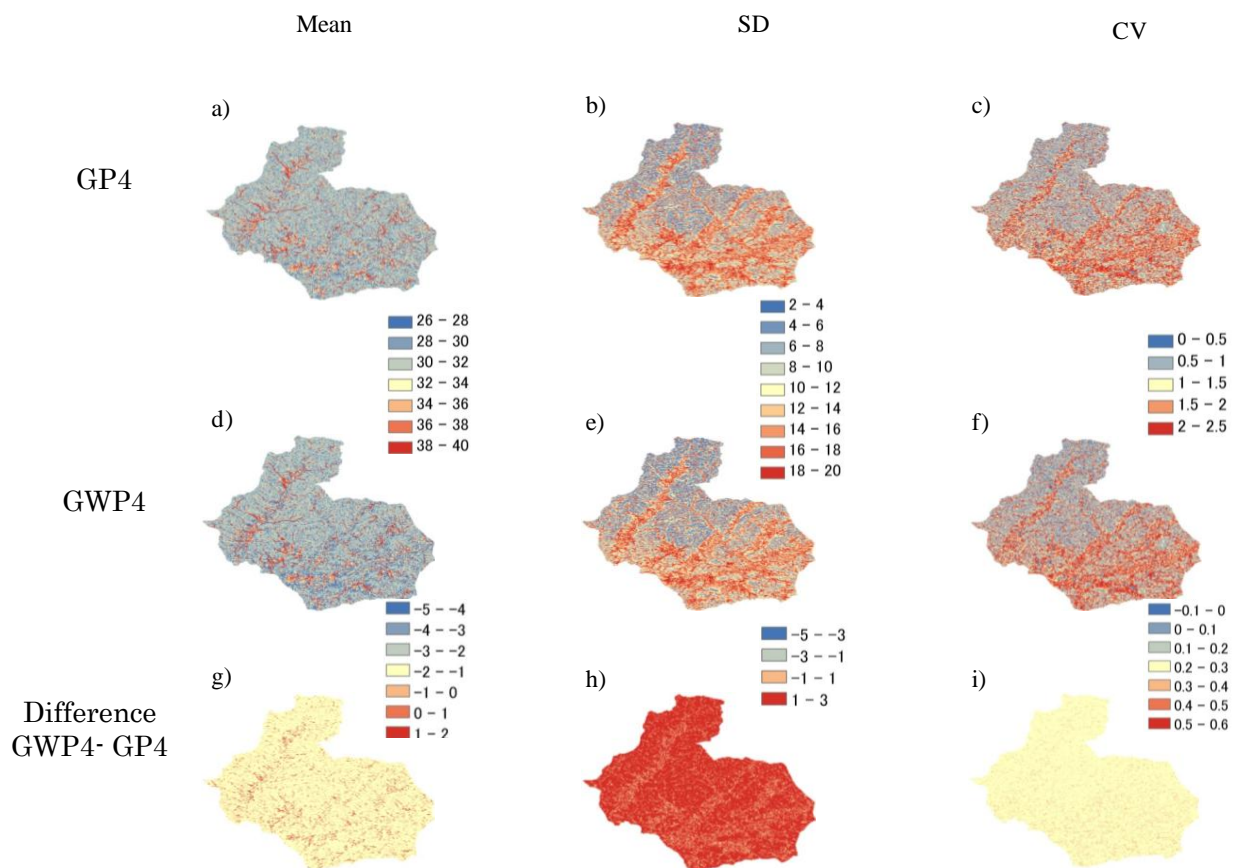


Fig. 146 Annual mean, standard deviation (SD) and coefficient of variation (CV) of soil moisture (*SM*) under GP3 and GWP3 scenarios. The panels a), b) and c) represent mean, SD and CV of *SM* in GP3 scenario. The panels d), e) and f) represent mean, SD and CV of *SM* under GWP3 scenario. The panels g), h) and i) represent the difference of mean, SD and CV of *SM* between GWP3 and GP3 scenarios. (Unit is %)

The flow duration curves of upper part of Kherlen river basin are shown in Figs. 147 and 148 under B scenario and GW scenario, respectively. The curves are designed to indicate the flow characteristics of upper part of Kherlen river basin. The daily mean discharge values of 10 years in GW and B scenario were ordered and shown from largest value to the left to the smallest value to the right. From these results, we found that simulated annual mean discharge was under B scenario $22 \text{ m}^3 \text{ s}^{-1}$ with standard deviation as 27 and coefficient of variation of 1.26. In GW scenario, annual mean of discharge was $19 \text{ m}^3 \text{ s}^{-1}$ with standard deviation of 21 and coefficient of variation of 1.13. The coefficient of variation of daily mean discharge of 10 years for GW scenario were smaller than that in B scenario. Table 26 shows the mean, standard deviation and coefficient of discharge of four different days of 95th, 185th, 275th and 355th of a year under all scenarios. From this analysis, daily mean discharge was decreased under GW and combination of two (GWP1-GWP4) in future. However, variation of daily mean discharge was increased in 355th day and partially increased in 95th and 275th day under GW and combination of two (GWP1-GWP4) in future as shown in Fig. 149.

Fig. 150 shows the influence of grazing pressure changes using present climate data on mean aboveground biomass of Kherlen river basin. At the grazing pressure intensity of 0.4, 0.6 and 0.8, simulated aboveground biomass decreased and then reached to equilibrium state. Under grazing pressure intensity of 1.0, aboveground biomass decreased during the investigated period. These results suggest that maximum sustainable grazing pressure was 0.8 for over the Kherlen river basin which is slightly larger than the value of 0.7 estimated by Chen et al. (2007). Chen et al. (2007) determined maximum sustainable grazing pressure is 0.7 at only KBU site. In our study, this maximum sustainable grazing pressure was determined over Kherlen river basin. Therefore, difference of these grazing pressure values can be explained by modeling scale. Fig. 151 shows and suggests that maximum sustainable grazing pressure was decreased up to 0.6 for over the Kherlen river basin due to global warming effect on aboveground biomass in future condition.

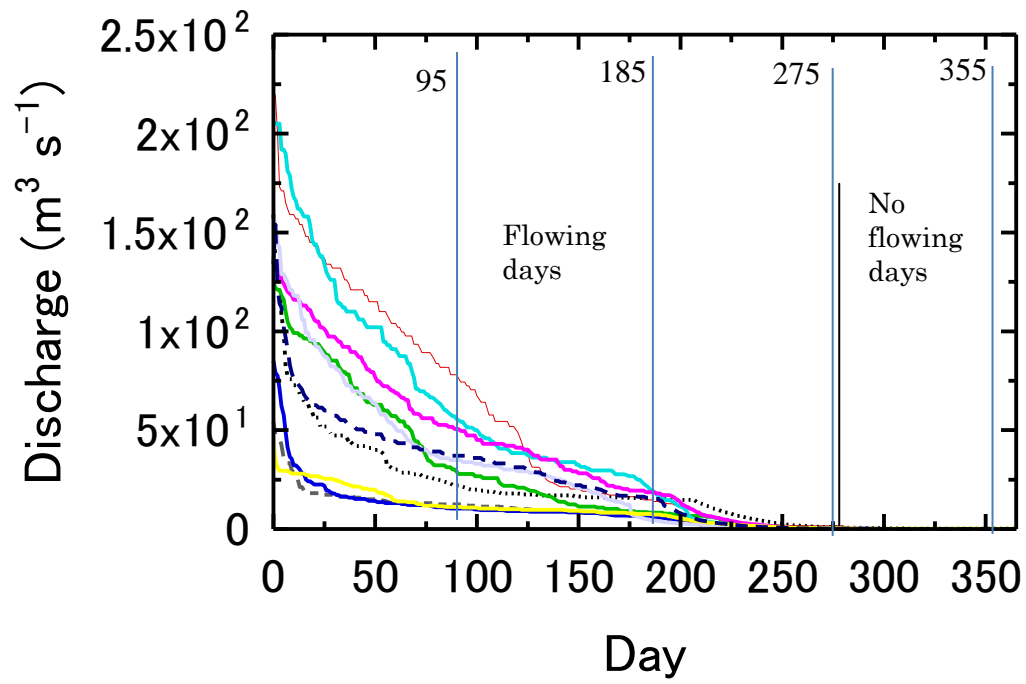


Fig. 147 Mean flow duration curve of upper part of Kherlen river watershed (Current condition)

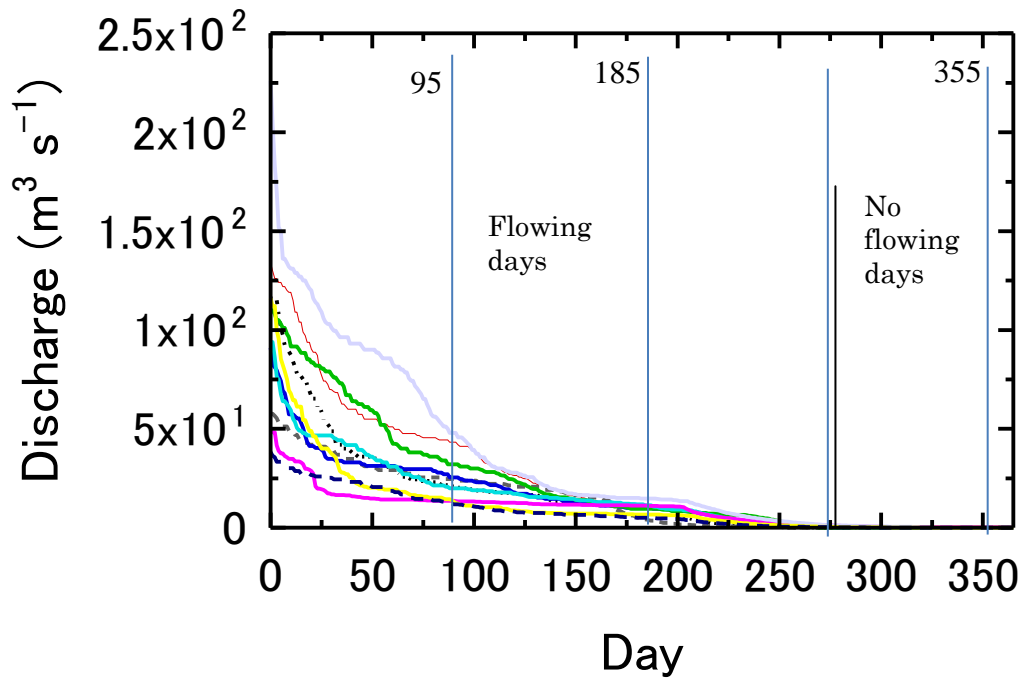


Fig. 148 Mean flow duration curve of upper part of Kherlen river watershed (Future condition)

Table 26 Mean, standard deviation and coefficient of discharge different scenarios

| Day | B scenario | | | GP1 scenario | | | GP2 scenario | | | GP3 scenario | | | GP4 scenario | | |
|-----|-------------|-------|-------|---------------|-------|-------|---------------|-------|-------|---------------|-------|------|---------------|-------|------|
| | Mean | SD | CV | Mean | SD | CV | Mean | SD | CV | Mean | SD | CV | Mean | SD | CV |
| 95 | 32.28 | 19.30 | 0.60 | 32.21 | 19.34 | 0.60 | 33.20 | 20.07 | 0.60 | 33.02 | 20.07 | 0.61 | 33.01 | 19.48 | 0.64 |
| 185 | 11.75 | 5.46 | 0.46 | 11.62 | 5.41 | 0.47 | 12.08 | 5.68 | 0.47 | 11.95 | 5.62 | 0.47 | 11.39 | 5.04 | 0.32 |
| 275 | 0.38 | 0.45 | 1.20 | 0.34 | 0.45 | 1.33 | 0.40 | 0.45 | 1.12 | 0.40 | 0.45 | 1.15 | 0.54 | 0.51 | 0.94 |
| 355 | 0.04 | 0.07 | 1.66 | 0.04 | 0.07 | 1.66 | 0.05 | 0.07 | 1.42 | 0.04 | 0.07 | 1.66 | 0.05 | 0.10 | 2.00 |
| Day | GW scenario | | | GWP1 scenario | | | GWP2 scenario | | | GWP3 scenario | | | GWP4 scenario | | |
| | Mean | Mean | SD | CV | Mean | SD | CV | Mean | SD | CV | SD | CV | Mean | SD | CV |
| 95 | 24.08 | 24.30 | 15.48 | 0.64 | 24.30 | 15.48 | 0.64 | 24.30 | 15.48 | 0.64 | 14.78 | 0.61 | 23.84 | 13.45 | 0.56 |
| 185 | 9.38 | 9.39 | 3.04 | 0.32 | 9.39 | 3.04 | 0.32 | 9.39 | 3.04 | 0.32 | 3.03 | 0.32 | 9.34 | 3.11 | 0.33 |
| 275 | 0.50 | 0.54 | 0.51 | 0.94 | 0.54 | 0.51 | 0.94 | 0.54 | 0.51 | 0.94 | 0.52 | 0.94 | 0.47 | 0.61 | 1.31 |
| 355 | 0.05 | 0.05 | 0.10 | 2.00 | 0.05 | 0.10 | 2.00 | 0.05 | 0.10 | 2.00 | 0.11 | 1.68 | 0.05 | 0.10 | 2.00 |

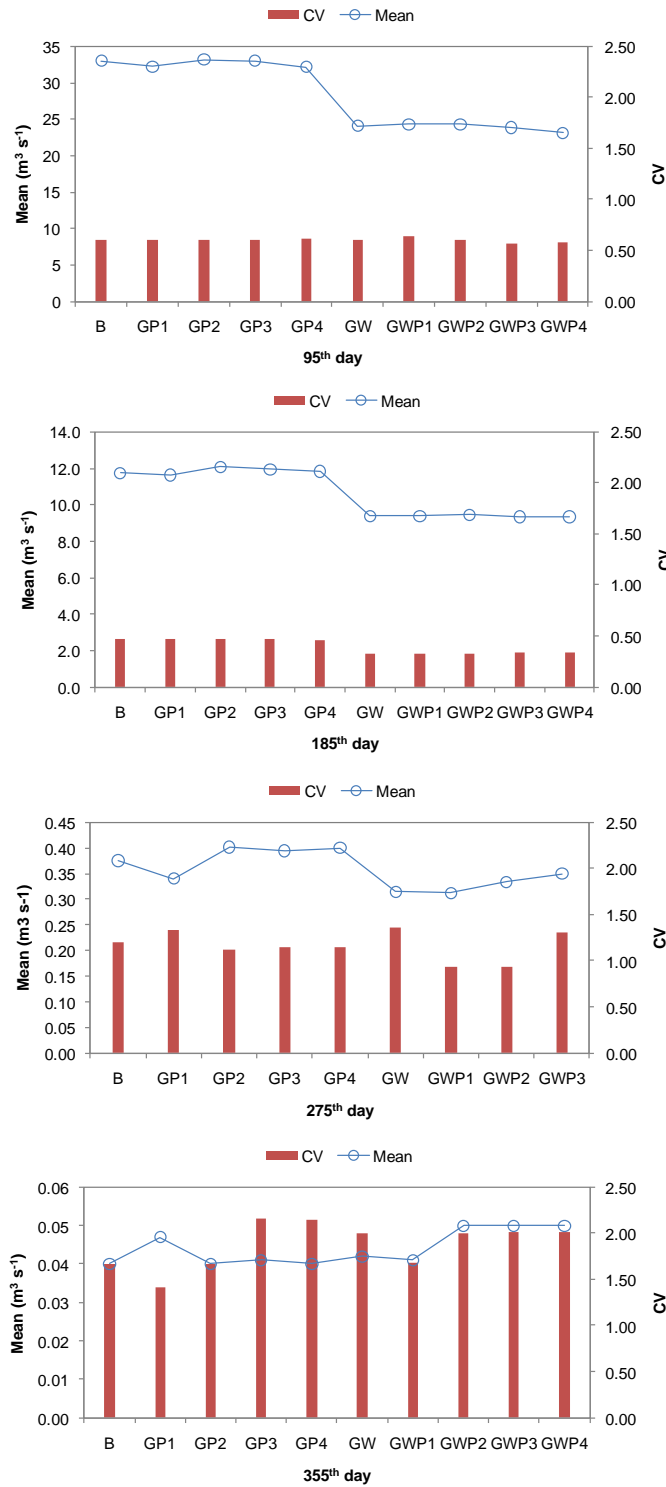


Fig. 149 Mean discharge and CV of 95th, 185th, 275th and 355th day of a year.

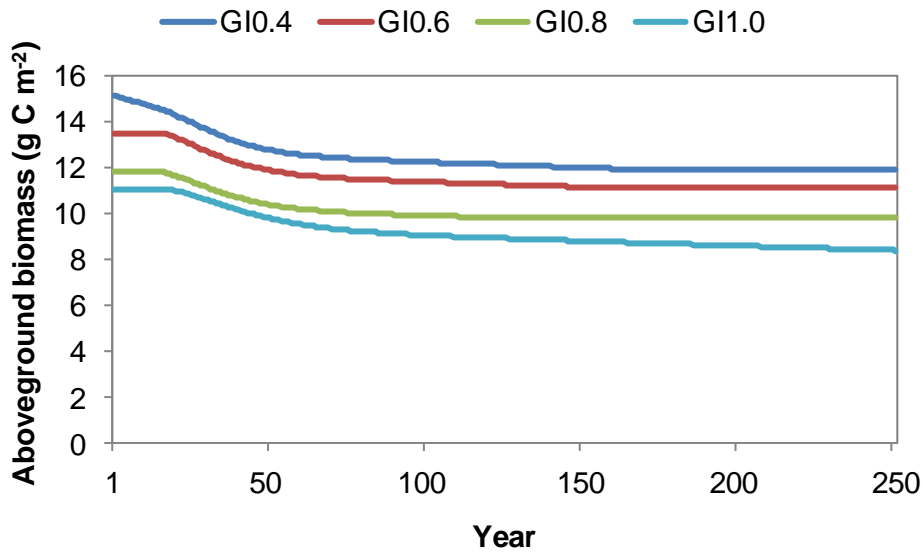


Fig. 150 The influence of grazing pressure on mean aboveground biomass under present climate in Kherlen river basin

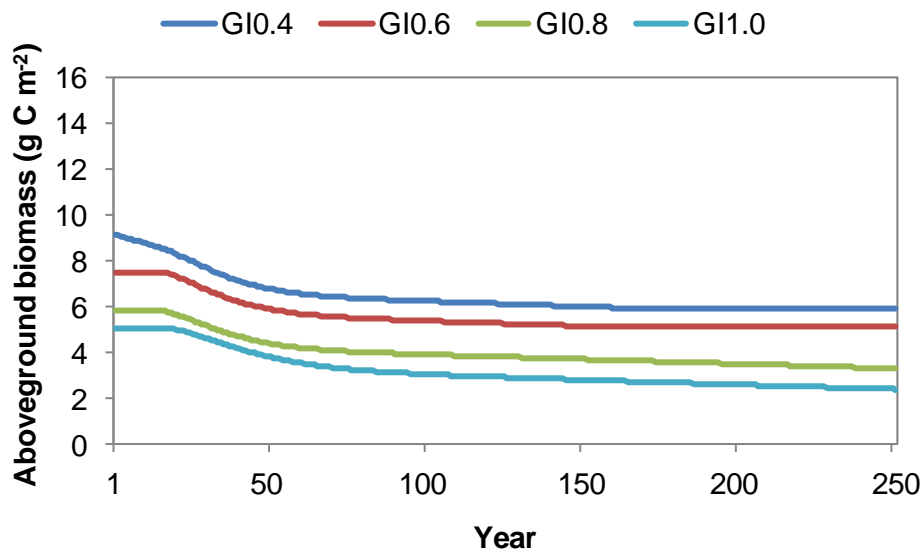


Fig. 151 The influence of grazing pressure on mean aboveground biomass under present climate in Kherlen river basin

Conclusions

The main objective of this thesis was to understand and clarify the influence of global warming and grazing pressure changes on ecohydrological components in Mongolian semi-arid region. To achieve main objective, four specific objectives were introduced as follows:

1. To calibrate the parameters of ecological and hydrological models and validate them using measured data in the study area at point and a regional scale.
2. To determine a variable, that can be used to ecological and hydrological models and to evaluate effectiveness of interactive application of them.
3. To simulate future ecohydrological components under the influence of global warming and grazing pressure changes.
4. To clarify the effects of global warming and grazing pressure changes on ecohydrological components.

The present study was carried out in one of the least environmental models studied regions of the world, i.e., Asian steppe region in Kherlen river basin (Byambakhuu et al., 2010) to test the applicability of the environmental models (i.e. century ecosystem model and TOPLATS hydrological model) to simulate ecohydrological components. The data in this study were obtained in Kherlen river basin (39400 km²) in Mongolian steppe region during RAISE (Rangeland Atmosphere-Hydrosphere-Biosphere Interaction Study Experiment in Northeastern Asia) project campaign between 2003 and 2006. In this study we presented a simple coupled modeling framework that consists of the century ecosystem model (version 4) and the TOPLATS hydrological model. The two models were directly coupled through a one-way data transfer method. Also we run the century ecosystem model and TOPLATS hydrological model at spatial scale within a Kherlen river watershed with 1 x 1 km resolution. This coupled environmental modeling system produced estimates of ecohydrological components at point and spatial scale. For future simulation of ecohydrological components, we applied the downscaled future projection of A2 scenario of IPCC by the regional climate model (Terrestrial Environment Research Center - Regional Atmospheric Modeling System (TERC - RAMS)).

1) Calibration, validation and application of century ecosystem model and TOPLATS hydrological model.

- A 60 years spun up period was found sufficient to produce aboveground biomass as well as evapotranspiration.
- The calibration of grazing pressure parameter by century ecosystem model was incorporated to establish linear equation between grazing pressure parameter of

century ecosystem model and statistical (*GIS*) that was proved as a useful tool to create grazing pressure distribution map from government animal number statistics.

- The effect of climate change to the aboveground biomass and evapotranspiration estimation was investigated and it was found that Mongolian semi-arid region was sensitive to change of precipitation than temperature.
- Total precipitation of growing season was important for plant growing in Mongolian semi-arid region.
- Simulation of evapotranspiration by means of century ecosystem model was found similar for grazing and nongrazing surface condition at point and spatial scale.
- Grazing pressure was one of controlling factors of plant growth in Mongolian semi-arid region. However, multiple correlation analysis showed that precipitation has greater effect than grazing pressure.
- The application and validation of century ecosystem model was equally applicable for both surface conditions of grazing and nongrazing at point and spatial scale in Mongolian semi-arid region. The application has verified the results of earlier studies of Parton et al., (1993) for the American, Russian and African ecosystems that century ecosystem model is capable of simulating aboveground biomass in good accuracy.
- Calibrated soil parameters were obtained which was showed good correspondence for soil moisture.
- The validation of TOPLATS hydrological model at grassland and forest site showed that TOPLATS hydrological model was applicable in the study area for studying energy and hydrological components.

2) Coupling of TOPLATS hydrological model and century ecosystem model.

To validate the coupled modeling system applicability at point scale in our study, extensive comparisons have been performed for hydrological and energy fluxes using flux measurement data from grassland and those were used for coupling of TOPLATS hydrological model and century ecosystem model.

- One-way data transfer methodology and leaf area index was found suitable for coupling between century ecosystem model and TOPLATS hydrological model and it suggests that this coupling procedure can be used for any ecology and hydrological model in arid region.
- This coupled modeling approach can be used for future projection.

3 and 4) Future projection of ecohydrological components and their responses to global warming and grazing pressure changes.

The simulation of ecohydrological components and their processes in this study area were performed based on four grazing pressure change scenarios, one climate change scenario based on A2 scenario of IPCC and four grazing + climate change scenarios. The results of simulation based on coupled modeling approach are summarized as follows;

- The simulated aboveground biomass with CO₂ level increase from current 350 ppm to 700 ppm under ideally the simulation of GW scenario with increased level of CO₂ under A2 scenario from which future climate projection has been done. However, the change of simulated aboveground biomass which obtained from the GW scenario and GW with increased CO₂ level was small.
- Under A2 scenario, annual mean of precipitation was decreased by 10%, whereas air temperature was increased about 5°C over Kherlen river basin.
- Simulated ecohydrological components showed that the Kherlen river basin was sensitive to both global warming and grazing pressure changes, especially more so precipitation changes than grazing pressure and air temperature. Considering climate change and grazing pressure changes scenario of this region ecohydrological component will decrease. However, combined effect of climate change and grazing pressure changes will have larger effect than grazing pressure changes only.
- In the Kherlen river basin, the maximum sustainable grazing pressure is 0.8 SE_u ha⁻¹ if there is no global warming effect on ecohydrological processes. However, the maximum sustainable grazing pressure will be decreased up to 0.6 SE_u ha⁻¹ under global warming effect.

As mentioned in this section, the application and validation of century ecosystem model and TOPLATS hydrological model showed that these models are applicable in Mongolian semi-arid region. One-way data transfer methodology with leaf area index was found suitable for coupling our mentioned environmental models and it implies that this coupling procedure can be used for any ecology and hydrological model in arid region. The coupled modeling approach were evaluated to determine the influence of global warming and grazing pressure changes on ecohydrological processes in Mongolian semi-arid region and showed combined effect of global warming and grazing pressure changes have larger effect than that the grazing pressure changes only.

Acknowledgements

Looking back, I am surprised and at the same time very grateful for all I have received throughout these years. It has certainly shaped me as a person and has led me where I am now. All these years of PhD studies are full of such great experiences. This thesis spans several years of work with environmental modeling system at Mongolia and many people have been involved and contributed to the presented ideas and understanding gained. The author acknowledges his debt to those who have helped along the way in this thesis.

I would like first to express my gratitude to my supervisor, Prof. M. Sugita for his endless attracting attentions during whole time, patience, enthusiasm, and expert guidance for my entire graduate work. For all the hope he has put on me, before I thought I could do any research at all. It is contrast encouragement for me to live intensively, made me remain focused to finish this work. During years of knowing him, he has helped me to see life and science in their full depth, and taught me how to appreciate the good scientific work that helps other researchers to build on it. He has enlightened me through his wide knowledge of natural science and his deep intuitions about where it should go and what is necessary to get there.

I am grateful to Prof. T. Tanaka, Prof. N. Tase, Dr. M. Tsujimura, Dr. J. Asanuma and Dr. T. Yamanaka for their countless suggestions, opportunity of plentiful discussions and guidance inspile of their busy schedule. I am grateful to MEXT fellowship, Japan for financial support that made my Ph.D. work possible. This study is also partially financed by the research assistance fellowship of University of Tsukuba. My work was also financed and supported by the RAISE project (The Rangeland Atmosphere - Hydrosphere - Biosphere Interaction Study Experimental in Northeastern Asia) of JST (Japan Science and Technology Agency).

Also I would like to express my thanks to Dr. W. T. Crow (USDA, Hydrology and Remote Sensing Laboratory, USA), who kindly provided us with TOPLATS hydrological model code.

I appreciate the supports got from these project members for giving chance to study in my own country to discuss some of the problems regarding to environmental issues. My time at Tsukuba was made enjoyable in large part due to the many friends and groups that became a part of my life. I am grateful for time spent with classmates, because whatever difficulties I have encountered as a student makes me appreciate all the more their extraordinary perseverance against fate in obtaining their own doctorates, and the tremendous sacrifices they have made for me throughout my life.

Lastly, for my parents who raised me with a love of science and supported me in all my pursuits. Also unexpressed immeude patience and encouregement given to me by my wife and

kids have sustained by energy lovers throughout the work and inspired me to put my best efforts in everything I do to complete this dissertation.

References

- Abe, Y. 2004. Study on groundwater flow system in the Kherlen river basin, Mongolia. Master's Thesis, Graduate School of Life and Environmental Sciences. University of Tsukuba. 63p.
- Abel, D. J., Kilby, P. J., and Davis, J. R. 1994. The systems integration problem. *Int. J. Geogr. inf. Syst.* **8**. 1-12.
- Aber, J. D. 1999. Can we close the water/carbon/nitrogen budget for complex landscapes? In: J.D. Tenhunen and P. Kabat (eds.), *Integrating Hydrology, Ecosystem Dynamics, and Biogeochemistry in Complex Landscapes*. John Wiley and Sons, Chichester, U.K. 313-333p.
- Albertson, J. D., and Kiely, G. 2001. On the structure of soil moisture time series in the context of land surfaces models. *J. Hydrol.* **243**. 101–119.
- Arakawa, A., and Schubert, W. H. 1974. Interaction of a cumulus cloud ensemble with the large-scale environment, Part I. *J. Atmos. Sci.* **31**. 674-701.
- Ardo, J., and Olsson, L. 2003. Assessment of soil organic carbon in semi-arid Sudan using GIS and the century model. *J. Arid Environ.* **54**. 633–651.
- Arora, V. K. 2002. Modeling vegetation as a dynamic component in soil vegetation-atmosphere transfer schemes and hydrological models. *Rev. Geophys.* **40**(2). 1006. doi:10.1029/2001RG000103.
- Arora, V. K., and Boer, G. J. 2002. A GCM-based assessment of simulated global moisture budget and the role of landsurface moisture reservoirs in processing precipitation. *Clim. Dyn.* **20**. 13-29.
- Batjargal, Z. 1997. Desertification in Mongolia. In Proceedings of an international workshop on rangeland desertification. RALA Report, volume 200.
- Betts, R. A., Cox, P. M., Lee, S. E., and Woodward, F. I. 1997. Constraining physiological and structural vegetation feedbacks in climate change simulations. *Nature*. **387**. 796-799.
- Beven, K. J., and Kirby, M. J. 1979. A physically based variable contributing area model of basin hydrology. *Hydrol. Sci. Bull.* **24**. 43-69.
- Bormann, H., and Diekkruger, B. 2003. Possibilities and limitations of regional hydrological models applied within an environmental change study in benin (west Africa). *Phys. Chem. Earth.* **28**. 1323-1332.
- Bormann, H., Fab, T., Junge, B., Diekkruger, B., Reichert, B., and Skowronek, A. 2005. From local hydrological process analysis to regional hydrological model application in benin: concept, results and perspectives. *Phys. Chem. Earth.* **30**. 347-356.
- Brandmeyer, J. E., and Karimi, H. A. 2000. Coupling methodologies for environmental models.

- Environ. Modell. Softw.* **15**. 479-488.
- Bremer, D. J., Auen, L. M., Ham, J. M., and Owens, C. E. 2001. Evapotranspiration in a prairie ecosystem: Effects of grazing by cattle. *Agron. J.* **93**. 338-348.
- Brovkin, V., Ganopolski, A., and Svirezhev, Y. 1997. A continuous climate-vegetation classification for use in climate-biosphere studies. *Ecol. Model.* **101**. 251-261.
- Bryant, N. A., Johnson, L. F., Brazel, A. J., Balling, R. C., Hutchinson, C. F., and Beck, F. R. 1990. Measuring the effect of overgrazing in the sonoran desert. *Climatic Change.* **17**. 243-264.
- Brusaert, W. 1982. *Evaporation into the Atmosphere: Theory, History, and Application*. D, Reidel Pub, Co. 299p.
- Brusaert, W. 2005. *Hydrology: An Introduction*. The Edinburgh Building, Cambridge CB2 2RU, U.K. 482p.
- Byambakhuu, I., Sugita, M., and Matsushima, D. (2010) Spectral unmixing model to assess land cover fractions in Mongolian steppe regions. *Remote Sens. Environ.* **144**. 2361-2372. doi:10.1016/j.rse.2010.05.013
- Chase, T. N., Pielke, R. A., Knaff, J., Kittel, T., and Eastman, J. 2000. A comparison of regional trends in 1979-1997 depth-averaged tropospheric temperatures. *Int. J. Climatol.* **20**. 503-518
- Chen, Y., Lee, P., Lee, G., Mariko, S., and Oikawa, T. 2006. Simulating root responses to grazing of a Mongolian grassland ecosystem. *Plant Ecology.* **183**(2). 265-275.
- Chen, Y., Lee, G., Lee, P., and Oikawa, T. 2007. Model analysis of grazing effect on above-ground biomass and above-ground net primary production of a Mongolian grassland ecosystem. *J. Hydrol.* **333**(1). 155-164.
- Coronato, F. R., and Bertiller, M. B. 1996. Precipitation and landscape related effects on soil moisture in semi-arid rangelands of patagonia. *J. Arid. Environ.* **34**. 1-9.
- Crow, W. T., and Wood, E. F. 2002. The value of coarse-scale soil moisture observations for regional surface energy balance modeling. *J. Hydrometeor.* **3**(4). 467-482.
- Crow, W. T., Ryu, D., and Famiglietti, J. S. 2005. Upscaling of field-scale soil moisture measurements using distributed land surface modeling. *Adv. Water Resour.* **28**(1). 1-14.
- Dai, Y., Zeng, X., Dickinson, R. E., Baker, I., Bonan, G. B., Bosilovich, M. G., Denning, A. S., Dirmeyer, P. A., Houser, P. R., Niu, G., Oleson, K. W., Schlosser, C. A. Z., and Yang, L. 2003. The common land model. *Bull. Amer. Meteor. Soc.* **84**(8). 1013-1023.
- Debruyckere, L. F. A., Franks, S. W., Beven, K. J., Troch, P. A., and Troch, F. P. De. 1996. Towards the upscaling of local surface flux models. *Phys. Chem. Earth.* **21**. 183-188.
- DeFries, R., and Eshleman, K.N., 2004. Land-use change and hydrologic processes: a major

- focus for the future. *Hydrol. Processes*. **18**(11). 2183-2186.
- Dickinson, R. E., Henderson-Sellers, A., Kennedy, P. J., and Wilson, M. F. 1986. Biosphere Atmosphere Transfer Scheme (BATS) for the NCAR Community Climate Model. *NCAR Technical Note NCAR/TN275+STR*, 69p.
- Dirmeyer, P. A., and Shukla, J., 1996. The effect on regional and global climate of expansion of the world's deserts. *Q. J. Roy. Meteor. Soc.* **122**(530). 451-482.
- D'Odorico, P., Ridolfi, L., Porporato, A., and Rodriguez-Iturbe, I. 2000. Preferential states of seasonal soil moisture: The impact of climate fluctuations, *Water Resour. Res.* **36**, 2209–2219.
- Earth Remote Sensing Data Analysis Center. 2009. Aster GDEM
- Endreny, T. A., Wood, E. F., and Lettenmaier, D. P. 2000. Satellite-derived digital elevation model accuracy: hydrological modelling requirements. *Hydrol. Processes*. **14**(2). 177-194.
- Famiglietti, J. S., and Wood, E. F. 1994b. Application of multiscale water and energy balance models on a tallgrass prairie. *Water Resour. Res.* **30**(11). 3079-3093.
- Famiglietti, J. S., Wood, E. F., Sivapalan, M., and Thongs, D. J. 1992. A catchment scale water balance model for FIFE. *J. Geophys. Res-Atmos.* **97**(D17). 18997-19007.
- Fernandez-Grimenez, M. E., and Allen-Diaz, B. 1999. Testing a non-equilibrium model of rangeland vegetation dynamics in Mongolia. *J. Arid. Environ.* **36**. 871-885.
- Foley, J. A., Levis, S., Prentice, I. C., Pollard, D., and Thompson, S. L. 1998. Coupling dynamic models of climate and vegetation. *Glob. Change. Biol.* **4**. 561-579.
- Frank, A. B. 2003. Evapotranspiration from northern semiarid grasslands. *Agron. J.* **95**. 1504-1509.
- Hannah, D. M., Wood, P. J., and Sadler, J. P. 2004. Ecohydrology and hydroecology: 'a new paradigm'?. *Hydrol. Processes*. **18**(17). 3439-3445.
- Holland, E. A., Parton, W. J., Detling, J. K., and Coppock, D. L. 1992. Physiological responses of plant populations to herbivory and their consequences for ecosystem nutrient flows. *Am. Nat.* **140** (4). 685–706.
- Hansen, J. W., 1996. Is agricultural sustainability a useful concept? *Agric. Syst.* **51**. 185-201.
- Hoffmann, W.A., and Jackson, R. B. 2000. Vegetation-climate feedbacks in the conversion of tropical savanna to grassland. *J. Climate*. **13**(9). 1593-1602.
- Hoffmann, W. A., and Jackson, R. B. 2000. Vegetation-climate feedbacks in the conversion of tropical savanna to grassland. *J. Climate*. **13**. 1593-1602.
- Isham, V., Cox, D. R., Rodriguez-Iturbe, I., Porporato, A., and Manfreda, S. 2005. Representation of space-time variability of soil moisture, *P. Roy. Soc. A-Math. Phy.* **461**. 4035–4055. doi:10.1098/rspa.2005.1568.

- Jacquemin, B., and Noilhan, J. 1990. Sensitivity study and validation of a land surface parameterization using the hapex-mobilhy data set. *Bound-Layer. Meteor.* **52**(1). 93-134.
- Jarvis, P. G., and McNaughton, K. G. 1986. Stomatal control of transpiration scaling up from leaf to region. *Adv. Ecol. Res.* **15**. 1–49.
- Jorgensen, S. E., and Bendoricchio, G., 2001. *Fundamentals of Ecological Modelling*, Elsevier, Amsterdam. 1-92p.
- Kalnay, E., Kanamitsu, M., Kistler, R., Collins, W., Deaven, D., Gandin, L., Iredell, M., Saha, S., White, G., Woollen, J., Zhu, Y., Leetmaa, A., Reynolds, B., Chelliah, M., Ebisuzaki, W., Higgins, W., Janowiak, J., Mo, K. C., Ropelewski, C., Wang, J., Jenne, R. and Joseph, D. 1996. The NCEP/NCAR 40-Year Reanalysis Project, *Bull. Amer. Meteor. Soc.* **77**, 437-472.
- Karimi, H. A., and Houston, B. H. 1996. Evaluating strategies for integrating environmental models with GIS: current trends and future needs. *Comput. Environ. Urban.* **20**(6). 413-425.
- Kato, H. 2007. Influence of Grazing on Vegetation, Surface Energy and Water Balance Over the Mongolian Steppe. Master's Thesis, Graduate School of Life and Environmental Sciences. University of Tsukuba. 111p.
- Kojima, T. (2004) Investigation on the Factors That Determine the Evapotranspiration in Kherlen River Basin in Mongolia. Master's Thesis, Master's Program in Environmental Sciences, the University of Tsukuba, 85pp. (in Japanese)
- Kotani, A. 2006. Characteristics of Scalar Admixture in the Atmospheric Boundary Layer and Estimation of Regional Surface Fluxes Over Semi-arid Area. PhD Thesis, Graduate School of Life and Environmental Sciences. University of Tsukuba. 123p
- Larcher, W. 2003. *Physiological plant ecology: Ecophysiological and stress physiology of functional groups*, Springer, Berlin, 3 edn., 513 p.
- Lean, J., and Rowntree, P. R. 1997. Understanding the sensitivity of a GCM simulation of Amazonian deforestation to the specification of vegetation and soil characteristics. *J. Climate.* **10**(6). 1216-1235.
- Li, S. G., Asanuma, J., Eugster, W., Kotani, A., Liu, J., Urano, T., Oikawa, T., Davaa, G., Oyunbaatar, D., and Sugita, M. 2005a. Net ecosystem carbon dioxide exchange over grazed steppe in central mongolia. *Global Change Biol.* **11**(11). 1941-1955.
- Li, S. G., Asanuma, J., Kotani, A., Eugster, W., Davaa, G., Oyunbaatar, D., and Sugita, M. 2005b. Year-round measurements of net ecosystem CO₂ flux over a montane larch forest in Mongolia. *J. Geophys. Res.* **110**. D09303, doi:10.1029/2004JD005456.
- Li, S. G., Asanuma, J., Kotani, A., Davaa, G., and Oyunbaatar, D. 2007. Evapotranspiration from a mongolian steppe under grazing and its environmental constraints. *J. Hydrol.* **333**(1).

133-143.

- Liang, X., Wood, F. E., Lettenmaier, F. D., Lohmann, D., Boone, A., Chang, S., Chen, F., Dai, Y., Desborough, D., Dickinson, R. E., Duan, Q., Ek, M., Gusev, M. Y., Habets, F., Irannejad, P., Koster, R., Mitchell, K. E., Nasonova, N. O., Noilhan, J., Schaake, J., Schlosser, A., Shao, Y., Shmakin, A. B., Verseghy, D., Warrach, K., Wetzell, P., Xue, Y., Yang, Z., Zeng, Q. 1998. The project for intercomparison of land-surface parameterization schemes (PILPS) phase-2c Red-Arkansas river basin experiment: 2. Spatial and temporal analysis of energy fluxes. *Global. Planet. Change.* **19**(1-4). 137-159.
- Linacre, E. T. 1977. A simple formula for estimating evaporation rates in various climates, using temperature data alone. *Agric. Meteorol.* **18**. 409-424.
- Liu, S., Li, S. G., Yu, G. R., Asanuma, J., Sugita, M., Zhang, L. M., Hu, Z. M., and Wei, Y. F. 2010. Seasonal and interannual variations in water vapor exchange and surface water balance over a grazed steppe in central Mongolia. *Agri. W. Manl.* **97**. 857-864
- Loveland, T. R., Reed, B. C., Brown, J. F., Ohlen, D. O., Zhu, J., Yang, L. and Merchant, J. W. 2000. Development of a global land cover characteristics database and IGBP DISCover from 1-km AVHRR Data. *Int. J. Remote Sens.* **21**. 1303-1330.
- Lu, L., Pielke, R. A., Liston, G. E., Parton, W. J., Ojima, D.S., and Hartman, M. 2001. Implementation of a two-way interactive atmospheric and ecological model and its application to the central united states. *J. Climate.* **14**. 900-919.
- Matthews, E. 1983. Global vegetation and land use: New high-resolution data bases for climate studies. *J. Appl. Meteor.* **22**. 474-487.
- Matsushima, D. 2007. Estimating regional distribution of surface heat fluxes by combining satellite data and a heat budget model over the Kherlen River Basin, Mongolia, *J. Hydro.* **333**(1). 86-99.
- McCarthy, J., Ganziani, O., Leary, D., Dokken, N., and White, K. 2001. Climate change 2001: Impacts, adaptation and vulnerability. Cambridge University Press. 1320p.
- Metherell, A. K., Harding, L. A., Cole, C. V., and Parton, W. J. 1993. Century soil organic matter model environment technical documentation, agroecosystem version 4.0. Great Plains System Research Unit Technical Report no.4. Colorado State University. 1-65p.
- Milchunas, D. G., and Lauenroth, W. K. 1993. Quantitative effects of grazing on vegetation and soils over a global range of environments. *Ecol. Monogr.* **63**(4). 327-366.
- Milly, P. C. D. 1986. An event-based simulation model of moisture and energy fluxes at a bare soil surface. *Water Resour. Res.* **22**. 1680-1692.
- Milly, P. C. D. 1991. A refinement of the combination equations for evaporation. *Surv. Geophys.*

12. 145-154.

- Myneni, R. B., Los, S. O., and Tucker, C. J. 1996. Satellite-based identification of linked vegetation index and sea surface temperature Anomaly areas from 1982-1990 for Africa, Australia and South America. *Geophys. Res. Lett.* **23**(7). 729-732.
- Nakicenovic, N., and Swart, R. 2000. Special Report on Emissions Scenarios : A Special Report of Working group III of the Intergovernmental Panel on Climate Change. Cambridge University Press, Cambridge, United Kingdom and New York, NY. USA. 599p.
- Nasrallah, H. A., and Balling Jr. R. C. 1994. The effect of overgrazing on historical temperature trends. *Agric. Forest Meteor.* **71**. 425-430.
- Nemani, R. R., Running, S. W., Pielke, R. A., and Chase, T. N. 1996. Global vegetation cover changes from coarse resolution satellite data. *J. Geophys. Res.* **101**. 7157-7162.
- Newman, B. D., Wilcox, B. P., Archer, S. R., Breshears, D. D., Dahm, C. N., Dufy, C. J., McDowell, N. G., Phillips, F. M., Scanlon, B. R., and Vivoni, E. R. 2006. Ecohydrology of water-limited environments: a scientific vision. *Water Resour. Res.* **42**(6). W06302.
- Odorico, P. D., and Porporato, A. 2006. Dryland Ecohydrology. Springer Netherlands, 1p
- Parton, W. J. 1984. Predicting soil temperatures in a shortgrass steppe. *Soil Sci.* **138**, 93-101.
- Parton, W. J., Scurlock, J. M., and Ojima, D. S. 1993. Observations and modeling of biomass and soil organic matter dynamics for the grassland biome worldwide. *Global Biogeochem. Cycles.* **7** (4). 785–809.
- Parton, W. J., Schimel, D. S. Cole, C. V., and Ojima, D. S. 1987. Analysis of factors controlling soil organic matter levels in great plains grasslands. *Soil. Sci. Am. J.* **51**(5). 1173-1987.
- Parton, W. J. Stewart, J. W. B., and Cole, C. V. 1988. Dynamics of C, N, P and S in grassland soil: a model. *Biogeochemistry.* **5**. 109–131.
- Pauwels, V. R. N., and Gabrielle, J. M. 2006 . Improvement of modeled soil wetness conditions and turbulent fluxes through the assimilation of observed discharge. *Journal of Hydro.* **7**. 458-477.
- Pauwels, V. R. N., and Wood, E. F. 1999a. A soil-vegetation-atmosphere transfer scheme for the modeling of water and energy balance processes in high latitudes. 1. model improvements. *J. Geophys. Res.* **104**(D22). 27 811-27 822.
- Pauwels, V. R. N., and Wood, E. F. 1999b. A soil-vegetation-atmosphere transfer scheme for the modelling of water and energy balance processes in high latitudes. 2. application and validation. *J. Geophys. Res.* **104**(D22). 27 823-27 840.
- Pauwels, V. R. N., Hoeben, R., Verhoest, N. E. C., Troch, F. P., and Troch, P. A. 2002. Improvement of toplats-based discharge predictions through assimilation of ERS-based

- remotely sensed soil moisture values. *Hydrol. Process.* **16**(5). 995-1013.
- Peters-Lidard, C. D. M., Zion, S., and Wood, E. F. 1997. A soil-vegetation-atmosphere transfer scheme for modeling spatially variable water and energy balance process. *J. Geophys. Res.* **102**(D2). 4303-4324.
- Porporato, A. and Rodriguez-Iturbe, I. 2002. Ecohydrology - A challenging multidisciplinary research perspective. *Hydrolog. Sci. J.* **47**, 811–822.
- Porporato, A., Laio, F., Ridolfi, L., and Rodriguez-Iturbe, I. 2001. Plants in water-controlled ecosystems: active role in hydrologic processes and response to water stress - III. Vegetation water stress. *Adv. Water Resour.* **24**. 725–744.
- Reynolds, R. W., Rayner, N. A., Smith, T. M., Stokes, D. C. and Wang, W. 2002. An improved in situ and satellite SST analysis for climate. *J. Climate.* **15**, 1609-1625.
- Rodriguez-Iturbe, I. 2000. Ecohydrology: A hydrologic perspective of climate-soil-vegetation dynamics. *Water Resour. Res.* **36**(1). 3-9.
- Rodriguez-Iturbe, I., Porporato, A., Laio, F., and Ridolfi, L. 2001. Plants in water-controlled ecosystems: Active role in hydrologic processes and response to water stress- I. Scope and general outline, *Adv. Water Resour.* **24**. 695–705.
- Saandar, M., and Sugita, M. 2004. Digital Atlas of Mongolian Natural Environments (1) Vegetation, Soil, Ecosystem and Water. CD-ROM, Monmap Engineering Service Co., Ltd, Ulaanbaatar 210646, Mongolia.
- Sato, T., Kimura, F., and Kitoh, A. 2007. Projection of global warming onto regional precipitation over mongolia using a regional climate model. *J. Hydrol.* **333**(1). 144-154.
- Shaver, G. R., W. D. Billings, F. S. Chapin III, A. E. Giblin, K. J. Nadelhoffer, W. C. Oechel, and E. B. Rastetter. 1992. Global change and the carbon balance of arctic ecosystems. *BioScienc.* **61**, 415–435.
- Silvert, W. 2001. Modelling as a discipline. *Int. J. Gen. Syst.* **30**(3). 261-282.
- Schimel, D. S. House, J. I., Hibbard, K. A., Bousquet, P., Ciais, P., Peylin, P., Braswell, B. H., Apps, M. J., Baker, D., and Bondeau, A. 2001. Recent patterns and mechanisms of carbon exchange by terrestrial ecosystems. *Nature.* **414**. 169-172.
- Schlesinger, W. H., Reynolds, J. F., Cunningham, G. L., Huenneke, L. F., Jarrell, W. M., Virginia, R. A., and Whitford, W. G. 1990. Biological feedbacks in global desertification. *Science.* **247**. 1043-1059.
- Scholes, R. J., and Archer, S. R. 1997. Tree- Grass interactions in savannas 1. *Annual Review of Ecology and Systematics.* **28**(1). 517-544.
- Seastedt, T. R., Hayden, B. P., Owensby, C. E., and Knapp, A. K. 1998 In: *Grassland Dynamics:*

- Long-Term Ecological Research in Tallgrass Prairie. Oxford Press, New York. 283-300p.
- Seuffert, G., Gross, P., Simmer, C., and Wood, E. F. 2002. The influence of hydrologic modeling on the predicted local weather: Two-way coupling of a mesoscale weather prediction model and a land surface hydrologic model. *J. Hydrometeor.* **3(5)**. 505-523.
- Shiirevdamba, Ts. 1998. Biological Diversity in Mongolia, First National Report, Ministry for Nature and the Environment. Admon Printing house. 106p.
- Sitch, S., Brovkin, V., Bloh, W., Vuuren, V., Eickhout, B., and Ganopolski, A. 2005. Impacts of future land cover changes on atmospheric CO₂ and climate. *Global, Biogeochem. Cycles*. **19**, GB2013, doi:10.1029/2004GB002311,
- Sivapalan, M., Beven, K., and Wood, E. F. 1987. On hydrologic similarity, 2, a scaled model of storm runoff production. *Wat. Resour. Res.* **23**. 2266-2278.
- Sugita, M. 2003. Interaction between hydrologic cycle and ecological system. *Science Journal Kagaku*, 73, 559-562 (in Japanese).
- Sugita, M., Asanuma, J., Tsujimura, M., Mariko, S., Lu, M., Kimura, F., Azzaya, D., and Adyasuren, Ts. 2007. An overview of the rangelands atmosphere-hydrosphere-biosphere interaction study experiment in northeastern Asia (RAISE). *J. Hydrol.* **333(1)**. 3-20.
- Sugita, M., Asanuma, J., Tsujimura, M., Mariko, S., Lu, M., Kimura, F., Azzaya, D., and Adyasuren, T. 2008. Rangelands Atmosphere-Hydrosphere-Biosphere Interaction Study Experiment in Northeastern Asian (RAISE) Database, *Tsukuba Geoenvironmental Sciences*, 4, 9-15, University of Tsukuba. (<http://raise.suiri.tsukuba.ac.jp/DVD/top/dat.htm>)
- Tenhunen, J. D., and Kabat, P. (eds.) 1999. Integrating hydrology, ecosystem dynamics, and biogeochemistry in complex landscapes. John Wiley and Sons, Chichester, UK, pp. 367.
- Urano, T., 2005. Seasonal Dynamics of Biomass and Carbon Dioxide Fluxes in a Mongolian Grassland. Master's Thesis, University of Tsukuba. 45p.
- Walko, R. L., Cotton, W. R., Meyers, M. P. and Harrington, J. Y. 1995. New RAMS cloud microphysics parameterization. Part 1: The single-moment scheme, *Atmos. Res.* **38**, 29-62.
- Watanabe, K., and Wake, T. 2009. Measurement of unfrozen water content and relative permittivity of frozen unsaturated soil using NMR and TDR, *Gold Regions Science and Technology*. **59**. 34-41.
- Watanabe, T., and Mizutan, K. 1996. Model study on micrometeorological aspects of rainfall interception over an evergreen broad-leaved forest. *Agric. Forest Meteor.* **80**. 195-214.
- Whitfield, B, Jacobs, J. M., and Judge, J. 2006. Intercomparison study of the land surface process model and the common land model for a prairie wetland in Florida. *J. Hydrometeorol.* **7(6)**. 1247-1258.

- Wilby, R. L., and Wigley, T. M. L. 1997. Downscaling general circulation model output: a review of methods and limitations. *Prog. Physical Geog.* **21**(4). 530-542.
- Xue, Y. 1997. Biosphere feedback on regional climate in tropical north Africa. *Quart. J. Roy. Met. Soc.* **123**, 1483-1515.
- Yukimoto, S., Noda, A., Kitoh, A., Sugi, M., Kitamura, Y., Hosaka, M., Shibata, K., Maeda, S. and Uchiyama, T. (2001). The new Meteorological Research Institute coupled GCM (MRI-CGCM2). - Model climate and variability. *Pap. Meteor. Geophys.* **51**, 47-88.
- Zalewski, M. Janauer, G. A. Jolankai, G. 1997. *Ecohydrology. A new paradigm for the sustainable use of aquatic resources*. International Hydrological Programme UNESCO Paris, Technical Document in Hydrology 7.
- Zalewski, M. 2002. Ecohydrology - the use of ecological and hydrological processes for sustainable management of water resources. *Hydro. Sci. J.* **47**(5). 823-832.
- Wardell, D. A., Reenberg, A., and Tottrup, C. 2003. Historical footprints in contemporary Sudano-Sahelian zone. *Global. Environ. Chang.* **13**. 235-254.
- Zhang, X., Drake, N. A., and Wainwright, J. 2004. Environmental modelling. Finding simplicity in complexity. chap. Scale, multiscale, Remote Sensing and GIS. John Wiley & Sons, Ltd, Chichester. 319-334p.
- Zhao, M., Pitman, A. J., and Chase, T. 2001. The impact of land cover change on the atmospheric circulation. *Clim. Dyn.* **17**. 467-477.

Appendix A

Governing equations of century ecosystem model

A.1. Carbon cycle

The century ecosystem model calculates aboveground biomass (AB) at monthly time step as the minimum of two rate-limited estimates:

$$AB = \min[AB_C, AB_N] \quad (A1)$$

where AB_C is expresses climatic limitations on AB as a function of air temperature, and water availability; AB_N is expresses constraints of nutrient availability to AB .

$$AB_C = AB_{\max} \cdot f_T(T) \cdot f_M(M) \cdot S_{sh} \quad (A2)$$

where AB_{\max} is maximum AB ; $f_T(T)$ is the function to show the effect of air temperature; $f_M(M)$ is the function to show the effect of water availability; S_{sh} is the parameter to show the effect of plant shading on plant growth.

$$f_T(T) = e^{\left(\frac{c}{d}(1-f^d)\right) \cdot f^c} \quad (A3)$$

$$f = \frac{b - T_a}{b - a} \quad (A4)$$

where c is left curve shape coefficient; d is right curve shape coefficient; b is maximum temperature for vegetation growth; T_a is air temperature at 2 m; a is optimum temperature for vegetation growth.

When $P/PET < 1.5$, the effect of water availability calculated by following equation

$$f_M(M) = \frac{1}{\left[1 + 30 \cdot \exp\left(-8.5 \frac{P}{PET}\right)\right]} \quad (A5)$$

When $P/PET > 1.5$, the effect of water availability calculated by following equation

$$f_M(M) = \frac{1 - 0.7 \left(\frac{P}{PET} - 1.5 \right)}{1.5} \quad (\text{A6})$$

where P is precipitation; PET is potential evapotranspiration.

A.2. Decomposition

In century ecosystem model decomposition at each soil pool is calculated by Parton (1983) as follows

$$\frac{dC_i}{dt} = K_i * f_M(M) * T_d * C_i \quad (\text{A7})$$

where C_i is carbon in state variable for soil pools; K_i is decomposition rate; T_d is the effect of soil temperature on decomposition.

$$T_d = \exp(-5.66 + 0.240T_s - 0.00239T_s^2) \quad (\text{A8})$$

where T_s is soil temperature.

In the century ecosystem model simple equation is used to calculate soil temperature by Eq. (A9). Here soil temperature is calculated as average of maximum soil temperature and minimum soil temperature.

$$T_s = \frac{T_{\max} + T_{\min}}{2} \quad (\text{A9})$$

For maximum soil temperature (A10), maximum air temperature and effect of aboveground biomass are used .

$$T_{\max} = T_{a,\max} + \left[\frac{25.4}{(1 + 18e^{-20T_{a,\max}})} \right] \cdot (e^{-0.000048AB} - 0.13) \quad (\text{A10})$$

Minimum air temperature is used to calculate maximum soil temperature (by Eq. (A11)).

$$T_{\min} = T_{a,\min} + 0.006AB - 1.82 \quad (\text{A11})$$

where T_{\max} is the maximum soil temperature (depending user, but range is between 0-50cm); T_{\min} is the minimum soil temperature (depending user, but range is between 0-50cm); $T_{a,\max}$ is the maximum air temperature and $T_{a,\min}$ is the minimum air temperature.

A.3. Water cycle

In the century ecosystem model, water loss occurs first as interception of canopy, followed by bare soil evaporation and transpiration from dry canopy. The maximum monthly evapotranspiration water lost rate is equal to potential evapotranspiration.

The potential evapotranspiration is calculated based on Linacre (1977) using Eq. (A12)

$$PET = \frac{700T_m / (100 - A) + 15(T_a - T_d)}{80 - T_a} \quad (\text{A12})$$

$$T_m = T_a + 0.006h \quad (\text{A13})$$

$$T_a - T_d = 0.0023h + 0.37T_a + 0.53R + 0.35R_{ann} - 10^\circ C \quad (\text{A14})$$

where T_m is sea-level equivalent of measured mean temperature; A is latitude; T_d is mean dew-point temperature; h is elevation; R is mean daily range of air temperature; R_{ann} is difference between temperature of hottest and coldest month.

Interception water loss is a function of aboveground biomass, P and PET . Interception and bare soil water losses are calculated as fractions of the monthly precipitation and are subtracted from the total monthly precipitation, with the remainder of the water is added to the soil.

$$I_C = 0.026P_aP + 0.094P_b \quad (\text{A15})$$

Interception of canopy is calculated by Eq. (A15) using P and parameters of P_a and P_b . These parameters (P_a and P_b) are calculated based on canopy height and leaf area index by Eqs. (A17)

- (A20).

$$I_L = (0.015P + 0.0635)P_d \quad (\text{A16})$$

Interception of litter is calculated by Eq. (A16) using P and parameters of P_d . This parameter is calculated based on litter biomass by Eq. (A21).

$$P_a = 0.9 + 0.016P_cP_h \quad (P_cP_h \leq 21.6) \quad (\text{A17})$$

$$P_a = 1.24 + (P_cP_h - 21.6)0.138 \quad (P_cP_h > 21.6) \quad (\text{A18})$$

$$P_b = P_cP_h0.13 \quad (P_cP_h \leq 7.6) \quad (\text{A19})$$

$$P_b = 1 + (P_cP_h - 7.6)0.072 \quad (P_cP_h > 7.6) \quad (\text{A20})$$

$$P_d = \exp(-1 + 0.45 \log_{10}(L)) \ln(10) \quad (\text{A21})$$

$$P_c = \frac{LAI}{3} \quad \left(\frac{LAI}{3} \leq 1\right) \quad (\text{A22})$$

$$P_c = 1 \quad \left(\frac{LAI}{3} > 1\right) \quad (\text{A23})$$

$$LAI = \frac{S_c}{100} \quad (\text{A24})$$

where I_C is canopy intercept; I_L is litter intercept; P_a , P_c and P_d are parameters; P_h is canopy height; L is litter biomass; LAI is leaf area index; S_c is AB and E_l is total evaporation from canopy.

Total evaporation is calculated by means of Eq. (A25)

$$E_l = I_C + I_L \quad (\text{A25})$$

Bare soil water loss is calculated by a function of standing dead and litter biomass, P and PET , as follows

$$E_{bs} = E_s A_e \left(1 - \frac{S_c}{999}\right) \quad (\text{A26})$$

where E_{bs} is bare soil evaporation; E_s is potential evaporation; A_e is fraction of evapotranspiration water loss due to bare soil calculated by Eq. (A27).

$$A_e = 1 - A_t \quad (A27)$$

$$A_t = S_c / 100 \quad (A28)$$

where A_t is LAI of S_c , that is AB .

Transpiration water loss calculated after the water was added to the soil by means of Eq.(A29).

$$E_{tr} = E_t A_t \quad (A29)$$

where E_{tr} is dry canopy transpiration; E_t is potential transpiration; A_t is fraction of evapotranspiration water loss due to dry canopy and calculated by Eq. (A30).

$$A_t = 1 - A_e \quad (A30)$$

Table A-2-1 Parameters list for Site- specific parameters of century ecosystem model

| Parameters | Definitions | Values |
|------------|---|--------|
| precip(1) | precipitation in January (cm/month) | 0.1375 |
| precip(2) | precipitation in February (cm/month) | 0.2495 |
| precip(3) | precipitation in March (cm/month) | 0.268 |
| precip(4) | precipitation in April (cm/month) | 0.7455 |
| precip(5) | precipitation in May (cm/month) | 1.439 |
| precip(6) | precipitation in June (cm/month) | 4.4838 |
| precip(7) | precipitation in July (cm/month) | 7.1658 |
| precip(8) | precipitation in August (cm/month) | 6.876 |
| precip(9) | precipitation in September (cm/month) | 2.4573 |
| precip(10) | precipitation in October (cm/month) | 0.80 |
| precip(11) | precipitation in November (cm/month) | 0.33 |
| precip(12) | precipitation in December (cm/month) | 0.24 |
| prcstd(1) | standard deviations in January precipitation value (cm/month) | 0.14 |
| prcstd(2) | standard deviations in February precipitation value (cm/month) | 0.23 |
| prcstd(3) | standard deviations in March precipitation value (cm/month) | 0.28 |
| prcstd(4) | standard deviations in April precipitation value (cm/month) | 0.76 |
| prcstd(5) | standard deviations in May precipitation value (cm/month) | 0.98 |
| prcstd(6) | standard deviations in June precipitation value (cm/month) | 2.99 |
| prcstd(7) | standard deviations in July precipitation value (cm/month) | 3.68 |
| prcstd(8) | standard deviations in August precipitation value (cm/month) | 4.17 |
| prcstd(9) | standard deviations in September precipitation value (cm/month) | 1.52 |
| prcstd(10) | standard deviations in October precipitation value (cm/month) | 0.72 |
| prcstd(11) | standard deviations in November precipitation value (cm/month) | 0.30 |
| prcstd(12) | standard deviations in December precipitation value (cm/month) | 0.18 |
| prcsw(1) | skewness value in January precipitation | 0.88 |
| prcsw(2) | skewness value in February precipitation | 1.16 |
| prcsw(3) | skewness value in March precipitation | 1.21 |
| prcsw(4) | skewness value in April precipitation | 1.00 |
| prcsw(5) | skewness value in May precipitation | 0.85 |
| prcsw(6) | skewness value in June precipitation | 1.75 |
| prcsw(7) | skewness value in July precipitation | 1.09 |
| prcsw(8) | skewness value in August precipitation | 1.30 |
| prcsw(9) | skewness value in September precipitation | 0.23 |
| prcsw(10) | skewness value in October precipitation | 2.05 |

| | | |
|-----------------------------|--|--------|
| prcsw(11) | skewness value in November precipitation | 1.31 |
| prcsw(12) | skewness value in December precipitation | 0.87 |
| tmn2m(1) | January minimum temperature at 2 meters (deg °C) | -28.89 |
| tmn2m(2) | February minimum temperature at 2 meters (deg °C) | -26.33 |
| tmn2m(3) | March minimum temperature at 2 meters (deg °C) | -16.58 |
| tmn2m(4) | April minimum temperature at 2 meters (deg °C) | -5.76 |
| tmn2m(5) | May minimum temperature at 2 meters (deg °C) | 2.21 |
| tmn2m(6) | June minimum temperature at 2 meters (deg °C) | 8.88 |
| tmn2m(7) | July minimum temperature at 2 meters (deg °C) | 12.44 |
| tmn2m(8) | August minimum temperature at 2 meters (deg °C) | 10.26 |
| tmn2m(9) | September minimum temperature at 2 meters (deg °C) | 2.52 |
| tmn2m(10) | October minimum temperature at 2 meters (deg °C) | -6.56 |
| tmn2m(11) | November minimum temperature at 2 meters (deg °C) | -18.12 |
| tmn2m(12) | December minimum temperature at 2 meters (deg °C) | -25.65 |
| tmx2m(1) | January maximum temperature at 2 meters (deg °C) | -15.15 |
| tmx2m(2) | February maximum temperature at 2 meters (deg °C) | -9.90 |
| tmx2m(3) | March maximum temperature at 2 meters (deg °C) | 0.28 |
| tmx2m(4) | April maximum temperature at 2 meters (deg °C) | 11.06 |
| tmx2m(5) | May maximum temperature at 2 meters (deg °C) | 19.50 |
| tmx2m(6) | June maximum temperature at 2 meters (deg °C) | 24.21 |
| tmx2m(7) | July maximum temperature at 2 meters (deg °C) | 25.71 |
| tmx2m(8) | August maximum temperature at 2 meters (deg °C) | 23.66 |
| tmx2m(9) | September maximum temperature at 2 meters (deg °C) | 17.90 |
| tmx2m(10) | October maximum temperature at 2 meters (deg °C) | 9.19 |
| tmx2m(11) | November maximum temperature at 2 meters (deg °C) | -3.77 |
| tmx2m(12) | December maximum temperature at 2 meters (deg °C) | -12.55 |
| Site and control parameters | | |
| ivauto | 0= the user has supplied the initial values; = 1 initialize using the grassland soil parameters; = 2 initialize using the crop soil parameters | 0 |
| nelem | number of elements (besides C) to be simulated; = 1 simulate N; = 2 simulate N and P; = 3 simulate N, P and S; Range: 1 or 2 or 3 | 1 |
| sitlat | latitude of model site (deg) (for reference only) | 47.32 |
| sitlng | longitude of model site (deg) (for reference only) | 110.67 |
| sand | fraction of sand in soil; Range: 0 to 1 | 0.62 |
| silt | fraction of silt in soil; Range: 0 to 1 | 0.278 |
| clay | fraction of clay in soil; Range: 0 to 1 | 0.103 |
| bulkd | bulk density of soil used to compute soil loss by erosion, wilting point, and field capacity (kg/liter) | 1.46 |

| | | |
|------------------------------------|--|-------|
| nlayer | number of soil layers in water model (maximum of 9); used only to calculate the amount of water available for survival of the plant | 4 |
| nlaypg | number of soil layers in the top level of the water model ; determines soil water content <i>Range: 1 to 10</i> | 3 |
| drain | the fraction of excess water lost by drainage; indicated whether a soil is sensitive for anaerobiosis; <i>Range: 0 to 1</i> | 1 |
| basef | the fraction of the soil water content of layer which is lost via base flow; <i>Range: 0 to 1</i> | 0 |
| stormf | the fraction of flow from first layer to next layer which goes into storm flow; <i>Range: 0 to 1</i> | 0 |
| swflag | flag indicating the source of the values for awilt and afield | 2 |
| awilt(1) | the wilting point of soil layer 1 (fraction); used only if swflag =0, 5, or 6 | 0.2 |
| awilt(2) | the wilting point of soil layer 2 (fraction); used only if swflag =0, 5, or 6 | 0.2 |
| awilt(3) | the wilting point of soil layer 3 (fraction); used only if swflag =0, 5, or 6 | 0.2 |
| awilt(4) | the wilting point of soil layer 4 (fraction); used only if swflag =0, 5, or 6 | 0.2 |
| awilt(5) | the wilting point of soil layer 5 (fraction); used only if swflag =0, 5, or 6 | 0.2 |
| awilt(6) | the wilting point of soil layer 6 (fraction); used only if swflag =0, 5, or 6 | 0.2 |
| awilt(7) | the wilting point of soil layer 7 (fraction); used only if swflag =0, 5, or 6 | 0.2 |
| awilt(8) | the wilting point of soil layer 8 (fraction); used only if swflag =0, 5, or 6 | 0.2 |
| awilt(9) | the wilting point of soil layer 9 (fraction); used only if swflag =0, 5, or 6 | 0.2 |
| awilt(10) | the wilting point of soil layer 10 (fraction); used only if swflag =0, 5, or 6 | 0.3 |
| afiel(1) | the field capacity of soil layer 1 (fraction); used only if swflag =0 | 0.3 |
| afiel(2) | the field capacity of soil layer 2 (fraction); used only if swflag =0 | 0.3 |
| afiel(3) | the field capacity of soil layer 3 (fraction); used only if swflag =0 | 0.3 |
| afiel(4) | the field capacity of soil layer 4 (fraction); used only if swflag =0 | 0.3 |
| afiel(5) | the field capacity of soil layer 5 (fraction); used only if swflag =0 | 0.3 |
| afiel(6) | the field capacity of soil layer 6 (fraction); used only if swflag =0 | 0.3 |
| afiel(7) | the field capacity of soil layer 7 (fraction); used only if swflag =0 | 0.3 |
| afiel(8) | the field capacity of soil layer 8 (fraction); used only if swflag =0 | 0.3 |
| afiel(9) | the field capacity of soil layer 9 (fraction); used only if swflag =0 | 0.3 |
| afiel(10) | the field capacity of soil layer 10 (fraction); used only if swflag =0 | 0 |
| ph | soil pH used to calculate the solubility of secondary P within the boundaries specified by phesp(1) and phesp(3) | 7 |
| pslsrb | slope term which controls the fraction of mineral P that is labile | 0.7 |
| sorpmx | maximum P sorption potential for a soil | 8 |
| External nutrient input parameters | | |
| epnfa(1) | intercept value for determining the effect of annual precipitation on atmospheric N fixation (wet and dry deposition) (g/m ² /y) | 0.05 |
| epnfa(2) | slope value for determining the effect of annual precipitation on atmospheric N fixation (wet and dry deposition) (g/m ² /yr/cm precip) | 0.007 |
| epnfs(1) | intercept value for determining the effect of annual precipitation on non-symbiotic soil N fixation; not used if nsnfix = 1 (g/m ² /y) | 0.6 |

| | | |
|-----------------------------------|---|-------|
| epnfs(2) | slope value for determining the effect of annual precipitation on non-symbiotic soil <i>N</i> fixation; not used if nsnfix = 1 (g/m ² /yr/cm precip) | 0.008 |
| satmos(1) | intercept for atmospheric <i>S</i> inputs as a linear function of annual precipitation (g S /m ² /yr) | 0 |
| satmos(2) | slope for atmospheric <i>S</i> inputs as a linear function of annual precipitation (g S /m ² /yr/cm precip) | 0 |
| sirri | <i>S</i> concentration in irrigation water (mg S / l) | 0 |
| Organic matter initial parameters | | |
| som1ci(1,1) | initial value for unlabeled <i>C</i> in surface organic matter with fast turnover; used only if user has supplied the initial values (gC/m ²) | 54.2 |
| som1ci(1,2) | initial value for labeled <i>C</i> in surface organic matter with fast turnover; used only if user has supplied the initial values (gC/m ²) | 0 |
| som1ci(2,1) | initial value for unlabeled <i>C</i> in soil organic matter with fast turnover; used only if user has supplied the initial values (gC/m ²) | 216.8 |
| som1ci(2,2) | initial value for labeled <i>C</i> in soil organic matter with fast turnover; used only if user has supplied the initial values (gC/m ²) | 0 |
| som2ci(1) | initial value for unlabeled <i>C</i> in soil organic matter with intermediate turnover; used only if user has supplied the initial values (gC/m ²) | 2710 |
| som2ci(2) | initial value for labeled <i>C</i> in soil organic matter with intermediate turnover; used only if user has supplied the initial values (gC/m ²) | 0 |
| som3ci(1) | initial value for unlabeled <i>C</i> in soil organic matter with slow turnover; used only if user has supplied the initial values (gC/m ²) | 2439 |
| som3ci(2) | initial value for labeled <i>C</i> in soil organic matter with slow turnover; used only if user has supplied the initial values (gC/m ²) | 0 |
| rceGW(1,1) | initial <i>C/N</i> ratio in surface organic matter with fast turnover (active soil organic matter) | 16 |
| rceGW(1,2) | initial <i>C/P</i> ratio in surface organic matter with fast turnover (active soil organic matter) | 50 |
| rceGW(1,3) | initial <i>C/S</i> ratio in surface organic matter with fast turnover (active soil organic matter) | 50 |
| rceGW(2,1) | initial <i>C/N</i> ratio in soil organic matter with fast turnover (active soil organic matter) | 12 |
| rceGW(2,2) | initial <i>C/P</i> ratio in soil organic matter with fast turnover (active soil organic matter) | 50 |
| rceGW(2,3) | initial <i>C/S</i> ratio in soil organic matter with fast turnover (active soil organic matter) | 50 |
| rceGWPI(1) | initial <i>C/N</i> ratio in soil organic matter with intermediate turnover (slow soil organic matter) | 17 |
| rceGWPI(2) | initial <i>C/P</i> ratio in soil organic matter with intermediate turnover (slow soil organic matter) | 117 |
| rceGWPI(3) | initial <i>C/S</i> ratio in soil organic matter with intermediate turnover (slow soil organic matter) | 117 |
| rceGWP2(1) | initial <i>C/N</i> ratio in soil organic matter with slow turnover (passive soil organic matter) | 8 |
| rceGWP2(2) | initial <i>C/P</i> ratio in soil organic matter with slow turnover (passive soil organic matter) | 62 |
| rceGWP2(3) | initial <i>C/S</i> ratio in soil organic matter with slow turnover (passive soil organic matter) | 62 |
| clittr(1,1) | initial value for surface unlabeled plant residue; used only if user has supplied the initial values (g/m ²) | 100 |
| clittr(1,2) | initial value for surface labeled plant residue; used only if user has supplied the initial values (g/m ²) | 0 |
| clittr(2,1) | initial value for soil unlabeled plant residue; used only if user has supplied the initial values (g/m ²) | 100 |

| | | |
|--|---|-----|
| clittr(2,2) | initial value for soil labeled plant residue; used only if user has supplied the initial values = 0 (g/m ²) | 0 |
| rcelit(1,1) | initial C/N ratio for surface litter | 66 |
| rcelit(1,2) | initial C/P ratio for surface litter | 300 |
| rcelit(1,3) | initial C/S ratio for surface litter | 300 |
| rcelit(2,1) | initial C/N ratio for soil litter | 66 |
| rcelit(2,2) | initial C/P ratio for soil litter | 300 |
| rcelit(2,3) | initial C/S ratio for soil litter | 300 |
| aglcis(1) | initial value for aboveground live unlabeled C isotope (gC/m ²) | 0 |
| aglcis(2) | initial value for aboveground live labeled C isotope (gC/m ²) | 0 |
| aglive(1) | initial value for aboveground live N; used only if user has supplied the initial values (gC/m ²) | 0 |
| aglive(2) | initial value for aboveground live P; used only if user has supplied the initial values (gC/m ²) | 0 |
| aglive(3) | initial value for aboveground live S; used only if user has supplied the initial values (gS/m ²) | 0 |
| bglcis(1) | initial value for belowground live unlabeled C; used only user has supplied the initial values (gC/m ²) | 150 |
| bglcis(2) | initial value for belowground live labeled C; used only user has supplied the initial values (gC/m ²) | 0 |
| bglive(1) | initial value for belowground live N; used only if user has supplied the initial values (gN/m ²) | 3 |
| bglive(2) | initial value for belowground live P; used only if user has supplied the initial values (gP/m ²) | 0.4 |
| bglive(3) | initial value for belowground live S; used only if user has supplied the initial values (gS/m ²) | 0.4 |
| stdcis(1) | initial value for standing dead unlabeled C; used only if user has supplied the initial values (gC/m ²) | 50 |
| stdcis(2) | initial value for standing dead labeled C; used only if user has supplied the initial values (gC/m ²) | 0 |
| stdede(1) | initial value for N in standing dead; used only if user has supplied the initial values (gN/m ²) | 0.8 |
| stdede(2) | initial value for P in standing dead; used only if user has supplied the initial values (gP/m ²) | 0.2 |
| stdede(3) | initial value for S in standing dead; used only if user has supplied the initial values (gS/m ²) | 0.2 |
| Forest organic matter initial parameters | | |
| rlvcis(1) | initial value for unlabeled C in forest system leaf component t (gC/m ²) | 0 |
| rlvcis(2) | initial value for labeled C in forest system leaf component (gC/m ²) | 0 |
| rleave(1) | initial value for N in a forest system leaf component (gN/m ²) | 0 |
| rleave(2) | initial value for P in a forest system leaf component (gP/m ²) | 0 |
| rleave(3) | initial value for S in a forest system leaf component (gS/m ²) | 0 |
| fbrcis(1) | initial value for unlabeled C in forest system fine branch component (gC/m ²) | 0 |
| fbrcis(2) | initial value for labeled C in forest system fine branch component (gC/m ²) | 0 |
| fbrche(1) | initial value for N in a forest system fine branch component (gN/m ²) | 0 |
| fbrche(2) | initial value for P in a forest system fine branch component (gP/m ²) | 0 |
| fbrche(3) | initial value for S in a forest system fine branch component (gS/m ²) | 0 |
| rlwcis(1) | initial value for unlabeled C in forest system large wood component (gC/m ²) | 0 |
| rlwcis(2) | initial value for labeled C in forest system large wood component (gC/m ²) | 0 |
| rlwode(1) | initial value for N in a forest system large wood component (gN/m ²) | 0 |
| rlwode(2) | initial value for P in a forest system large wood component (gP/m ²) | 0 |

| | | |
|----------------------------|---|------|
| rlwode(3) | initial value for S in a forest system large wood component (gS/m^2) | 0 |
| frtcis(1) | initial value for unlabeled C in forest system fine root component (gC/m^2) | 0 |
| frtcis(2) | initial value for labeled C in forest system fine root component (gC/m^2) | 0 |
| froote(1) | initial value for N in a forest system fine root component (gN/m^2) | 0 |
| froote(2) | initial value for P in a forest system fine root component (gP/m^2) | 0 |
| froote(3) | initial value for S in a forest system fine root component (gS/m^2) | 0 |
| crtcis(1) | initial value for unlabeled C in forest system coarse root component (gC/m^2) | 0 |
| crtcis(2) | initial value for labeled C in forest system coarse root component (gC/m^2) | 0 |
| croote(1) | initial value for N in a forest system coarse root component (gN/m^2) | 0 |
| croote(2) | initial value for P in a forest system coarse root component (gP/m^2) | 0 |
| croote(3) | initial value for S in a forest system coarse root component (gS/m^2) | 0 |
| wd1cis(1) | initial unlabeled C values for forest system dead fine branch material (g/m^2) | 0 |
| wd1cis(2) | initial labeled C values for forest system dead fine branch material (g/m^2) | 0 |
| wd2cis(1) | initial unlabeled C values for forest system dead large wood material (g/m^2) | 0 |
| wd2cis(2) | initial labeled C values for forest system dead large wood material (g/m^2) | 0 |
| wd3cis(1) | initial unlabeled C values for forest system dead coarse root material (g/m^2) | 0 |
| wd3cis(2) | initial labeled C values for forest system dead coarse root material (g/m^2) | 0 |
| w1lig | initial lignin content of dead fine branches; <i>Range:0 to 1</i> | 0.3 |
| w2lig | initial lignin content of dead large wood ; <i>Range:0 to 1</i> | 0.3 |
| w3lig | initial lignin content of dead coarse roots ; <i>Range:0 to 1</i> | 0.3 |
| Mineral initial parameters | | |
| minerl(1,1) | initial value for mineral N for layer 1 (gN/m^2) | 0.25 |
| minerl(2,1) | initial value for mineral N for layer 2 (gN/m^2) | 0 |
| minerl(3,1) | initial value for mineral N for layer 3 (gN/m^2) | 0 |
| minerl(4,1) | initial value for mineral N for layer 4 (gN/m^2) | 0 |
| minerl(5,1) | initial value for mineral N for layer 5 (gN/m^2) | 0 |
| minerl(6,1) | initial value for mineral N for layer 6 (gN/m^2) | 0 |
| minerl(7,1) | initial value for mineral N for layer 7 (gN/m^2) | 0 |
| minerl(8,1) | initial value for mineral N for layer 8 (gN/m^2) | 0 |
| minerl(9,1) | initial value for mineral N for layer 9 (gN/m^2) | 0 |
| minerl(10,1) | initial value for mineral N for layer 10 (gN/m^2) | 0 |
| minerl(1,2) | initial value for mineral P for layer 1 (gP/m^2) | 0.5 |
| minerl(2,2) | initial value for mineral P for layer 2 (gP/m^2) | 0 |
| minerl(3,2) | initial value for mineral P for layer 3 (gP/m^2) | 0 |
| minerl(4,2) | initial value for mineral P for layer 4 (gP/m^2) | 0 |
| minerl(5,2) | initial value for mineral P for layer 5 (gP/m^2) | 0 |
| minerl(6,2) | initial value for mineral P for layer 6 (gP/m^2) | 0 |

| | | |
|--------------|--|-----|
| minerl(7,2) | initial value for mineral <i>P</i> for layer 7 (gP/m ²) | 0 |
| minerl(8,2) | initial value for mineral <i>P</i> for layer 8 (gP/m ²) | 0 |
| minerl(9,2) | initial value for mineral <i>P</i> for layer 9 (gP/m ²) | 0 |
| minerl(10,2) | initial value for mineral <i>P</i> for layer 10 (gP/m ²) | 0 |
| minerl(1,3) | initial value for mineral <i>S</i> for layer 1 (gS/m ²) | 0.5 |
| minerl(2,3) | initial value for mineral <i>S</i> for layer 2 (gS/m ²) | 0 |
| minerl(3,3) | initial value for mineral <i>S</i> for layer 3 (gS/m ²) | 0 |
| minerl(4,3) | initial value for mineral <i>S</i> for layer 4 (gS/m ²) | 0 |
| minerl(5,3) | initial value for mineral <i>S</i> for layer 5 (gS/m ²) | 0 |
| minerl(6,3) | initial value for mineral <i>S</i> for layer 6 (gS/m ²) | 0 |
| minerl(7,3) | initial value for mineral <i>S</i> for layer 7 (gS/m ²) | 0 |
| minerl(8,3) | initial value for mineral <i>S</i> for layer 8 (gS/m ²) | 0 |
| minerl(9,3) | initial value for mineral <i>S</i> for layer 9 (gS/m ²) | 0 |
| minerl(10,3) | initial value for mineral <i>S</i> for layer 10 (gS/m ²) | 0 |
| parent(1) | initial <i>N</i> value for parent material (gN/m ²) | 0 |
| parent(2) | initial <i>P</i> value for parent material (gP/m ²) | 50 |
| parent(3) | initial <i>S</i> value for parent material (gS/m ²) | 50 |
| secndy(1) | initial <i>N</i> value for secondary <i>N</i> (gN/m ²) | 0 |
| secndy(2) | initial <i>P</i> value for secondary <i>P</i> (gP/m ²) | 15 |
| secndy(3) | initial <i>S</i> value for secondary <i>S</i> (gS/m ²) | 2 |
| occlud | initial value for occluded <i>P</i> (gP/m ²) | 0 |

Table A-2-2 Parameters list for grazing pressure parameters of century ecosystem model

| parameters | Definitions | Value |
|------------|--|-------|
| flgrem | fraction of live shoots removed by a grazing event; <i>Range: 0 to 1</i> | 0.45 |
| fdgrem | fraction of standing dead removed by a grazing event; <i>Range: 0 to 1</i> | 0.07 |
| gfcfet | fraction of consumed C which is excreted in faeces and urine; <i>Range 0 to 1</i> | 0.3 |
| gret(1) | fraction of consumed N which is excreted in faeces and urine (should take into account N losses due to leaching or volatilization from the manure); <i>Range: 0 to 1</i> | 0.8 |
| gret(2) | fraction of consumed P which is excreted in faeces and urine (should take into account P losses due to leaching or volatilization from the manure); <i>Range: 0 to 1</i> | 0.95 |
| gret(3) | fraction of consumed S which is excreted in faeces and urine (should take into account S losses due to leaching or volatilization from the manure); <i>Range: 0 to 1</i> | 0.95 |
| grzeff | effect of grazing on production; =0 grazing has no direct effect on production; =1 linear impact on aboveground biomass; =2 quadratic impact on aboveground biomass and root/shoot ratio; =3 quadratic impact on root/shoot ratio; =4 linear impact on root/shoot ratio; =5 quadratic impact on aboveground biomass and linear impact on root/shoot ratio; =6 linear impact on aboveground biomass and root/shoot ratio; | 1 |
| fecf(1) | fraction of excreted N which goes into faeces (rest goes into urine); <i>Range: 0 to 1</i> | 0.5 |
| fecf(2) | fraction of excreted P which goes into faeces (rest goes into urine); <i>Range: 0 to 1</i> | 0.9 |
| fecf(3) | fraction of excreted S which goes into faeces (rest goes into urine); <i>Range: 0 to 1</i> | 0.5 |
| feclig | lignin content of feces; <i>Range: 0 to 1</i> | 0.25 |

Table A-2-3 Parameters list for crop parameters of century ecosystem model

| Parameters | Definitions | Value |
|--------------|---|-------|
| 'PRDX(1)' | potential aboveground monthly production for crops (gC/m^2) | 270 |
| 'PPDF(1)' | optimum temperature for production for parameterization of a Poisson Density Function curve to simulate temperature effect on growth | 18 |
| 'PPDF(2)' | maximum temperature for production for parameterization of a Poisson Density Function curve to simulate temperature effect on growth | 35 |
| 'PPDF(3)' | left curve shape for parameterization of a Poisson Density Function curve to simulate temperature effect on growth | 1 |
| 'PPDF(4)' | right curve shape for parameterization of a Poisson Density Function curve to simulate temperature effect on growth | 3 |
| 'BIOFLG' | flag indicating whether production should be reduced by physical obstruction | 1 |
| | = 0 production should not be reduced; = 1 production should be reduced; <i>Range: 0 to 1</i> | |
| 'BIOK5' | level of aboveground standing dead + 10% surface litter C at which production is reduced to half maximum due to physical obstruction by the dead material, used only when bioflg = 1 (gC/m^2) | 60 |
| 'PLTMRF' | planting month reduction factor to limit seedling growth; should be 1.0 for grass; <i>Range: 0 to 1</i> | 1 |
| 'FULCAN' | value of aglvc at full canopy cover, above which potential production is not reduced | 100 |
| 'FRTC(1)' | initial fraction of C allocated to roots; for Great Plains equation based on precipitation, set to 0; <i>Range: 0 to 1</i> | 0 |
| 'FRTC(2)' | final fraction of C allocated to roots; <i>Range: 0 to 1</i> | 0 |
| 'FRTC(3)' | time after planting (months with soil temperature greater than rdtmp) at which the final value is reached; must not equal 0 | 0 |
| 'BIOMAX' | biomass level above which the minimum and maximum C/E ratios of the new shoot increments equal to minimum C/P ratio with zero biomass and minimum C/P ratio with biomass equal biomax, respectively ($\text{g biomass}/\text{m}^2$) | 400 |
| 'PRAMN(1,1)' | minimum C/N ratio with zero biomass | 30 |
| 'PRAMN(2,1)' | minimum C/P ratio with zero biomass | 390 |
| 'PRAMN(3,1)' | minimum C/S ratio with zero biomass | 340 |
| 'PRAMN(1,2)' | minimum C/N ratio with biomass equal biomax | 90 |
| 'PRAMN(2,2)' | minimum C/P ratio with biomass equal biomax | 390 |
| 'PRAMN(3,2)' | minimum C/S ratio with biomass greater than or equal to biomax | 340 |
| 'PRAMX(1,1)' | maximum C/N ratio with zero biomass | 35 |
| 'PRAMX(2,1)' | maximum C/P ratio with zero biomass | 440 |
| 'PRAMX(3,1)' | maximum C/S ratio with zero biomass | 440 |
| 'PRAMX(1,2)' | maximum C/N ratio with biomass equal biomax | 95 |
| 'PRAMX(2,2)' | maximum C/P ratio with biomass equal biomax | 440 |
| 'PRAMX(3,2)' | maximum C/S ratio with biomass greater than or equal to biomax | 440 |
| 'PRBMN(1,1)' | intercept parameter for computing minimum C/N ratio for below ground matter as a linear function of annual precipitation | 50 |
| 'PRBMN(2,1)' | intercept parameter for computing minimum C/P ratio for belowground matter as a linear function of annual precipitation | 390 |
| 'PRBMN(3,1)' | intercept parameter for computing minimum C/S ratio for below ground matter as a linear function of annual precipitation | 340 |
| 'PRBMN(1,2)' | slope parameter for computing minimum C/N ratio for below ground matter as a linear function of annual precipitation | 0 |
| 'PRBMN(2,2)' | slope parameter for computing minimum C/P ratio for below ground matter as a linear function of annual precipitation | 0 |
| 'PRBMN(3,2)' | slope parameter for computing minimum C/S ratio for below ground matter as a linear function of annual precipitation | 0 |
| 'PRBMX(1,1)' | intercept parameter for computing maximum C/N ratios for below ground matter as a linear function of annual precipitation | 55 |
| 'PRBMX(2,1)' | intercept parameter for computing maximum C/P ratios for below ground matter as a linear function of annual precipitation | 420 |
| 'PRBMX(3,1)' | intercept parameter for computing maximum C/S ratios for below ground matter as a linear function of annual precipitation | 420 |
| 'PRBMX(1,2)' | slope parameter for computing maximum C/N ratios for below ground matter as a linear | 0 |

| | | |
|-----------------|---|-------------|
| | function of annual precipitation | |
| 'PRBMX(2,2)' | slope parameter for computing maximum C/P ratios for below ground matter as a linear function of annual precipitation | 0 |
| 'PRBMX(3,2)' | slope parameter for computing maximum C/S ratios for below ground matter as a linear function of annual precipitation | 0 |
| 'FLIGNI(1,1)' | intercept for equation to predict lignin content fraction based on annual rainfall for aboveground material; <i>Range: 0 to 1</i> | 0.02 |
| 'FLIGNI(2,1)' | slope for equation to predict lignin content fraction based on annual rainfall for aboveground material. For crops, set to 0.; <i>Range: 0 to 1</i> | 0.001 2 |
| 'FLIGNI(1,2)' | intercept for equation to predict lignin content fraction based on annual rainfall for belowground material; <i>Range: 0 to 1</i> | 0.26 |
| 'FLIGNI(2,2)' | slope for equation to predict lignin content fraction based on annual rainfall for belowground material. For crops, set to 0. <i>Range: 0 to 1</i> | -0.00 15 |
| 'HIMAX' | harvest index maximum (fraction of aboveground live C in grain); <i>Range: 0 to 1</i> | 0 |
| 'HIWSF' | harvest index water stress factor; = 0 no effect of water stress; = 1 no grain yield with maximum water stress; <i>Range: 0 to 1</i> | 0 |
| 'HIMON(1)' | number of months prior to harvest in which to begin accumulating water stress effect on harvest index | 2 |
| 'HIMON(2)' | number of months prior to harvest in which to stop accumulating water stress effect on harvest index; <i>Range: 0 to 12</i> | 1 |
| 'EFRGRN(1)' | fraction of the aboveground N which goes to grain; <i>Range 0 to 1</i> | 0 |
| 'EFRGRN(2)' | fraction of the aboveground P which goes to grain; <i>Range 0 to 1</i> | 0 |
| 'EFRGRN(3)' | fraction of the aboveground S which goes to grain; <i>Range 0 to 1</i> | 0 |
| 'VLOSSP' | fraction of aboveground plant N which is volatilized (occurs only at harvest); <i>Range 0 to 1</i> | 0.15 |
| 'FSDETH(1)' | maximum shoot death rate at very dry soil conditions (fraction/month); for getting the monthly shoot death rate, this fraction is multiplied times a reduction factor depending on the soil water status; <i>Range 0 to 1</i> | 0.2 |
| 'FSDETH(2)' | fraction of shoots which die during senescence month; must be greater than or equal to 0.4; <i>Range 0 to 1</i> | 0.95 |
| 'FSDETH(3)' | additional fraction of shoots which die when aboveground live C is greater than fsdeth(4); <i>Range 0 to 1</i> | 0.2 |
| 'FSDETH(4)' | the level of aboveground C above which shading occurs and shoot senescence increases | 150 |
| 'FALLRT' | fall rate (fraction of standing dead which falls each month); <i>Range 0 to 1</i> | 0.15 |
| 'RDR' | maximum root death rate at very dry soil conditions (fraction/month); for getting the monthly root death rate, this fraction is multiplied times a reduction factor depending on the soil water status; <i>Range: 0 to 1</i> | 0.05 |
| 'RTDTMP' | physiological shutdown temperature for root death and change in shoot/root ratio | 2 |
| 'CRPRTF(1)' | fraction of N retranslocated from grass/crop leaves at death; <i>Range: 0 to 1</i> | 0 |
| 'CRPRTF(2)' | fraction of P retranslocated from grass/crop leaves at death; <i>Range: 0 to 1</i> | 0 |
| 'CRPRTF(3)' | fraction of S retranslocated from grass/crop leaves at death; <i>Range: 0 to 1</i> | 0 |
| 'SNFXMX(1)' | symbiotic N fixation maximum for grassland | 0.002 |
| 'DEL13C' | delta 13C value for stable isotope labeling | -24 |
| 'CO2IPR(1)' | in a grassland/crop system, the effect on plant production of doubling the atmospheric CO ₂ concentration from 350 ppm to 700 ppm | 1.3 |
| 'CO2ITR(1)' | in a grassland/crop system, the effect on transpiration rate of doubling the atmospheric CO ₂ concentration from 350 ppm to 700 ppm | 0.6 |
| 'CO2ICE(1,1,1)' | in a grassland/crop system, the effect on minimum C/N ratio of doubling the atmospheric CO ₂ concentration from 350 ppm to 700 ppm | 1 |
| 'CO2ICE(1,1,2)' | in a grassland/crop system, the effect on minimum C/P ratio of doubling the atmospheric CO ₂ concentration from 350 ppm to 700 ppm | 1 |
| 'CO2ICE(1,1,3)' | in a grassland/crop system, the effect on minimum C/S ratio of doubling the atmospheric CO ₂ concentration from 350 ppm to 700 ppm | 1 |
| 'CO2ICE(1,2,1)' | in a grassland/crop system, the effect on maximum C/N ratio of doubling the atmospheric CO ₂ concentration from 350 ppm to 700 ppm | 1 |
| 'CO2ICE(1,2,2)' | in a grassland/crop system, the effect on maximum C/P ratio of doubling the atmospheric CO ₂ concentration from 350 ppm to 700 ppm | 1 |
| 'CO2ICE(1,2,3)' | in a grassland/crop system, the effect on maximum C/S ratio of doubling the atmospheric CO ₂ concentration from 350 ppm to 700 ppm | 1 |
| 'CO2IRS(1)' | in a grassland/crop system, the effect on root to shoot ratio of doubling the atmospheric CO ₂ concentration from 350 ppm to 700 ppm | 1.3 |

Appendix B

Governing equations of TOPLATS hydrological model

B.1. Hydrological balance.

Separate hydrological fluxes are solved at each time step, and for each computational element, for the following four reservoirs: the canopy, root, surface zone-1, surface zone-2 and transmission zone. The root zone depth was from surface down to 0.05 m. The surface zone-1 was ranged from land surface to 0.5 m. The surface zone-2 was down to 1.5 m from the ground surface. The transmission zone was below 1.5 m to water table.

B.1.1. Canopy water balance

Canopy water balance is performed to determine net precipitation (P_{net}) and actual evapotranspiration from canopy (e_{wc}) for given precipitation P amount as follows;

$$\frac{dw_c}{dt} = P - e_{wc} - P_{net} \quad (0 \leq w_c \leq w_{sc}) \quad (B)$$

where w_c is the canopy storage, w_{sc} is the maximum storage capacity.

The maximum storage capacity is calculated based on Dickinson (1984) as a function of the LAI as follows;

$$w_{sc} = 0.0002LAI \quad (B2)$$

The wet canopy evaporation (e_{wc}) is calculated from potential evaporation pe_{wc} and fraction of wet canopy, obtained by Deardorff (1978), as

$$\left\{ \begin{array}{l} f_{wc} = \left(\frac{w_c}{w_{sc}} \right)^{\frac{2}{3}} \quad (pe_{wc} > 0) \\ f_{wc} = 1 \quad (pe_{wc} \leq 0) \end{array} \right. \quad (B3)$$

$$(B4)$$

Bare soil evaporation (e_{bs}) is determined as the minimum of the exfiltration capacity ($e(E_c)$) and potential evaporation (pe_{bs}) is determined from the energy balance), so that

$$e_{bs} = \min[e(E_c), pe_{bs}] \quad (B5)$$

Transpiration from dry canopy (e_{dc}) is determined as the minimum of transpiration capacity (t_c) and transpiration rate (t_r) as follow

$$e_{dc} = \min[t_c, t_r] \quad (B6)$$

B.1.2. Root zone water balance

Separate hydrological fluxes are solved at each time step, and for each computational element, for the following four reservoirs: the root, surface zone1, surface zone2, and transmission zone.

For root zone:

$$\left\{ \begin{array}{l} z_{rz} \frac{d\theta_{rz}}{dt} = f_{bs}i_{bs} + f_v f_{r,rz} i_{v,rz} + f_v f_{r,lz} i_{v,lz} - d_{rz} - f_{bs}e_{bs} - f_v f_{r,rz} t_{v,rz} - g_{rz} \quad (z_{rz} > 0) \\ \theta_{rz} = \theta \quad (z_{rz} = 0) \end{array} \right. \quad (B7) \quad (B8)$$

where the subscript $_{rz}$ refers to the root zone; the subscripts $_{lz}$ refers to lower zone; $_{bs}$ refer to bare soil; $_{v}$ refers to vegetated surface; f_r is root fraction in a given zone; z_{rz} is the depth of the root zone; θ_{rz} is the soil moisture in the root zone; g_{rz} is the gravitational drainage into the root zone; d_{rz} is diffusive flux from above soil layer to below soil layer; f is fractional area with a given land cover type; i , e , and t are the respective infiltration, evaporation and transpiration rates for given land cover type.

For surface zone 1:

$$\left\{ \begin{array}{l} z_{sz1} \frac{d\theta_{sz1}}{dt} = g_{rz} - g_{sz1} + d_{rz} - d_{sz1} - f_{v,sz1} t_{v,sz1} \quad (z_{sz1} > 0) \\ \theta_{sz1} = \theta \quad (z_{sz1} = 0) \end{array} \right. \quad \begin{array}{l} \text{(B9)} \\ \text{(B0)} \end{array}$$

Where the variables are similar those root zone water balance equation.

For transmission zone:

$$z_{ts} \frac{d\theta_{ts}}{dt} = g_{rz} - g_{ts} \quad \text{(B1)}$$

The infiltration rate for bare soil is taken as the minimum of infiltration capacity, or precipitation rate, such as

$$i_{bs} = \min[i(I), P] \quad \text{(B2)}$$

where I is actual infiltration capacity.

Actual infiltration into vegetated surface is taken as the minimum of infiltration capacity, or net precipitation rate, so that

$$i_v = \min[i(I), P_{net}] \quad \text{(B3)}$$

The infiltration capacity of bare soil and vegetated surface was given by Milly (1986) in term of cumulative infiltration rate (I_{cum}), and soil parameters as follows

$$I = CK_s \left(1 + \frac{1}{\sqrt{1 + \frac{4CK_s I_{cum}}{S^2} - 1}} \right) \quad \text{(B4)}$$

$$C = 0.5 \left(1 + \left(\frac{\theta_{rz} - \theta_r}{\theta_s - \theta_r} \right)^{\frac{2+3B}{B}} \right) \quad \text{(B5)}$$

where C is effect of gravity; θ_s is saturated soil moisture; θ_r is residual soil moisture; B is

pore size index and K_s is saturated hydraulic conductivity

Drainage from base of the root, surface zone1, surface zone2 and transmission zone is assumed to proceed at gravity driven rates. These fluxes are described by

$$g_{rz} = K_s \left[\frac{\theta_{rz} - \theta_r}{\theta_s - \theta_r} \right]^{\frac{2+3B}{B}} \quad (\text{B6})$$

The diffusive flux for each soil layers is calculated by Peters-Lidard et al. (1997) in term of Brooks and Corey (1964) parameters, so that

$$d_{rz} = D(\theta) \frac{(\theta_{rz} - \theta_{ts})}{(z_{rz}/2 - z_{sz1}/2)} \quad (\text{B7})$$

$$D(\theta) = BK_{s,ave} \frac{\psi_b}{(\theta_s - \theta_r)} \left[\frac{\theta_a - \theta_r}{\theta_s - \theta_r} \right]^{\frac{2+3B}{B}+2} \quad (\text{B8})$$

where ψ_b ; bubbling pressure; θ_a is arithmetic average of soil layers and $K_{s,ave}$ is a harmonic average saturated hydraulic conductivity at two depths.

$$K_{s,ave} = \frac{1}{\frac{1}{2K_{zone}} + \frac{1}{2K_{zone+1}}} \quad (\text{B9})$$

$$\theta_a = \frac{\theta_{zone} + \theta_{zone+1}}{2} \quad (\text{B20})$$

where the subscript +1 indicates the change of soil layers.

Changes in the vertical saturated hydraulic conductivity along the soil column are described by

$$K_{srz} = K_s \exp\left(-f \frac{Z_{rz}}{2}\right) \quad (\text{B21})$$

$$K_{sz1} = K_s \exp\left(-f \left(Z_{rz} + \frac{Z_{sz1}}{2}\right)\right) \quad (\text{B22})$$

$$K_{sz2} = K_s \exp\left(-f \left(Z_{rz} + Z_{sz1} + \frac{Z_{sz2}}{2}\right)\right) \quad (\text{B23})$$

$$K_{ts} = K_s \exp\left(-f\left(Z_{rz} + Z_{sz1} + Z_{sz2} + \frac{Z_{ts}}{2}\right)\right) \quad (\text{B24})$$

where f is exponential decay of K_s .

B.1.3. Runoff

The topographic index is calculated as follows;

$$\lambda = \ln\left(\frac{a}{\tan B}\right) \quad (\text{B25})$$

where λ is topographic index ; a is the upslope area and $\tan B$ is the local slope angle acting on a grid.

$$z = \bar{z} - \frac{1}{f}(\bar{\lambda} - \lambda) \quad (\text{B26})$$

where z is the depth to water table in each grid; \bar{z} is basin average water table depth; $\bar{\lambda}$ is basin average topographic index values.

Saturated excess runoff (R_{sat}) can occur at saturated soil region, so that it is determined by P_{net} ,

$$R_{sat} = P_{net} \quad (\text{B27})$$

Infiltration excess runoff (R_{inf}) can occur when infiltration rate is greater than the amount of P_{net} , such as

$$R_{inf} = P_{net} - I \quad (\text{B28})$$

Baseflow (Q_b) from the saturated zone is calculated by Sivapalan et al. (1987), so that

$$Q_b = Q_0 \exp(-f\bar{z}) \quad (\text{B30})$$

$$Q_b = AT_e \exp(\bar{\lambda}) \quad (\text{B31})$$

where A is watershed area; T_e is the catchment average transmissivity coefficient (i.e., $\frac{K_s}{f}$)

B.2. Energy balance

Definitions of all parameters of energy balance are shown in Table B-2-1. Local energy balance is expressed in the following equation.

$$R_n = \rho_w LE + H + G \quad (\text{B32})$$

$$R_n = R_{sd}(1 - \alpha) + \varepsilon R_{ld} + \delta T_s^4 \quad (\text{B33})$$

The latent heat flux is given by Milly (1991).

$$\rho_w LE = \frac{\rho_a c_p}{\gamma(r_{av} + r_c)} (e_s(T_s) - e_a) \quad (\text{B34})$$

The sensible heat flux is calculated by following equation.

$$H = \frac{\rho_a c_p}{r_{ah}} (T_s - T_a) \quad (\text{B35})$$

Ground heat flux is calculated by following equation.

$$G = \frac{k_1 k_2 dt \cdot 2(T_s - T_p) + c_1 k_2 z_d^2 (T_s - T_m)}{G_d} \quad (\text{B36})$$

$$G_d = k_1 z_d dt + 2k_2 z_m dt + c_2 z_d^2 z_m \quad (\text{B37})$$

Aerodynamic resistance is a function of the bulk Richardson number calculated based on Ek and Mahrt (1991) with a stability correction developed by Peters-Lidard et al. (1997). The function of the bulk Richardson number is given by Ek and Mahrt, (1991)

$$r_{ah} = r_{av} = \frac{1}{k^2 u F(R_{iB})} \ln\left(\frac{z_a - d}{z_{0,m}}\right) \ln\left(\frac{z_a - d}{z_{0,h}}\right) \quad (\text{B38})$$

The stability correction is given by Peters-Lidard et al. (1997)

$$F(R_{iB}) = \exp[-R_{iB}], R_{iB} \geq 0 \quad (\text{B39})$$

$$F(R_{iB}) = 1 - \frac{15R_{iB}}{1 - 7.5F_1F_2}, R_{iB} \leq 0 \quad (\text{B40})$$

$$F1 = \left[\frac{10k2}{\ln\left(\frac{z_a - d}{z_{0,m}}\right) \ln\left(\frac{z_a - d}{z_{0,h}}\right)} \right] \quad (\text{B41})$$

$$F2 = \left(-R_{iB} \left(\frac{z_a - d}{z_{0,m}} \right) \right)^{1/2} \quad (\text{B42})$$

$$R_{iB} = \frac{g_z (\theta_{vz} - \theta_{vs})}{\theta_{vz} |V_z|^2} \quad (\text{B43})$$

$$\theta_v = \theta(1 + 0.61q) \quad (\text{B44})$$

$$\theta = T \left(\frac{1000}{p} \right)^{0.286} \quad (\text{B45})$$

Canopy resistance is calculated using the method of Jacquemin and Noilhan (1990), which allows for the effects of solar radiation, the air humidity deficit, ambient temperature and water stress as expressed in the following equations.

$$r_c = \frac{r_{st \min}}{LAI} (F_1 F_2 F_3 F_4)^{-1} \quad (\text{B46})$$

$$F_1 = \frac{r_{st \min} / r_{st \max} + f_a}{1 + f_a} \quad (\text{B47})$$

$$f_a = 0.55 \frac{R_{sd}}{R_{pl}} \frac{2}{LAI} \quad (\text{B48})$$

$$F_2 = \frac{1}{1 - \beta [q_s(T_s) - q_a]} \quad (\text{B49})$$

$$F_3 = 1 - B1 [T_{ref} - T_a]^2 \quad (\text{B50})$$

$$F_4 = \frac{\theta_i - \theta_\omega}{\theta_{cap} - \theta_\omega} \quad (\text{B51})$$

Table B -2-1 List of Symbols for energy balance equations.

| | |
|------------------|---|
| α | Albedo |
| β | Parameter for vapour pressure deficit adjustment to canopy resistance |
| ε | Emissivity |
| γ | Psychrometric constant |
| $\rho_w LE$ | Latent heat flux |
| ρ_w | Density of water |
| ρ_a | Density of air |
| σ | Stefan-Boltzmann constant |
| θ_w | Wilting soil moisture |
| θ_{cap} | Field capacity |
| θ_i | Wilting soil moisture |
| B | Parameter for temperature adjustment to canopy resistance |
| C_p | Specific heat of air |
| D | Damping depth of diurnal temperature variations |
| d | Zero plane displacement |
| E | Evapotranspiration rate |
| ea | Vapor pressure in the air |
| $es(T_s)$ | saturated vapor pressure at temperature T_s |
| $F(RiB)$ | Stability correction |
| $F1$ | Effect of solar radiation |
| $F2$ | Effect of vapor pressure deficit |
| $F3$ | Effect of air temperature |
| $F4$ | Effect of soil moisture |
| G | ground heat flux |
| k | Von Karman's constant |
| k_s | Soil thermal conductivity |
| L | latent heat of evaporation |
| LAI | Leaf area index |
| $q_s(T_s) - q_a$ | Specific humidity deficit of surrounding air |
| r_a | Aerodynamic resistance for vapor transport |
| r_{ah} | Aerodynamic resistance for heat transport |
| r_c | Canopy resistance |
| R_{ld} | Downward longwave radiation |
| R_n | Net radiation |
| R_{pl} | Radiation parameter for PAR adjustment to canopy resistance |
| R_{sd} | Downward shortwave radiation |
| r_{stmax} | Maximum stomatal resistance used in PAR adjustment to canopy resistance |
| r_{stmin} | Minimum stomatal resistance |
| T_a | Air temperature |
| T_{ref} | Reference temperature used in temperature adjustment to canopy resistance |
| T_s | Surface or skin temperature |
| $u(z_a)$ | Wind speed at height z_a |
| $z_{0;h}$ | Roughness length for heat |
| $z_{0;m}$ | Roughness length for momentum |
| z_a | Wind speed observation height |

Table B -2-2 Parameter list of TOPLATS hydrological model at grassland site (KBU site)

| Parameter | Symbol | Value |
|---|---------------|--------------------|
| Model geometry | | |
| Meteorological data height (m) | z_a | 2.5 |
| Wind data height (m) | z_w | 2.31 |
| Middle soil layer depth (m) | z_1 | 0.5 |
| Deep soil layer depth (m) | z_2 | 0.85 |
| Surface zone soil moisture depth (m) | z_{sz} | 0.1 |
| Vegetation parameter | | |
| Minimum stomatal resistance (s m-1) | r_{stmin} | 50 |
| $F1 (PAR)$ (s m ⁻¹) | r_{stmax} | 5000 |
| $F2 (PAR)$ (W m ⁻²) | R_{pl} | 100 |
| $F3 (q)$ | β | 0.0002 |
| $F4 (T)$ (K ⁻²) | B | 0.00016 |
| Albedo (dry vegetation) | α_d | Time variable |
| Albedo (wet vegetation) | α_w | Time variable |
| Emissivity | ε | 0.98 |
| LAI (m ² m ⁻²) | | Time variable |
| Zero-displacement (m) | d_0 | Time variable |
| Roughness length for momentum (m) | $z_{o,m}$ | Time variable |
| Roughness length for heat (m) | $z_{o,h}$ | Time variable |
| Soil parameter | | |
| Saturated hydraulic conductivity (m s-1) | K_s | 7.05×10^6 |
| Saturated soil moisture content (m ³ m ⁻³) | θ_s | 0.40 |
| Residual soil moisture content (m ³ m ⁻³) | θ_r | 0.01 |
| Pore size index | B | 0.65 |
| Bubbling pressure (m) | ψ_c | 0.35 |
| Dry soil heat capacity (J K ⁻¹ kg ⁻¹) | C_s | 1.34×10^6 |
| Quartz content | q | 0.60 |

Table B -2-3 Parameter list of TOPLATS hydrological model at forest site (FOR site)

| Parameter | Symbol | Value |
|---|---------------|--------------------|
| Model geometry | | |
| Meteorological data height (m) | z_a | 29 |
| Wind data height (m) | z_w | 29 |
| Middle soil layer depth (m) | z_1 | 0.5 |
| Deep soil layer depth (m) | z_2 | 0.85 |
| Surface zone soil moisture depth (m) | z_{sz} | 0.1 |
| Vegetation parameter | | |
| Minimum stomatal resistance (s m-1) | r_{stmin} | 50 |
| $F1 (PAR)$ (s m ⁻¹) | r_{stmax} | 5000 |
| $F2 (PAR)$ (W m ⁻²) | R_{pl} | 100 |
| $F3 (q)$ | β | 0.0002 |
| $F4 (T)$ (K ⁻²) | B | 0.00016 |
| Albedo (dry vegetation) | α_d | Time variable |
| Albedo (wet vegetation) | α_w | Time variable |
| Emissivity | ε | 0.98 |
| LAI (m ² m ⁻²) | | Time variable |
| Zero-displacement (m) | d_0 | Time variable |
| Roughness length for momentum (m) | $z_{o,m}$ | Time variable |
| Roughness length for heat (m) | $z_{o,h}$ | Time variable |
| Soil parameter | | |
| Saturated hydraulic conductivity (m s-1) | K_s | 6.05×10^6 |
| Saturated soil moisture content (m ³ m ⁻³) | θ_s | 0.35 |
| Residual soil moisture content (m ³ m ⁻³) | θ_r | 0.02 |
| Pore size index | B | 0.51 |
| Bubbling pressure (m) | ψ_c | 0.30 |
| Dry soil heat capacity (J K ⁻¹ kg ⁻¹) | C_s | 1.38×10^6 |
| Quartz content | q | 0.60 |

Appendix C

Method of determining residual soil moisture (Brooks and Corey, 1966)

$$S_e = \frac{S - S_r}{1 - S_r} \quad \text{for } S_r < S \leq 1.0 \quad (1)$$

where S_e is effective saturation; S is soil moisture content; S_r is residual soil moisture.

Step 1. It is necessary to have measurement of soil moisture content as function of suction to determine those parameters as shown Fig. c1. Here we used actual measured data that measured on 16 June of 2003. (Location: near KBU site)

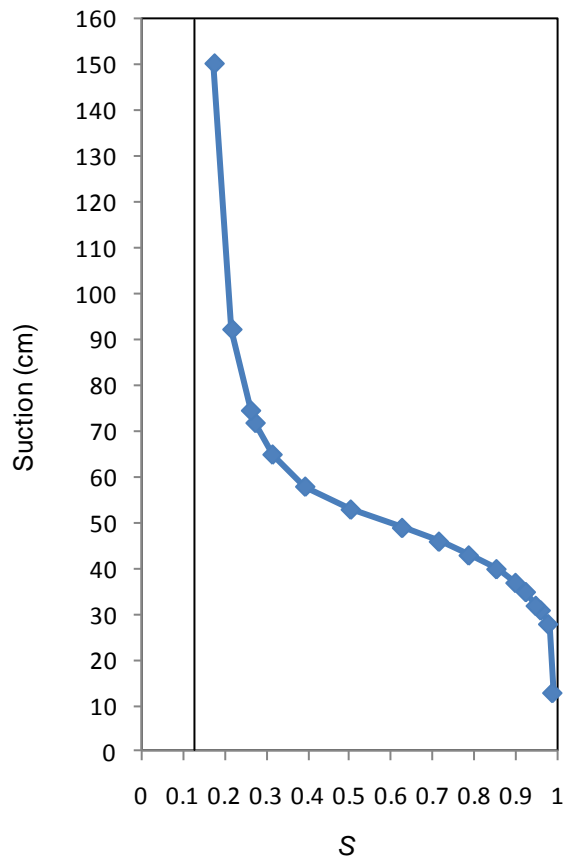


Fig. c1 Suction as a function of soil moisture

Step2. An approximate value of S_r is obtained by selecting a value of S (soil moisture) at which the curve of suction versus S appears to approach a vertical curve as shown in Fig. c1. Here, S_r has been decided as approximately equal to 0.15. With this estimate of S_r , tentative values of $\log S_e$ are computed and plotted as function of suction and then bubbling pressure is determined in Fig. c2.

Step 3. Determination of P_b/γ (Bubbling pressure).

The bubbling pressure is determined by the intercept where the straight line meets ordinate representing $S_e=1.0$ and it is called bubbling pressure. P_b/γ was determined approximately as a value of 31.0 cm

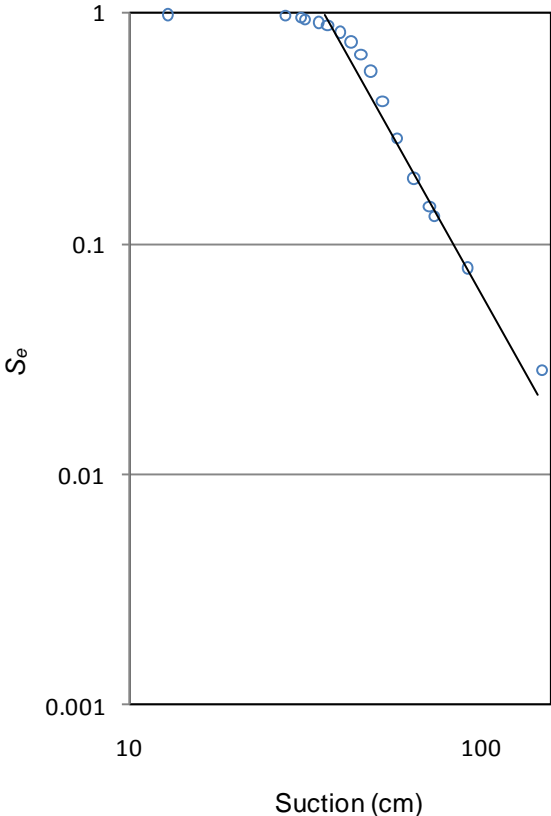


Fig. c2 Log-log plot of S_e and suction

This idea is based on independent domain approach. This approach allows calculating curve from the boundary wetting and drying curve and it would be represented by straight line. Concept of independent domain is suction range over the elements drains out of the body and the latter that over which it re-enters the body.

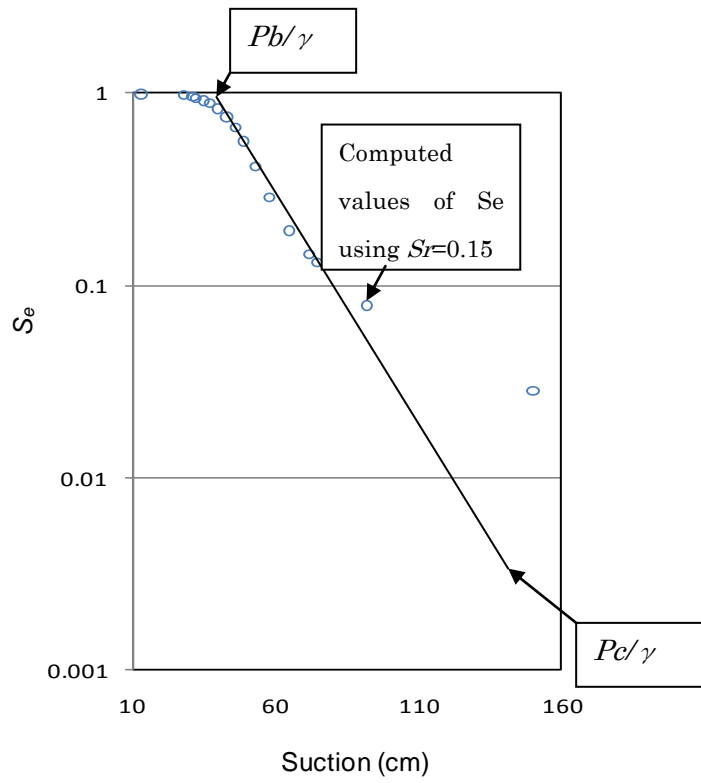


Fig. c3 Effective saturation as function of suction

Usually, plot will not be a straight line, but intermediate portion of the computed values will fall on straight line as shown in Fig. c2.

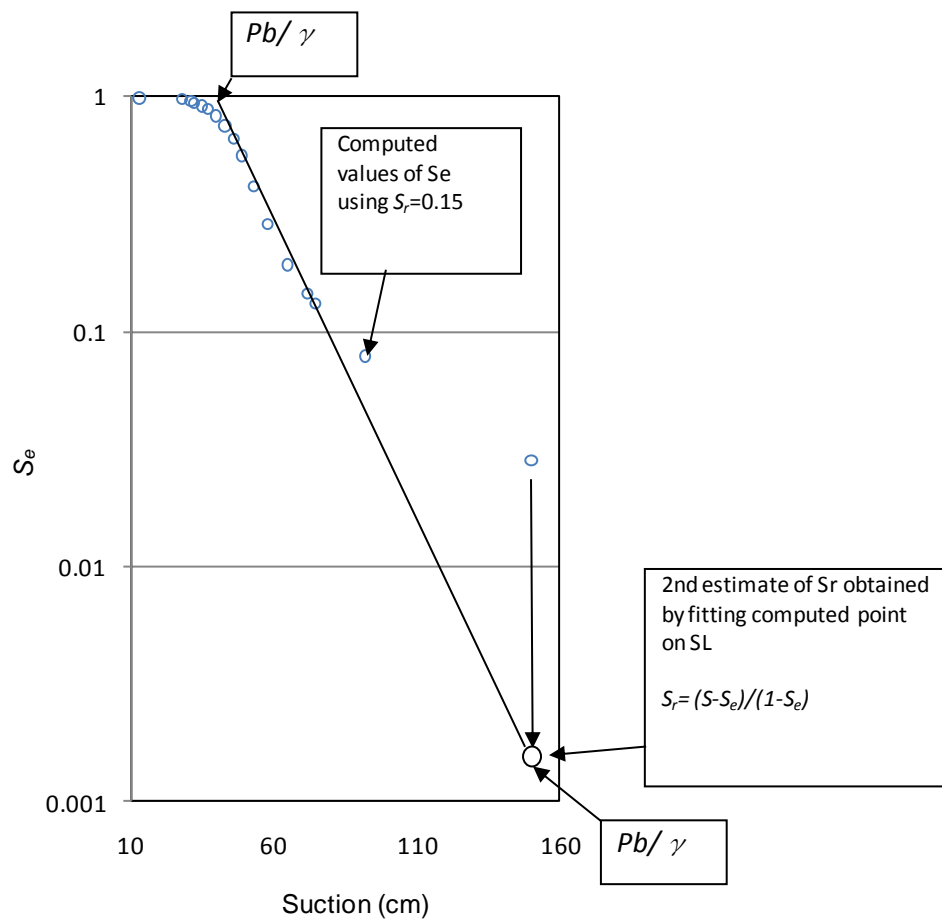


Fig. c4 Effective saturation as function of suction

Step 4. A second estimate of S_r is then obtained such that value of S_e , in the high suction range which does not lie on the straight line as shown in Fig. c2. Second estimate of S_r is usually adequate; all points of S_e will lie sufficiently close to straight line when points are recomputed using new value of S_r . If this is not case, the process is repeated until a value of S_r is obtained that results in straight line for most values of $Pc/\gamma > Pb/\gamma$. Once we obtained the results, that most of points within range $Pc/\gamma > Pb/\gamma$ lies closely on straight line with a value of S_r , which will be served as S_r value for any application.